SILESIAN UNIVERSITY OF TECHNOLOGY
FACULTY OF MECHANICAL ENGINEERING
DEPARTMENT OF COMPUTATIONAL MECHANICS AND ENGINEERING

Anna Skorupa, BEng, MSc

Multi-scale modelling of heat and mass transfer in tissues and cells during cryopreservation including interval methods

PhD dissertation

Supervisor:
Alicja Piasecka-Belkhayat, BEng, PhD, DSc

Gliwice 2023

Contents

Nomenclature

Symbol		***Meaning***
Latin symbols		
A	[m^2]	Sell surface area or microchannel
A_{Lp}	[$m^2 \cdot s \cdot kg^{-1}$]	Pre-exponential factors for L_p
A_{Ps}	[$m \cdot s^{-1}$]	Pre-exponential factors for P_s
a, e, i, j	–	Variable
B	[$K \cdot s^{-1}$]	Constant cooling rate
B_i or B_j	[$kg \cdot mol^{-1}$]	Second osmotic virial coefficient for types *i or j*
C_{STC}	[$J \cdot m^{-3} \cdot K^{-1}$]	Substitute thermal capacity
c, c_s, c_n, c_d, c_k, c_w	[$mol \cdot m^{-3}$]	Molar concentration
c_p, c_{cw}, c_f, c_{in}, c_N, c_{sl}	[$J \cdot kg^{-1} \cdot K^{-1}$]	Specific heat capacity
c_v	[$J \cdot m^{-3} \cdot K^{-1}$]	Volumetric heat capacity
D	[$m^2 \cdot s^{-1}$]	Molecular diffusion coefficient
$E_{A,Lp}$, $E_{A,Ps}$	[$J \cdot mol^{-1}$]	Activation energies L_p and P_s
f_s	–	State function
$G_{\boldsymbol{b}}$	[$m^3 \cdot s^{-1} \cdot m^{-3}$]	Blood perfusion rate
$\mathbf{g}$	[$m \cdot s^{-2}$]	Fluid acceleration vector
H	[J]	Enthalpy function
H, H_f, R, W_f, W_w	[m]	Dimensions
h_1, h_2, h	[m]	Mesh steps
$\mathbf{J}$	[$mol \cdot m^{-2} \cdot s^{-1}$]	Diffusion flux vector
k, k_1, k_2, k_{cw}, k_f, k_{in}, k_N, k_{sl}	[$W \cdot m^{-1} \cdot K^{-1}$]	Thermal conductivity
k_a	[$s^{-1} \cdot K^{-1}$]	Characteristic coefficient
k_B	[$J \cdot K^{-1}$]	Boltzmann constant

k_{diss}	–	Dissociation constant
k_w and k_s	[m·s^{-1}]	Water and solute permeability constant
L	[J·kg^{-1}]	Latent heat
L_p	[m^2·s·kg^{-1}]	Hydraulic conductivity
M	[mol·m^{-3}]	Osmolarity
$M_{at.}$	[kg·mol^{-1}]	Molar mass
M_u	[u]	Molecular mass
m	[kg]	Mass of the sample
m, n	–	Number of nodes
m_i or m_j	[mol·kg^{-1}]	Molality of species i or j
m_η		Fin parameter
N_s (e.g. N_d)	[mol]	Intracellular number of permeating solute molecules
n	–	Normal vector to the sub-domain
n	–	Characteristic coefficient in Einstein-Stokes equation
P_s	[m·s^{-1}]	Solute permeability
p	[Pa]	Pressure
Q	[J]	Amount of heat (energy)
Q_{en}	[cal·mol^{-1}]	Activation energy
Q_f	[J]	Internal heat sources for freezing
Q_{int}, Q_{met}, Q_{perf}	[J]	Internal, metabolic, perfusion heat source
Q_{vol}	[m^3·s^{-1}]	Volumetric flow rate
q	[W·m^{-2}]	Heat flux (vector)
R	[J·mol^{-1}·K^{-1}]	Gas constant
R_e, R_α, R_Γ	[m^2·K·W^{-1}]	Thermal resistance
R_s	–	Source term
r, z	[m]	Geometric coordinates of the cylindrical coordinate system
r_{cell}	[m]	Isotonic cell radius of cell
$r_{i,j}$	[m]	Radial coordinate of the node (i, j)
r_s	[m]	Radius of the spherical particle
S	[mol]	Intracellular amount of permeating solute
T, T_o	[°C] or [K]	Temperature

T_{bath}	[°C]	Temperature of bath solution
T_{ext}	[°C] or [K]	Temperature of the surrounding mediums
T_l, T_s	[K]	Liquidus and solidus temperature
T_m	[K]	Freezing (melting) temperature
T_Γ	[°C]	Temperature on the boundary
t	[s]	Time
Δt	[s]	Time step
$\mathbf{u}$	[$m \cdot s^{-1}$]	Flow velocity field (vector)
u, v, w	[$m \cdot s^{-1}$]	Velocity vector components
u_{in}	[$m \cdot s^{-1}$]	Inlet velocity
u_Γ, v_Γ, w_Γ	[$m \cdot s^{-1}$]	Components of the velocity vectors on the edge
V	[m^{-3}]	Volume
V_b	[m^3]	Osmotically inactive volume
V_{cell}	[m^3]	Total volume of cell
V_s, V_w	[m^3]	Intracellular solute and water volume
V_{w+s}	[m^3]	Intracellular volume of water and solute
Vm	[$m^3 \cdot kg^{-1}$]	Volume per unit of mass
v_j	[$L \cdot mol^{-1}$]	Partial molar volume of component j
W_e	[$s \cdot m^{-1}$]	Mass diffusion resistance
w, w_d, w_k, w_w	[% (w/w)]	Mass fraction
x	[m]	Displacement or component of the Cartesian coordinate system

Greek letters

α_Γ	[$W \cdot m^{-2} \cdot K^{-1}$]	Convection heat transfer coefficient
η	–	Fin efficiency
μ	[Pa·s]	Dynamic viscosity
ν	[$m^2 \cdot s^{-1}$]	Kinetic viscosity coefficient
π	[$mol \cdot kg^{-1}$]	Osmolality
ρ	[$kg \cdot m^{-3}$]	Density
σ	–	Reflect coefficient
τ_t, τ_q	[s]	Thermalization and relaxation time
Φ, Φ_e	–	Shape function

φ	$[\mathrm{mol \cdot m^{-3}}]$	Concentration of the substance (quantities)
χ	–	Degree of ice crystallisation
Other		
∇		Nabla operator
$\dot{(\cdot)}$		First-order time derivative
$\ddot{(\cdot)}$		Second-order time derivative
$\widetilde{(\cdot)}$		Fuzzy number
$\overline{(\cdot)}$		Interval number
$(\cdot)'$		First-order derivative
$\partial(\cdot)/\partial n$		Normal derivative
Subscript		
a		Variable
b		Blood parameters
bath		Bath solution
cw, sl		Chip wall and sample layer
d		DMSO
e		Given node
ext		Value of variable of surrounding mediums
f		State below freezing (melting) point sub-domain
i, j		Nodes (in numerical model) or given component, types (in mathematical model)
in		Intermediate sub-domain
k		KCl
l, s		Liquid and solid sub-domain
N		Natural state sub-domain
w		Water
wf		Working fluid
Γ		Variable on the boundary of the domain
Superscript		
0		Initial moment
e, i		Extracellular and intracellular solute
f		Moment of time
s		Domain of solution: *e* or *i*

1. Aim and scope of the work

Cryopreservation is a process that aims to preserve cells or tissues without significantly affecting their basic functions, including viability and mechanical properties. During this process, biological activity is initially slowed down by cooling to a temperature below zero Celsius degrees (for example to about −80 °C or −196 °C) and afterward reclaimed by warming to physiological temperature. Cryopreservation is an important field of cryobiology and a continuously developing discipline. Cryopreservation involves freezing of animal as well as human cells and tissues. The following cells and tissues can be frozen: oocytes, embryos, sperm, semen, testicular tissue, hepatocytes and others. Research in this field additionally includes the preservation of organs for transplantation. Low-temperature stem cell storage is a step in developing tissue engineering, which is an opportunity to regenerate soft tissues and treat many diseases. Cryopreservation also makes it possible to bank cells or various pathogens in order to preserve them for further research [57, 182].

In order for this process be effective, it cannot negatively impact the quality of the sample after restoring. Cell damage during cryopreservation is related to biophysical changes including cell dehydration as well as intracellular and extracellular ice crystal formation. Determining the optimum cooling/warming rate is one of the approaches to protect the cryopreserved material, thus controlling both water transport across cell membranes and intracellular water freezing processes. Another concept to prevent cryogenic damage of the biological sample is to use appropriate cryoprotectants (CPA) such as glycerol or dimethyl sulfoxide (DMSO) [94, 173].

According to the cooling rate and the concentration of CPA, the cryopreservation can be performed by slow freezing or vitrification, which are the most common methods. Slow freezing is mainly characterised by a low cooling rate and low CPA concentration compared to vitrification. In contrast, vitrification, in which the glass state transforms from the liquid state, is typified by a high cooling rate and high CPA concentration [182]. Some other techniques of cryopreservation are also known, such as “liquidus tracking” (LT) method. The main idea of the LT approach is to immerse the biological sample

in a solution of CPA while controlling its temperature and concentration. There is then a change in the freezing (melting) point, and the thermodynamic conditions of the solution “track” the liquidus line for the system [65].

The cryopreservation process is also accompanied by transport. First and foremost, alternations related to heat transfer occur during this process. The mechanism of bioheat transfer is considered as a combination of convection and thermal conduction. The thermal distribution is most often described by the Fourier equation, the Pennes equation, the Cattaneo-Vernotte equation and the dual phase lag equation. When preparing a heat transport model for the cryopreservation process, it is also important to consider the phase transition phenomena that are associated with ice crystallisation [182].

In addition to heat exchange, mass transfer also occurs during cryopreservation. It should then be considered a momentum transfer described, for example, by the Navier-Stokes equations. Modelling of the delivery of the cryoprotectant to the sample chamber, especially in microfluidic systems, is examined as a fluid flow problem [159, 182].

Mass transport is also related to the movement of molecules. It occurs when a concentrated cryoprotectant solution diffuses into the extracellular space. Consequently, the convection-diffusion equation is used to express this phenomenon. In cases where advection is neglected, particle diffusion is characterised by Fick's laws [7, 9].

When modelling cryopreservation, osmotic transport should also be analysed. This describes the changes in cell volume caused by changes in the molar number of cryoprotectant and the volume of water in the intracellular solution. The two-parameter formalism approach or the Kedem-Katchalsky equations can be used to determine these values [36].

It is evident that cryopreservation is an extremely complex process and its modelling requires a combination of knowledge from mechanics, biology and chemistry. This dissertation is devoted to multi-scale modelling of the heat and mass transfer during cryopreservation. Figure 1.1 shows a diagram of the multiphysical coupled phenomena of the cryopreservation problem.

It is important to emphasise that efficient solutions to the more complicated boundary–initial problems of heat and mass transfer at tissue and cell level can only be obtained by numerical methods, for example, by the finite difference method (FDM) [88].

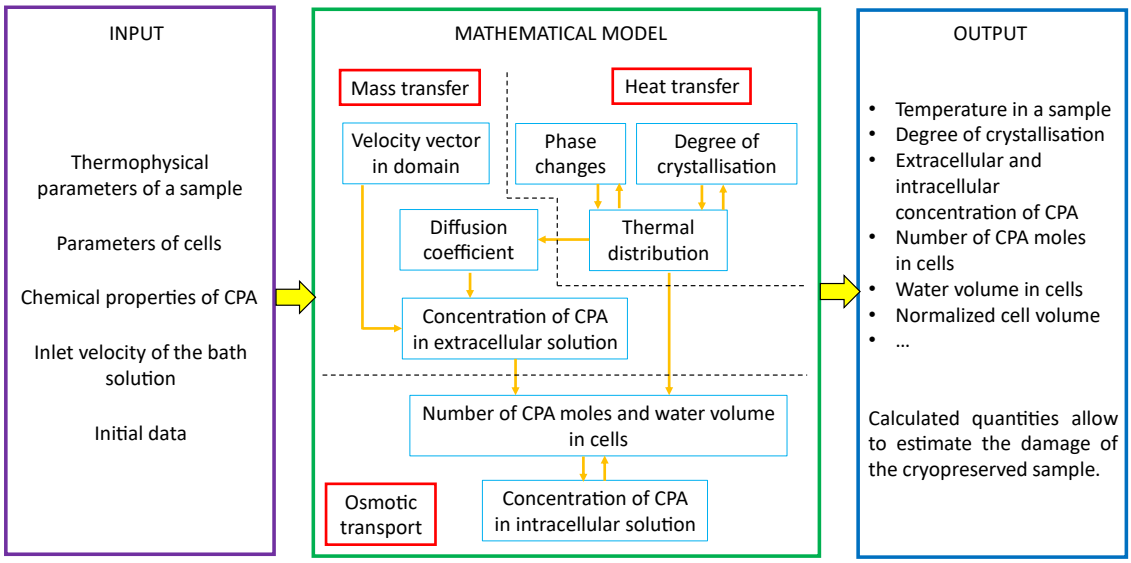

Figure 1.1. Multiphysics cryopreservation model

In addition, some physical quantities used for calculations are determined experimentally. As a result, it is common to encounter parameters with approximate values that are subject to some imprecision. In order to correctly interpret such inaccurate values and apply them in the analysis of technical problems, interval or fuzzy arithmetic can be used for calculations. Imprecisely defined quantities are represented as interval numbers or fuzzy numbers without sharp boundaries. Interval numbers are considered to be the "precursors" of fuzzy numbers. Parameters for which the exact value is not given, but the exact values of lower and upper limits of the interval to which the numerical value always belongs are known, can be interpreted as interval numbers [68].

The use of both fuzzy set theory and interval numbers allows many physical phenomena to be better represented in a mathematical model.

The aim of this dissertation is to present various mathematical models of heat and mass transfer in biological tissue during the cryopreservation process with imprecisely defined parameters in the mathematical description by introducing interval and fuzzy numbers. The interval and fuzzy finite difference method was used to solve the problem as formulated. In some of the cases presented in the dissertation, the numerical simulation results were compared with experimental data reported in the literature [187, 196]. The author's computer programmes using directed interval arithmetic and fuzzy arithmetic are an integral part of the work.

The thesis of the work can be formulated as follows:

Consideration of the imprecise parameters occurring in the mathematical description allows for effective multi-scale modelling of heat and mass transfer during cryopreservation of tissues and cells.

The work consists of six chapters, bibliography and abstracts in Polish and English.

Chapter 2 provides a literature review related to the cryopreservation method. The different approaches for conducting this process are presented. It also discusses the procedures for the cooling step and the delivery of the cryoprotectant solution to the sample. In the chapter the most commonly used cryoprotectants are also described.

Chapter 3 is devoted to the transport mechanisms that occur during cryopreservation. It reviews the mechanism of heat transfer and presents some of the widely applied models for defining thermal processes and crystallisation phenomenon in biological samples. In addition, the chapter contains mass transfer model related firstly to the flow of the bath solution containing the cryoprotectant into the sample (fluid flow) and secondly to diffusion of the molecules into the extracellular solution of the biological tissue (molecular diffusion). Also, the model for the transfer of water and cryoprotectants molecules across the cell membranes (osmotic transport) is depicted in the chapter.

Chapter 4 introduces the theory of interval sets and fuzzy sets. Basic mathematical operations performed on the sets of fuzzy numbers and interval numbers are formulated.

Chapter 5 considers the problem of the heat transfer presented in three examples. Example 1 demonstrates the model defined by the Fourier equation. In contrast, Example 2 supplements the thermal model with phase changes introduced into the governing equation by the one domain method. Example 3 explores, besides the heat transfer model, the phenomenon of crystallisation using the zone model and the non-isothermal equation proposed by Boutron and Mehl.

Chapter 6 contains three examples related to the mass transfer problem. Example 1 analyses the mass transfer described by the Fick's second law, where the advection phenomenon is neglected. In Example 2, the osmotic transport model is investigated by applying the two-parameter formalism. Example 3 provides a model of a microfluidic system in which the advection phenomenon is considered, therefore for this case the mass transfer model is represented by the convection-diffusion equation.

Chapter 7 concludes the dissertation and proposes some directions for further research.

The dissertation was realised in the years 2019-2023 at the Joint Doctoral School led by Silesian University of Technology. The research was funded by the InterPOWER project (grant POWR.03.05.00-00-Z305, European Union through the European Social Fund) and from financial resources from the statutory subsidy (under projects 10/040/BKM20/0099, 10/040/BKM21/0115 and 10/040/BKM22/0125).

The thesis is associated with Priority Research Area POB1: Computational Oncology and Personalized Medicine, being developed at Silesian University of Technology.

2. Cryopreservation process

2.1. Introduction

The mechanism of cryopreservation has been observed in animals inhabiting in cold regions with seasonal weather change, for example, in the northern forests of Canada and Alaska. Over time, science has begun to exploit this mechanism for its own benefit. During cryopreservation, many changes in cells may cause cell damage. To prevent this, the cooling rate can be regulated. Another milestone in research on the freezing process of biomaterials is the discovery of the properties of cryoprotectants. These are chemical adjuvants that impact the properties of the cell solution, for example, modify the freezing point. Using cryoprotectants also protects cells against injury during the freezing process.

Various cryopreservation methods are currently distinguished. They differ mainly in the cooling rate and the concentration of the cryoprotectant solution. The following approaches are the most commonly adopted: slow freezing and vitrification. Alternative techniques are also known, for example, the liquidus-tracking protocol.

In the case of cryopreservation, it is also worth considering how a given sample is cooled. The tube in which the biomaterial is placed is often immersed in a refrigerant. This approach is called the channel-based method. Other cooling techniques are also known, such as the droplet method, which involves immersing the sample solution directly into the refrigerant in droplet form.

The researchers also explore how to deliver the cryoprotectant to the sample. This is important, because cells can be damaged due to osmotic changes. For this reason, microchannels with different shapes and properties are designed and used.

2.2. History of cryopreservation

Nature continues to amaze us in many ways. The northern forests of Canada and Alaska are home to the North American wood frog (*Rana sylvatica*), which has

developed an extraordinary strategy for surviving cold winters. Namely, when the temperature drops below zero, breathing and heartbeat of the frog stop completely, and the water in the body is transformed into ice. This amphibian spends several months in a frozen state, after which the animal returns to normal life activities with the arrival of spring. This phenomenon is possible because the frog's liver produces glucose, and because the body fluids contain cryoprotective agents also called cryoprotectants (CPAs), such as glycerol, sugars, proteins, or urea. As a result, the freezing point of the frog's body decreases, and ice crystals in the cells do not form, as well as shrinking of the cell membranes does not occur. Ice grows only around cells and organs, "on the outside part of the corpus". This prevents cell and tissue damage that would lead to the death of the animal [3, 4, 77, 110, 197].

Similar behaviour is also observed in other vertebrates. In addition to the frog mentioned above (*Rana sylvatica)*, there are four other species of frog (*Pseudacris triseriata*, *Hyla crucifer*, *Hyla versicolor*, *Hyla chrysoscelis*), as well as one species of salamander (*Salamandrella keyserlingii*), one species of snake (*Thamnophis sirtalis*) and three species of turtle (*Chrysemys picta*, *Terrapene carolina*, *Terrapene ornata*), which also exhibit this conduct [25].

The described mechanism is named cryopreservation. The word cryopreservation comes from Greek *κρύος,* [kryos] meaning "icy cold" and Latin *praeservare* or *conservare* meaining "to preserve" [200]. It is defined as the process of storing biological constructs, such as cells, tissues, or organelle at low temperature. The preservation temperature depends on the use of the refrigerant, for example, for solid carbon dioxide it is −80 °C or for liquid nitrogen it is −196 °C. Cryopreservation methods are designed to avoid cell damage. One of the problems is the crystallisation of the water contained in the cells into ice. As a result, the cell mechanism seeks to equalize osmotic pressure. Therefore, solutes in the cytosol become increasingly concentrated, leading to the dehydration of organelles. The permeability of the lipid membrane is also altered, which is crucial to cell integrity. Damage caused by osmotic stress, membrane permeability, and cytoskeletal distortion destabilizes the cell. In addition, the physical injury induced by the formation of ice crystals inside ultimately leads the cell to death [60, 110].

Despite this, scientists would like to use the cryopreservation for its own purposes. The basic assumption of cryopreservation is to prevent any damage to a given biological structure. This is done by regulating the properties of the cell fluid with the CPAs and the

cooling rate. As research was conducted in this area, the cellular mechanisms that occur during cryopreservation were better understood [110].

In history, a breakthrough moment for the development of this process was the discovery of the effect of glycerol on the survival of frozen cells by Polge et al. in 1949 [133]. Polge et al. demonstrated that poultry sperm preserved in a 15% glycerol solution at −79 °C (solid carbon dioxide) or −192 °C (liquid air) gain full motility and the ability to fertilize the ovum after thawing. In 1952, Polge et al. [134] confirmed that frozen avian spermatozoa were capable of fertilizing eggs. At the same time, they found that freezing mammalian spermatozoa posed a greater problem for researchers.

In 1957, in a paper also published by Polge et al. [135], an experiment was performed on the spermatozoa of a ram, boar, colt, and bull. It was then found that there was a critical temperature range for the cells between −15 °C and −25 °C. To some extent, this can be prevented by leaving the spermatozoa at −2 °C for 18 h or by varying the cooling rate within the critical temperature range.

Further research confirmed the effectiveness of this method for other animals as well, for instance rabbits, horses, guinea-pigs, cattle, fowl, pigs, sheep, and goats. These inventions are used in animal husbandry. As described in [42, 110], today virtually all industrially bred cows are inseminated by cryopreserved semen.

Over time, cryopreservation has also been used on human materials. Living at the turn of the 20th century, Italian scientist and visionary Paolo Mantegazza made attempts to freeze frog and human sperm at temperatures between −14 °C and −17 °C. Based on his own studies, in 1866 Mantegazza proposed the existence of sperm banks. Mantegazza claimed that in the future science would make it possible to improve breeds of oxen and horses without the expense of transporting suitable individuals and that fertilization would be accomplished through frozen sperm. He also said “It may also be possible for a husband fallen on the battlefield to impregnate his wife from his corpse and have legitimate children even after his death” [90]. His vision came true almost 100 years later. In 1954, the *Cedar Rapids Gazette* [198] published an article reporting the birth of three babies by insemination of sperm that had been previously frozen and stored [15, 167, 168].

Increasingly, more and more researchers began to explore ways to preserve both male gametic cells and other reproductive cells, such as oocytes and embryonic cells, as well as the possibility of preserving whole animal and human tissues. For example, in 1986

Christopher Chen [22] described a case of pregnancy and birth of twins using a slow freezing and rapid thawing procedure on a human oocyte applying DMSO [45].

In the 1960s, researchers began to think about freezing the entire human body. According to rumours, Walt Disney wanted to have his body frozen so that he could come back to life years later. He was diagnosed with a developing cancer of the left lung, which back then was an incurable disease. When it became known that the famous entertainer was terminally ill, a claim spread that he had undergone a cryopreservation procedure. The procedure was allegedly performed with the hope that 100 years after the philanthropist's death, due to the huge advancement of medicine, it would be possible to bring him back to the world of the living and cure the disease. As it turned out, Disney did not participate in cryonics treatment, but died of cardiac arrest and his body was cremated and buried in a California cemetery in Glendale [83].

It was not long before the first typical human body cryopreservation procedure was performed. In April 1966, the human body was frozen for the first time. A middle-aged woman of unknown name underwent the procedure. About two months after being embalmed, her body was placed in liquid nitrogen and stored in the morgue, with the temperature in the refrigerator slightly above freezing. The experiment ended with her body thawed and then buried by family members [121].

A more famous cryopreservation treatment is the freezing of James Bedford's body. Bedford suffered from kidney cancer with metastases to the lungs. As mentioned in the book *We Froze the First Man* [107], on January 12, 1967, Bedford's body was frozen in Nelson's newly established organization by a team consisting of Robert Prehoda, Dante Brunol, and Robert Nelson. The procedure was performed after death without embalming. In addition, an appropriate CPA solution (DMSO) was injected into Bedford’s corpse. Bedford is the only cryopreserved person before 1974 whose body is still stored [83, 121].

Currently, the techniques associated with cooling human and animal bodies and storing them at liquid nitrogen temperatures (−196 °C) are named cryonics. The main idea of this approach is to restore frozen terminally ill organisms to life when medicine will be developed sufficiently [203]. This type of treatment can, of course, be conducted after patients are clinically dead using CPAs to prevent the formation of ice crystals. Interestingly, approximately 250 human corpses had been frozen in the US by 2014, and about 1,500 people were preparing for this procedure [83, 101].

2.3. Cryopreservation methods

The freezing techniques described previously are called slow freezing. In 1963, Mazur proposed a cooling rate needed to obtain liquid nitrogen temperature (−196 °C) using appropriate CPAs such as glycerol or DMSO [95]. Mazur showed that if sufficiently slow cooling is applied, intracellular freezing that destroys the cell can be avoided. Meanwhile, as the extracellular fluid is frozen, water can leave the cell. According to Mazur, the typical cooling rate for mammalian cells is assumed to be about 1 °C/min, with this value varying for individual cells of different sizes or water permeability. Furthermore, appropriate CPAs should be used at low concentrations [42, 94]

As early as 1973, Basile Luyet proposed a cryopreservation method based on ultra-fast cooling [82]. In 1985 William Rall and Greg Fahy presented the concept of cryopreservation by vitrification [139]. The novel approach was based on supercooling the medium to very low temperatures. This process occurs in the presence of highly concentrated solutions of CPAs. The low temperature causes the solutions to be viscous and to solidify (or rather to vitrify) without the formation of cell-dangerous ice. In fact, the solution does not crystallize but becomes amorphous ice. Rall and Fahy conducted research on mouse embryos [139, 168].

Using high concentrations of CPA interferes with the chemical composition of the cell. Osmotic shock is mainly responsible for the toxic effects of CPA on cells. Therefore, vitrification raises concerns about its security. Several studies related to embryo vitrification were conducted in the 1990s. These revealed an unclear relationship between high concentrations of DMSO, which is one of the CPAs, in the vitrification medium and high losses of normal developing embryos in the post-implantation phase. Other studies have suggested that CPA contributes to chromosome breakdown, aneuploidy, and other chromosomal abnormalities. Such ambiguities in the research results have diminished interest in vitrification as a cryopreservation method [45, 110].

In 1999, Lilia Kuleshova et al. [71] reported the first case of the birth of a healthy baby, which was fertilized by the in vitro method using vitrified oocytes. Vitrification research has also been conducted in the field of tissue engineering. Importantly, biomaterials must maintain their structural integrity and cells must be viable and retain their function. These conditions will only be met by processes in which no ice

formation occurs. In 2004, Lilia Kuleshova et al. presented vitrification of tissue engineering constructs [72].

The two main methods of cryopreservation, slow freezing and vitrification, are briefly compared in Table 2.1 [57]. They differ, for example, in the duration and cost of the process, the concentration of CPAs, or the risks present during the procedure. Table 2.1 also contains information about the size of the sample being frozen, the status of the system, the possibility of contamination, and the ability to manipulate the process.

Table 2.1. Comparison of slow freezing and vitrification [57]

Feature	**Method**	
	Slow freezing	**Vitrification**
Working time	More than 3 h	Less than 10 min
Cost	Expensive, freezing machine needed	Inexpensive, no special machine needed
Concentration of CPAs	Low	High
Risk of freeze injury, including ice crystal formation	High	Low
Risk of toxicity of CPA	Low	High
Sample volume	100 – 250 μL	1 – 2 μL
Status of system	Isolated system only	Opened or isolated system
Potential contamination with pathogenic agents	Low	High
Manipulation difficulty	Easy	Difficult
Post-thaw viability	High	High

Since both slow freezing and vitrification have disadvantages, efforts have also been made to develop alternative cryopreservation techniques. In 1965 John Farrant proposed a novel way to prevent cell damage, now called the “liquidus tracking” (LT) approach [37]. This method was later developed by Barry C. Elford and Clive A. Walter in 1972 [35]. Elford and Walter demonstrated that gradual cooling of biological

constructs incubated in solution, in which the increase in CPA concentration was also achieved in a gradual manner, prevented the freezing of the sample.

The main idea of the LT protocol is to immerse the biological sample in a CPA solution, whose temperature and concentration are controlled. Hence, the freezing (melting) point is changed, and thermodynamic conditions of the solution "tracks" the liquidus line for the system. For a well-prepared procedure, no ice crystallisation occurs in the biomaterial while the sample is not exposed to CPA-induced toxicity. The important consideration is the time required to ensure the diffusion process. It involves the replacement of water with CPA, for example, in tissues, so that the eutectic temperature of the composition coincides with the liquidus conditions [65].

In 2006, David Pegg's team became interested in the topic of cryopreservation of articular cartilage cells, chondrocytes. Initial attempts were conducted to freeze chondrocytes using conventional methods [117, 118]. Pegg et al. also analysed experiments to cryopreserve these cells by vitrification proposed by Song et al. [155–157]. According to Pegg et al., another advantage of LT protocol in comparison to effective vitrification is the very low cooling and heating rates. It is a criterion required by orthopaedic surgeons for the methods used in tissue banks. Research on the LT technique continued, and in 2007 a paper was published that improves the procedure proposed previously [178].

2.4. Cooling methods

In a previous section of this paper, a basic classification of cryopreservation methods related to different cooling rates and different concentrations of CPA is presented. Another subdivision criterion can also be applied. Note that it is extremely important to determine how the solution is cooled with the sample.

A common technique for cryopreserving samples placed in CPA solution is to immerse the sample tube in a Dewar vacuum flask containing a refrigerant. Cryogenic storage Dewar vacuum flasks are a type of thermos for storing cryogenic liquids with a boiling point below room temperature. Xu et al. termed this cryopreservation as channel-based method [182].

Xu et al. also mentioned another novel technique, the droplet-based method. The approach is inspired by bioprinting. It is basically freezing by vitrification,

where samples mixed with a medium (for example CPA) are injected directly into liquid nitrogen. The cooling rate is high, up to 106 °C/min. This ensures that once the solidification point is exceeded, the cell-encapsulating liquid solidifies. The rapid transition between the freezing (melting) point and the glass transition temperature prevents crystal formation and the droplet becomes amorphous ice [148, 158, 182].

The channel-based and droplet-based methods are schematically illustrated in Figure 2.1 [182].

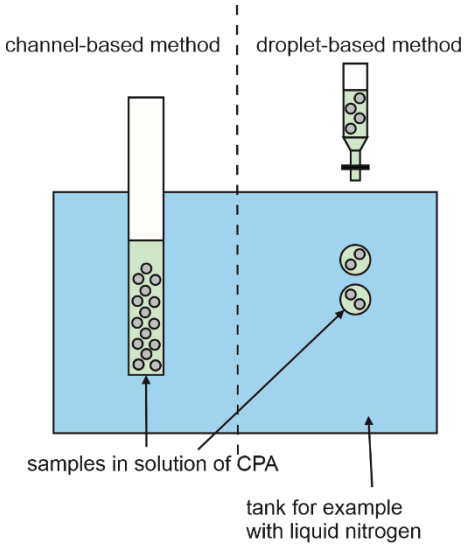

Figure 2.1. Visualization of channel-based and droplet-based methods of cryopreservation

2.5. CPA delivering methods

It is worth also considering the process of delivering CPAs to a sample. Despite appearances, it is an important part of the cryopreservation process that directly affects the survival of biological structures.

In fact, the CPA delivery before cryopreservation and removal during thawing exposes cells to isotonic solutions. As a result, the cell volume changes. During the addition of CPA, the chemical potential of water is higher in the intracellular space than in the extracellular space. Therefore, the cell first dehydrates and its volume decreases. The volume then increases again as the solution of CPA and water is transported into the cell. CPA molecules are larger than water molecules, so diffusion of water across the cell membrane occurs earlier. Figure 2.2 shows a diagram of the cell response during the addition and removal of permeable CPAs [192].

The cell's response to these volume changes can cause osmotic damage, toxicity, and finally its destruction. Hence, an essential role is to optimize the addition and removal of CPA to reduce cell volume changes and to neutralize toxic properties of CPA. Note that loading/unloading of CPA makes these processes often costly and time-consuming, especially for vitrification, which requires a higher concentration of CPA [191].

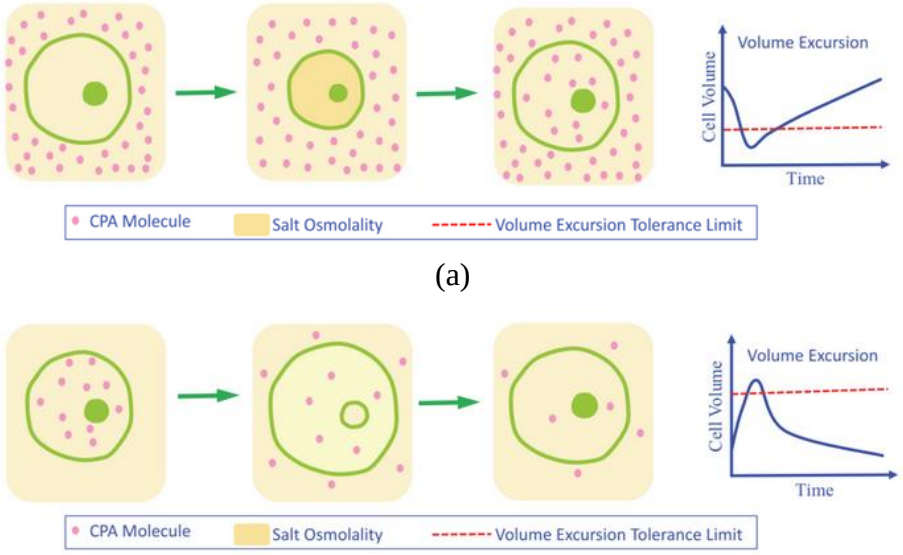

Figure 2.2. Cell's volume response during (a) addition and (b) removal of permeable CPAs [192]

Standard methods for the supply and elimination of CPAs involve centrifuging the mixture with the cells several times. Then the "old" solution is removed, the "new" solution is added, and the cell suspension is created again. In recent years, microfluidic platforms have been introduced to prevent cell damage induced by toxicity and osmotic shock. Microchannels are often made of polydimethylsiloxane (PDMS) or non-PDMS materials. The use of microchannels allows the precise control of CPAs loading and unloading considering cell behaviour at the microscale. Additionally, microfluidic devices can determine the permeability properties of the cell membrane [191].

Various microchannel designs using microfluidic perfusion are currently investigated. One of the suggestions is the sandwich-structured chamber. This concept has been explored by many research groups [23, 79, 143, 144, 159, 169, 193–196]. The papers also considered different ways of loading and unloading CPAs. For example, two-stream microfluidic devices, three-inlet T-junction or Y-junction microchannels, or membrane-

based devices can be implemented. Recently, the MEMS Coulter counter has also been applied to microfluidic devices to monitor changes in the sample [191].

2.6. Cryoprotectants

The following section briefly describes the CPAs. As mentioned previously, to avoid injury of biological material during cryopreservation, the properties of the cell fluid are altered by CPAs. The added protective chemicals are expected to be low in toxicity and biocompatible, as well as to have ability cell penetration. The CPAs can be divided as follows: permeating through cell membranes and remaining outside the cell (non-permeating) [57, 110].

The first category, permeating CPA, includes chemical compounds such as glycerol, ethylene glycol (EG), propylene glycol (1,2-propanediol), or dimethyl sulfoxide (DMSO). Permeable cell membrane CPAs are low molecular weight organic substances with a low melting (freezing) point and high viscosity. Due to them, the cell fluid is transformed from a liquid to a glass-like form without forming ice crystals. This mechanism is called nitrification [110].

The second category, the non-permeable cell membrane CPAs are high molecular weight substances like sugars (glucose, sucrose, sorbitol, and disaccharides) or polymers (polyvinyl pyrrolidone, hydroxyethyl starch). The compounds increase the osmotic pressure of the cell fluid, causing controlled dehydration. The application of non-penetrating CPA reduces the concentration of penetrating CPA. Therefore, a mixture of CPAs typically contains both types with the addition of, for example, pH buffers that provide the right environment for samples, as well as protein macromolecules, which increase the viscosity of the liquid and have a positive effect on the balance of the frozen cell. The chemical composition depends on the type of cryopreservation procedure and cell type [110].

Different types of CPAs are adapted to reduce damage to biological structures. Below some examples of cryoprotective chemicals are given. The first commonly used CPA is glycerol. Its cryoprotective properties were discovered by Polge et al. [133] in 1949. Glycerol is a non-electrolyte that reduces the electrolyte concentration in the unfrozen part of the cell solution and around them. It is applied in cryopreservation of animal sperm or bacteria, for example [57].

The second example is DMSO. DMSO also has properties similar to glycerol, as described by Lovelock and Bishop in 1959 [80]. DMSO was first synthesized as early as 1866 by Alexander Zaytsev. Additional advantages of DMSO include its relatively low cost and low cytotoxicity. However, DMSO can induce DNA methylation and histone alteration, causing an observed decrease in cell survival and induction of cell differentiation. It is commonly used in the freezing of mammalian cells, for example [57].

Natural compounds such as proteins can also be used as CPAs. One example is sericin, which is a viscous water-soluble protein. Sericin is produced by isolating the relevant protein from the silkworm cocoon. It is applied instead of DMSO, for instance, during cryopreservation of human cells such as stem cells, progenitor cells, hepatocytes or foetal bovine serum [57].

The above examples describe CPAs as chemical compounds or proteins delivered to biological material. A different strategy is used when the CPAs are synthetic polymers that belong to the group of non-penetrating CPAs. This approach involves entrapment of the CPA in the capsule while loading it into the sample and resuspending the cells in the encapsulating material. Such CPAs protect cell scaffolds thereby omitting diffusion limitations in the same time [57].

3. Transport phenomena

3.1. Introduction

Transport phenomena are defined as the general effects associated with the movement of particles, molecules, mass, energy, etc. from one place to another. These are irreversible processes that result from the continuous and random movement of particles (molecules). According to the minimum energy principle, all systems tend towards the lowest energy state, which is closely related to transport phenomena. Examples of transport phenomena involve energy transfer (heat conduction), momentum transfer (fluid flow), mass transfer (molecular diffusion), electric charge transfer, radiation, etc.

Transport processes are governed by conservation laws as well as the constitutive equations. First and foremost among conservation laws is the assumption of continuity, which implies that the analysed medium is a continuum, without gaps, and its microstructure is negligible. Other conservation laws include conservation of mass, conservation of energy, and conservation of momentum.

The constitutive relationships used to describe transport processes contain, for example, the Fourier's law, the Navier-Stokes equations, or the Fick's laws. The Fourier's law describes the correlation of heat flux and temperature gradient. In this case, the transport of heat in the system strives to reach thermodynamic equilibrium. Meanwhile, the Navier-Stokes equations define the motion of a viscous fluid. The Fick's laws express the connection between diffusion flux and concentration gradient. Momentum and mass transport aim to achieve mechanical and chemical equilibrium in the system, respectively.

When momentum transfer for fluid with low Reynolds number according to Newton's law is considered, such a fluid flow is called a Stokes flow. Then, it is possible to see the similarities in the differential equations used to characterize the transfer of heat, momentum, and mass. When a fluid flow is described by the Navier-Stokes equations, the analogy is not observed for momentum transport with reference to energy and mass transfer.

Transport phenomena also occur during cryopreservation. In the first instance, the changes associated with heat transfer are present during the process. Analysing the thermal transfer in the context of inhomogeneous biological structures is complicated. Generally, the mechanism of bioheat transfer is considered as a combination of convection and thermal conduction. The thermal distribution is most often described by the following relations: the Fourier equation, the Pennes equation, the Cattaneo-Vernotte equation and the dual phase lag equation.

When preparing a heat transport model for the cryopreservation process, it is also important to include the phase changes phenomena. Macroscopically, this issue can be modelled using the method known as “one domain method” or “fixed domain method”. It introduces a substitute thermal capacity into the heat transport equation.

On the other hand, the phase transition is also related to ice crystallisation. In the microscopic approach, ice crystal formation is expressed by the degree of crystallisation. It can be defined by the uncoupled method, Stefan approach (sharp interface method), or zone model.

Besides heat transfer, mass transfer also occurs during cryopreservation. Firstly, there is the momentum transfer described, for example, by the Navier-Stokes equations. It is used to model the delivery of CPA to the chamber with samples.

Mass transport is also related to the movement of molecules. It occurs when a concentrated solution of CPA diffuses into the extracellular space. It is often associated not only with diffusion, but also with the convection (advection) of the fluid resulting from its movement. As a consequence, the convection-diffusion equation is used to express this phenomenon. In cases where convection is neglected, the diffusion of molecules is characterized by the Fick’s laws.

Last but not least, during cryopreservation modelling, osmotic transport should be analysed. It describes the changes in cell volume caused by the alterations in the moles number of CPA and in the volume of water in the intracellular solution. The two-parameter formalism approach or the Kedem-Katchalsky equations can be applied to determine these values.

3.2. Mechanism of heat transfer

Heat transfer is one of the basic phenomena occurring in nature. In fact, it is the result of a temperature difference that exists between two objects and energy is transferred between them in the form of heat. There are three basic mechanisms of heat transfer: thermal radiation, convection and thermal conduction [21].

The first, thermal radiation, is the heat transfer by quanta of radiation in a certain range of electromagnetic wavelengths initiated by the motion of particles in matter. Interestingly, all matter whose temperature is higher than absolute zero emits heat through thermal radiation. For example, by using a thermographic camera, it is possible to detect infrared radiation (IR) emitted by humans and animals. Compared to thermal conduction and convection, thermal radiation does not require the existence of a material medium in which it propagates (it can occur in a vacuum). In addition, radiation energy propagates at the speed of light. The amount of thermal radiation depends on the type of body surface and its temperature [21].

The other mechanism of heat transfer is convection. Convection occurs when individual particles of a body change their position and transfer heat at the same time. The phenomenon is characteristic for fluids – liquids and gases. Energy transfer is caused by mixing of fluids, and a necessary condition for convection is the movement of the medium. In fact, convection is a combination of conduction in the form of thermal diffusion and advection related to the movement caused by fluid flow [21].

Convection can be divided into two different types. The phenomenon of natural (named also free) convection is initiated by buoyancy forces owing to density differences caused by temperature differences. Fluid movement can also be artificially generated by an external source, for example pumps, fans. When convection currents are induced, it is the phenomenon of forced convection [21].

Please note that the given definition of convection refers to the heat transfer, not in the context of fluid mechanics. Convection as part of fluid mechanics will be defined in the next part of the chapter.

The third mechanism of heat transfer is thermal conduction. It involves the transfer of energy from one particle to the other. Heat is spontaneously transferred from warmer to colder parts of body (or between two bodies), with the result that the temperature of the cooler parts of body increases and that of the warmer parts of body decreases

The process continues until the temperature of the body (or bodies) is equalised in the whole considered volume. It refers to direct body-to-body contact or parts of the body [21].

Continuing on the topic of thermal conduction, it is worth mentioning a few of material constants that provide some measure of the body's ability to conduct heat. One of such thermophysical parameters is the specific heat capacity. It represents the tendency of a substance or material to change temperature when it is supplied with the thermal energy. The specific heat capacity often depends on the temperature of the body and its state of matter. It can be defined by the following relationship [21]:

$$c_p = \frac{1}{m}\frac{\mathrm{d}Q}{\mathrm{d}T}, \tag{3.1}$$

where c_p represents the specific heat capacity, m is the mass of the sample, dQ denotes the increment of heat, which is needed to raise the body's temperature by a small amount represented by dT.

The volumetric heat capacity is sometimes used in engineering. It expresses the proportion dQ/dT in relation to a unit of volume [21]:

$$c_V = \frac{1}{m}\frac{\mathrm{d}Q}{\mathrm{d}T}\rho = \frac{1}{V}\frac{\mathrm{d}Q}{\mathrm{d}T}, \tag{3.2}$$

where c_v is the volumetric heat capacity, ρ and V are the density and the volume of the sample, respectively.

The next thermophysical parameter which determines a material's ability to conduct heat is thermal conductivity. It describes the potential of a substance or material to transfer internal energy in the form of heat. It is not a constant quantity, as it depends on factors such as temperature, density or the structure of the sample [21].

Thermal conductivity is defined by the Fourier's law [21]:

$$\mathbf{q} = -k\nabla T, \tag{3.3}$$

where $\mathbf{q}$ is the heat flux, k is the thermal conductivity and ∇T denotes the temperature gradient.

The Fourier's law is a constitutive equation that explains the phenomenon of heat conduction. It is a tensorial relationship between the heat flow as a scalar and the temperature gradient as a vector. In fact, thermal conductivity is a second-order tensor, which is important for the case of, for example, anisotropic materials [21].

3.3. Mechanism of bioheat transfer

As read in the *Encyklopedia biologiczna*, an organism is described as a living system characterised by the ability to perform vital processes and to exist independently as an individual [61]. The organism is composed of an organ system, which is a group of organs specialised to execute specific physiological activities. At the same time, an organ consists of a collection of tissues that fulfil characteristic functions. Tissue is defined as an ensemble of cells and their extracellular matrix that has a specific structure and origin, occupies a given place in the body, and performs the corresponding activities. Whereas a cell is the smallest naturally occurring viable, self-reproducing structure with a complex organisation [202, 204, 206, 207].

To understand it better, it is sensible to consider the structure of biological tissues. As mentioned above, tissues are made up of cells that differ in shape and size according to their function. Meanwhile, cells generally consist of a membrane enclosing the internal components, for example, a nucleus surrounded by a mass of protoplasm. Importantly, the cell is mainly constructed of about 75% water, and the remaining components are lipids, salts, protein, sugars, as well as nucleic acids suspended in water, such as DNA and RNA. The semi-permeable membrane is basically composed of lipids and its role is to exchange water molecules and ions with the extracellular matrix [201].

Analysing the entire human body globally, water is the main component (for males, it is about 50% – 70%, for females, it is about 46% – 65%). Body water can be classified as follows: extracellular and intracellular. As the name suggests, it is contained in the extracellular matrix and inside the cells, respectively. Extracellular water can be further split into interstitial (or intercellular) water and plasma, while interstitial water represents about 25% of the total water mass and plasma is about 8% of the total water mass. To compare, intracellular water contained in the protoplasm is about two-thirds of the total water mass. It exists in two types, as free and bound water. Free water can freely flow and participate in metabolic processes. Bound water is linked to protein molecules by hydrogen bonding induced by dipole attraction, therefore, it is not able to contribute to metabolic processes. Obviously, extracellular and intracellular water molecules can migrate by osmosis [201].

Various tissues are characterised by different water contents. However, this does not change the fact that water is the essential component of biological tissues. As a result,

the thermal parameters of tissues and cells are similar to the data for water. Table 3.1 presents examples of thermal conductivity values for selected human tissues and water [148, 201].

Table 3.1. Thermal conductivity values for selected human tissues [148]

Tissue of	**Thermal conductivity, k [W·m^{-1}·K^{-1}]**
Brain	0.503
Cheek	0.487
Skin	0.476
Leg	0.450
Muscle	0.385
Water	0.609

Due to the structures of organisms, explanation of the heat transfer mechanism in living organisms is more complex and complicated than in solids, liquids, or gases. The bioheat transfer mechanism is a combination of convection and thermal conduction. For instance, convection is related to blood flow in blood vessels. In contrast, thermal conduction is the result of metabolic processes and the presence of small blood vessels in tissues [58].

The individual bioheat transfer equations attempt to reflect, to some extent, the inhomogeneous structure of tissues, which are the building materials of organisms. Some models treat elements of the vasculature, for example, arteries and veins, and tissue, as separate subareas. Unfortunately, this approach is inapplicable for intricate capillary structures. In this case, the capillaries can be modelled as a porous structure. It can be claimed that no single universal equation for heat transfer in living systems exists [58].

The heat equation proposed in 1882 by Jean B. J. Fourier is the governing equation used to describe thermal processes [40]:

$$c_p \rho \dot{T} = \nabla \left(k \nabla T \right) + Q_{\text{int}} , \tag{3.4}$$

where Q_{int} in this case is the internal heat source. Please note that the thermal parameters changes according to temperature $c_p = c_p(T)$, $\rho = \rho(T)$ and $k = k(T)$ as well as the internal heat source is equal to $Q_{int} = Q_{int}(T)$.

The Fourier heat equation is a parabolic partial differential equation (PDE) that describes the unsteady heat transfer in an isobaric, isotropic medium in the presence of

internal volumetric heat sources. This equation calculates the temperature distribution in a certain medium. The heat transfer is a result of a thermal wave which propagates with infinite velocity [98, 136].

Moreover, independently of the state of a living organism, heat is generated inside the body. This phenomenon is described by:

$$Q_{\text{int}} = Q_{met} + Q_{perf} \tag{3.5}$$

where subscript *met* and *perf* denote metabolic and perfusion heat sources, respectively.

The metabolic heat source is often considered to be a constant value. It depends on whether the body is at rest or in motion. For example, at rest, the metabolic heat source is assumed to be between 245 and 420 $W \cdot m^{-3}$. During physical exercise, this value increases significantly, even a hundredfold [32, 58].

On the other hand, the perfusion heat source is associated with the presence of blood, which is a component of many tissues. The perfusion parameter characterises the quantitative content of blood in the tissue and informs about its flow rate. It also depends on the state of the human body because blood circulation in the body is one of the mechanisms of thermoregulation. The perfusion heat sources are commonly defined:

$$Q_{perf} = G_b c_b \rho_b \left(T_b - T\right), \tag{3.6}$$

where G_b is the blood perfusion rate and subscript *b* denotes the blood of the temperature, the specific heat capacity and the density. Table 3.2 contains the blood perfusion rate for different tissues [58].

The heat equation, which includes internal heat sources such as metabolic heat sources and perfusion heat sources, was formulated in 1948 by Harry Pennes [120]. The parabolic Pennes model assumes that the blood temperature in the arteries is constant and that the blood temperature in the veins corresponds to the tissue temperature. The Pennes equation is effective in describing heat transfer in soft tissues where small capillaries are present. In such cases, the blood in the capillaries achieves the temperature of the tissue. The Pennes equation is applied to the modelling of skin tissue burns [84, 99], laser effects on tissue [58], electromagnetic field effects on tissue [86], and also tissue freezing [27, 43, 152, 179].

Table 3.2. Perfusion ratio for a given tissues [58, 74, 166]

Tissue of	**Blood perfusion rate, G_b [m·s^{-1}·m$^{-3}_{\text{tissue}}$]**
Aorta	78.613
Thyroid	70.667
Kidney	60.067 – 62.892
Brain	8.127 – 17.667
Liver	15.726
Skin	2.650 – 8.833
Urinary bladder	4.717
Bone	0.509
Muscle	0.353 – 1.237
Fat	0.212 – 0.265

The Fourier equation and the Pennes equation as the parabolic heat equations involve some disadvantages. As mentioned earlier, the thermal wave spreads with infinite velocity, so the thermal distribution also occurs at an infinite rate. It is an unphysical approach, because dissipation of the thermal energy requires a certain amount of time. To solve this problem, in 1958 Carlo Cattaneo [18, 19] and Pierre Vernotte [175] independently invented the following hyperbolic PDE (CV equation):

$$c_p\rho\left(\dot{T}+\tau_q\ddot{T}\right)=\nabla\left(k\nabla T\right)+Q_{\text{int}}+\tau_q\dot{Q}_{\text{int}}, \tag{3.7}$$

where τ_q is the relaxation time, which reflects a delay in the appearance of heat flux and, as a consequence, a delay in thermal conduction through the tissue.

Dual phase lag model (DPL model) represents a similar approach:

$$c_p\rho\left(\dot{T}+\tau_q\ddot{T}\right)=\nabla\left(k\nabla T\right)+\tau_t\nabla\left(k\frac{\partial\nabla T}{\partial t}\right)+Q_{\text{int}}+\tau_q\dot{Q}_{\text{int}}, \tag{3.8}$$

where τ_t is the thermalization time, which depicts delay in the temperature gradient caused by thermal conduction through structures of small size.

The problem in applying the CV equation and the DPL model is the difficulty in estimating the τ_q and τ_t variables. Their values are determined mainly experimentally. Despite this, both equations are applied for modelling bioheat transfer, examples can be found in the literature: for the CV equation [2, 115, 136, 149] and for the DPL model [73, 87, 89, 98, 103].

Another approach used in modelling thermal processes is the application of porous body theory. The idea of this method is to divide biological tissue into two subareas: the vascular region, and the extravascular region including interstitial tissue and cells. The vascular region is considered as a pore, while the extravascular region is the matrix of the whole structure. However, equations of this type will not be analysed in the work [58, 81, 106].

3.4. Crystallisation

When analysing the heat transfer for cryopreservation, it is necessary to consider other physical phenomena. One of them is crystallisation. This is a process involving the formation of solids with a crystalline structure. The crystal lattice is characterised by a high order of constituents such as molecules, atoms, or ions. The attributes of a crystal depend on several aspects, for example, cooling rate, pressure or homogeneity of the liquid [105].

Crystallisation proceeds in two major stages: ice crystal nucleation and growth. Nucleation is the first step of phase change, where the molecules collide with each other. As a result, they randomly aggregate to create an amorphous cluster and then gradually transform into stable nuclei. Nucleation is caused by local fluctuations that appear on the molecular scale in a metastable medium, for instance due to supersaturation or supercooling [105, 170, 199].

Nucleation can be categorized as follows: primary and secondary. In primary nucleation, no crystals are present, or their existence does not affect the process. Depending on the conditions, two types of primary nucleation are distinguished: homogeneous and heterogeneous. Homogeneous nucleation happens spontaneously as a result of fluctuations in the density of a substance without the involvement of foreign bodies. On the other hand, heterogeneous nucleation can be observed when impurities present in the substance, such as particles from the walls of the device, become seed crystals (named also nucleus). Heterogeneous nucleation is more common, as it requires less energy than homogeneous nucleation, for which a large supercooling of the liquid is necessary [105, 199].

The term “secondary” is reserved for nucleation in the presence of crystalline matter. Secondary nucleation is initiated by shearing action, contact between seeds, attrition,

or fracture [199]. The difference between secondary nucleation and heterogeneous (primary) nucleation is that for secondary nucleation the process is induced by crystals, whereas for heterogeneous nucleation it is initiated by a foreign particle, for example from the device [105].

The next step of crystallisation is ice crystal growth. Appearance of first seed crystal serves as a convergence point for adjacent particles. As a result, successive layers of crystals are formed around the nuclei, causing an increase in their dimensions. The growth rate depends on temperature, pressure, surface tension of the solution, etc. It can be established as a constant parameter for a particular process [105, 199].

If crystallisation is completed at the growth step, applying the appropriate conditions it is possible to obtain a monocrystalline. Otherwise, the subsequent process involves the reorganisation of the surface layer and the creation of a so-called crystalline microstructure. Single crystals clump together to create larger structures, producing a polycrystalline structure [105, 170, 199].

For a typical clean water crystallisation process, the following stages can be identified. Initially, the temperature in the sample is reduced below the freezing point (precooling). Once the phase change temperature and the energy barrier are exceeded, nucleation begins. During this period, the temperature suddenly increases to the freezing point. At the same time, latent heat is removed, crystal growth occurs, and new nuclei form. Finally, solidification happens while the temperature of the sample continuously decreases. After formation of the crystals, recrystallisation can sometimes take place. This is characterised by changes in the number of crystals, their shape and size [170].

For cryopreservation, the crystallisation occurs in biological structures in both extracellular and intracellular regions, when the temperature approaches the freezing point. Obviously, the application of CPAs and the regulation of cooling rate are aimed at avoiding the crystallisation of water in tissues and cells, which could damage them. However, it is worth examining these phenomena, while the heat transfer is modelled in microscopic aspect. In 1990, Pierre Boutron and Patrick Mehl introduced the following non-isothermal kinetic equation to describe crystallisation [11]:

$$\dot{\chi} = k_a \chi^{\frac{2}{3}} (1-\chi)(T_m - T) e^{\frac{-Q_{en}}{RT}}, \tag{3.9}$$

where χ represents the degree of ice crystallisation ($0 < \chi < 1$), k_a is the characteristic coefficient depending on the solution composition, T_m is the freezing (melting) temperature, Q_{en} is the activation energy, R is the gas constant ($R = 8.314$ J·mol^{-1}·K^{-1}).

Please note that the crystallisation is the first-order phase transition that involves the release of energy as latent heat. It is a concept that contributes to a change in the substance state without an increase or decrease of the temperature [21]. Considering the heat transfer in the macroscopic approach, the latent heat should be included as an additional element of the internal heat source mentioned in the Equation (3.5).

The three basic methods of creating a macroscopic model of liquid solidification can be distinguished: uncoupled method, Stefan approach (sharp interface method) and zone model [148, 158, 196]. The first of them, the uncoupled method, assumes that latent heat during freezing is negligible. Therefore, the energy equation is decoupled from the liquid kinetics. It means the heat transfer equation (Equations (3.4), (3.7) or (3.8)) and the crystallisation equation (Equation (3.9)) are calculated independently; the degree of ice crystallisation does not affect for the internal heat sources [182].

The Stefan problem is a moving boundary issue between a solid and a liquid, whereby the boundary between these phases is a sharp interface. This method was proposed by the Austrian physicist Josef Stefan in 1891 [162] and developed by Franz E. Neumann et al. in 1927 [109].

In this approach, the whole analysed area is divided into three time-dependent sub-domains: solid, liquid and transition interface. In the classical Stefan problem, which describes the solidification or melting of ice, the contributions of convection and diffusion can be neglected. Therefore, in sub-domains where the solid or the liquid is contained, the thermal distribution is determined using classical heat transfer models, for instance applying the PDE Equation (3.4) [100, 182].

At the solid-liquid interface, a boundary condition described by the continuity of the heat flux was established, considering latent heat [100, 182]:

$$\begin{cases} -k_l \nabla T \cdot \mathbf{n} = -k_s \nabla T \cdot \mathbf{n} + L\rho_s \dot{x}, \\ T_l = T_s = T_m, \end{cases} \tag{3.10}$$

where **n** is the normal vector to the sub-domain, L is the latent heat, dx/dt is the normal component of the interface velocity, subscript l and s denote to liquid and solid sub-domain, respectively. The temperature with subscript l or s represent the boundary temperatures for given state, i.e. the liquidus temperature and the solidus temperature.

However, an assumption of the sharp solid-liquid interface is not always proper. André Bénard and Suresh G. Advani believed that a smooth phase change is more appropriate to characterize the underlying physics, i.e. the smooth ice crystal

formation [7]. Therefore, the different groups of researchers introduced a zone model, for example, Berger and Schneider [9], Astarita and Kenny [5, 111], Eder et al. [33]. The crystallisation phenomenon is described as a propagation zone. The material parameters and process conditions impact on the size of the propagation zone, which can be very narrow (a sharp interface) or very large (an entire domain). The main postulate of the zone model is that the total heat in the system (include sum of latent heat and specific heat) is expressed as an enthalpy function:

$$H(T) = \int_{T_o}^{T} \rho(\theta) c_p(\theta) \mathrm{d}\theta + \rho L \left(1 - f_s(T)\right), \tag{3.11}$$

where H is the enthalpy function, T_o is the fixed temperature ($T_o < T_m$) and f_s is the volume solid fraction.

For heat transfer problem (for example, Equation (3.4)), the internal heat source is calculated [7, 182]:

$$Q_{\text{int}} = Q_f = \rho L \dot{\chi} \tag{3.12}$$

where Q_f represents the internal heat transfer for freezing. Please remember that Q_{perf} and Q_{met} below the solidus temperature T_s are equal to 0.

As mentioned earlier, crystallisation microscopically refers to the creation of ice crystals, whereas macroscopically it is the first type of phase change. Let us consider the modelling of macroscopic heat transfer including phase transition phenomena from a slightly different perspective.

The approach presented below is known in the literature as the “one domain method” or the “fixed domain method”. This technique is particularly suitable if the phase transformation proceeds over a certain temperature interval. The idea of this method is to introduce “a substitute thermal capacity” (STC) into the heat transfer equation. STC replaces the internal heat sources and the volumetric specific heat. STC is defined by a state function that depends on the temperature in the sub-domain under examination [20, 33, 69].

When analysing the freezing of biological structures including phase changes, the source function can take the form [32]:

$$Q_{\text{int}} = Q_f = L \dot{f}_s, \tag{3.13}$$

where $\dot{f}_s$ denotes the local variation of the volume fraction in the intermediate region. Please note that the state function f_s varies according to the domain under consideration. The function f_s is equal to 0 and 1 in the liquid and solid sub-domains, respectively.

In the intermediate region, it is assumed that $f_s = f_s(T)$. Therefore the Equation (3.13) is transformed [32]:

$$Q_f = L\dot{f}_s = L\frac{\mathrm{d}f_s}{\mathrm{d}T}\dot{T}\,. \tag{3.14}$$

After introducing this relationship into Equation (3.4) and organising the equation accordingly, STC is defined as [32]

$$C_{STC} = c_V - L\frac{\mathrm{d}f_s}{\mathrm{d}T}\,, \tag{3.15}$$

where C_{STC} is the substitute thermal capacity, which depends on the temperature $C_{STC} = C_{STC}(T)$. Using STC, the entire tissue is treated as a homogeneous domain. The non-homogeneity of the area and the associated with that subdivision into sub-domains is included in the C_{STC} parameter.

3.5. Mechanism of mass transfer. Fluid mechanics

Another very important phenomenon is mass transfer. In the simplest terms, this phenomenon describes the movement of mass in the form of a particle, component, phase, fraction, stream, etc. from one place to a different location. For example, the causes of mass transfer can be concentration difference, where mass migrates between areas from higher to lower concentration [21].

It is worth mentioning that fluid mechanics, as a discipline of physics, mechanics, and engineering, explains the mechanisms of mass transfer in liquids and gases. Fluid mechanics involves both fluid statics and fluid dynamics. As a fundament, for any mechanical system considered in terms of fluid mechanics the following axioms are assumed: conservation of mass, conservation of energy, conservation of momentum, the continuum assumption [20].

Conservation of mass implies that the mass of a system is constant over time in a closed and isolated system. The mass cannot be removed or added to the system, which means that it cannot be destroyed or created, but it can instead only modify its form. Obviously, this assumption is valid only in classical mechanics. In the context of quantum

mechanics and special relativity theory, the law should be revised according to the principles of mass-energy equivalence [20].

In fluid mechanics, conservation of mass is formulated by means of the continuity equation. The differential form of the continuity equation is as follows:

$$\dot{\rho} + \nabla \cdot (\rho \mathbf{u}) = 0\,, \tag{3.16}$$

where **u** is the flow velocity field. The continuity equation assumes continuity of the fluid medium. This means that the flow area is completely filled with fluid and that no gaps form in it [46].

The conservation of energy is defined similarly. This law states that in an isolated (closed) system, the total energy cannot be destroyed or created; it remains constant. Energy can only be transformed into another form. A special instance of the conservation of energy is represented by the first law of thermodynamics, which holds that a perpetual motion machine of the first kind does not exist [20].

Conservation of momentum also asserts that total momentum in a closed and isolated system is constant. It is based on Newton's laws of motion. By the third law, it is known that the interaction of two particles with each other measured by a force is equal in magnitude but with opposite directions [20].

Next it is worth exploring the continuum assumption. According to continuum mechanics, the fluid is analysed as a continuous medium. In reality, however, the fluid is assembled from particles that collide with each other. This fact is neglected, and parameters such as velocity, pressure, temperature, density, etc. are described at infinitely small points called Reference Volume Element (RVE). The distance between these points is large compared to the molecular scale and small with respect to the whole system. Fluid properties change continuously between RVEs [20, 46].

The motion of a viscous fluid is described by equations developed in the 19th century by Claude-Louis Navier and George Gabriel Stokes. The Navier-Stokes equations are expressed as follows [20]:

$$\frac{\partial(\rho \mathbf{u})}{\partial t} + (\mathbf{u} \cdot \nabla)(\rho \mathbf{u}) = \rho \mathbf{g} - \nabla p + \mu \nabla^2 \mathbf{u} + \frac{\mu}{3} \nabla(\nabla \cdot \mathbf{u})\,, \tag{3.17}$$

where **g** represents fluid acceleration vector (mass forces, for instance, earth acceleration), p is the pressure and μ is dynamic viscosity.

The Navier-Stokes equations are a set of non-linear parabolic PDEs. The equations define the laws of conservation of momentum and conservation of mass in a flowing fluid.

According to them, changes in the momentum of the fluid's RVE depend only on the external pressure and internal viscous forces in the medium. Obviously, the Navier-Stokes equations obey all the principles of conservation [20].

Moreover, the Navier-Stokes equations are correct only for Newtonian fluids. Newtonian fluids indicate a linear dependence of shear stress on shear rate over time (local strain rate). At the same time, the stresses are proportional to the change rate of the velocity vector of the fluid layer. In fact, the viscosity stress tensor is associated with the strain rate through the dynamic viscosity tensor, which does not correlate with the flow velocity and the stress state. When an isotropic fluid is considered, the dynamic viscosity tensor is reduced to two independent coefficients that describe the resistance of the medium to continuous expansion (compression) as well as shear deformation. Fluids that do not correspond to this relationship (Newton's law of viscosity) are called non-Newtonian fluids [20].

Finding a solution based on the Navier-Stokes equations for complex cases is only possible using numerical methods. Such issues are the subject of computational fluid dynamics (CFD). However, the solution can be obtained for the simpler instances of fluid mechanics problems, for example, when the flow is assumed to be laminar without disturbance and the fluid is incompressible [20].

3.6. Mechanism of mass transfer. Molecular diffusion

The previous subchapter describes the mechanisms of mass transfer understood mainly in the context of fluid mechanics. Nevertheless, it is important to remember that mass transfer is primarily related to the convective and diffusive transport of molecules and chemical species in physics systems.

Diffusion (from the Latin *diffundere*, which means "to spread out") is the process of spontaneous spreading and penetration of particles, atoms, ions, energy, etc. in a given medium. Different types of diffusion are considered. Tracer diffusion is defined as the chaotic movement of a single particle in microscopic aspect. An example of this process is Brownian motion, in which the collisions between suspension and fluid particle cause chaotic movement of particles in the fluid. This phenomenon was noticed by the Scottish botanist Robert Brown in 1827 [21].

Macroscopically, chemical diffusion of matter (mass) or energy proceeds, which leads to an equilibrium of the concentration of diffusing substances in the system. In 1855, the German scientist Adolf Fick formulated the laws, which describe the diffusion phenomena [38, 39]. The Fick's first law is expressed by the following formula [21]:

$$\mathbf{J} = -D\nabla\varphi, \tag{3.18}$$

where **J** represents the diffusion flux vector, which determines the quantity of substance flowing through a unit section per unit time, D is the diffusion coefficient (molecular diffusion coefficient), φ is the concentration of the substance (quantities), for example molar concentration identify as c.

Similarly to the Fourier's law, this is a constitutive equation that describes a tensorial dependence of the diffusion flux vector and the concentration gradient. It implies that the solute diffuses from regions with higher to lower concentration.

On the basis of the Fick's first law and the conservation of mass law, it is possible to derive the relationship concerning the Fick's second law [21]:

$$\dot{c} = \nabla\left(D\nabla c\right). \tag{3.19}$$

It is the PDE that specifies the change in local concentration due to diffusion of a substance over time.

In both of these relationships (Equations (3.18) and (3.19)), the diffusion coefficient is involved. It predicts the ability of particles to diffuse in a medium under the impact of a concentration gradient. The diffusion coefficient depends on many factors, for example temperature, viscosity and structure of the medium, speed of diffusing molecules, and size of the fluid particles [21].

The diffusion coefficient was defined in papers describing Brownian motion presented independently by scientists [24]: William Sutherland (1904) [165], Albert Einstein (1905) [34], and Marian Smoluchowski (1906) [154]. The diffusion coefficient is expressed by the Einstein equation based on the Stokes assumption (Einstein-Stokes equation) [24, 79, 100, 177]:

$$D = \frac{k_B T}{n\pi r_s \mu}, \tag{3.20}$$

where k_B is the Boltzmann constant ($k_B = 1.38 \cdot 10^{-23}$ J·K^{-1}), n is the coefficient depending on the relationship between the size of the diffusing particle and the size of the structural units of the medium, r_s is the radius of the spherical particle. For example, when spherical

particles diffuse in a liquid having a low Reynolds number, the coefficient *n* is equal to 6 [24].

As mentioned earlier, mass transfer occurs not only by diffusion, but also by convection. In contrast to convection as a heat transfer mechanism, convection in the context of mass transfer is the spontaneous movement of a single or multiphase fluid. It is caused by the density variation in the fluid resulting from the temperature gradient between the sub-areas. The convection flow is also influenced by forces acting on a body immersed in a fluid, for example buoyancy, gravity, and by the heterogeneous properties of the fluid. In the stationary state, convection flows create closed loops, called convection cells [21].

A very similar phenomenon to convection is advection. The advection is the transfer of a substance by a fluid in motion. The velocity of the transported substance is equal to the velocity of the flowing fluid; as is the case with other advected quantities like energy or enthalpy, etc [21].

The advection phenomenon is described by a hyperbolic PDE:

$$\dot{c} + \nabla \cdot (\mathbf{u}c) = 0 . \tag{3.21}$$

The advection equation predicts the behaviour of a given quantity expressed by a scalar field under the effect of a velocity vector field. Mathematically, this relationship takes the form of a continuity equation. It is obtained by using the conservation laws, Gauss-Ostrogradsky theorem and assuming an infinitely small limit.

However, the advection rarely occurs in an independent form in nature. The advection phenomenon is mainly coupled with diffusion. The advection-diffusion equation, also known as the convection-diffusion equation, is as follows [79]:

$$\dot{c} = \nabla (D \nabla c) - \nabla \cdot (\mathbf{u}c) + R_s , \tag{3.22}$$

where R_s denotes the source term, which indicates the occurrence of chemical reactions. If particles are created as a result of a chemical reaction, $R_s > 0$, and if particles are destroyed, $R_s < 0$. In the case of chemical equilibration, R_s is equal to 0.

The convection-diffusion equation combines parabolic and hyperbolic PDEs. This equation determines the change in the concentration of quantities (particles, energy, etc.) in the system as a result of movement induced by diffusion and advection (convection). It can be seen that Fick's second law is a special case of the convection-diffusion equation, where advection is ignored.

3.7. Mass transfer during cryopreservation process. Osmotic transport

Mass transfer mechanisms in the concept of cryopreservation are considered in relation to the delivery and removal of CPAs. The techniques used for this are described in detail in the previous chapter. It is worth noting that the models mainly introduce the flow of CPA through microfluidic systems and its transport in the extracellular matrix of tissues. As can be found in the literature, these phenomena are expressed, for example, by using the convection-diffusion equation [79, 129, 159, 182, 194] or its special case, the equation resulting from Fick's second law [8, 104, 132, 147, 148, 150, 153, 187, 189].

Furthermore, while developing a complete description of cryopreservation, it is crucial to understand osmotic transport, i.e. the transfer of water and solutes, across the cell membrane (see Subsection 2.5). The cell membrane is a plasma membrane that is designed to isolate the extracellular from the intracellular space. Substances such as water can diffuse through the cell membrane under the influence of a concentration gradient until an osmotic equilibrium is reached. Unfortunately, the incorrect selection of parameters for the cryopreservation process can result in osmotic changes that are lethal to cells [36].

The phenomenon of osmotic transport can be explained mathematically. Jacobs and Steward in 1932 published the results of an experiment in which cell membrane permeability was measured [55, 56]. Based on this, they derived two coupled ODEs that simulate the transport of water and solute across the cell membrane [36]:

$$\dot{V}_w = k_w A\left(\frac{S + c_n^0 V_w^0}{V_{cell}} - c_s^e - c_n^e\right), \tag{3.23}$$

$$\dot{S} = k_s A\left(c_s - \frac{S}{V_{cell}}\right), \tag{3.24}$$

where V_w is the intracellular water volume, V_{cell} is the total volume of the cell, S is the intracellular amount of permeating solute, A is the cell surface area, c_s and c_n are the molar concentration of the permeating solutes (s) and the nonpermeating solutes (n), k_w and k_s are the water and solute permeability constant, respectively. The superscript e and 0 denote the extracellular solute and the initial values of the variables; while the subscript s and n represent the permeating and nonpermeating solute, respectively.

Please note that the total volume of the cell is the sum of the intracellular water (V_w), the intracellular solute volume (V_s) and the osmotically inactive volume (V_b) [36, 67]:

$$V_{cell} = V_w + V_s + V_b . \tag{3.25}$$

The above Equations (3.23) and (3.24) were deduced from Fick's laws. The following assumptions were also applied. During the experiment, the concentration of the extracellular solution and the thickness of the membrane were constant. Only diffusion through the cell membrane was considered, other diffusion phenomena were neglected. In addition, the concentration gradient was expressed as the ratio of the concentration difference in the extracellular and intracellular solution to the membrane thickness; while the osmotic pressure was assumed as proportional to the concentration [36].

Based on the above model, a two-parameter (2-P) formalism was formulated. The 2-P formalism approach is currently widely used to estimate changes in the volume of water and the number of moles in cells during osmotic transport (see examples in [8, 36, 67, 76, 129, 132, 184, 193–195]). It is represented by the following equations [36]:

$$\dot{V}_w = -L_p ART\left(M^e - M^i\right), \tag{3.26}$$

$$\dot{N}_s = P_s A\left(M^e - M^i\right), \tag{3.27}$$

where N_s is the intracellular number of permeating solute molecules, L_p and P_s represent the hydraulic conductivity and the solute permeability, respectively; M is the osmolarity with the superscripts denoting the extracellular (e) and intracellular (i) area.

Please note that osmolarity determines the moles number of osmotically active substance in 1 L of solution. The osmolarity can be confused with the osmolality, which refers to the number of moles osmotically active substances dissolved in 1 kg of a solvent, for instance., water. The osmolarity can be computed from the osmolality. For example, the osmolality for an undiluted solution of two solutes can be defined [36]:

$$\pi = m_i + m_j + B_i m_i^2 + B_j m_j^2 + \left(B_i + B_j\right) m_i m_j , \tag{3.28}$$

where π is the osmolality, B_i or B_j is the second osmotic virial coefficient for species i or j, m_i or m_j is the molality of species i or j, which expresses the number of moles of the dissolved substance in 1 kg of solvent. If one of the components in the solution dissociates (for example NaCl or KCl), the molality (m_i) should be replaced by the expression $m_i \cdot k_{diss}$, where k_{diss} is the dissociation constant.

In subsequent years, research on osmotic transport in cells was continued. In 1951-1952, Staverman described osmotic transport applying the linear theory of irreversible thermodynamics [160, 161]. This theory assumes that osmotic transport associated with permeation and diffusion are irreversible. This includes the phenomena of cell volume changes resulting from the transfer of substances across the cell membrane. The linear theory of irreversible thermodynamics was formalized by Lars Onsager in 1931 [113, 114].

Based on Onsager's and Staverman's approach, in 1958 Kedem and Katchalsky proposed a novel theory [66]. Their model assumes that for systems close to equilibrium, the flux is linearly proportional to, for instance, the gradient or the driving force. The osmotic transport involving the transfer of water and solute are coupled to each other. Therefore, water and solute react with each other, which can be described by the reflection coefficient [36, 67]. The Kedem-Katchalsky (K-K) equations are given as [36]:

$$\dot{V}_{w+s} = -L_p ART\left[\left(c_n^e - c_n^i\right) + \sigma\left(c_s^e - c_s^i\right)\right], \tag{3.29}$$

$$\dot{N}_s = (1-\sigma)\left(\frac{1}{2}\right)\left(c_s^e - c_s^i\right)\dot{V}_{w+s} + P_s A\left(c_s^e - c_s^i\right), \tag{3.30}$$

where V_{w+s} is the intracellular volume of water and solute, σ is the reflect coefficient.

Compared to the 2-P formalism, in the K-K equations the membrane permeability is characterised by three parameters: hydraulic conductivity, solute mobility, and reflection coefficient [36]. The K-K equation, like the 2-P formalism, is also commonly used for osmotic transport calculations [36, 67, 183–185, 195].

In later years, subsequent researchers proposed other models of osmotic transport. In 1963, Peter Mazur presented a quantitative temperature dependence of water transport, assuming that solute transport is negligible [94]. The relationship is as follows:

$$\frac{\mathrm{d}V_w}{\mathrm{d}T} = -\frac{L_p ART}{Bv_w}\ln\left(p^e / p^i\right), \tag{3.31}$$

where B is the constant cooling rate, v_w is the partial molar volume of water, p^e and p^i is the extracellular and the intracellular pressure of water.

The ODE shown above was revised in 1976 by Levin et al. [78]. The modification aims to include the action of CPAs. Examples of the application of the Mazur and Levin et al. models can be found in [29, 172, 181].

4. Fuzzy and interval numbers

4.1. Introduction

The “language of mathematics” can describe the behaviour of a given system, process, or phenomenon. Mathematical modelling is used in the natural sciences, (for example biology, physics, chemistry), in engineering, and also in non-physical fields such as sociology.

Mathematical models are classified in different ways. For example, models can be categorised as linear or non-linear, static or dynamic, explicit or implicit, discrete or continuous as well as deterministic or stochastic (probabilistic). The last couple of model types are worth considering in the context of cryopreservation. In a deterministic model, variables or parameters are uniquely determined by an input or dataset from a previous state. These models always work in the same way and produce the same results based on the given inputs. In contrast, stochastic models involve randomness. Variables are not introduced as unique values but, for instance, as probability distributions or random variables from a given set of states. The products of the calculations performed by the stochastic model for a given initial state vary with each calculation.

The cryopreservation process is most often modelled in a deterministic manner (see examples in [79, 182, 187, 196]). Meanwhile, in modelling this phenomenon, input variables are often used that are imprecisely defined. Often approximate values are used, especially for the properties of biological constructs, such as thermophysical and chemical parameters, which are determined experimentally. This means that the use of a deterministic model provides some simplification.

The phenomenon of cryopreservation can be described by a stochastic model. This would allow the calculations performed to better reflect the natural phenomena occurring during this process. Unfortunately, stochastic models are time-consuming [16, 17].

There is another way to model quantities that are inaccurately or imprecisely defined. Fuzzy set theory can be used for this type of issue. It involves introducing imprecise

parameters in the form of fuzzy or interval numbers. The fuzzy number is a quantity that has no "sharp" ends. Each such number that is a part of a fuzzy set is described by a characteristic function. The characteristic function, called the membership function, can have values in the range from 0 to 1. For comparison, in classical set theory, the characteristic function takes the value 1 when an element belongs to the set, or 0 when the element is outside the set [48]. Meanwhile, an interval number is defined by the boundary values of a closed range. The characteristic function for the interval numbers is equal to 0 or 1, as in the case of the classical sets.

Examples of the application of interval and fuzzy number concepts in engineering modelling can be found in the literature [48, 49, 68, 99, 123, 124, 126, 127].

4.2. Fuzzy sets

In 1965, Lofti A. Zadeh proposed the concept of fuzzy sets as an extension of classical sets, where each element of the set is assigned to them by a degree of membership [188]. For some non-empty space $\mathbb{X}\left(\widetilde{\mathrm{A}} \subseteq \mathbb{X}\right)$, the fuzzy set $\widetilde{\mathrm{A}}$ is defined by the following set of ordered pairs [26, 48, 62, 125]:

$$\widetilde{\mathrm{A}} = \left\{\left(x,\, \mu_{\widetilde{\mathrm{A}}}(x)\right);\; x \in \mathbb{X}\right\}, \tag{4.1}$$

where the function $\mu_{\widetilde{\mathrm{A}}}$ is known as the membership function of the fuzzy set.

The membership function can be expressed as [48, 125]:

$$\mu_{\widetilde{\mathrm{A}}} : \mathbb{X} \to [0,\, 1]. \tag{4.2}$$

It means that the membership function $\mu_{\widetilde{\mathrm{A}}}$ can take any values of the real numbers set [0, 1]. It is worth noting that, for a classical set, the value of membership function $\mu_{\widetilde{\mathrm{A}}}$ determined in this way is equal to only 0 or 1.

Three basic types of membership for individual elements $x \in \mathbb{X}$ to the fuzzy set $\widetilde{\mathrm{A}}$ are considered:

- when $\mu_{\widetilde{\mathrm{A}}}(x) = 1$, the membership of an element to the set is full, hence $x \in \widetilde{\mathrm{A}}$;
- when $\mu_{\widetilde{\mathrm{A}}}(x) = 0$, the membership of an element to the set is empty, hence $x \notin \widetilde{\mathrm{A}}$;
- when $0 < \mu_{\widetilde{\mathrm{A}}}(x) < 1$, the membership of an element to the set is partial, hence $x \in (0,1)$.

The partial membership of the element *x* to the set does not occur for classical sets, which distinguishes them from fuzzy sets.

Figure 4.1 illustrates an example of the fuzzy set $\widetilde{\mathrm{A}} = \{[(x_1, x_2), \mu_{\widetilde{\mathrm{A}}}(x_1, x_2)]; x \in \mathbb{R}^2\}$ in a two-dimensional space for which the membership function is equal to $\mu_{\widetilde{\mathrm{A}}}(x_1, x_2) = 2 \cdot \exp\left(-\frac{1}{2}x_1^2 - 3x_2^2\right)$ [125].

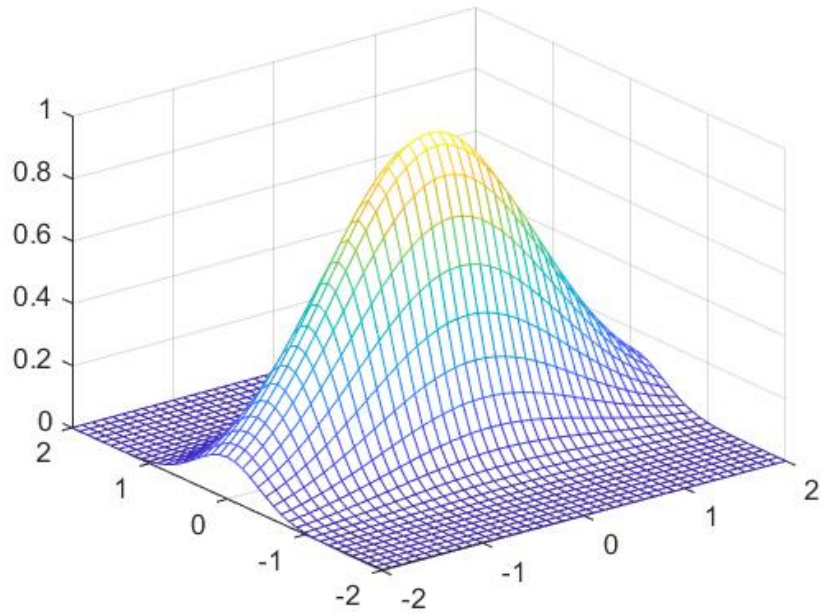

Figure 4.1. Example of fuzzy set $\widetilde{\mathrm{A}}$ in $\mathbb{R}^2$ space

An important consideration is the concept known as α-cut of a fuzzy set [14, 30, 41]. The α-cut of a fuzzy set $\widetilde{\mathrm{A}}$ in space $\mathbb{X}$ is defined as a crisp set of all elements for which the values of membership functions are greater than or equal to α, where $\alpha \in [0,1]$:

$$\tilde{\mathrm{A}}_{\alpha} = \left\{x \in \mathbb{X}: \mu_{\tilde{\mathrm{A}}}(x) \geq \alpha\right\}, \tag{4.3}$$

which is determined by the following characteristic function [30]:

$$\chi_{\tilde{\mathrm{A}}_{\alpha}} = \begin{cases} 1 & \text{for } \mu_{\tilde{\mathrm{A}}}(x) \geq \alpha, \\ 0 & \text{for } \mu_{\tilde{\mathrm{A}}}(x) < \alpha. \end{cases} \tag{4.4}$$

The process of subdividing a fuzzy set into α-cuts is called decomposition.

Figure 4.2 shows an example of a two-dimensional fuzzy set with a marked α-cut, where $\alpha = 0.5$ [125].

It is worth mentioning that for α-cuts, the relation is true [125]:

$$a_1 < a_2 \rightarrow \tilde{\mathrm{A}}_{\alpha_2} \subset \tilde{\mathrm{A}}_{\alpha_1}, \tag{4.5}$$

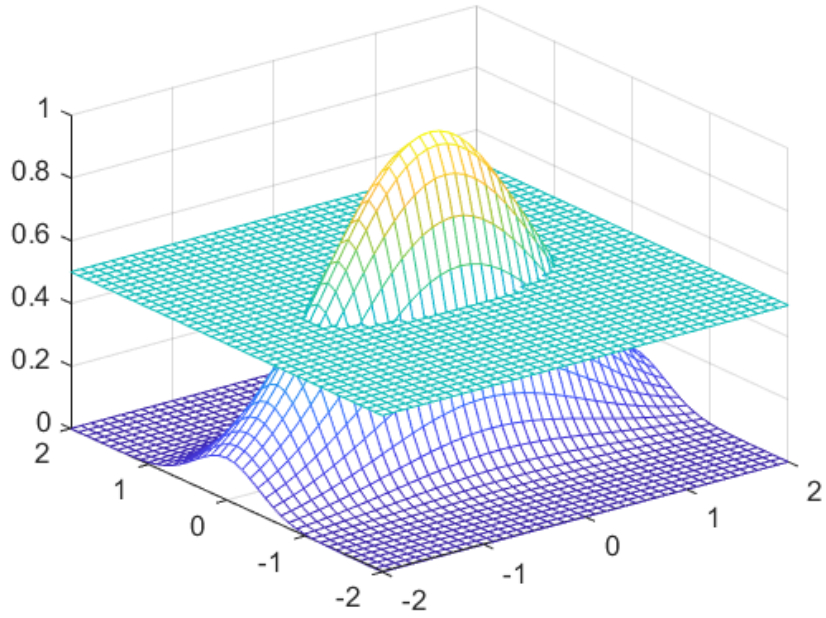

Figure 4.2. Fuzzy set $\widetilde{\mathrm{A}}$ in $\mathbb{R}^2$ space with a marked α-cut ($\alpha = 0.5$)

The following theorem is important. Any fuzzy set $\widetilde{\mathrm{A}}$ can be written as the sum of all its α-cuts [51]:

$$\tilde{\mathrm{A}} = \sum_{\alpha \in [0,\,1]} \alpha \cdot \tilde{\mathrm{A}}_{\alpha}, \tag{4.6}$$

where $\alpha \cdot \widetilde{\mathrm{A}}_{\alpha}$ is a fuzzy set in $\mathbb{X}$, which the membership function is specified as:

$$\mu_{\alpha \cdot \tilde{\mathrm{A}}_{\alpha}} = \begin{cases} \alpha & \text{for } x \in \tilde{\mathrm{A}}_{\alpha}, \\ 0 & \text{for } x \notin \tilde{\mathrm{A}}_{\alpha}. \end{cases} \tag{4.7}$$

4.3. Fuzzy numbers

In the following section, concepts related to fuzzy numbers will be introduced. A fuzzy number $\tilde{a}$ is defined as a fuzzy set of the real line, which is normal (maximum of the membership function is equal to 1), bounded convex (all α-cuts are bounded and convex) and the membership function is at least piecewise continuous [48].

The fuzzy number $\tilde{a} \subseteq \mathbb{R}$ is called positive ($\tilde{a} > 0$), if $\forall x \leq 0, \mu_{\tilde{a}}(x) = 0$ and is called negative ($\tilde{a} < 0$), if $\forall x \geq 0, \mu_{\tilde{a}}(x) = 0$. The fuzzy number is called mixed if it is non-positive and non-negative and contains zero [48, 125].

In a set of fuzzy numbers, the fundamental arithmetic operations can be formulated. Applying Zadeh extension principle, basic arithmetic operations performed on a classical set are extended to fuzzy numbers [62, 188].

Elementary operations for the fuzzy numbers $\tilde{a}$ and $\tilde{b}$ can be performed using the relations below [26, 31, 62, 69]:

a. addition:

$$\tilde{a} + \tilde{b} = \tilde{c}, \quad \mu_{\tilde{c}}(y) = \sup_{\substack{x_1, x_2 \\ y = x_1 + x_2}} \min\left\{\mu_{\tilde{a}}(x_1), \mu_{\tilde{b}}(x_2)\right\}, \tag{4.8}$$

b. subtraction:

$$\tilde{a} - \tilde{b} = \tilde{c}, \quad \mu_{\tilde{c}}(y) = \sup_{\substack{x_1, x_2 \\ y = x_1 - x_2}} \min\left\{\mu_{\tilde{a}}(x_1), \mu_{\tilde{b}}(x_2)\right\}, \tag{4.9}$$

c. multiplication:

$$\tilde{a} \cdot \tilde{b} = \tilde{c}, \quad \mu_{\tilde{c}}(y) = \sup_{\substack{x_1, x_2 \\ y = x_1 \cdot x_2}} \min\left\{\mu_{\tilde{a}}(x_1), \mu_{\tilde{b}}(x_2)\right\}, \tag{4.10}$$

d. division:

$$\tilde{a} / \tilde{b} = \tilde{c}, \quad \mu_{\tilde{c}}(y) = \sup_{\substack{x_1, x_2 \\ y = x_1 / x_2}} \min\left\{\mu_{\tilde{a}}(x_1), \mu_{\tilde{b}}(x_2)\right\}, \tag{4.11}$$

e. inverse of a fuzzy number (it is assumed $\tilde{a} > 0$ or $\tilde{a} < 0$):

$$\mu_{\tilde{a}^{-1}}(x) = \mu_{\tilde{a}}(x^{-1}) \quad \text{for } \tilde{a} > 0 \text{ or } \tilde{a} < 0. \tag{4.12}$$

It is worth mentioning that the presented formulas concern both two- and one-argument operations. As can be seen, two-argument operations executed on a set of fuzzy numbers are complex. It is caused by the presence of a supremum, which requires an infinite number of operations on the membership degrees of the arguments. In order to avoid complicated arithmetic operations, the fuzzy numbers can be created with specific parameters and different types of membership functions. These include triangular or trapezoidal fuzzy numbers as well as fuzzy numbers written in the *L-R* convention [42, 110].

In addition, the problem of fuzzy arithmetic is that there is no fuzzy number opposite to addition, nor inverse to multiplication [125]:

$$\tilde{a} - \tilde{a} \neq 0, \quad \frac{\tilde{a}}{\tilde{a}} \neq 1. \tag{4.13}$$

It is a significant disadvantage mainly during the solution of fuzzy systems of equations. This limitation can be avoided by using directed fuzzy numbers, the idea of which will be explained on the example of directed interval numbers later in the thesis.

4.4. Triangular and trapezoidal fuzzy numbers

Let us introduce the definition of triangular fuzzy numbers. The triangular fuzzy number $\tilde{a}$ represents a fuzzy set with a given membership function [49, 125]:

$$\mu_{\tilde{a}}(x) = \begin{cases} 0, & x < a^-, \\ \dfrac{x - a^-}{a_0 - a^-}, & a^- \le x \le a_0, \\ \dfrac{a^+ - x}{a^+ - a_0}, & a_0 \le x \le a^+, \\ 0, & x > a^+, \end{cases} \tag{4.14}$$

where a_0 is the core of the number, while the values of a^- and a^+ denote the left and right ends of the fuzzy number respectively. The fuzzy triangular number is written as an ordered triple $\tilde{a} = (a^-, a_0, a^+)$.

Figure 4.3 depicts an example of the fuzzy number $\tilde{a} = (-5, -4, 1)$ for which the membership function is:

$$\mu_{\tilde{a}}(x) = \begin{cases} 0, & x < -5, \\ x + 5, & -5 \le x \le -4, \\ \dfrac{1 - x}{5}, & -4 \le x \le 1, \\ 0, & x > 1. \end{cases} \tag{4.15}$$

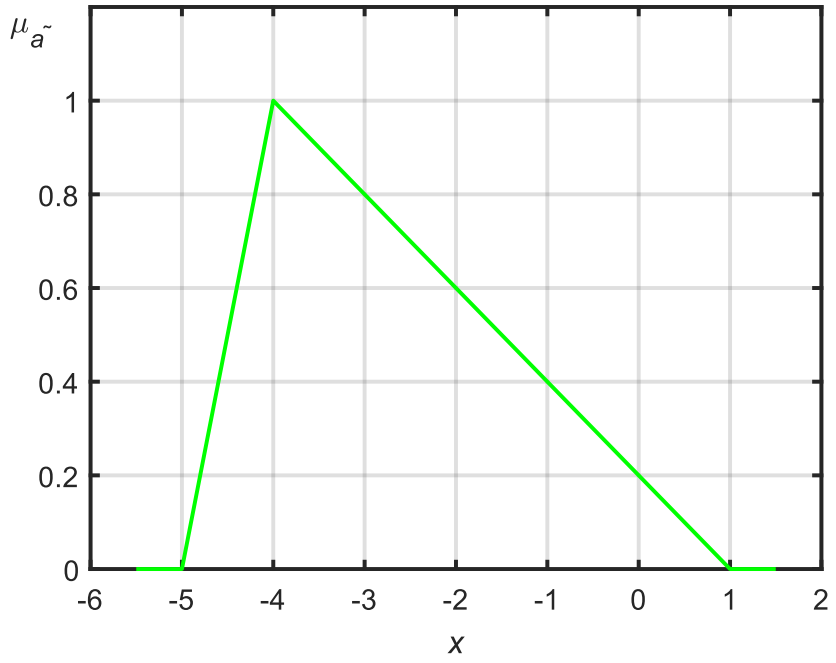

Figure 4.3. Triangular fuzzy number $\tilde{a} = (-5, -4, 1)$

Elementary mathematical operations can be performed in the set of triangular fuzzy numbers, assuming that $\tilde{a}$ and $\tilde{b}$ are fuzzy numbers [14]:

a. addition:

$$\tilde{a} + \tilde{b} = \left(a^- + b^-,\ a_0 + b_0,\ a^+ + b^+\right), \tag{4.16}$$

b. subtraction:

$$\tilde{a} - \tilde{b} = \left(a^- - b^+,\ a_0 - b_0,\ a^+ - b^-\right), \tag{4.17}$$

c. multiplication:

$$\tilde{a} \cdot \tilde{b} \cong \left(a^- \cdot b^-,\ a_0 \cdot b_0,\ a^+ \cdot b^+\right), \tag{4.18}$$

d. division:

$$\tilde{a} / \tilde{b} \cong \left(\frac{a^-}{b^+},\ \frac{a_0}{b_0},\ \frac{a^+}{b^-}\right), \quad b^-, b_0, b^+ \neq 0\,. \tag{4.19}$$

Besides triangular fuzzy numbers, trapezoidal fuzzy numbers are also used in the literature [126, 150]. A trapezoidal fuzzy number is a fuzzy set for which the membership function is specified as [10]:

$$\mu_{\tilde{a}}(x)=\begin{cases}\dfrac{x-(x_0-\sigma)}{\sigma}, & x_0-\sigma\le x\le x_0,\\ 1, & x_0\le x\le y_0,\\ \dfrac{y_0+\beta-x}{\beta}, & y_0\le x\le y_0+\beta,\\ 0, & x\ge y_0+\beta \text{ or } x\le x_0-\sigma,\end{cases} \tag{4.20}$$

where x_0 and y_0 are the defuzzifiers from the left and the right side, respectively; σ and β are the left and the right fuzzinesses. Please note that the trapezoidal fuzzy number is described as $\tilde{a}=(x_0,y_0,\sigma,\beta)$.

The example of the trapezoidal fuzzy number $\tilde{a}=(3,5,1,3)$ is presented in Figure 4.4. The membership function for this example is as follows:

$$\mu_{\tilde{a}}(x)=\begin{cases}x-2, & 2\le x\le 3,\\ 1, & 3\le x\le 5,\\ \dfrac{8-x}{3}, & 5\le x\le 8,\\ 0, & x\ge 8 \text{ or } x\le 2.\end{cases} \tag{4.21}$$

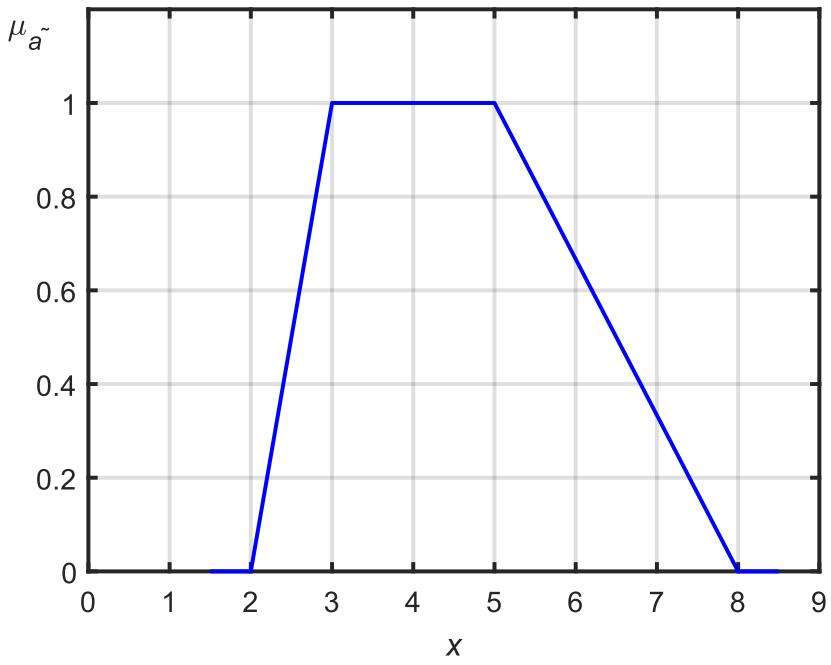

Figure 4.4. Trapezoidal fuzzy number $\tilde{a}=(3,5,1,3)$

Arithmetic operations performed in a set of fuzzy numbers are complicated. In order to simplify this arithmetic, the concept of α-cut of fuzzy numbers can be used, as will be shown in the next subsection.

4.5. α-cuts

As mentioned earlier, the concept of α-cuts is adopted to omit complicated mathematical calculations performed on fuzzy numbers. For a pair of functions $a^-: [0,1] \to \mathbb{R}$ and $a^+: [0,1] \to \mathbb{R}$ defining a fuzzy number, α-cuts are expressed as a set of closed intervals [47, 180]:

$$\forall \alpha \in [0, 1]: \quad \tilde{a}_\alpha = \left[a_\alpha^-, a_\alpha^+ \right]. \tag{4.22}$$

In addition, the following conditions need to be satisfied:

$$\begin{aligned} &1. \quad a^- : \alpha \to a_\alpha^- \in \mathbb{R}, \\ &2. \quad a^+ : \alpha \to a_\alpha^+ \in \mathbb{R}, \\ &3. \quad a_\alpha^- \le a_\alpha^+, \end{aligned} \tag{4.23}$$

where a^- and a^+ are bounded and monotonic functions for each $\alpha \in [0,1]$, while a^- and a^+ are increasing and decreasing functions, respectively.

Importantly, it is possible to write any fuzzy number as the sum of all its α-cuts [30, 49]:

$$\tilde{a} = \sum_{\alpha \in [0,\,1]} \tilde{a}_\alpha \,. \tag{4.24}$$

Considering the case of a triangular fuzzy number $\tilde{a} = (a^-, a_0\,, a^+)$, we can define the α-cut as a set of closed intervals of the following form [125]:

$$\tilde{a}_\alpha = \left[\left(a_0 - a^-\right)\alpha + a^-, \left(a_0 - a^+\right)\alpha + a^+ \right]. \tag{4.25}$$

On the other hand, for a trapezoidal fuzzy number $\tilde{a} = (x_0, y_0, \sigma, \beta)$, the α-cut is given as [126]:

$$\tilde{a}_\alpha = \left[x_0 - (1-\alpha)\sigma, y_0 - (1-\alpha)\beta \right]. \tag{4.26}$$

Figure 4.5 presents an example of the triangular fuzzy number $\tilde{a} = (1, 3, 7)$ for which the α-cut is determined:

$$\tilde{a}_\alpha = \left[(3-1)\alpha + 1, (3-7)\alpha + 7 \right] = \left[2\alpha + 1, -4\alpha + 7 \right]. \tag{4.27}$$

In addition, it is possible to calculate a specific value for a given α, for instance for α = 0.5:

$$\tilde{a}_{0.5} = \left[2 \cdot 0.5 + 1, -4 \cdot 0.5 + 7 \right] = \left[2, 5 \right]. \tag{4.28}$$

The proposed decomposition of fuzzy numbers eliminates the need for complex arithmetic operations. Due to it, elementary mathematical operations are performed at the ends of intervals.

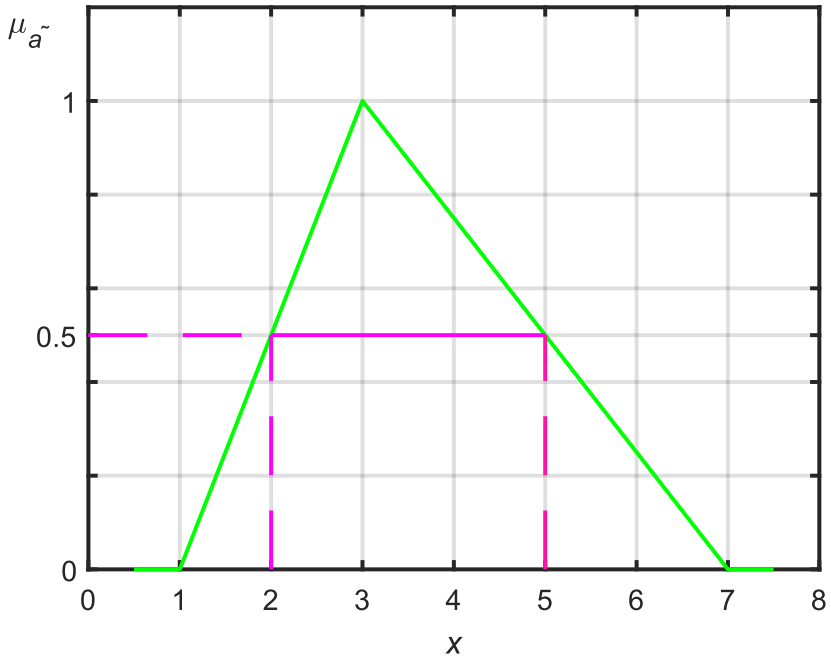

Figure 4.5. Triangular fuzzy number $\tilde{a} = (1, 3, 7)$ with α = 0.5

The fundamental mathematical operations for α-cuts can be conducted using classical or directed interval arithmetic. Applying the rules of the classical interval arithmetic for two fuzzy numbers $\tilde{a}$ and $\tilde{b}$ ($\forall \alpha \in [0,1]$), the basic operations can be defined as follows [125]:

a. addition:

$$\left(\tilde{a}+\tilde{b}\right)_\alpha = \left[a_\alpha^- + b_\alpha^-,\ a_\alpha^+ + b_\alpha^+\right]_\alpha, \tag{4.29}$$

b. subtraction:

$$\left(\tilde{a}-\tilde{b}\right)_\alpha = \left[a_\alpha^- - b_\alpha^+,\ a_\alpha^+ - b_\alpha^-\right]_\alpha, \tag{4.30}$$

c. multiplication:

$$\left(\tilde{a}\cdot\tilde{b}\right)_\alpha = \left[\min\left\{a_\alpha^- b_\alpha^-,\ a_\alpha^- b_\alpha^+,\ a_\alpha^+ b_\alpha^-,\ a_\alpha^+ b_\alpha^+\right\}, \max\left\{a_\alpha^- b_\alpha^-,\ a_\alpha^- b_\alpha^+,\ a_\alpha^+ b_\alpha^-,\ a_\alpha^+ b_\alpha^+\right\}\right]_\alpha, \tag{4.31}$$

d. division($0 \notin [b_\alpha^-, b_\alpha^+]$):

$$\left(\frac{\tilde{a}}{\tilde{b}}\right)_\alpha = \left[\min\left\{\frac{a_\alpha^-}{b_\alpha^-}, \frac{a_\alpha^-}{b_\alpha^+}, \frac{a_\alpha^+}{b_\alpha^-}, \frac{a_\alpha^+}{b_\alpha^+}\right\}, \max\left\{\frac{a_\alpha^-}{b_\alpha^-}, \frac{a_\alpha^-}{b_\alpha^+}, \frac{a_\alpha^+}{b_\alpha^-}, \frac{a_\alpha^+}{b_\alpha^+}\right\}\right]_\alpha, \tag{4.32}$$

e. multiplication by a scalar ($k \in \mathbb{R}$):

$$k \cdot \tilde{a}_\alpha = \left[\min\left\{ka_\alpha^-, ka_\alpha^+\right\}, \max\left\{ka_\alpha^-, ka_\alpha^+\right\}\right]_\alpha, \tag{4.33}$$

f. inverse ($0 \notin [a_\alpha^-, a_\alpha^+]$):

$$\left(\frac{1}{\tilde{a}}\right)_\alpha = \left[\frac{1}{a_\alpha^+}, \frac{1}{a_\alpha^-}\right]_\alpha. \tag{4.34}$$

4.6. Classical and directed interval arithmetic

Classical and directed interval arithmetic have been mentioned in the work many times before. Publication of the book *Interval Analysis* by Ramon E. Moore'a in 1966 [102] is considered as the beginning of interval arithmetic. However, the idea of performing calculations on sets and intervals originated earlier, for example in the works of Rosalind C. Young (1931) [186] or Teruo Sunaga (1958) [164]. It is worth noting that interval numbers can be used to describe uncertain parameters in an interval form [49].

Let us introduce the definition of an interval number. A closed interval number is the set of all real numbers specified as [53]:

$$\bar{a} = \left[a^-, a^+\right] = \left\{a \in \bar{a} : a^- \le a \le a^+\right\}, \tag{4.35}$$

where $a^-, a^+ \in \mathbb{R}$ represent the beginning and the end of the given interval.

Compared to fuzzy numbers, partial set membership is not possible for interval numbers. For each real number $a \in \mathbb{R}$, the characteristic function adopts only two different values. If the number a belongs to the interval $[a^-, a^+]$, the value of the characteristic function is equal to 1, otherwise the value of the characteristic function is 0 [49, 125].

The set of all closed intervals is marked as $\mathbb{IR}$. The interval is called narrow if $a^- = a^+$ or wide if $a^- < a^+$. Its width is defined as $\dim(\bar{a}) = a^+ - a^-$ [49, 125].

The basic arithmetic operations in the set of interval numbers are an extension of the basic operations in the set of real numbers. For two interval numbers $\bar{a} = [a^-, a^+]$

and $\bar{b} = [b^-, b^+]$), ($\bar{a}, \bar{b} \in \mathbb{IR}$) the elementary mathematical operations are analogous to the ones performed on α-cuts (see Equations (4.29)-(4.34)). The difference is that previously fuzzy numbers were used as opposed to interval numbers [49, 125].

Importantly, in the set of interval numbers $\mathbb{IR}$, there is an element equal to zero ($\bar{0} = [0,0]$) and an element equal to one ($\bar{1} = [1,1]$). Unfortunately, in classical interval arithmetic there are no operations such as the opposite of addition ($\bar{a} - \bar{a}_{\neq}\bar{0}$) and the inverse of multiplication ($\bar{a}/\bar{a}_{\neq}\bar{1}$). This is obviously a major complication when solving linear equations and inequalities. To avoid this complication, directed interval arithmetic can be applied [91, 92, 137].

The set of directed interval numbers is defined as the set of all pairs of real numbers that are ordered [137]:

$$\bar{a} = \left[a^-,\, a^+\right] = \left\{\bar{a} \in \mathbb{D}:\; a^-,\, a^+ \in \mathbb{R}\right\}, \tag{4.36}$$

where $a^-, a^+ \in \mathbb{R}$ denote the beginning and the end of the interval.

There are three types of directed interval numbers, taking into account the position of the interval limits [92, 137]:

- proper, when $a^- \leq a^+$,
- improper, when $a^- \geq a^+$,
- degenerate, when $a^- = a^+$.

The set of all directed interval numbers is denoted as $\mathbb{D} = \mathbb{P} \cup \mathbb{I}$, where $\mathbb{P}$ and $\mathbb{I}$ represent the set of all directed proper and improper intervals, respectively. In addition, in the theory of directed interval numbers, a subset $\mathbb{Z} = \mathbb{Z}_{\mathbb{P}} \cup \mathbb{Z}_{\mathbb{I}}$ is defined, containing all directed intervals with element 0 [92]:

$$\begin{aligned} \mathbb{Z}_{\mathbb{P}} &= \left\{\bar{a} \in \mathbb{P} : a^- \leq 0 \leq a^+\right\}, \\ \mathbb{Z}_{\mathbb{I}} &= \left\{\bar{a} \in \mathbb{I} :\; a^+ \leq 0 \leq a^-\right\}. \end{aligned} \tag{4.37}$$

In the set of all directed interval numbers $\mathbb{D}$, a direction functional and a sign functional are defined. The direction functional is expressed as [92, 137]:

$$\tau\left(\bar{a}\right) = \begin{cases} +, & a^- \leq a^+, \\ -, & a^- > a^+, \end{cases} \tag{4.38}$$

as well as the sign functional is stated as:

$$\sigma\left(\bar{a}\right) = \begin{cases} +, & a^-,\, a^+ > 0, \\ -, & a^-,\, a^+ < 0. \end{cases} \tag{4.39}$$

In the set of directed interval numbers $\mathbb{D}$ two additional mathematical operators are performed [125]:

- opposite of addition ($\forall \bar{a} \in \mathbb{D}$): $-\bar{a} = \left[-a^{-}, -a^{+}\right]$,
- inverse of multiplication ($\forall \bar{a} \in \mathbb{D}\backslash\mathbb{Z}$): $1/\bar{a} = \left[1/a^{-}, 1/a^{+}\right]$.

Thanks to these additional mathematical operators and functionals, elementary mathematical operations on directed interval numbers can be formulated [125, 137]:

a. addition ($\forall \bar{a}, \bar{b} \in \mathbb{D}$):

$$\bar{a} + \bar{b} = \left[a^{-} + b^{-},\ a^{+} + b^{+}\right], \tag{4.40}$$

b. subtraction ($\forall \bar{a}, \bar{b} \in \mathbb{D}$):

$$\bar{a} - \bar{b} = \left[a^{-} - b^{-},\ a^{+} - b^{+}\right], \tag{4.41}$$

c. multiplication:

$$\bar{a} \cdot \bar{b} = \begin{cases} \left[a^{-\sigma(\bar{b})} \cdot b^{-\sigma(\bar{a})},\ a^{\sigma(\bar{b})} \cdot b^{\sigma(\bar{a})}\right], & \bar{a}, \bar{b} \in \mathbb{D}\backslash\mathbb{Z}, \\ \left[a^{\sigma(\bar{a})\tau(\bar{b})} \cdot b^{-\sigma(\bar{a})},\ a^{\sigma(\bar{a})\tau(\bar{b})} \cdot b^{\sigma(\bar{a})}\right], & \bar{a} \in \mathbb{D}\backslash\mathbb{Z}, \bar{b} \in \mathbb{Z}, \\ \left[a^{-\sigma(\bar{b})} \cdot b^{\sigma(\bar{b})\tau(\bar{a})},\ a^{\sigma(\bar{b})} \cdot b^{\sigma(\bar{b})\tau(\bar{a})}\right], & \bar{a} \in \mathbb{Z}, \bar{b} \in \mathbb{D}\backslash\mathbb{Z}, \\ \left[\min\left\{a^{-} \cdot b^{+},\ a^{+} \cdot b^{-}\right\},\ \max\left\{a^{-} \cdot b^{-},\ a^{+} \cdot b^{+}\right\}\right], & \bar{a}, \bar{b} \in \mathbb{Z}_{\mathbb{P}}, \\ \left[\max\left\{a^{-} \cdot b^{-},\ a^{+} \cdot b^{+}\right\},\ \min\left\{a^{-} \cdot b^{+},\ a^{+} \cdot b^{-}\right\}\right], & \bar{a}, \bar{b} \in \mathbb{Z}_{\mathbb{I}}, \\ 0, & \left(\bar{a} \in \mathbb{Z}_{\mathbb{P}}, \bar{b} \in \mathbb{Z}_{\mathbb{I}}\right) \cup \left(\bar{a} \in \mathbb{Z}_{\mathbb{I}}, \bar{b} \in \mathbb{Z}_{\mathbb{P}}\right), \end{cases} \tag{4.42}$$

d. division:

$$\bar{a} / \bar{b} = \begin{cases} \left[a^{-\sigma(\bar{b})} / b^{-\sigma(\bar{a})},\ a^{\sigma(\bar{b})} / b^{\sigma(\bar{a})}\right], & \bar{a}, \bar{b} \in \mathbb{D}\backslash\mathbb{Z}, \\ \left[a^{-\sigma(\bar{b})} / b^{\sigma(\bar{b})},\ a^{\sigma(\bar{b})} / b^{\sigma(\bar{b})}\right], & \bar{a} \in \mathbb{Z}, \bar{b} \in \mathbb{D}\backslash\mathbb{Z}. \end{cases} \tag{4.43}$$

With these two additional operations it is possible to obtain $\bar{0} = [0,0]$ for subtraction ($\bar{a} - \bar{a} = \bar{0}$) and $\bar{1} = [1,1]$ for division ($\bar{a}/\bar{a} = \bar{1}$). This is the main difference between directed and classical interval arithmetic [125].

The use of directed interval arithmetic also affects the width of the intervals obtained, which is shown in the literature, for example, in [128]. Applying classical interval arithmetic to solve systems of equations sometimes receives very wide, non-realistic intervals. Therefore, modifications of this technique, such as the directed interval arithmetic described above, are becoming more popular. Other methods that are currently in use are, for example, generalised interval arithmetic or segmented mathematics [146].

4.7. Solving fuzzy or interval systems of linear equations

One of the more difficult issues in fuzzy and interval arithmetic is solving systems of equations. As a result of many mathematical operations performed on fuzzy or interval numbers, the width of the obtained intervals is increased. The method that is most commonly used to solve interval systems of equations is the interval Gauss elimination method. Other algorithms presented in the literature include the combinatorial method, Krawczyk's method or Gauss-Seidel iteration [70, 108, 141].

Please note that in the case of fuzzy systems of equations, the application of the concept of α-cuts of fuzzy numbers allows to implement all of the above-mentioned methods for solving interval systems of equations [13].

As an example, the interval Gauss elimination method is described in this work [108, 125]. The basic term used to define the interval systems of linear equations is an interval matrix. An interval matrix is the matrix $\overline{\mathbf{A}}$, whose elements are interval numbers:

$$\overline{\mathbf{A}} = \begin{bmatrix} \overline{a}_{11} & \overline{a}_{12} & \dots & \overline{a}_{1m} \\ \overline{a}_{21} & \overline{a}_{22} & \dots & \overline{a}_{2m} \\ \vdots & \vdots & \ddots & \vdots \\ \overline{a}_{n1} & \overline{a}_{n2} & \dots & \overline{a}_{nm} \end{bmatrix}, \tag{4.44}$$

where $\overline{a}_{ij} \in \mathbb{IR};\ i = 1, 2, \dots, n;\ j = 1, 2, \dots, m.$ In a set of interval matrices, the elementary mathematical operations are defined [108].

The interval system of linear equations can be expressed in the following form:

$$\overline{\mathbf{A}} \cdot \overline{\mathbf{x}} = \overline{\mathbf{b}}, \tag{4.45}$$

where $\overline{\mathbf{A}}$ is the interval matrix with dimension $n \times n$ and $\overline{\mathbf{b}}$ is the interval vector with dimension $n \times 1$. The above equation can be written:

$$\begin{bmatrix} \overline{a}_{11} & \overline{a}_{12} & \dots & \overline{a}_{1n} \\ \overline{a}_{21} & \overline{a}_{22} & \dots & \overline{a}_{2n} \\ \vdots & \vdots & \ddots & \vdots \\ \overline{a}_{n1} & \overline{a}_{n2} & \dots & \overline{a}_{nn} \end{bmatrix} \cdot \begin{bmatrix} \overline{x}_1 \\ \overline{x}_2 \\ \vdots \\ \overline{x}_n \end{bmatrix} = \begin{bmatrix} \overline{b}_1 \\ \overline{b}_2 \\ \vdots \\ \overline{b}_n \end{bmatrix}. \tag{4.46}$$

According to the interval Gaussian elimination method, the decomposition of the matrix $\overline{\mathbf{A}}$ needs to be performed [108]. As a consequence, the matrix $\overline{\mathbf{A}}$ consists of two triangular matrices $\overline{\mathbf{L}}$ and $\overline{\mathbf{U}}$ defined as:

$$\bar{\mathbf{L}} = \begin{bmatrix} 1 & 0 & \dots & 0 \\ \bar{l}_{21} & 1 & \dots & 0 \\ \vdots & \vdots & \ddots & \vdots \\ \bar{l}_{n1} & \bar{l}_{n2} & \dots & 1 \end{bmatrix}, \quad \bar{\mathbf{U}} = \begin{bmatrix} \bar{u}_{11} & \bar{u}_{12} & \dots & \bar{u}_{1n} \\ 0 & \bar{u}_{22} & \dots & \bar{u}_{2n} \\ \vdots & \vdots & \ddots & \vdots \\ 0 & 0 & \dots & \bar{u}_{nn} \end{bmatrix}, \tag{4.47}$$

where the individual elements of matrices $\bar{\mathbf{L}}$ and $\bar{\mathbf{U}}$ are computed by relations:

$$\begin{cases} \bar{u}_{ij} = \bar{a}_{ij} - \sum_{k=1}^{i-1} \bar{l}_{ik}\bar{u}_{kj}, & j = i, i+1, \dots, n, \\ \bar{l}_{ji} = \dfrac{1}{u_{ii}}\left(\bar{a}_{ji} - \sum_{k=1}^{i-1} \bar{l}_{jk}\bar{u}_{ki} \right), & j = i+1, i+2, \dots, n. \end{cases} \tag{4.48}$$

By substituting the matrices $\bar{\mathbf{L}}$ and $\bar{\mathbf{U}}$ into an interval system of linear equations (Equation (4.45)), one obtains:

$$\bar{\mathbf{A}} \cdot \bar{\mathbf{x}} = \left(\bar{\mathbf{L}} \cdot \bar{\mathbf{U}}\right) \cdot \bar{\mathbf{x}} = \bar{\mathbf{L}} \cdot \left(\bar{\mathbf{U}} \cdot \bar{\mathbf{x}}\right) = \bar{\mathbf{b}}. \tag{4.49}$$

Taking into account that the interval vector $\bar{\mathbf{z}}$ is equal to:

$$\bar{\mathbf{z}} = \bar{\mathbf{U}} \cdot \bar{\mathbf{x}}, \tag{4.50}$$

one receives:

$$\bar{\mathbf{L}} \cdot \bar{\mathbf{z}} = \bar{\mathbf{b}}. \tag{4.51}$$

The interval vector $\bar{\mathbf{x}}$ which is the solution is calculated from the system of equations presented in the Equation (4.50).

4.8. Example of using fuzzy and interval numbers

In order to better understand and perceive the subtle difference between fuzzy and interval numbers, the following examples are provided.

The aim of the problem is to determine a steady-state ($\dot{T}$ = 0), sourceless (Q_{int} = 0) temperature field in a one-dimensional region with a length of 0.1 m. It is also assumed that the thermal conductivity coefficient does not depend on temperature (k = constant). In this case, the Fourier equation (compare with Equation (3.4)) has the form:

$$k \frac{\mathrm{d}^2 T}{\mathrm{d}x^2} = 0, \tag{4.52}$$

where x is the component of the Cartesian coordinate system.

Completing the mathematical model with boundary conditions, the temperature on the left edge is equal to 10 °C, while on the right edge the heat flux 10^4 W·m^{-2} is given. The domain is divided into 5 elements (6 nodes including 2 boundary nodes and 3 internal nodes), where the distance between nodes is constant. The calculations have been carried out applying the finite difference method (FDM). Explanation of FDM is not the main idea of the demonstrated example; therefore, it will not be discussed in detail in this section of the thesis. More information on FDM can be found in [88, 100].

First, an analysis has been performed for a deterministic value of the thermal conductivity coefficient, where k = 30 W·m^{-1}·K^{-1}. The results are shown in Figure 4.6.

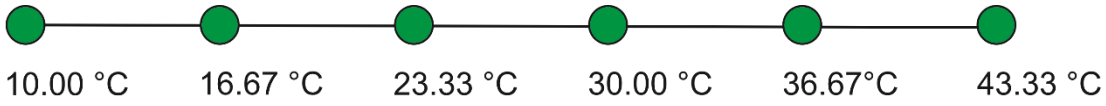

Figure 4.6. Results for deterministic thermal conductivity coefficient

Let us consider the same task for the parameter k introduced as a fuzzy number. The thermal conductivity coefficient is a triangular fuzzy number, $\tilde{k} = (28.5; 30; 31.5)$ W·m^{-1}·K^{-1}. As mentioned earlier, calculations for fuzzy numbers can be complicated; therefore, it is recommended to use α-cuts, taking specific values of the parameter α. In the example, it is assumed that the parameter α = 0.5. Based on the relationship presented in Equation (4.25), the following transformation has been performed:

$$\begin{aligned}\tilde{k}_{0.5} &= \left(28.5;\ 30;\ 31.5\right) = \left[\left(30-28.5\right)\cdot 0.5+28.5;\ \left(30-31.5\right)\cdot 0.5+31.5\right] \\ &= \left[29.25;\ 30.75\right].\end{aligned} \tag{4.53}$$

Then, all mathematical operations have been conducted according to the rules based on interval arithmetic, for instance classical or directed arithmetic. Figure 4.7 illustrates the results obtained for the coefficient $\tilde{k}_{0.5} = (28.5; 30; 31.5) = [29.25; 30.75]$ W·m^{-1}·K^{-1}. Analysing Equation (4.52) in detail, one can notice that in this case only the operation of multiplication by a scalar is required (see Equation (4.33)).

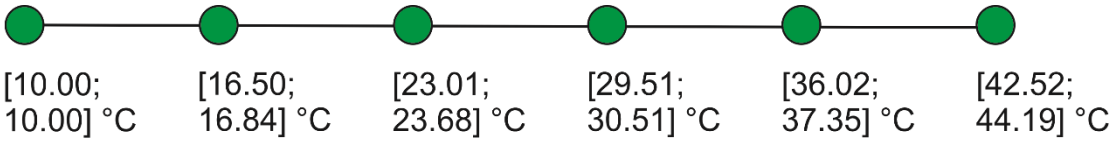

Figure 4.7. Results for fuzzy thermal conductivity coefficient for α = 0.5

For comparison, a solution to this example has also been prepared for the interval heat transfer coefficient, where $\bar{k} = [28.5; 31.5]$ W·m^{-1}·K^{-1}. To perform operations for equations with interval numbers, it is necessary to use, for example, the Equations (4.40)-(4.43). Figure 4.8 shows the results of calculations involving directed interval arithmetic. Similar to the problem with the fuzzy thermal conduction coefficient, the calculation of the temperature field is reduced to multiplication interval number by a scalar.

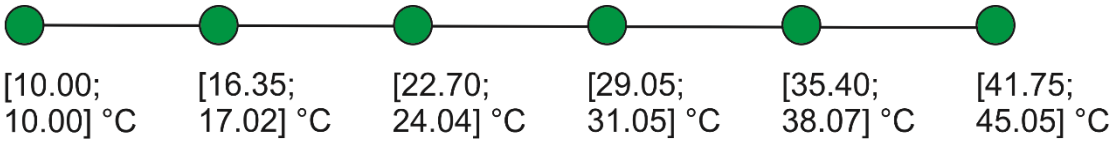

Figure 4.8. Results for interval thermal conductivity coefficient

In summary, it can be noted that the deterministic temperatures distribution is in the range of fuzzy and interval temperatures. Therefore, it is concluded that both approaches are correct. However, it is important to remember the essential difference between fuzzy and interval numbers in the interpretation of the membership function.

It should also be remembered that these examples are very simple and did not require much calculation on fuzzy or interval numbers. More complex problems need more mathematical operations on fuzzy or interval numbers. For example, the heat transfer process in the one-dimensional domain is more complicated to model. In this case, Equation (4.52) for fuzzy and interval number can be expressed:

$$\frac{\partial \tilde{T}}{\partial t} = \frac{\tilde{k}}{\tilde{c}_p \tilde{\rho}} \frac{\partial^2 \tilde{T}}{\partial x^2} \text{ (fuzzy no.)} \quad \text{and} \quad \frac{\partial \bar{T}}{\partial t} = \frac{\bar{k}}{\bar{c}_p \bar{\rho}} \frac{\partial^2 \bar{T}}{\partial x^2} \text{ (interval no.)}. \tag{4.54}$$

As one can see, there are multiplication and division operations. In this case, the thermophysical parameters are assumed to be fuzzy and interval numbers, respectively, where $\tilde{k} = (33.25; 35.00; 36.75)$ W·m^{-1}·K^{-1}, $\tilde{c} = (7125; 7500; 7875)$

$\mathrm{J\cdot kg^{-1}\cdot K^{-1}}$, $\tilde{\rho} = (655.5; 690.0; 724.5)$ $\mathrm{kg\cdot m^{-3}}$ and $\bar{k} = [33.25;\ 36.75]$ $\mathrm{W\cdot m^{-1}\cdot K^{-1}}$, $\bar{c} = [7125;\ 7875]$ $\mathrm{J\cdot kg^{-1}\cdot K^{-1}}$, $\bar{\rho} = [655.5;\ 724.5]$ $\mathrm{kg\cdot m^{-3}}$.

Firstly, let us consider this problem for fuzzy numbers. In order to avoid complex calculations, the α-cuts approach is implemented, where α = 0.5. Therefore:

$$\begin{aligned}
\tilde{k}_{0.5} &= (33.25;\ 35.00;\ 36.75) = \left[(35.00-33.25)\cdot 0.5+33.25;\right.\\
&\quad \left.(35.00-36.75)\cdot 0.5+36.75\right],\\
\tilde{k}_{0.5} &= [34.125; 35.875],\\
\tilde{c}_{0.5} &= (7125;\ 7500;\ 7875) = \left[(7500-7125)\cdot 0.5+7125;\right.\\
&\quad \left.(7500-7875)\cdot 0.5+7875\right],\\
\tilde{c}_{0.5} &= [7312.5; 7687.5],\\
\tilde{\rho}_{0.5} &= (655.5;\ 690.0;\ 724.5) = \left[(690.0-655.5)\cdot 0.5+655.5;\right.\\
&\quad \left.(690.0-724.5)\cdot 0.5+724.5\right],\\
\tilde{\rho}_{0.5} &= [672.75; 707.25].
\end{aligned} \tag{4.55}$$

In the next step, calculations can be performed using classical interval arithmetic. Based on Equations (4.29)-(4.34):

1.
$$\begin{aligned}
\tilde{c}_{0.5}\cdot\tilde{\rho}_{0.5} &= [7312.5; 7687.5]\cdot[672.75; 707.25]\\
&= \left[\min\{7312.5\cdot 672.75; 7312.5\cdot 707.25; 7687.5\cdot 672.75; 7687.5\cdot 707.25\},\right.\\
&\quad \left.\max\{7312.5\cdot 672.75; 7312.5\cdot 707.25; 7687.5\cdot 672.75; 7687.5\cdot 707.25\}\right],\\
\tilde{c}_{0.5}\cdot\tilde{\rho}_{0.5} &= \left[4.920\cdot 10^{6}; 5.437\cdot 10^{6}\right],
\end{aligned} \tag{4.56}$$

2.
$$\begin{aligned}
\frac{\tilde{k}_{0.5}}{\tilde{c}_{0.5}\cdot\tilde{\rho}_{0.5}} &= \frac{[34.125; 35.875]}{\left[4.920\cdot 10^{6}; 5.437\cdot 10^{6}\right]}\\
&= \left[\min\left\{\frac{34.125}{4.920\cdot 10^{6}}, \frac{34.125}{5.437\cdot 10^{6}}, \frac{35.875}{4.920\cdot 10^{6}}, \frac{35.875}{5.437\cdot 10^{6}}\right\},\right.\\
&\quad \left.\max\left\{\frac{34.125}{4.920\cdot 10^{6}}, \frac{34.125}{5.437\cdot 10^{6}}, \frac{35.875}{4.920\cdot 10^{6}}, \frac{35.875}{5.437\cdot 10^{6}}\right\}\right],\\
\frac{\tilde{k}_{0.5}}{\tilde{c}_{0.5}\cdot\tilde{\rho}_{0.5}} &= \left[6.276\cdot 10^{-6}; 7.292\cdot 10^{-6}\right].
\end{aligned} \tag{4.57}$$

Using α-cuts, it is also possible to implement the rules of directed interval arithmetic. In a further thermal analysis, the obtained coefficient $\tilde{k}/(\tilde{c}\cdot\tilde{\rho})$ should be entered into the bioheat transfer equation. Please note that the temperatures included in the derivatives are also fuzzy numbers.

Let us similarly demonstrate the procedure for the interval thermophysical parameters. Applying directed interval arithmetic (see Equations (4.40)-(4.43)), one can obtain the following:

1. $$\begin{aligned}&\overline{c}\cdot\overline{\rho}=\left[7125.0;7875.0\right]\cdot\left[655.5;724.5\right]\\&=\left[c^{-\sigma(\overline{b})}\cdot\rho^{-\sigma(\overline{a})};c^{\sigma(\overline{b})}\cdot\rho^{\sigma(\overline{a})}\right],\quad\text{because}\quad\overline{c},\overline{\rho}\in\mathbb{D}\setminus\mathbb{Z},\\&\left|\begin{array}{ll}\overline{c}=\left[7125.0;7125.0\right] & \sigma\left(\overline{c}\right)=+,\quad\text{because}\quad c^{-},c^{+}>0\\ \overline{\rho}=\left[655.5;724.5\right] & \sigma\left(\overline{c}\right)=+,\quad\text{because}\quad\rho^{-},\rho^{+}>0\end{array}\right|\\&\overline{c}\cdot\overline{\rho}=\left[c^{-}\cdot\rho^{-};c^{+}\cdot\rho^{+}\right]=\left[4.670\cdot10^{6};5.705\cdot10^{6}\right],\end{aligned}\tag{4.58}$$

2. $$\begin{aligned}&\frac{\overline{k}}{\overline{c}\cdot\overline{\rho}}=\frac{\left[33.250;36.750\right]}{\left[4.670\cdot10^{6};5.705\cdot10^{6}\right]}\\&=\left[k^{-\sigma(\overline{b})}/\left(c\cdot\rho\right)^{-\sigma(\overline{a})};k^{\sigma(\overline{b})}/\left(c\cdot\rho\right)^{\sigma(\overline{a})}\right],\quad\text{because}\quad\overline{c},\overline{\rho}\in\mathbb{D}\setminus\mathbb{Z},\\&\left|\begin{array}{ll}\overline{k}=\left[33.250;36.750\right] & \sigma\left(\overline{c}\right)=+,\quad\text{because}\quad k^{-},k^{+}>0\\ \overline{c}\cdot\overline{\rho}=\left[4.670\cdot10^{6};5.705\cdot10^{6}\right] & \sigma\left(\overline{c}\right)=+,\quad\text{because}\quad\left(c\cdot\rho\right)^{-},\left(c\cdot\rho\right)^{+}>0\end{array}\right|\\&\frac{\overline{k}}{\overline{c}\cdot\overline{\rho}}=\left[k^{-}/\left(c\cdot\rho\right)^{-)};k^{+}/\left(c\cdot\rho\right)^{+}\right]=\left[7.119\cdot10^{-6};6.441\cdot10^{-6}\right].\end{aligned}\tag{4.59}$$

As a result of performing operations using directed interval arithmetic, the parameter $\overline{k}/(\overline{c}\cdot\overline{\rho})$ is an improper interval number. This should be noted for subsequent calculations, which additionally require consideration of the interval temperature present in the heat transfer equation.

5. Numerical examples: heat transfer

5.1. Introduction

Preparing a simulation of the cryopreservation process, it is undoubtedly necessary to include the bioheat transfer. As already mentioned in Chapter 3, various relationships are applied for analysis and modelling of heat transfer. Among the most popular are the Fourier equation, the Pennes equation, the CV equation or the DPL model. The analysis of changes in the temperature distribution in the sample is important because they are coupled to other transport phenomena, which will be discussed in the next chapter.

To supplement heat transfer model, another physical phenomena should be considered. Phase changes occur when the temperature of a certain material is reduced below the freezing (melting) point. Obviously, the CPAs provided during cryopreservation change the properties of the sample. However, the CPAs do not guarantee full protection against the crystallisation of ice crystals, which is a danger to biological structures.

Phase transitions can be analysed using different approaches. The first of them represents phenomena in macroscale. It involves dividing the area under consideration into sub-domains according to the state of matter that is present in them. Applying the one domain method, a component is introduced into the heat transfer equation that takes a specific form depending on the current state of matter in the sub-domain.

On the other hand, the microscopic approach estimates the degree of crystallised water in relation to the total volume of the cell solution. The crystallisation can be explained by the non-isothermal equation proposed by Boutron and Mehl. It can be said that the crystallisation is one of the markers of damage to a biological sample.

In the following section, some examples of calculations related to heat transfer and phase transitions during cryopreservation are presented. Importantly, the particular simulations are performed for models introducing, for example, interval or fuzzy numbers. Example 1 demonstrates a model of bioheat transfer in biological tissue described by the Fourier equation. In contrast, Example 2 completes the thermal model

with phase changes introduced into the governing equation by the one domain method. Example 3 analyses also the heat transfer in the biological material, although the model additionally considers the phenomenon of crystallisation using the zone model and the non-isothermal equation proposed by Boutron and Mehl.

5.2. Example 1: Bioheat transfer model

In this example, a mathematical model is prepared to describe the changes in thermal distribution in a cylindrical sample of articular cartilage. To begin with, a few words about the articular cartilage. The articular cartilage is located at the end of a bone inside the joint. This tissue is elastic and carries the loads acting in the joint during movement. It is mainly composed of water (65%-80%). The other elements of articular cartilage include collagen (10%-20%) and proteoglycan matrix (5%-10%). The extracellular matrix (proteoglycan) contains cells named chondrocytes. The articular cartilage has no innervation, no nerves, no blood and no lymph vessels [1]. Therefore, it is not necessary to consider the perfusion of the tissue, and as a result our proposed heat transfer model is based on the Fourier equation.

It should be mentioned that the issue of cryopreservation of articular cartilage is discussed in the literature. Many publications with experimental studies can be found, for example [1, 12, 59, 75, 112, 118, 122]. Likewise, many scientists have prepared a mathematical model of this process to improve its efficiency [76, 104, 147, 183, 187, 189]. In Chapter 2 (see Subsection 2.3) the case of using the LT protocol to perform cryopreservation of articular cartilage is described. This idea has been developed by, among others, Pegg et al. [116], Wang et al. [178] or Kay et al. [65]. As this is a constantly developing technique, our computational model investigates the temperature distribution in an articular cartilage sample cryopreserved by the LT method.

In addition, using the LT protocol, the temperature and the concentration of the bath solution are properly regulated. This modifies the properties of the sample, for example, its freezing (melting) point, while preventing ice crystallisation. For this reason, the phase transitions and crystallisation phenomena have been omitted in this example.

At the start, it is worth repeating that the basic equation describing heat transfer in biological structures is the Fourier equation (see Equation (3.4)) [21]:

$$c_p \rho \dot{T} = \nabla \left(k \nabla T \right) + Q_{\text{int}} . \tag{5.1}$$

Please note that the energy equation has to be completed with appropriate unambiguity conditions. They determine, for example, the geometry and the physical conditions such as thermophysical parameters of the analysed sample. It is also important to define initial and boundary conditions. The initial temperature is specified at the starting moment [21]:

$$T(X,0) = T^0, \tag{5.2}$$

where T^0 is the initial temperature when $t = 0$ and X is the geometric coordinate.

Four fundamental boundary conditions are considered. The boundary condition of the 1st type (Dirichlet) describes the temperature distribution that occurs on the given boundary [21]:

$$T\left(X,t\right) = T_\Gamma , \tag{5.3}$$

where T_Γ is the temperature on the boundary.

The boundary condition of the 2nd type (Neumann) describes the heat flux, which is normal to the boundary [21]:

$$q_\Gamma \left(X,t\right) = -\mathbf{n}k \cdot \nabla T , \tag{5.4}$$

where q_Γ is the heat flux and $\mathbf{n}$ is the normal vector to the boundary.

The boundary condition of the 3rd type (Robin) represents the heat exchange between the external environment and the boundary :

$$q_\Gamma \left(X,t\right) = -\mathbf{n}k \cdot \nabla T = \alpha_\Gamma \left[T\left(X,t\right) - T_{ext} \right], \tag{5.5}$$

where α_Γ is natural convection heat transfer coefficient, T_{ext} is the temperature of the surrounding mediums.

The last one is the boundary condition of the 4th type, which concerns the boundary between heterogeneous bodies. In the case of ideal contact between the bodies, this condition has the following form [21]:

$$\begin{cases} -\mathbf{n}k_1 \cdot \nabla T = -\mathbf{n}k_2 \cdot \nabla T, \\ T_1\left(X,t\right) = T_2\left(X,t\right), \end{cases} \tag{5.6}$$

where subscripts 1 and 2 represent the first and the second body, respectively.

It is also possible to consider the boundary between bodies without ideal (imperfect) contact with thermal resistance [21]:

$$-\mathbf{n}k_1 \cdot \nabla T = \frac{T_1(X,t) - T_2(X,t)}{R_\Gamma(X,t)} = -\mathbf{n}k_2 \cdot \nabla T, \tag{5.7}$$

where R_Γ is the thermal resistance.

Thermophysical parameters such as specific heat, density or thermal conductivity coefficient appear in the governing equation. Normally, the values of these variables are obtained deterministically from the experiment. However, in reality these parameters depend on a variety of circumstances in the case of humans such as sex, age, and also occupation. Hence, our work proposes the introduction of thermophysical parameters in the form of interval numbers or fuzzy numbers. This removes the need to apply a stochastic model, while replacing a simplified deterministic model. As a result, the obtained temperature distributions are also in the form of intervals or fuzzy numbers.

5.2.1. Example 1 – interval numbers

First, an example where interval numbers are introduced into the model will be demonstrated. Let the volumetric specific heat capacity ($c_v = c_p \cdot \rho$) and the thermal conductivity (k) be interval numbers. Then Equation (5.1) has the form:

$$\overline{c}_V\left(\overline{T}\right)\frac{\partial \overline{T}(X,t)}{\partial t} = \nabla\left[\overline{k}\left(\overline{T}\right)\nabla\overline{T}(X,t)\right] + Q_{\text{int}}, \tag{5.8}$$

In this study it is also assumed that the analysed sample domain is sourceless (internal heat sources Q_{int} are neglected) and that interval thermophysical parameters are independent of temperature, therefore:

$$\overline{c}_V \frac{\partial \overline{T}(X,t)}{\partial t} = \overline{k}\nabla^2\overline{T}(X,t). \tag{5.9}$$

For an axisymmetric two-dimensional (2D) sample located in a cylindrical coordinate system, this equation is formulated as follows:

$$\overline{c}_V \frac{\partial \overline{T}(r,z,t)}{\partial t} = \overline{k}\left[\frac{1}{r}\frac{\partial}{\partial r}\left(r\frac{\partial \overline{T}(r,z,t)}{\partial r}\right) + \frac{\partial^2 \overline{T}(r,z,t)}{\partial z^2}\right], \tag{5.10}$$

or in the form:

$$\overline{c}_V \frac{\partial \overline{T}(r,z,t)}{\partial t} = \overline{k}\left[\frac{1}{r}\frac{\partial \overline{T}(r,z,t)}{\partial r} + \frac{\partial^2 \overline{T}(r,z,t)}{\partial r^2} + \frac{\partial^2 \overline{T}(r,z,t)}{\partial z^2}\right], \tag{5.11}$$

where r, z are the geometric coordinates of the cylindrical coordinate system.

The heat transfer equation should be supplemented with appropriate boundary and initial conditions. These conditions are compliant with the LT protocol, proposed by Pegg et al. [116]. The assumptions are as follows. A cylindrical sample is immersed in a chamber filled with bath solution. The temperature of the bath solution is computer-controlled and varies according to the time at which the sample is exposed to the solution. Pegg's protocol involves 8 stages in the cooling phase and 7 stages in the heating phase. Table 5.1 contains the assumptions of this protocol, where the entire simulation time is 425 min.

Table 5.1. The LT protocol according to Pegg et al. [116, 187]

Phase	**Step**	**Time, *t* [min]**	**Temperature of bath solution, T_{bath} [°C]**
Cooling	1	10	22
	2	10	22
	3	30	−5
	4	30	−8.5
	5	30	−16
	6	30	−23
	7	30	−35
	8	30	−48.5
Heating	1	30	−48.5
	2	30	−35
	3	30	−23
	4	30	−16
	5	30	−8.5
	6	30	−5
	7	45	22

Knowing how the temperature of the bath solution changes, it is necessary to consider how the bath solution affects the model of an articular cartilage fragment. The study analyses a two-dimensional domain of a homogenised sample inserted in a cylindrical system. The cylindrical sample has the following dimensions: R = 3 mm and H = 1 mm.

Figure 5.1 depicts a model of a sample inside a chamber filled with bath solution containing CPA, on which the area to be analysed is marked (Ω). As can be seen,

the boundary conditions are symmetrically distributed, hence computations can be performed for domain Ω with dimensions equal to R and $H/2$. As a consequence, an adiabatic condition is applied at the boundaries Γ_2 and Γ_3 [21]:

$$\bar{q}_\Gamma\left(r,z,t\right) = -\mathbf{n}\bar{k}\cdot\nabla\bar{T} = \bar{0}\,. \tag{5.12}$$

On the other boundaries (Γ_1 and Γ_4), a condition of the 3rd type is determined:

$$\bar{q}_\Gamma\left(r,z,t\right) = -\mathbf{n}\bar{k}\cdot\nabla\bar{T} = \alpha_\Gamma\left[\bar{T}\left(r,z,t\right) - T_{bath}\right]. \tag{5.13}$$

It can be observed that the temperature of bath solution T_{bath} corresponds to the temperature of the surrounding medium T_{ext} (compare with the Equation (5.5)). In this case, the natural convection heat transfer coefficient is equal to $\alpha_\Gamma = 525\ \mathrm{W\cdot m^{-2}\cdot K^{-1}}$ [187].

It is worth adding that the LT protocol also provides the initial temperature $T^0 = 22\ ^\circ\mathrm{C}$. This value coincides with the T_{bath} value in the first step of the cooling phase.

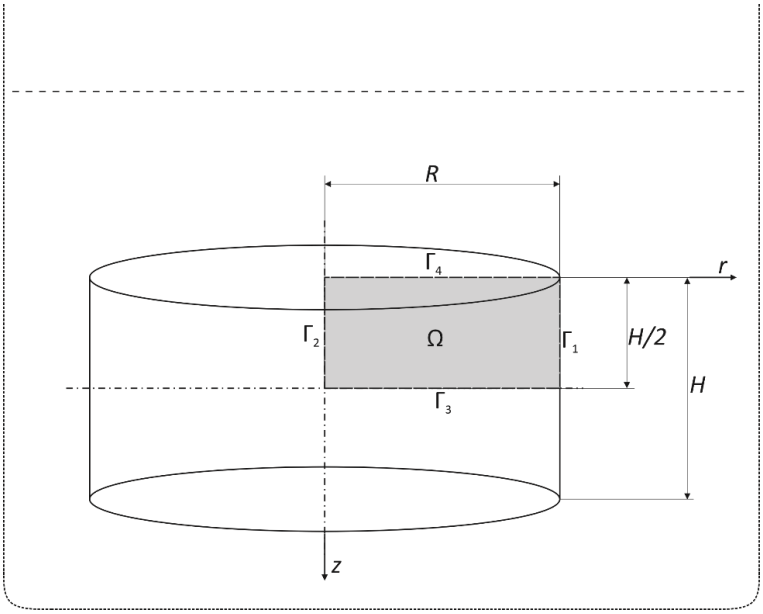

Figure 5.1. Model of the cylindrical sample immersed in bath solution inside

Let us introduce the information about physical conditions. The interval thermophysical parameter are as follows: the interval thermal conductivity $\bar{k} = [0.492;\ 0.544]\ \mathrm{W\cdot m^{-1}\cdot K^{-1}}$ and the interval volumetric specific heat $\bar{c}_V = [3.728\cdot10^6;\ 4.120\cdot10^6]\ \mathrm{J\cdot m^{-3}\cdot K^{-1}}$. Please note that the deviation from the deterministic value ($k = 0.518\ \mathrm{W\cdot m^{-1}\cdot K^{-1}}$ and $c_v = 3.924\cdot10^6\ \mathrm{J\cdot m^{-3}\cdot K^{-1}}$) is equal to 5% [129, 132, 152, 153, 187].

In this part of the work a numerical simulation based on the mathematical model demonstrated above is presented. The thermal distribution calculated from Equation (5.11) is estimated applying the finite difference method (FDM).

The concept of FDM is to substitute differential quotients, which are obtained from the Taylor series expansion, into the differential equation. Due to this, differential equations, such as ODEs or PDEs, are solved as a system of linear equations (algebraic equations) The derivation of the governing equations in the explicit scheme is performed according to the method presented in [88, 100].

To begin, a time and domain mesh should be created. For unsteady states, a discretisation of the time axis can be formulated [100]:

$$t^0 < t^1 < ... < t^{f-2} < t^{f-1} < t^f < ... < t^F < \infty . \tag{5.14}$$

The time step $\Delta t = t^{f+1} - t^f$ is constant.

Meanwhile the domain mesh is regular. The nodes are distributed by means of a five-points star formed by the central node and its neighbouring nodes. Figure 5.2 illustrates the five-points star. Please note that the boundary nodes are $0.5h_1$ and $0.5h_2$ distance from the external edge of the domain Ω, where h_1 and h_2 are the mesh step in the *r*- and *z*-direction, respectively.

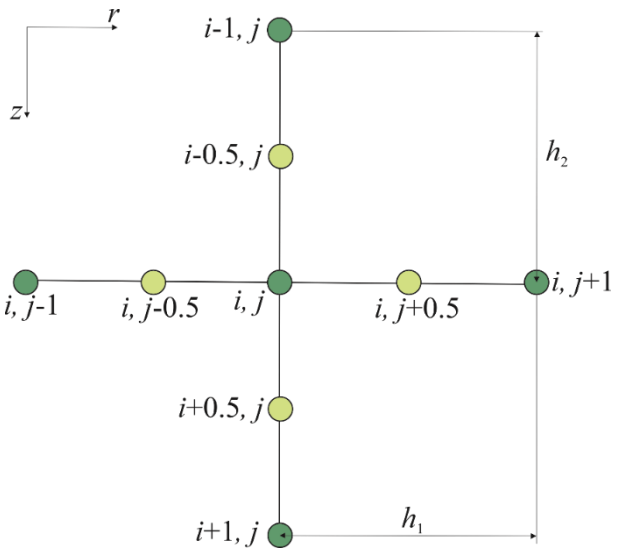

Figure 5.2. Five-points star scheme

After discretisation of the time and domain, the relationships describing the temperature at the internal and boundary nodes should be specified. The time

derivative appearing on the left-hand side of the energy equation (Equation (5.11)) is replaced by the following differential quotient [88, 100]:

$$\left(\frac{\partial \overline{T}\left(r,z,t\right)}{\partial t}\right)_{i,j}^{f}=\frac{\overline{T}_{i,j}^{\,f}-\overline{T}_{i,j}^{\,f-1}}{\Delta t}. \tag{5.15}$$

The temperature distribution in the internal nodes (i, j) for explicit scheme are estimated by the mean quotients in the form [88, 100]:

$$\begin{aligned}\left[\overline{k}\nabla^2\overline{T}\left(r,z,t\right)\right]_{i,j}^{f-1}=&\frac{1}{r_{i,j}}\frac{1}{h_1}\overline{k}\left[\left(r_{i,j+0.5}\frac{\partial \overline{T}(r,z,t)}{\partial r}\right)_{i,j+0.5}^{f-1}-\left(r_{i,j-0.5}\frac{\partial \overline{T}(r,z,t)}{\partial r}\right)_{i,j-0.5}^{f-1}\right]\\&+\frac{1}{h_2}\overline{k}\left[\left(\frac{\partial \overline{T}(r,z,t)}{\partial z}\right)_{i+0.5,j}^{f-1}-\left(\frac{\partial \overline{T}(r,z,t)}{\partial z}\right)_{i-0.5,j}^{f-1}\right],\end{aligned} \tag{5.16}$$

where $i = 2, 3, \ldots, n-1$ and $j = 2, 3, \ldots, m-1$; n and m are the number of nodes; $r_{i,j}$ is the radial coordinate of the node (i, j).

In addition:

$$\begin{aligned}&1.\quad \left(r_{i,j+0.5}\frac{\partial \overline{T}\left(r,z,t\right)}{\partial r}\right)_{i,j+0.5}^{f-1}=\left(r_{i,j}+\frac{1}{2}h_1\right)\frac{\overline{T}_{i,j+1}^{\,f-1}-\overline{T}_{i,j}^{\,f-1}}{h_1},\\&2.\quad \left(r_{i,j-0.5}\frac{\partial \overline{T}\left(r,z,t\right)}{\partial r}\right)_{i,j-0.5}^{f-1}=\left(r_{i,j}-\frac{1}{2}h_1\right)\frac{\overline{T}_{i,j}^{\,f-1}-\overline{T}_{i,j-1}^{\,f-1}}{h_1},\\&3.\quad \left(\frac{\partial \overline{T}\left(r,z,t\right)}{\partial z}\right)_{i+0.5,j}^{f-1}=\frac{\overline{T}_{i+1,j}^{\,f-1}-\overline{T}_{i,j}^{\,f-1}}{h_2},\\&4.\quad \left(\frac{\partial \overline{T}\left(r,z,t\right)}{\partial z}\right)_{i-0.5,j}^{f-1}=\frac{\overline{T}_{i,j}^{\,f-1}-\overline{T}_{i-1,j}^{\,f-1}}{h_2}.\end{aligned} \tag{5.17}$$

Hence, Equation (5.11) has a form:

$$\begin{aligned}\overline{c}_V\frac{\overline{T}_{i,j}^{\,f}-\overline{T}_{i,j}^{\,f-1}}{\Delta t}=&\overline{k}\left[\frac{1}{r_{i,j}}\frac{\overline{T}_{i,j+1}^{\,f-1}-\overline{T}_{i,j-1}^{\,f-1}}{2h_1}+\frac{\overline{T}_{i,j+1}^{\,f-1}-2\overline{T}_{i,j}^{\,f-1}+\overline{T}_{i,j-1}^{\,f-1}}{h_1^2}\right.\\&\left.+\frac{\overline{T}_{i+1,j}^{\,f-1}-2\overline{T}_{i,j}^{\,f-1}+\overline{T}_{i-1,j}^{\,f-1}}{h_2^2}\right],\end{aligned} \tag{5.18}$$

and after conversion:

$$\overline{T}_{i,j}^{\,f} = \overline{T}_{i,j}^{\,f-1} + \frac{\overline{k}\,\Delta t}{\overline{c}_V}\left[\frac{1}{r_{i,j}}\frac{\overline{T}_{i,j+1}^{\,f-1} - \overline{T}_{i,j-1}^{\,f-1}}{2h_1} + \frac{\overline{T}_{i,j+1}^{\,f-1} - 2\overline{T}_{i,j}^{\,f-1} + \overline{T}_{i,j-1}^{\,f-1}}{h_1^2} + \frac{\overline{T}_{i+1,j}^{\,f-1} - 2\overline{T}_{i,j}^{\,f-1} + \overline{T}_{i-1,j}^{\,f-1}}{h_2^2}\right]. \tag{5.19}$$

Applying the explicit scheme for FDM, it is important to define and check the stability condition. For Equation (5.20) it is formulated:

$$1 - \frac{2\overline{k}\,\Delta t}{\overline{c}_V}\left(\frac{1}{h_1^2} + \frac{1}{h_2^2}\right) \geq 0\,, \tag{5.20}$$

and as a result:

$$\Delta t \leq \frac{\overline{c}_V}{2\overline{k}}\left(\frac{h_1^2 h_2^2}{h_1^2 + h_2^2}\right). \tag{5.21}$$

The energy equation for boundary nodes has also been determined. For instance, for boundary Γ_1 with assumption of the 3rd type condition, the differential quotients are the same as in Equations (5.18) excluding the formula for i, j+0.5, where:

$$\left(r_{i,j+0.5}\frac{\partial \overline{T}(r,z,t)}{\partial r}\right)_{i,j+0.5}^{f-1} = \left(r_{i,j} + \frac{1}{2}h_1\right)\frac{T_{bath}^{\,f-1} - \overline{T}_{i,j}^{\,f-1}}{\frac{1}{2}h_1 + \frac{\alpha_\Gamma}{\overline{k}}}, \tag{5.22}$$

where $i = 2, 3, \ldots, n-1$ and $j = m$.

On the other hand, for a boundary condition of the 2nd type (adiabatic condition $q_\Gamma = 0$), which was given at the boundary Γ_2, in Equations (5.18) replacing the relation i, j–0.5:

$$\left(r_{i,j-0.5}\frac{\partial \overline{T}(r,z,t)}{\partial r}\right)_{i,j-0.5}^{f-1} = \left(r_{i,j} - \frac{1}{2}h_1\right)\frac{q_\Gamma}{\overline{k}} = \overline{0}\,, \tag{5.23}$$

where $i = 2, 3, \ldots, n-1$ and $j = 1$.

In analogy, the differential quotients transform for boundary Γ_3 (where $i = n$ and $j = 2, 3, \ldots, m-1$):

$$\left(\frac{\partial \overline{T}(r,z,t)}{\partial z}\right)_{i+0.5,j}^{f-1} = -\frac{q_\Gamma}{\overline{k}} = \overline{0}\,, \tag{5.24}$$

and Γ_4 (where i =1 and j = 2, 3, …, m – 1):

$$\left(\frac{\partial \bar{T}(r,z,t)}{\partial z}\right)_{i-0.5,\,j}^{f-1} = \frac{T_{bath}^{f-1} - \bar{T}_{i,j}^{f-1}}{\frac{1}{2}h_2 + \frac{\alpha_\Gamma}{\bar{k}}}. \tag{5.25}$$

The simulation is executed for the following parameters concerning the numerical model: time step $\Delta t = 10^{-3}$ s, mesh steps $h_1 = 10^{-4}$ m and $h_2 = 5 \cdot 10^{-5}$ m [152, 153].

The simulation of the defined problem has been performed in an author's program created in Embarcadero Delphi 10.4 Community Edition environment (Embarcadero Technologies, Inc.). Figure 5.3 contains a flowchart that briefly shows the algorithm's operation.

Example results of calculation are presented in Figures 5.4-5.5 and in Table 5.2. Figure 5.4 depicts the change of temperature over time for selected points with geometrical coordinates r = 0.050 mm and z = 0.475 mm (solid line) and r = 2.950 mm and z = 0.125 mm (dashed line). These diagrams refer to 3rd step in the cooling phase (a) and to 7th in the heating phase (b). The results have been obtained as interval numbers, therefore the upper line (red line) indicates the upper limit of the interval, while the lower line (blue line) is the lower limit of the interval. From the graphs it can be deduced that the stabilisation of the temperature in the sample is relatively fast compared to the total time required for the individual steps. Obviously, it can be seen that a point located closer to the edge has a quicker response to changes in the temperature of the bath solution.

Figure 5.5 shows maps of the temperature distribution in domain Ω at a specific moment in time for the nodes with the geometrical coordinates r = 0.050 mm and z = 0.475 mm. The temperature distributions clearly illustrate the axisymmetric character of the defined boundary conditions.

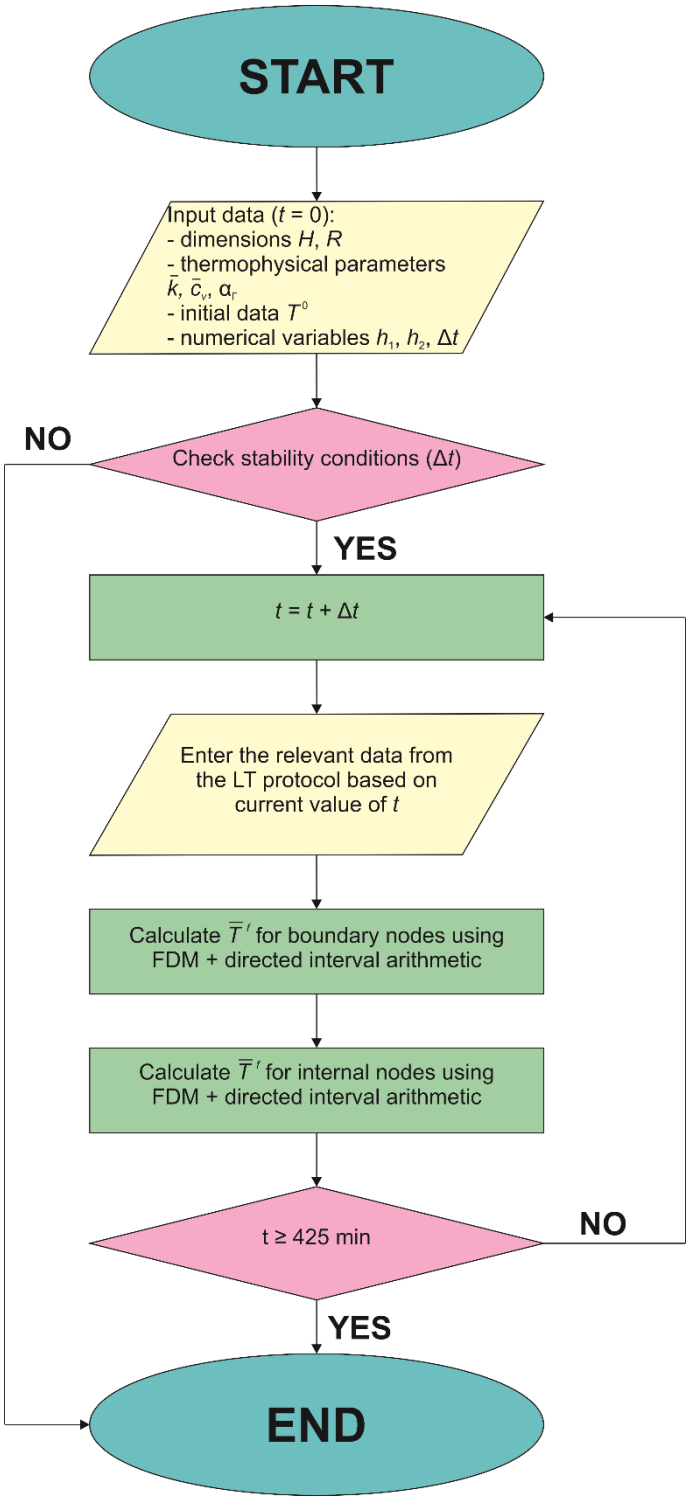

Figure 5.3. Flowchart of algorithm to simulate heat transfer phenomena (interval arithmetic)

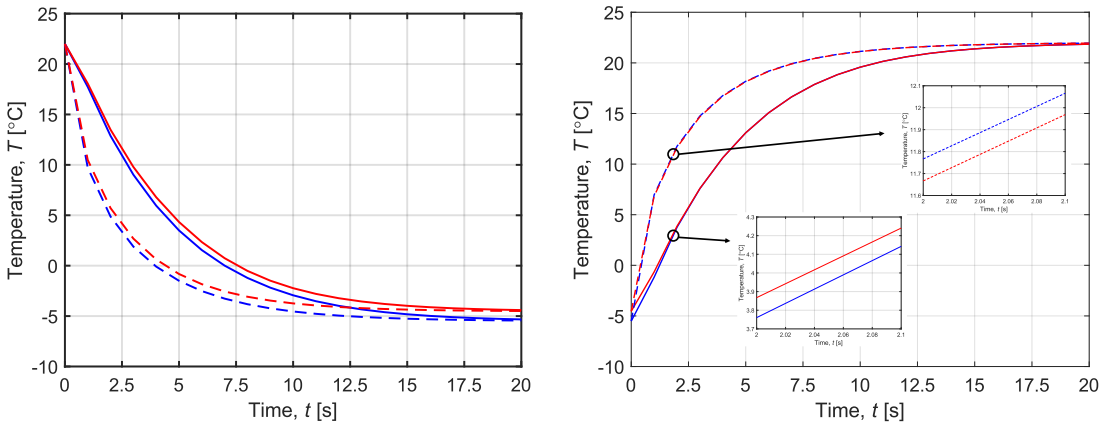

(a) (b)

Figure 5.4. Interval temperature as function of time for a change:
(a) from 22 to −5 °C and (b) from −5 °C to 22 °C

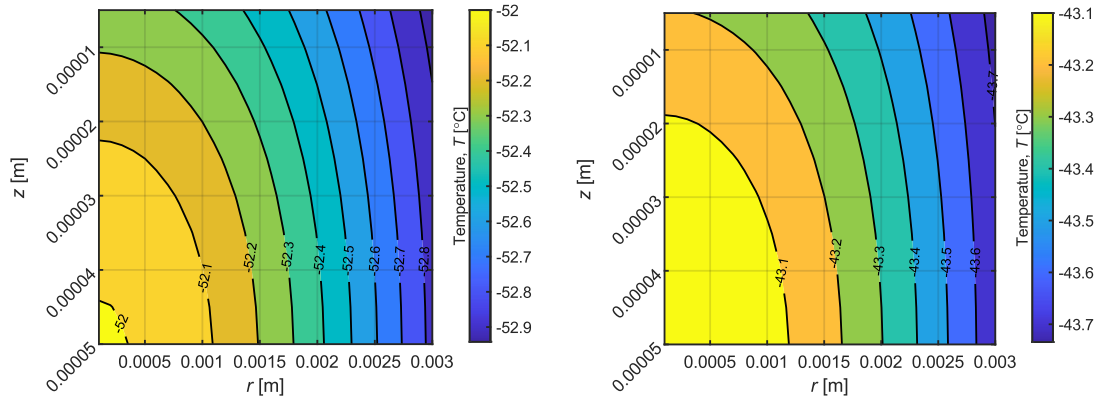

(a) (b)

Figure 5.5. Distribution of the temperature for step 8 after 10 s in the cooling phase:
(a) T^- and (b) T^+

Table 5.2 contains the results obtained at the last moment of each step for the point with the geometrical coordinates r = 2.950 mm and z = 0.125 mm. Each temperature interval includes the nominal temperature determined by the temperature of the bath solution.

Table 5.2. Interval temperatures obtained in the simulation

Phase	Step	Interval temperature, $\overline{T}$ [°C]
Cooling	1	[22.000; 22.000]
	2	[22.000; 22.000]
	3	[−5.507; −4.540]
	4	[−9.362; −7.718]
	5	[−17.622; −14.528]
	6	[−25.332; −20.884]
	7	[−38.548; −31.779]
	8	[−53.417; −44.037]
Heating	1	[−53.417; −44.037]
	2	[−38.548; −31.779]
	3	[−25.332; −20.884]
	4	[−17.622; −14.528]
	5	[−9.362; −7.718]
	6	[−5.507; −4.540]
	7	[22.000; 22.000]

5.2.2. Example 1 – fuzzy numbers

Let us consider the same case with application of a different model including fuzzy arithmetic. Then, the bioheat transfer equation given in Equations (5.11)-(5.12) has the form:

$$\tilde{c}_V \frac{\partial \tilde{T}(r,z,t)}{\partial t} = \tilde{k}\left[\frac{1}{r}\frac{\partial}{\partial r}\left(r\frac{\partial \tilde{T}(r,z,t)}{\partial r}\right)+\frac{\partial^2 \tilde{T}(r,z,t)}{\partial z^2}\right], \tag{5.26}$$

or:

$$\tilde{c}_V \frac{\partial \tilde{T}(r,z,t)}{\partial t} = \tilde{k}\left[\frac{1}{r}\frac{\partial \tilde{T}(r,z,t)}{\partial r}+\frac{\partial^2 \tilde{T}(r,z,t)}{\partial r^2}+\frac{\partial^2 \tilde{T}(r,z,t)}{\partial z^2}\right]. \tag{5.27}$$

Similarly, the particular boundary conditions are prepared. For Γ_2, Γ_3:

$$\tilde{q}_\Gamma(r,z,t) = -\mathbf{n}\tilde{k}\cdot\nabla\tilde{T} = \tilde{0}, \tag{5.28}$$

and for Γ_1, Γ_4:

$$\tilde{q}_{\Gamma}\left(r,z,t\right) = -\mathbf{n}\tilde{k}\cdot\nabla\tilde{T} = \alpha_{\Gamma}\left[\tilde{T}\left(r,z,t\right) - T_{bath}\right]. \tag{5.29}$$

In this instance, the temperature of the bath solution is also controlled according to the LT protocol. This time, however, the regulation proposed by Yu et al. [187] was implemented. This approach is a modification of the Pegg et al.'s protocol [116]. Comparing the two methods, Yu et al.'s protocol omits the last step in the cooling phase and the first step in the heating phase, when the temperature of the bath solution is equal to −48.5 °C. The other temperatures of the bath solution remain unchanged. As a result, this protocol consists of 7 steps in the cooling phase and 6 in the heating phase. In addition, Yu et al. introduce shorter individual step times, hence the total process time is equal to 276 min. The detailed assumptions of Yu et al.'s protocol can be found in Table 5.3 [187].

Table 5.3. LT protocol according to Yu et al. [187]

Phase	**Step**	**Time, *t* [min]**	**Temperature of bath solution, T_{bath} [°C]**
Cooling	1	10	22
	2	9.8	22
	3	18.2	−5
	4	25	−8.5
	5	19.8	−16
	6	26.4	−23
	7	23.8	−35
Heating	1	23.8	−35
	2	26.4	−23
	3	19.8	−16
	4	25	−8.5
	5	18.2	−5
	6	29.8	22

The thermophysical parameters are defined as fuzzy numbers. Two types of fuzzy numbers are specified: triangular and trapezoidal, as shown in Table 5.4 [131, 150].

The other unambiguity conditions presented in the previous example remain exactly the same.

Table 5.4. Fuzzy thermophysical parameters [131, 150]

	Triangular fuzzy number	**Trapezoidal fuzzy number**
Thermal conductivity, $\tilde{k}$ [W·m^{-1}·K^{-1}]	(0.492; 0.518; 0.544)	(0.505; 0.531; 0.013; 0.013)
Volumetric specific heat capacity, $\tilde{c}_V$ [J·m^{-3}·K^{-1}]	(3.728×10^6; 3.924×10^6; 4.120×10^6)	(3.826×10^6; 4.022×10^6; 0.098×10^6; 0.098×10^6)

The numerical model was also created using FDM. Taking into account advantage of the relationships presented earlier for interval numbers (see Equations (5.20)), the energy equation for the internal nodes is expressed as follows:

$$\tilde{T}_{i,j}^{f} = \tilde{T}_{i,j}^{f-1} + \frac{\tilde{k}\Delta t}{\tilde{c}_V}\left[\frac{1}{r_{i,j}}\frac{\tilde{T}_{i,j+1}^{f-1} - \tilde{T}_{i,j-1}^{f-1}}{2h_1} + \frac{\tilde{T}_{i,j+1}^{f-1} - 2\tilde{T}_{i,j}^{f-1} + \tilde{T}_{i,j-1}^{f-1}}{h_1^2} + \frac{\tilde{T}_{i+1,j}^{f-1} - 2\tilde{T}_{i,j}^{f-1} + \tilde{T}_{i-1,j}^{f-1}}{h_2^2}\right], \tag{5.30}$$

where $i = 2, 3, \ldots, n-1$ and $j = 2, 3, \ldots, m-1$.

The stability condition is as follows (compare with Equation (5.22)):

$$\Delta t \le \frac{\tilde{c}_V}{2\tilde{k}}\left(\frac{h_1^2 h_2^2}{h_1^2 + h_2^2}\right). \tag{5.31}$$

The formulas for boundary nodes are determined in a manner analogous to the example applying interval numbers, hence this derivation will be omitted in this part of dissertation.

The parameters of the numerical model are as follows: time step $\Delta t = 10^{-3}$ s, mesh steps $h_1 = 10^{-4}$ m and $h_2 = 5\cdot10^{-5}$ m [131, 150, 152, 153].

It is worth mentioning that computations in the set of fuzzy numbers have been conducted using the α-cuts introduced in Chapter 4. In this way, complicated arithmetic operations on fuzzy numbers are avoided. The calculations carried out involved different values of the parameter α.

The calculation of the example using fuzzy arithmetic, as in Subsection 5.2.1, was performed in an author's program prepared in Embarcadero Delphi 10.4 Community Edition environment (Embarcadero Technologies, Inc.). Figure 5.6 shows a flowchart which contains the general procedures of the algorithm.

Figures 5.7-5.10 present the results received for triangular and trapezoidal fuzzy numbers, respectively. The effects of the calculations have been observed for the points with the geometrical coordinates r = 0.050 mm, z = 0.475 mm (point A) and r = 2.950 mm, z = 0.125 mm (point B).

Figure 5.7 illustrates the interval temperatures after 20 s of step 7 in the cooling phase for selected values of parameter α in the point B. It can be seen that for α = 0, the width of the interval is the largest; while as the value of α increases, the interval is getting narrower. When α = 1 the interval width is equal to 0.

The interval widths for different values of the parameter α are also compared in Figure 5.8. The graphs show the temperature development over time at the selected points at the beginning of the step 3 of the cooling phase (see Table 5.3). Please note that point A is marked with a solid line and point B with a dashed line. In this case, it can be deduced that the interval width depends on the chosen value of the parameter α.

Analogous results were obtained using trapezoidal fuzzy numbers. Figure 5.9 depicts the interval temperatures for different values of the parameter α. These are the results for a moment after 20 s of step 7 in cooling phase in the point B. It can be seen that, as for triangular fuzzy numbers, the width of the temperature interval increases as the parameter α comes closer to 0. However, the difference between triangular and trapezoidal fuzzy numbers occurs for α = 0; then the interval width is the narrowest, but for trapezoidal fuzzy numbers it is not equal to 0.

Figure 5.10 shows the interval temperature changes at the start of step 3 of the cooling phase in the point B. Different widths of interval were achieved for various values of the parameter α.

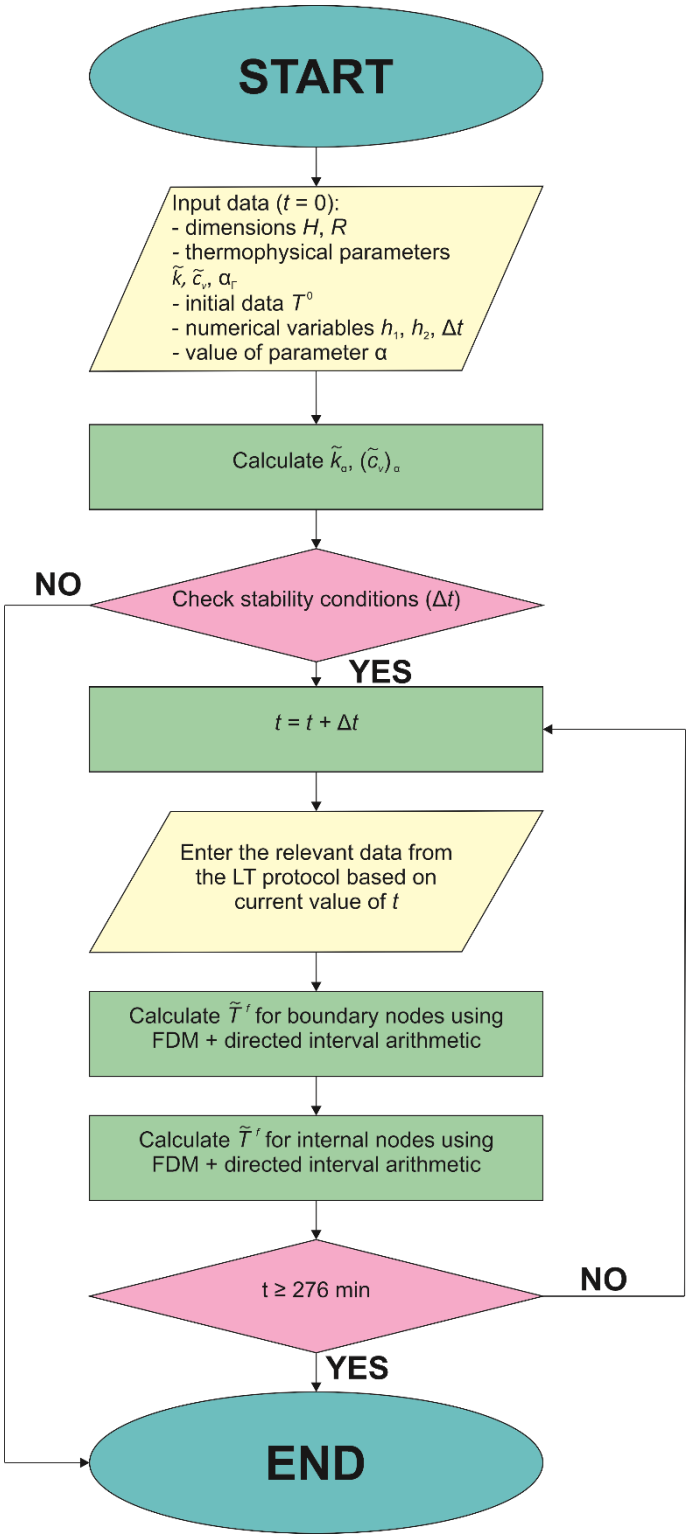

Figure 5.6. Flowchart of algorithm to simulate heat transfer phenomena (fuzzy arithmetic)

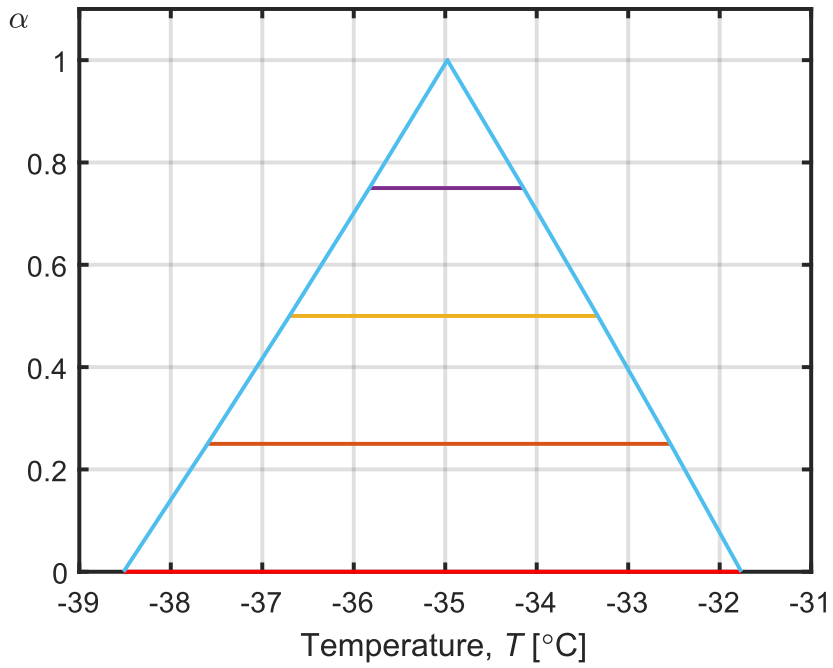

Figure 5.7. Values of interval temperature after 20 s of step 3 in cooling phase for different values of parameter α – triangular fuzzy number

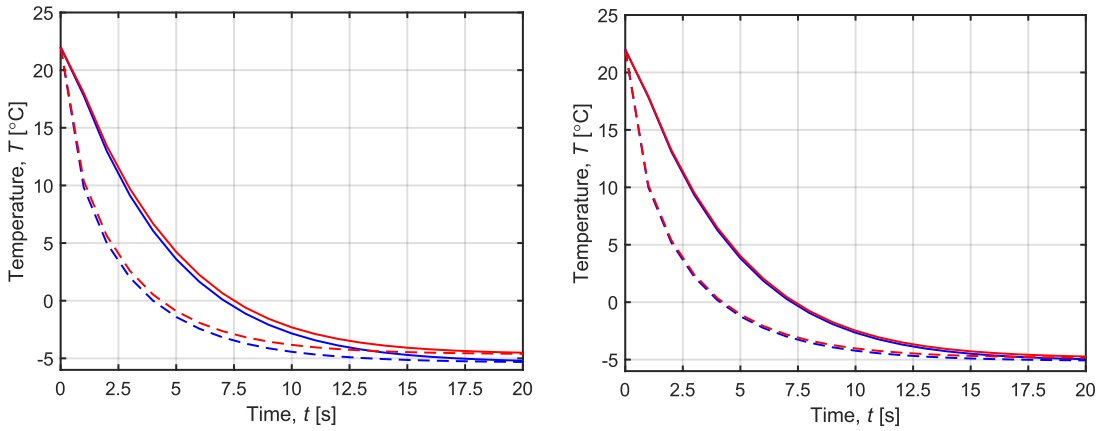

(a) (b)

Figure 5.8. Temperature as function of time for a change from 22 ºC to −5 ºC for: (a) α = 0.25; (b) α = 0.75

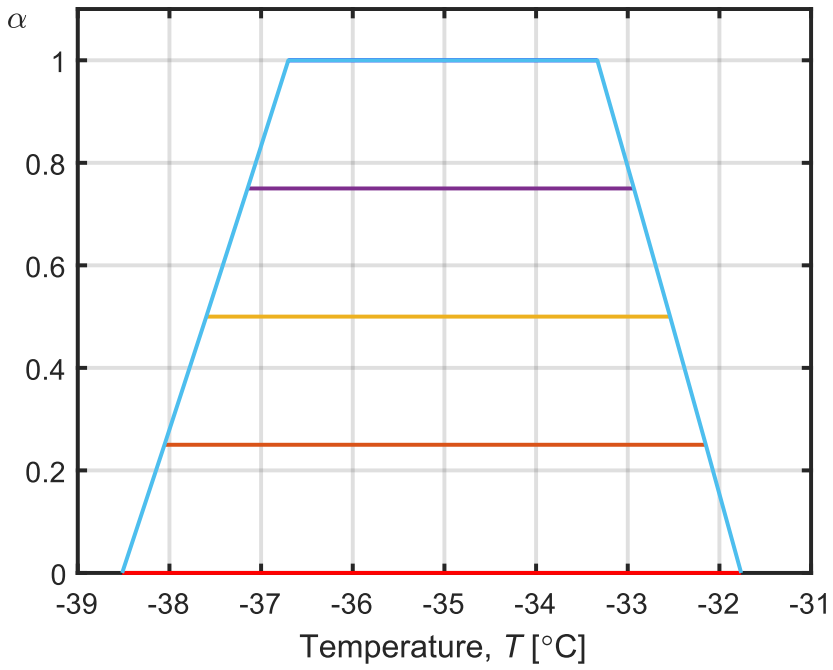

Figure 5.9. Values of interval temperature after 20 s of step 7 in cooling phase for different values of parameter α – trapezoidal fuzzy number

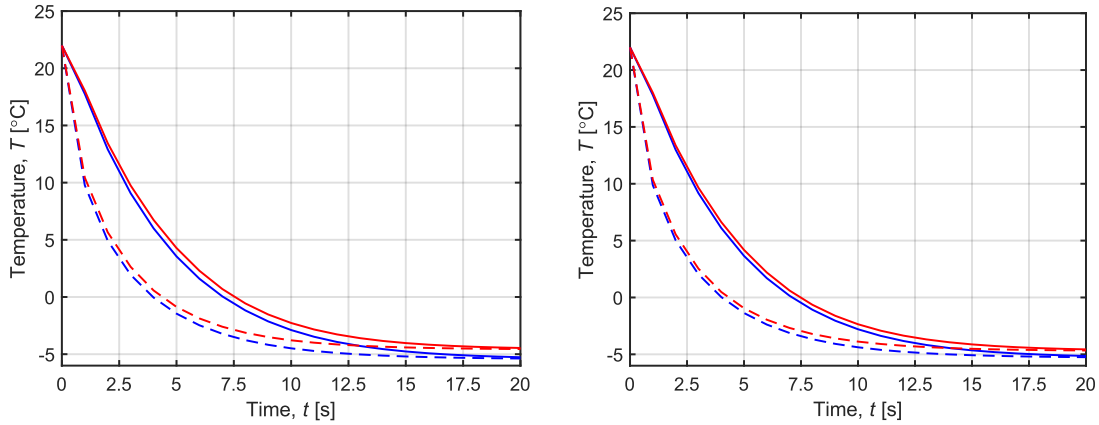

(a) (b)

Figure 5.10. Temperature as function of time for a change from 22 ºC to -5 ºC for: (a) α = 0.25; (b) α = 0.75

Table 5.5 presents the interval temperature values at the point A at the end of each step for α = 0.5. For comparison, the results are given for both triangular fuzzy numbers and trapezoidal fuzzy numbers. It can be deduced that the calculated interval temperatures include the temperatures that are a consequence of the bath solution temperatures. Additionally, the width of the temperature intervals obtained for trapezoidal fuzzy numbers is wider than the width of the intervals achieved for triangular fuzzy numbers.

The difference increases for higher values of the parameter α (for α = 0 the width of the interval is the same in both cases).

Table 5.5. Temperatures obtained in the simulation for α = 0.5 (fuzzy arithmetic)

Phase	**Step**	**Interval temperature, $\widetilde{T}$ [°C]**	
		Triangular fuzzy numbers	Trapezoidal fuzzy numbers
Cooling	1	[22.000; 22.000]	[22.000; 22.000]
	2	[22.000; 22.000]	[22.000; 22.000]
	3	[−5.250; −4.762]	[−5.379; −4.648]
	4	[−8.924; −8.096]	[−9.145; −7.901]
	5	[−16.799; −15.239]	[−17.213; −14.872]
	6	[−24.148; −21.906]	[−24.744; −21.379]
	7	[−36.747; −33.336]	[−37.654; −32.533]
Heating	1	[−36.747; −33.336]	[−37.654; −32.533]
	2	[−24.148; −21.906]	[−24.744; −21.379]
	3	[−16.799; −15.239]	[−16.799; −15.239]
	4	[−8.924; −8.096]	[−9.145; −7.901]
	5	[−5.250; −4.762]	[−5.379; −4.648]
	6	[22.000; 22.000]	[22.000; 22.000]

5.2.3. Summary and conclusions

In conclusion, the use of directed interval arithmetic and fuzzy arithmetic is valid for the study of bioheat transfer in a biological sample. It enables the introduction of imprecise defined parameters that are determined, for example, by experiment.

It is also noteworthy that, in each of simulations presented, the interval results coincident with the expected temperatures resulting from the bath solution temperature. That confirms the correctness of the created LT process model. Moreover, the stabilisation of the temperature distribution in the sample domain to the required temperature occurs relatively quick in comparison with the total execution time of the individual steps. Therefore, the modifications introduced by Yu et al. [187] to the protocol of Pegg et al. [116] reducing the simulation time seem to be appropriate. However, it is important to note that it is difficult to assess the behaviour of the sample

during cryopreservation based only on thermal analysis. It is crucial to examine the interaction between sample and CPA, as well as to investigate the degree of ice crystallisation. In Chapter 6 one will find a continuation of this example.

5.3. Example 2: Bioheat transfer model with phase changes

In this subsection, a model of biological heat transfer, taking into account the phenomenon of phase transitions, will be presented. In this case, thermal changes are modelled in unspecified soft tissue. It is assumed that the biological material contains blood vessels, which means that heat sources for perfusion and metabolism have to be considered.

The topic of phase change processes is present in literature [2, 43, 85, 98, 149, 179]. Most of the referred publications are concerned with modelling the phenomena which occur during cryosurgery and hyperthermia [43, 85, 98, 149, 179]. An analysis of cryopreservation with phase transitions is presented by, among others, Ahmadikia and Moradi [2]. In their research, they used the parabolic and hyperbolic heat transfer equation (Fourier equation and non-Fourier equation). In contrast, our work presents a parabolic model based on the Pennes equation. The aim of this investigation is also to implement phase transitions relationships into the governing equation using the one domain method.

In this study, simulations have been carried out for both techniques of cryopreservation: slow freezing and vitrification. These two popular methods have been also compared with regard to differences in temperature distribution.

The basic equation describing thermal processes is the Fourier equation (see Equation (3.4)). For bioheat problems, it is appropriate to use the Pennes equation, which considers internal heat sources related to perfusion and metabolism [120] as well as a component related to phase changes, thus the heat transfer equation has the form [32]:

$$c_p \rho \dot{T} = \nabla \left(k \nabla T \right) + Q_{perf} + Q_{met} + Q_f \,, \tag{5.32}$$

where:

$$Q_{perf} = G_b c_b \left(T_b - T \right), \tag{5.33}$$

and:

$$Q_f = L \dot{f}_s \,. \tag{5.34}$$

It is assumed that three types of sub-domains can exist in the entire sample, defined according to their physical state: natural state, intermediate region, state below freezing (melting) point. Identifying the physical state of the given domain is important for the determination of the function f_s. For the natural state: $f_s = 0$, while for the state below the freezing (melting) point: $f_s = 1$. For the intermediate state, the function f_s depends on the temperature: $f_s = f_s(T)$ therefore:

$$Q_f = L\frac{\partial f_s}{\partial t} = L\frac{\mathrm{d}f_s}{\mathrm{d}T}\dot{T}\,. \tag{5.35}$$

The above relationship is inserted into Equation (5.33):

$$\left[c_p\rho - L\frac{\mathrm{d}f_s}{\mathrm{d}T}\right]\dot{T} = \nabla\left(\lambda\nabla T\right) + Q_{perf} + Q_{met}\,, \tag{5.36}$$

where:

$$C_{STC} = \left[c_p\rho - L\frac{\mathrm{d}f_s}{\mathrm{d}T}\right] = c_v - L\frac{\mathrm{d}f_s}{\mathrm{d}T}\,. \tag{5.37}$$

As in Example 1, the mathematical model assumes that some thermophysical parameters are uncertain and non-deterministic. In this case, only interval numbers were used. In the governing equation, the input interval parameters are the thermal conductivity and the volumetric specific heat included in the substitute thermal capacity.

5.3.1. Example 2 – interval numbers

Assuming a cylindrical system, the heat transfer equation (see Equation (5.32)) is expressed as follows:

$$\begin{aligned}\bar{C}_{STC}\left(\bar{T}\right)\frac{\partial\bar{T}\left(r,z,t\right)}{\partial t} = \frac{1}{r}\frac{\partial}{\partial r}\left(r\bar{k}\left(\bar{T}\right)\frac{\partial\bar{T}\left(r,z,t\right)}{\partial r}\right) + \frac{\partial}{\partial z}\left(\bar{k}\left(\bar{T}\right)\frac{\partial\bar{T}\left(r,z,t\right)}{\partial z}\right)\\ +\bar{Q}_{met}\left(\bar{T}\right) + \bar{Q}_{perf}\left(r,z,t\right),\end{aligned} \tag{5.38}$$

where:

$$\bar{Q}_{perf}\left(r,z,t\right) = \bar{G}_b\left(\bar{T}\right)c_b\rho_b\left[T_b - \bar{T}\left(r,z,t\right)\right]. \tag{5.39}$$

It is worth noting that variables such as the substitute heat capacity, the thermal conduction, the internal heat source resulting from the organism's metabolism and perfusion depend on the temperature. The values of these parameters are established individually at each point (node) of the sample domain according to the physical state of a particular sub-domain. These variables are constant for the natural state and for the state

below the freezing (melting) point, while for the intermediate region a linear function describes them. The temperature-dependent variables are specified by [32, 98, 151]:

$$\bar{C}_{STC}\left(\bar{T}\right)=\begin{cases}\bar{c}_N & \bar{T}>T_l,\\ \bar{c}_{in}+\dfrac{L}{T_l-T_s} & T_s\le\bar{T}\le T_l,\\ \bar{c}_f & \bar{T}>T_s,\end{cases} \tag{5.40}$$

$$\bar{k}\left(\bar{T}\right)=\begin{cases}\bar{k}_N & \bar{T}>T_l\\ \bar{k}_{in} & T_s\le\bar{T}\le T_l\\ \bar{k}_f & \bar{T}>T_s\end{cases} \tag{5.41}$$

$$\bar{G}_b\left(\bar{T}\right)=\begin{cases}\left(G_b\right)_N & \bar{T}>T_l,\\ \dfrac{\left(G_b\right)_N}{T_l-T_s}\left[\bar{T}\left(r,z,t\right)-T_s\right] & T_s\le\bar{T}\le T_l,\\ 0 & \bar{T}>T_s,\end{cases} \tag{5.42}$$

$$\bar{Q}_{met}\left(\bar{T}\right)=\begin{cases}Q_{met\,N} & \bar{T}>T_l,\\ \dfrac{Q_{met\,N}}{T_l-T_s}\left[\bar{T}(r,z,t)-T_s\right] & T_s\le\bar{T}\le T_l,\\ 0 & \bar{T}>T_s,\end{cases} \tag{5.43}$$

where the subscripts *N*, *in*, *f* represent the following sub-domains: natural state, intermediate region and state below freezing (melting) point, respectively. The subscripts *l* and *s* denote the temperatures of the initial and final phase transition phenomena, respectively.

The mathematical model should be completed with unambiguous conditions. This case simulates the cryopreservation of a cylindrical, homogeneous biological tissue. Figure 5.11 illustrates the conceptual sample model with the selected two-dimensional domain Ω, where R = 0.02 m and H = 0.02 m [151]. It is placed in a bath solution, whose temperature is linearly modified at a specific cooling rate. The chemical composition of the bath solution will not be discussed in detail in this example.

As the example compares two cryopreservation methods, two different cooling rates are considered. For slow freezing, according to Mazur's research, it is assumed to be equal to 1 $K\cdot s^{-1}$ [95]. On the other hand, for vitrification, the temperature increases (decreases) with a cooling rate of 100 $K\cdot s^{-1}$ [183]. The cooling process continues until the

temperature of working fluid is reduced to $T_{wf} = -196$ °C. This is the temperature provided by liquid nitrogen.

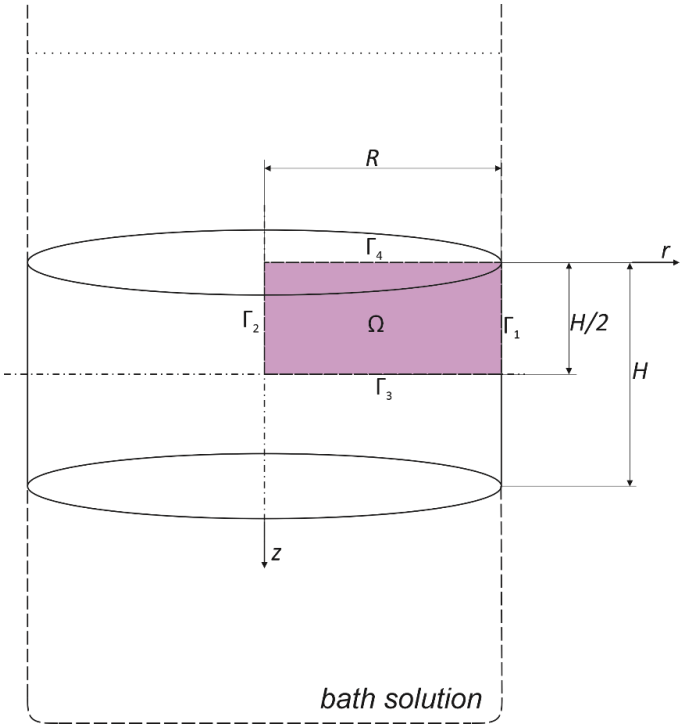

Figure 5.11. Model of the cylindrical sample immersed in bath solution

As can be seen in Figure 5.11, the bath solution is in contact with the sample domain (Ω) only at the base of the cylinder. As a result, a condition of the 3rd type is given on the boundary Γ_4:

$$\bar{q}_\Gamma(r,z,t) = -\mathbf{n}\bar{k}\cdot\nabla\bar{T} = \alpha_\Gamma\left[\bar{T}(r,z,t) - T_{bath}\right], \tag{5.44}$$

where the temperature T_{bath} changes linearly with a defined cooling rate, the natural convection heat transfer coefficient is $\alpha_\Gamma = 525\ \mathrm{W\cdot m^{-2}\cdot K^{-1}}$ [187].

The boundary Γ_1 is isolated from the external environment, consequently the heat flux at this edge is negligible. Due to the symmetries existing in the model, an adiabatic condition is applied to the other boundaries (Γ_2 and Γ_3). For Γ_1, Γ_2, Γ_3 it is assumed that:

$$\bar{q}_\Gamma(r,z,t) = -\mathbf{n}\bar{k}\cdot\nabla\bar{T} = \bar{0}. \tag{5.45}$$

The model also needs to be supplemented with initial conditions and other sample's parameters. At the first moment of simulation, the temperature in the entire domain Ω is $T^0 = 37$ °C. To determine the blood perfusion rate, the following blood parameters must be taken into account: the perfusion in the natural state $G_{b\,N} = 0.53\ \mathrm{kg\cdot m^{-3}\cdot s^{-1}}$, the specific

heat capacity of the blood $c_b = 3770$ J·kg^{-1}·K^{-1}, the blood temperature $T_b = 37$ °C. The metabolic heat source in natural state is equal to $Q_{met\,N} = 250$ W·m^{-3}. The model also includes phase change phenomena; therefore it is important to define their initial (liquidus) and final (solidus) temperatures equal to $T_l = -1$ °C and $T_s = -8$ °C, respectively, as well as the latent heat $L = 3.3 \cdot 10^8$ J·m^{-3} [98].

Table 5.6 contains the interval thermophysical parameters for each physical state. These values are a deviation of 5% of the deterministic data, where $c_N = 3.60 \cdot 10^6$ J·K^{-1}·m^{-3}, $c_{in} = 2.78 \cdot 10^6$ J·K^{-1}·m^{-3}, $c_f = 1.93 \cdot 10^6$ J·K^{-1}·m^{-3}, $k_N = 0.52$ W·m^{-1}·K^{-1}, $k_{in} = 1.26$ W·m^{-1}·K^{-1}, $k_f = 2.00$ W·m^{-1}·K^{-1} [98].

Table 5.6. Interval thermophysical parameters [151]

Physical state	**Interval thermophysical parameter**	
	Interval volumetric specific heat, ×10^6 [J·K^{-1}·m^{-3}]	**Interval thermal conductivity, [W·m^{-1}·K^{-1}]**
Natural	$\overline{c}_N = [3.42;\ 3.78]$	$\overline{k}_N = [0.494;\ 0.546]$
Intermediate region	$\overline{c}_{in} = [2.641;\ 2.919]$	$\overline{k}_{in} = [1.197;\ 1.323]$
Below freezing (melting) point	$\overline{c}_f = [1.834;\ 2.027]$	$\overline{k}_f = [1.9;\ 2.1]$

A numerical model was prepared. For this purpose, the explicit scheme of FDM was adopted. In this case, the equations were derived in an analogous manner to that shown in Example 1.

A discretisation of time and domain was performed. The time mesh was divided into constant time steps Δt according to the relationship presented in Equation (5.14). The domain mesh was constructed based on the five-points star concept already illustrated in Figure 5.2. In this case, the boundary nodes also are located at distances $0.5h_1$ and $0.5h_2$ away from the boundary.

The next part of this work derives expressions for calculating the temperatures in internal and boundary nodes. It should be noted that the thermophysical parameters depend on the temperature, which causes Equation (5.38) to become non-linear. In practice, the values of the temperature-dependent variables introduced into the energy equation are determined for the moment $f-1$:

$$\bar{C}_{STC}\left(\bar{T}\right)=\bar{C}_{STC}\left(\bar{T}_{i,j}^{\,f-1}\right), \tag{5.46}$$

$$\bar{k}\left(\bar{T}\right)=\bar{k}\left(\bar{T}_{i,j}^{\,f-1}\right), \tag{5.47}$$

$$\bar{Q}_{met}\left(\bar{T}\right)=\bar{Q}_{met}\left(\bar{T}_{i,j}^{\,f-1}\right) \tag{5.48}$$

$$\bar{G}_{b}\left(\bar{T}\right)=\bar{G}_{b}\left(\bar{T}_{i,j}^{\,f-1}\right), \tag{5.49}$$

where $i = 1, 2, \ldots, n$ and $j = 1, 2, \ldots, m$.

The left-hand side of the heat transfer equation (Equation (5.39)), in which the time derivative occurs, is calculated from Equation (5.16). The derivatives on the right-hand side of the Equation (5.39) are estimated from the mean quotient:

$$\begin{aligned}\left[\nabla\left(\bar{k}\nabla T\right)\right]_{i,j}^{f-1}=&\frac{1}{r_{i,j}}\frac{1}{h_1}\left[r_{i,j+0.5}\bar{k}\left(\bar{T}_{i,j+0.5}^{\,f-1}\right)\left(\frac{\partial\bar{T}}{\partial r}\right)_{i,j+0.5}^{f-1}-r_{i,j-0.5}\bar{k}\left(\bar{T}_{i,j-0.5}^{\,f-1}\right)\left(\frac{\partial\bar{T}}{\partial r}\right)_{i,j-0.5}^{f-1}\right]\\&+\frac{1}{h_2}\left[\left(\bar{k}\left(\bar{T}_{i+0.5,j}^{\,f-1}\right)\frac{\partial\bar{T}}{\partial z}\right)_{i+0.5,j}^{f-1}-\left(\bar{k}\left(\bar{T}_{i-0.5,j}^{\,f-1}\right)\frac{\partial\bar{T}}{\partial z}\right)_{i-0.5,j}^{f-1}\right],\end{aligned} \tag{5.50}$$

where $i = 2, 3, \ldots, n-1$ and $j = 2, 3, \ldots, m-1$.

The approximation of the above derivatives proceeds as follows:

$$\begin{aligned}&1.\quad r_{i,j+0.5}\bar{k}\left(\bar{T}_{i,j+0.5}^{\,f-1}\right)\left(\frac{\partial\bar{T}(r,z,t)}{\partial r}\right)_{i,j+0.5}^{f-1}=\left(r_{i,j}+\frac{1}{2}h_1\right)\frac{\bar{T}_{i,j+1}^{\,f-1}-\bar{T}_{i,j}^{\,f-1}}{R_{i,j+1}^{f-1}},\\&2.\quad r_{i,j-0.5}\bar{k}\left(\bar{T}_{i,j+0.5}^{\,f-1}\right)\left(\frac{\partial\bar{T}(r,z,t)}{\partial r}\right)_{i,j-0.5}^{f-1}=\left(r_{i,j}-\frac{1}{2}h_1\right)\frac{\bar{T}_{i,j}^{\,f-1}-\bar{T}_{i,j-1}^{\,f-1}}{R_{i,j-1}^{f-1}},\\&3.\quad \bar{k}\left(\bar{T}_{i+0.5,j}^{\,f-1}\right)\left(\frac{\partial\bar{T}(r,z,t)}{\partial z}\right)_{i+0.5,j}^{f-1}=\frac{\bar{T}_{i+1,j}^{\,f-1}-\bar{T}_{i,j}^{\,f-1}}{R_{i+1,j}^{f-1}},\\&4.\quad \bar{k}\left(\bar{T}_{i-0.5,j}^{\,f-1}\right)\left(\frac{\partial\bar{T}(r,z,t)}{\partial z}\right)_{i-0.5,j}^{f-1}=\frac{\bar{T}_{i,j}^{\,f-1}-\bar{T}_{i-1,j}^{\,f-1}}{R_{i-1,j}^{f-1}},\end{aligned} \tag{5.51}$$

where R_e^{f-1} is the interval thermal resistances expressed as:

$$\begin{cases}\bar{R}_e^{\,f-1}=\dfrac{h_1}{2\bar{k}\left(\bar{T}_{i,j}^{\,f-1}\right)}+\dfrac{h_1}{2\bar{k}\left(\bar{T}_e^{\,f-1}\right)}, & \text{if} \quad e=\left\{(i,j+1)\text{ or }(i,j-1)\right\},\\ \bar{R}_e^{\,f-1}=\dfrac{h_2}{2\bar{k}\left(\bar{T}_{i,j}^{\,f-1}\right)}+\dfrac{h_2}{2\bar{k}\left(\bar{T}_e^{\,f-1}\right)}, & \text{if} \quad e=\left\{(i+1,j)\text{ or }(i-1,j)\right\}.\end{cases} \tag{5.52}$$

The temperature at internal nodes is calculated from the relationship:

$$\bar{C}_{STC}\left(\bar{T}_{i,j}^{f-1}\right)\frac{\bar{T}_{i,j}^{f}-\bar{T}_{i,j}^{f-1}}{\Delta t}=\left[\left(\sum_{a=1}^{4}\frac{\Phi_e}{\bar{R}_e^{f-1}}\left(\bar{T}_e^{f-1}-\bar{T}_{i,j}^{f-1}\right)\right)+\bar{Q}_{met}\left(\bar{T}_{i,j}^{f-1}\right)+\bar{G}_b\left(\bar{T}_{i,j}^{f-1}\right)c_b\left(T_b-\bar{T}_{i,j}^{f-1}\right)\right], \tag{5.53}$$

after sorting:

$$\bar{T}_{i,j}^{f}=\bar{T}_{i,j}^{f-1}+\frac{\Delta t}{\bar{C}_{STC}\left(\bar{T}_{i,j}^{f-1}\right)}\left[\left(\sum_{a=1}^{4}\frac{\Phi_e}{\bar{R}_e^{f-1}}\left(\bar{T}_e^{f-1}-\bar{T}_{i,j}^{f-1}\right)\right)+\bar{Q}_{met}\left(\bar{T}_{i,j}^{f-1}\right)+\bar{G}_b\left(\bar{T}_{i,j}^{f-1}\right)c_b\left(T_b-\bar{T}_{i,j}^{f-1}\right)\right], \tag{5.54}$$

where i = 2,3, …, n – 1 and j = 2,3, …, m – 1, the individual a corresponds to $e = \{(i, j + 1); (i, j – 1); (i + 1, j) ; (i – 1, j)\}$ and Φ_e is the shape function given by:

$$\begin{cases}\Phi_e=\dfrac{1}{h_1}\left(1-\dfrac{h_1}{2r_{i,j}}\right), & \text{if} \quad e=(i,j-1),\\ \Phi_e=\dfrac{1}{h_1}\left(1+\dfrac{h_1}{2r_{i,j}}\right), & \text{if} \quad e=(i,j+1),\\ \Phi_e=\dfrac{1}{h_2}, & \text{if} \quad e=\{(i+1,j)\ \text{or}\ (i-1,j)\}.\end{cases} \tag{5.55}$$

For the FDM explicit scheme, the following stability condition must be met:

$$1-\Delta t\left[\sum_{a=1}^{4}\frac{\Phi_e}{\bar{R}_e^{f-1}}-\bar{Q}_{met}\left(\bar{T}_{i,j}^{f-1}\right)+\bar{G}_b\left(\bar{T}_{i,j}^{f-1}\right)c_b\right]\geq 0 \tag{5.56}$$

where a corresponds to $e = \{(i, j + 1); (i, j – 1); (i + 1, j) ; (i – 1, j)\}$.

By analogy, the temperatures at the boundary nodes are defined. On the boundary Γ_4, on which the condition of the 3rd type is applied, one of the differential quotients is "exchanged", thus the equation has the form:

$$\bar{C}_{STC}\left(\bar{T}_{1,j}^{f-1}\right)\frac{\bar{T}_{1,j}^{f}-\bar{T}_{1,j}^{f-1}}{\Delta t}=\left(\sum_{a=1}^{3}\frac{\Phi_e}{\bar{R}_e^{f-1}}\left(\bar{T}_e^{f-1}-\bar{T}_{1,j}^{f-1}\right)\right)+\frac{\Phi_{i-1,j}}{\bar{R}_\alpha^{f-1}}\left(\bar{T}_{bath}^{f-1}-\bar{T}_{1,j}^{f-1}\right)+\bar{Q}_{met}\left(\bar{T}_{1,j}^{f-1}\right)+\bar{G}_b\left(\bar{T}_{1,j}^{f-1}\right)c_b\left(T_b-\bar{T}_{1,j}^{f-1}\right), \tag{5.57}$$

and after conversion:

$$\bar{T}_{1,j}^{\,f} = \bar{T}_{1,j}^{\,f-1} + \frac{\Delta t}{\bar{C}_{STC}\left(\bar{T}_{1,j}^{\,f-1}\right)}\left[\left(\sum_{a=1}^{3}\frac{\Phi_e}{\bar{R}_e^{\,f-1}}\left(\bar{T}_e^{\,f-1} - \bar{T}_{1,j}^{\,f-1}\right)\right) + \frac{\Phi_{i-1,j}}{\bar{R}_\alpha^{\,f-1}}\left(\bar{T}_{bath}^{\,f-1} - \bar{T}_{1,j}^{\,f-1}\right)\right.$$
$$\left. + \bar{Q}_{met}\left(\bar{T}_{1,j}^{\,f-1}\right) + \bar{G}_b\left(\bar{T}_{1,j}^{\,f-1}\right)c_b\left(T_b - \bar{T}_{1,j}^{\,f-1}\right)\right], \tag{5.58}$$

where $j = 2, 3, \ldots, m-1$, individual a corresponds to $e = \{(i, j+1); (i, j-1); (i+1, j)\}$ and:

$$\bar{R}_\alpha^{\,f-1} = \frac{h_2}{2\bar{k}\left(\bar{T}_{1,j}^{\,f-1}\right)} + \frac{1}{\alpha}. \tag{5.59}$$

In contrast, an adiabatic condition is given at the other boundaries. For instance, the temperature at the boundary nodes on the boundary Γ_3 is specified:

$$\bar{C}_{STC}\left(\bar{T}_{n,j}^{\,f-1}\right)\frac{\bar{T}_{n,j}^{\,f} - \bar{T}_{n,j}^{\,f-1}}{\Delta t} = \left(\sum_{a=1}^{3}\frac{\Phi_e}{\bar{R}_e^{\,f-1}}\left(\bar{T}_e^{\,f-1} - \bar{T}_{n,j}^{\,f-1}\right)\right) + \bar{q}\cdot\Phi_{i+1,j}$$
$$+ \bar{Q}_{met}\left(\bar{T}_{n,j}^{\,f-1}\right) + G_b\left(\bar{T}_{n,j}^{\,f-1}\right)c_b\left(T_b - \bar{T}_{n,j}^{\,f-1}\right), \tag{5.60}$$

after transforming this relationship:

$$\bar{T}_{n,j}^{\,f} = \bar{T}_{n,j}^{\,f-1} + \frac{\Delta t}{\bar{C}_{STC}\left(\bar{T}_{n,j}^{\,f-1}\right)}\left[\left(\sum_{a=1}^{3}\frac{\Phi_e}{\bar{R}_e^{\,f-1}}\left(\bar{T}_e^{\,f-1} - \bar{T}_{n,j}^{\,f-1}\right)\right) + \bar{q}\cdot\Phi_{i+1,j}\right.$$
$$\left. + \bar{Q}_{met}\left(\bar{T}_{n,j}^{\,f-1}\right) + \bar{G}_b\left(\bar{T}_{n,j}^{\,f-1}\right)c_b\left(T_b - \bar{T}_{n,j}^{\,f-1}\right)\right], \tag{5.61}$$

where $j = 2, 3, \ldots, m-1$ and individual a corresponds to $e = \{(i, j+1); (i, j-1); (i-1, j)\}$.

The temperatures at the boundary nodes on edges Γ_1 and Γ_2 are determined by an analogous method.

The numerical model is characterised by the following parameters: the mesh steps are $h_1 = h_2 = 0.0002$ m ($m = n = 100$) and the time step is $\Delta t = 0.005$ s [151].

Let us demonstrate the calculation algorithm for this example – see Figure 5.12. A program dedicated to the phenomenon of heat flow complemented by phase changes was created in MATLAB R2021a environment (The MathWorks, Inc.).

Tests were carried out for cryopreservation by slow freezing and vitrification. In Figures 5.13 and 5.14, the temperature changes at selected points are studied: A (0.0001 m; 0.0001 m), B (0.0009 m; 0.0001 m), C (0.0029 m; 0.0001 m), D (0.0049 m; 0.0001 m). Figures 5.15 and 5.16 represent temperature distributions in the form of maps with isotherms.

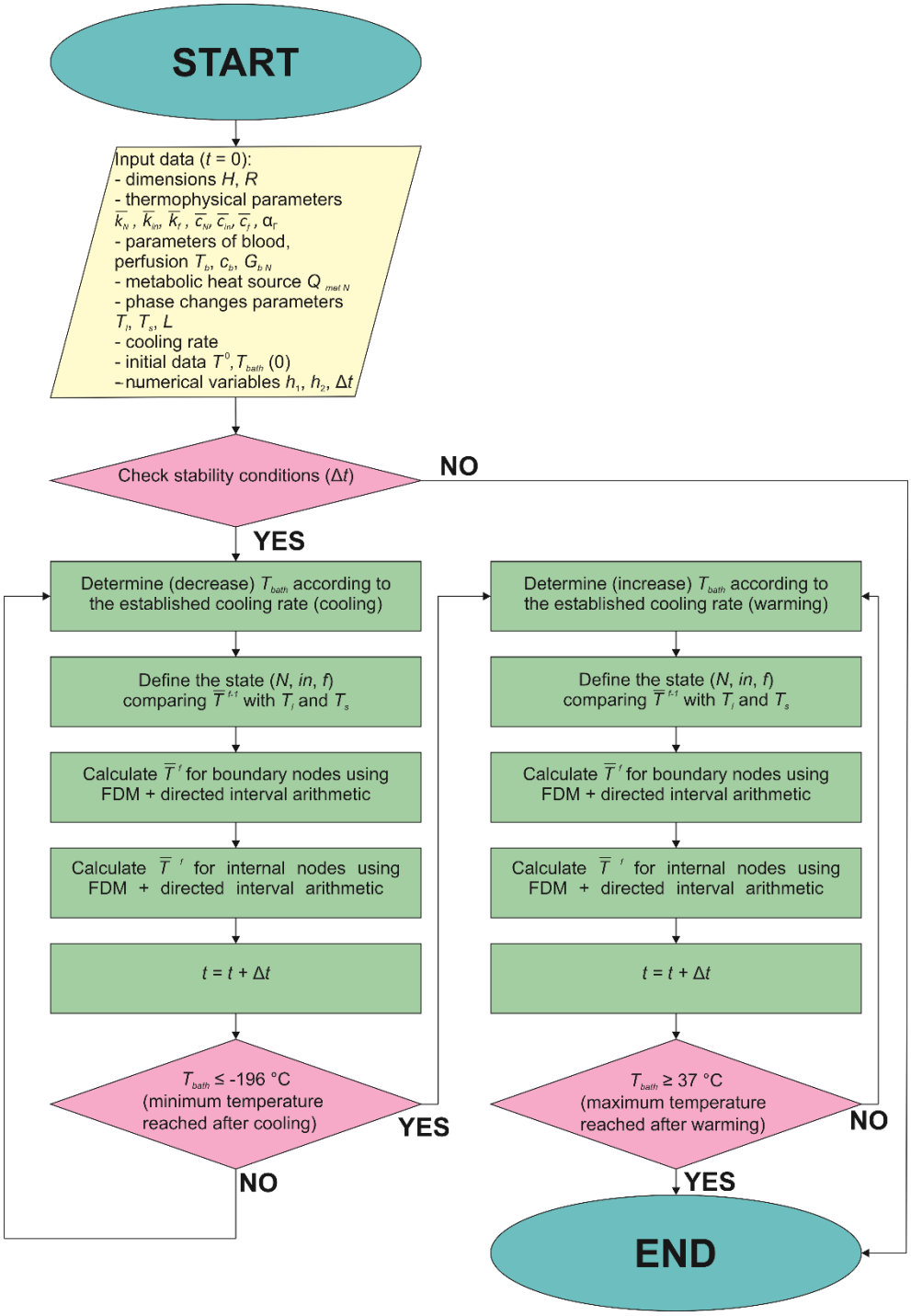

Figure 5.12. Flowchart of algorithm to simulate heat transfer phenomena including phase change (interval arithmetic)

Figure 5.13 illustrates the variations of the mean value of the interval temperature for points A-D and the temperature of the bath solution (solid line) over time. Note that the graphs presented above demonstrate the mean values of interval temperatures. Calculations for slow freezing are very time-consuming and, as a result, only cooling was

simulated in the study. For vitrification, however, computations were carried out for both cooling and heating. It can be observed that there are some differences between the results obtained by the two methods.

Figure 5.14 depicts the interval temperature history at point A in the first 20 s of the simulation. It would seem that the interval temperature-time curves for both methods are the same. However, please note the y-axis scale (temperature scale), indicating how little change there is in the slow freezing at 20 s compared to vitrification.

Table 5.7 includes the interval temperatures in particular time at point A. The width of the interval increases as the temperature of the bath solution decreases.

Figures 5.15 and 5.16 show the distribution of the mean values of the interval temperatures in the sample domain for slow freezing and for vitrification, respectively. Two different distribution maps were prepared for each cryopreservation technique: when the freezing process is at half-time and when the temperature of the bath solution reaches a minimum value (T_{bath} = −196 °C).

At half time of the cooling simulation, a wide intermediate region is observed for slow freezing. In contrast, it is not present when T_{bath} = −196 °C, because then the entire domain is below the freezing (melting) temperature ($\bar{T} < T_s$).

Vitrification is characterised by a different temperature distribution. A small intermediate region exists in both diagrams. Interestingly, when T_{bath} = −196 °C, all three physical states appear inside the sample domain.

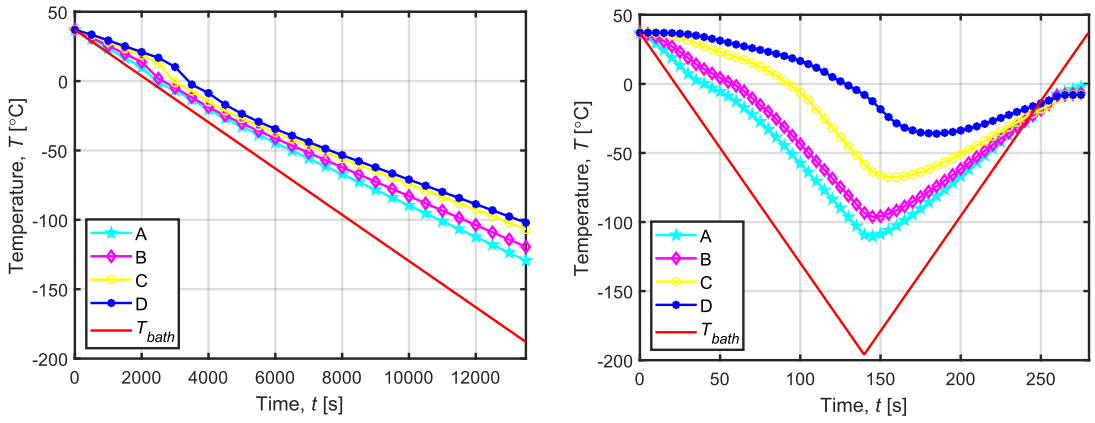

Figure 5.13. Mean value of interval temperature as function of time for:
(a) slow freezing; (b) vitrification

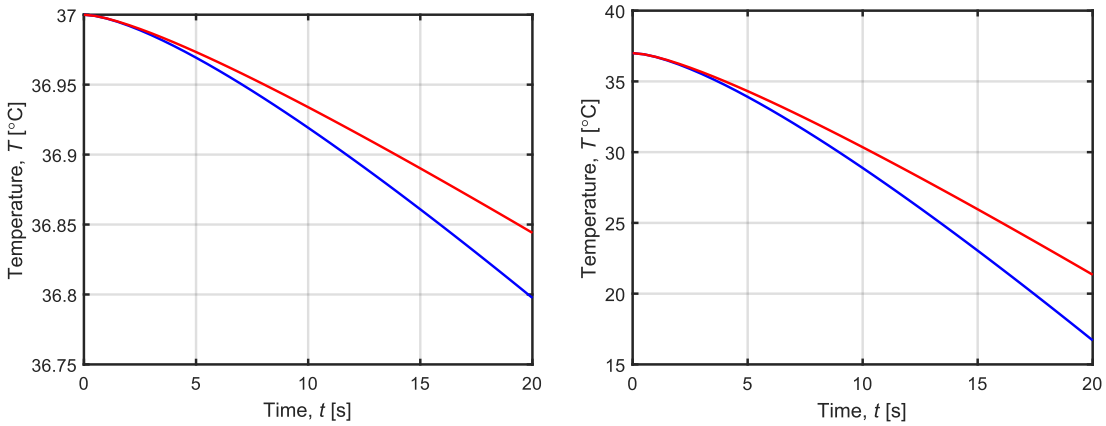

(a) (b)

Figure 5.14. Interval temperature as function of time (20 s) for point A: (a) slow freezing; (b) vitrification

Table 5.7. Interval temperatures in point A

Time, t [s]	**Interval temperature, $\overline{T}$ [°C]**	
	Slow freezing	**Vitrification**
0	[37.00; 37.00]	[37.00; 37.00]
10	[36.92; 36.93]	[28.88; 30.35]
20	[36.80; 36.84]	[16.70; 21.34]
30	[36.66; 36.75]	[3.07; 11.68]
40	[36.52;36.65]	[−3.21; 3.82]
50	[36.37; 365]	[−6.64; −4.37]
139.5	[34.94; −36.61]	[−152.13; −65.22]
13980	[−195.86; −73.71]	–

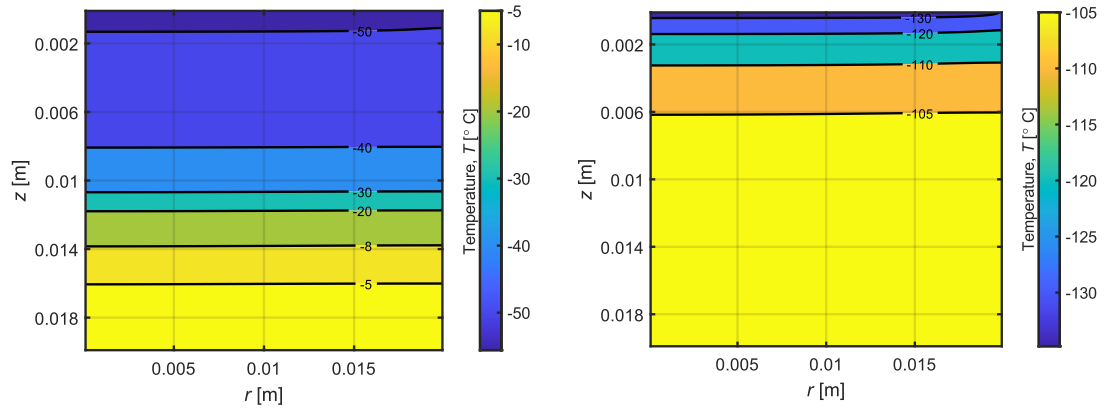

(a) (b)

Figure 5.15. Distribution of mean value of interval temperature for slow freezing method: (a) t = 6990 s, T_{bath} = −79.5 °C; (b) t = 13980 s, T_{bath} = −196 °C

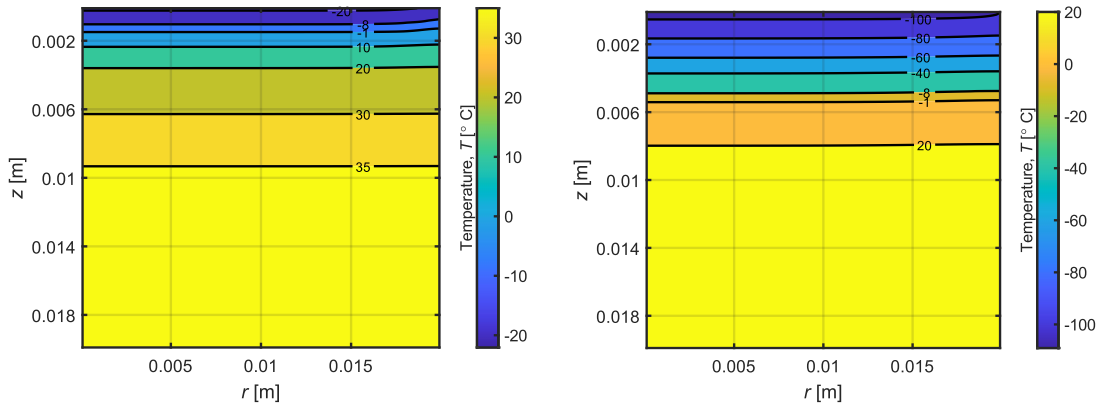

(a) (b)

Figure 5.16. Distribution of mean value of interval temperature for vitrification method: (a) t = 70 s, T_{bath} = −79.67 °C; (b) t = 139.8 s, T_{bath} = −196 °C

5.3.2. Summary and conclusions

In summary, it is worth to compare the two cryopreservation approaches with each other. In the case of slow freezing, the temperature distribution is more stable and regular. That means that the heat flow in the sample requires a certain amount of time. In the context of cryopreservation, it is confirmed by the assumptions formulated by Mazur [95]. He noted that the application of an appropriate cooling rate enables the osmotic transport of water into the extracellular matrix from the intracellular solution while protecting the cell from damage. Unfortunately, a quite wide intermediate region is observed over a certain period of time simulation. It suggests a high risk of ice crystallisation. However, in order to assess the potential tissue damage caused by the formation of ice crystals, the mass transport phenomenon and the degree of crystallisation should be additionally investigated.

For vitrification, on the other hand, all three physical states can be observed during the cooling process as well as when T_{bath} = −196 °C. It can therefore be concluded that it is not complete freezing after the cooling time. In fact, vitrification consists in receiving amorphous ice while the solution vitrifies (solidifies) without ice crystallisation. This process is achieved by using a highly concentrated solution of CPA. The interaction of CPA causes changes in the properties of the solution (for example its freezing/melting point). Therefore, it is difficult to assess the condition of the vitrified sample on the basis of thermal analysis alone. Furthermore, misaligned concentrations of CPA lead to

cytotoxicity and damage to the biological structure. For this reason, it is important to analyse the impact of CPA and to study osmotic transport phenomena.

5.4. Example 3: Bioheat transport with degree of ice crystallisation

The final example in this Chapter describes thermal processes including the phenomenon of ice crystallisation in microscopic terms. As cells and tissues consist mainly of water, a cell-free CPA solution is modelled instead of a biological sample.

It is possible to find publications in which the degree of crystallisation is determined in the context of cryopreservation [148, 190, 196]. The indicated works are devoted to vitrification by cryopreservation. The aim of this method is to achieve an amorphous structure avoiding ice crystallisation. Consequently, the degree of crystallisation should be reduced to minimum.

Zhou et al. [196] proposed a special microfluidic system in which a working fluid flows through microchannels. In addition, the geometry of the thin-film sample ensures a uniform thermal distribution inside the piece of biological tissue. Our model is based on their device concept and the geometry invented by Tuckerman and Pease [174].

Figure 5.17 illustrates the conceptual project of microfluidic system with a single cell unit marked. It can be seen that a thin layer of sample is located in the microcavities in the central part of the device. During simulation, the sample layer is substituted by the cell-free solution which consists of 55% water and 45% ethylene glycol (EG). The entire system is enclosed in a housing in which microchannels are extracted. This housing (chip wall) is made of silicone. The microchannels provide the working fluid that regulates the cooling rate. The thermal insulation (heatproof cover) encapsulates the entire device. This ensures that the heat flux between the system and the environment is negligible.

The analysis is performed for a microfluidic system, where the heat transfer model is coupled with the degree of crystallisation. To describe the solidification process, a zone model is adopted. Moreover, the thermophysical parameters depend on the temperature and introduce a weak non-linearity into the heat transfer equation.

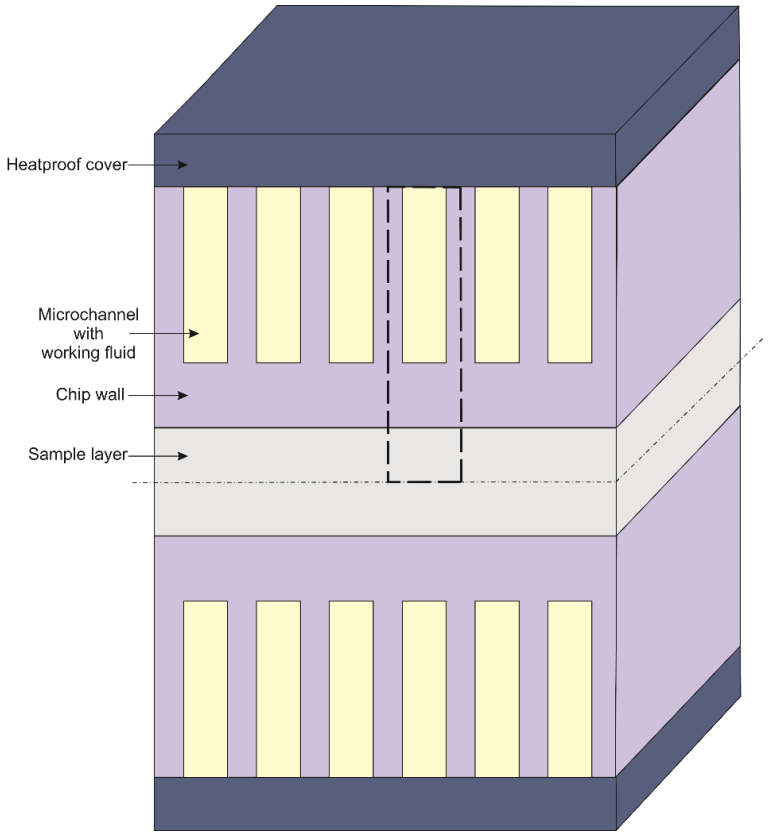

Figure 5.17. Concept of microfluidic system

The energy equation was defined according to the Fourier equation. The internal heat source in the sample layer is related to the ice crystallisation, therefore:

$$c_p \rho \dot{T} = \nabla \left(k \nabla T \right) + \rho L \dot{\chi} \,. \tag{5.62}$$

It is important to note that the internal heat source associated with crystallisation appears only in the sample layer, while for the silicon chip wall $\rho L \dot{\chi} = 0$.

In the above equation exists a derivative defining the change in the degree of crystallisation over time. As it can be read in Chapter 3, Boutron and Mehl proposed the calculation of the degree of crystallisation using the non-isothermal kinetic equation:

$$\dot{\chi} = k_a \chi^{\frac{2}{3}} \left(1-\chi\right)\left(T_m - T\right) e^{\frac{-Q_{en}}{RT}} \,. \tag{5.63}$$

One of the variables appearing in Equation (5.63) is the activation energy, which induces nucleation and growth of ice crystals. Its value is calculated using the Kissinger method, the Augis-Bennett method, the Baswell method, or the Gao-Wang method. These techniques determine the relationship between the degree of heating (cooling) and the freezing point. The activation energy affects the degree of

crystallisation, because the smaller the ratio of activation energy to average kinetic energy (*RT*), the greater the time derivative of the degree of crystallisation [6].

As mentioned, the sample is a layer of thin film. This guarantees that heat transfer proceeds mainly in one direction and that the temperature distribution is uniform in the other directions. Therefore, the problem analysed can be examined as a one-dimensional problem. Figure 5.18 shows the sample cross-section under consideration. Points A, B and C represent the boundary nodes where the boundary conditions are defined.

Analogous to Example 1, this example introduces thermophysical parameters into the mathematical model in the form of both interval and fuzzy numbers. This is a novel approach compared to other research from the literatures, for example in [148, 190, 196]. First, research for interval numbers will be demonstrated.

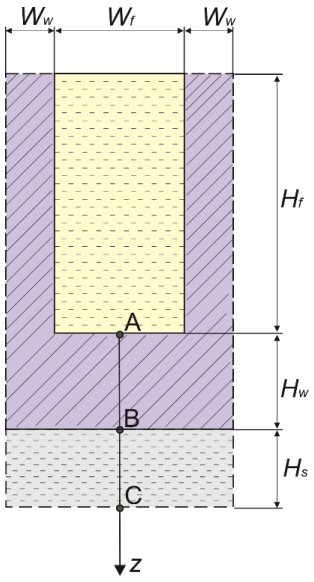

Figure 5.18. One-dimensional sample model (cross-section)

5.4.1. Example 3 – interval numbers

Applying the interval numbers and specific coordinate system, the governing equation is of a form:

$$\rho\frac{\partial\left(\overline{c}_p\left(\overline{T}\right)\overline{T}\left(z,t\right)\right)}{\partial t}=\frac{\partial}{\partial z}\left(\overline{k}\left(\overline{T}\right)\frac{\partial\overline{T}\left(z,t\right)}{\partial z}\right)+\rho_w L_w\frac{\partial\overline{\chi}\left(\overline{\chi},\overline{T}\right)}{\partial t}, \qquad (5.64)$$

where ρ, $\overline{k}$, $\overline{c}_p$ can be defined as parameters in chip wall (*cw*) or in sample layer (*sl*) and subscript *w* denotes parameters of water. The growth rate of degree of crystallisation is defined:

$$\frac{\partial\overline{\chi}\left(\overline{\chi},\overline{T}\right)}{\partial t}=k_a\overline{\chi}^{\frac{2}{3}}\left(1-\tilde{\chi}\right)\left(T_m-\overline{T}\left(z,t\right)\right)e^{\frac{-Q_{en}}{R\overline{T}(z,t)}}. \tag{5.65}$$

Please note that in this case the values of thermal parameters depend on the temperature. They are expressed by polynomials whose coefficients were obtained from experimental studies. This is an argument for using a non-deterministic approach, as the values of these parameters are imprecise and unpredictable.

We will first investigate the specific heat capacity as well as the thermal conductivity for the silicon chip wall. Thermal parameter characteristics were prepared based on the measurements reported in the literature [28, 44, 205]. The interesting thing is that in the literature (for example in [28]), the molar specific heat capacity is sometimes given in $J\cdot mol^{-1}\cdot K^{-1}$. Then, to obtain the specific heat, the molar specific heat capacity has to be divided by the molar mass.

According to experimental data, in the range 20-300 K (from –253 °C to 27 °C), fourth- and fifth-order polynomial functions of $\overline{T}$ (in °C) were estimated using the linear regression method:

$$\begin{aligned}\overline{c}_{cw}(\overline{T}) &= 2.4923\cdot10^{-7}\overline{T}^4+9.1657\cdot10^{-5}\overline{T}^3+0.0023\overline{T}^2\\ &\quad +1.395\overline{T}+677.6804,\\ \overline{k}_{cw}(\overline{T}) &= 1.3496\cdot10^{-8}\overline{T}^5+1.1636\cdot10^{-5}\overline{T}^4+0.0024\overline{T}^3+0.1416\overline{T}^2\\ &\quad -2.0261\overline{T}+54.3813,\end{aligned} \tag{5.66}$$

where subscript c*w* denotes the chip wall. The coefficients of determination are equal to R^2 = 0.999 and R^2 = 0.989 for the specific heat capacity and the thermal conductivity, respectively.

On the other hand, polynomial functions of $\overline{T}$ in °C were used to determine the thermophysical parameters for the EG solution. The characteristics were based on product information provided by the producer MEGlobal™ [97, 196]:

$$\begin{aligned}\overline{c}_{sl}(\overline{T}) &= 2.8467\overline{T}+2727.7,\\ \overline{k}_{sl}(\overline{T}) &= \left(-2.7041\cdot10^{-2}\overline{T}^2-17.741\overline{T}+1442.8\right)/1000,\end{aligned} \tag{5.67}$$

where subscript *s* represents the sample layer.

In our study, the deviation is introduced at the first time step (t = 0), when the initial condition is specified in the entire domain. The deterministic value for the interval specific heat and for the thermal conductivity are equal to 5%, hence

$\bar{k} = [k - 0.05k; k + 0.05k]$ and $\bar{c} = [c - 0.05c; c + 0.05c]$. In the next steps of the simulation, the interval temperature are applied to the Equations (5.66) and (5.67).

The model also includes thermophysical parameters assumed to be constant values. The chip wall made of silicone is characterized by its density ρ_{cw} = 2330 kg·m^{-3}. A cell-free solution consisting of water and EG is described by the properties for water: $L_w = 334 \cdot 10^3$ J·kg^{-1}, ρ_w = 1000 kg·m^{-3} [93]. Whereas, the crystallisation parameters of the sample layer are $k_a = 3.933 \cdot 10^7$ s^{-1}·K^{-1} for cooling [138, 196] and k_a = 1.287 s^{-1}·K^{-1} for warming [63, 196], T_m = 243.5 K, $Q_{en} = 4.187 \cdot 10^3$ J·mol^{-1} [11, 140].

After discussing the mathematical model, it is necessary to define also the initial and boundary conditions. The initial temperature that dominates the entire domain at the first moment of simulation time is equal to T^0 = 22 °C. The initial condition should also include the initial degree of crystallisation, where, $\chi^0 = 0$ [130].

Then, it is worth exploring the boundary conditions established at the boundary nodes marked A, B and C (see Figure 5.18). The working fluid contained in the microchannels causes thermal modifications in the system. In the study, as the working fluid is adopted liquid nitrogen and water for cooling and warming, respectively. The temperatures assured by the working fluid are T_{wf} = −196 °C and T_{wf} = 40 °C. In the one-dimensional model, the point of contact between the working fluid and the chip wall is point A. The heat flux at this point defines a boundary condition of the 3rd type. The condition also includes the geometry of the unit cell. The heat flux can be expressed [196]:

$$\bar{q}_{\Gamma_A}\left(\bar{T}\right)\cdot\left(W_f + 2W_w\right) = \alpha_\Gamma\left(\bar{T}(z,t) - T_f\right)\left(W_f + 2\bar{\eta}H_f\right), \tag{5.68}$$

where W_f, W_w, H_f are the microchannel dimensions (see in Figure 5.19) and $\bar{\eta}$ is the interval fin efficiency.

The interval fin efficiency is formulated as [196]:

$$\bar{\eta} = \frac{\tanh\left(\bar{m}_\eta H_f\right)}{\bar{m}H_f}, \tag{5.69}$$

where $\bar{m}_\eta$ is the interval fin parameter calculated from the relation [196]:

$$\bar{m}_\eta = \sqrt{\frac{2\alpha_\Gamma}{\bar{k}_{cw}\left(\bar{T}\right)\cdot 2W_w}}. \tag{5.70}$$

One of the components of Equation (5.70) is the external heat transfer coefficient (α_Γ). Determining its value experimentally for a working fluid placed in microchannels is

difficult. Instead, a theoretical relationship was developed to compute it. Considerations for the external heat transfer coefficient are presented, for example, in [196].

In our work, two types of flows related to the type of working fluid are modelled. During cooling, there is a two-phase flow, which is due to the properties of liquid nitrogen. In fact, not only liquid nitrogen but also small quantities of vapour nitrogen are present in the microchannel. On the other hand, water is responsible for warming the sample. Water exists only in liquid form and therefore it represents a single-phase flow. In our study, the constant values of the external heat transfer coefficient are assumed for the particular flows.

Other boundary conditions are given at points B and C. The contact between the sample layer and the silicon chip wall (point B) is described by the condition of the 4th type. As it is assumed that there is no thermal resistance in the system, this condition can be expressed as [130]:

$$\begin{cases} -\mathbf{n}\bar{k}_{cw} \cdot \dfrac{\partial \bar{T}_{cw}(z,t)}{\partial z} = -\mathbf{n}\bar{k}_{sl} \cdot \dfrac{\partial \bar{T}_{sl}(z,t)}{\partial z}, \\ \bar{T}_{cw}(z,t) = \bar{T}_{sl}(z,t), \end{cases} \tag{5.71}$$

where subscripts *cw* and *sl* represent the chip wall and the sample layer, respectively.

In contrast, at point C exists an adiabatic condition. It results from the fact that the system is symmetrical [130]:

$$\bar{q}_{\Gamma_c}(z,t) = -\mathbf{n}\bar{k} \cdot \frac{\partial \bar{T}(z,t)}{\partial z} = \bar{0}\,. \tag{5.72}$$

In order to determine the individual relationships at the boundary nodes, let us introduce the following variables. Firstly, the dimensions of a single unit cell (see Figure 5.18) are equal to $W_f = 5 \cdot 10^{-5}$ m, $W_w = 2.5 \cdot 10^{-5}$ m, $H_f = 3.5 \cdot 10^{-4}$ m, $H_w = 10^{-4}$ m and $H_s = 10^{-4}$ m [196].

As mentioned, the working fluids are liquid nitrogen and water at appropriate temperatures. The constant external heat transfer coefficients (natural convection heat transfer coefficients) are determined according to their thermal properties and for cooling $\alpha_\Gamma = 1.048 \cdot 10^4$ W·m^{-2}·K^{-1}, as well as for warming $\alpha_\Gamma = 4.74 \cdot 10^4$ W·m^{-2}·K^{-1} [196].

After deriving the mathematical model, its numerical form should be developed. Analogous to the previous examples, the interval FDM is applied. It should be noted that this time a one-dimensional domain is analysed. In addition, the governing equation is

non-linear, as the thermophysical parameters depend on the temperature and the internal heat sources depend on the degree of crystallisation.

As FDM is a mesh method, therefore the timeline and space are segmented into nodes. The time step Δt (compare with Equation (5.14)) and the mesh step h are assumed constant. Figure 5.19 illustrates three-points star, which generates the domain mesh.

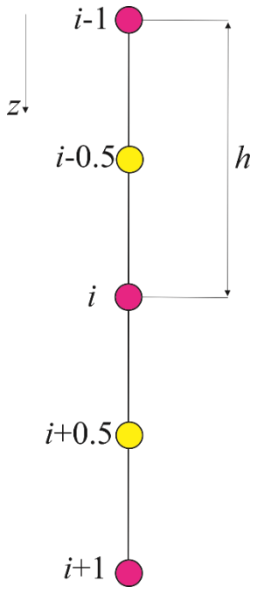

Figure 5.19. Three-points star scheme

The elements introducing non-linearity into the equation are defined for the temperature values at moment $f-1$:

$$\overline{c}_p\left(\overline{T}\right)=\overline{c}_p\left(\overline{T}_i^{\,f-1}\right), \tag{5.73}$$

$$\overline{k}\left(\overline{T}\right)=\overline{k}\left(\overline{T}_i^{\,f-1}\right), \tag{5.74}$$

where $i = 1, 2, \ldots, n$. It is also assumed that these variables are weakly non-linear.

In contrast to the previous examples, an implicit scheme is used here. The implicit scheme is always stable, so there is no need to define a stability condition and a maximum time step condition [88, 100].

The temperature time derivative is determined according to the relationship presented earlier in Equation (5.15). In a similar procedure, the time derivative of the degree of crystallisation is estimated:

$$\left(\frac{\partial\overline{\chi}\left(\overline{\chi},\overline{T}\right)}{\partial t}\right)_i^f=\frac{\overline{\chi}_i^{\,f}-\overline{\chi}_i^{\,f-1}}{\Delta t}. \tag{5.75}$$

The substitution of the differential quotients into the derivative of the coordinates on the right-hand side of the Equation (5.64) is slightly different. As the implicit scheme is used, the time derivative of the temperature in is computed for the moment *f*; hence for internal nodes:

$$\left[\frac{\partial}{\partial z}\left(\bar{k}\left(\bar{T}\right)\frac{\partial \bar{T}\left(z,t\right)}{\partial z}\right)\right]_i^f = \frac{1}{h}\left[\bar{k}\left(\bar{T}_{i+0.5}^{f-1}\right)\left(\frac{\partial \bar{T}\left(z,t\right)}{\partial z}\right)_{i+0.5}^f - \left(\bar{k}\left(\bar{T}_{i-0.5}^{f-1}\right)\frac{\partial \bar{T}\left(z,t\right)}{\partial z}\right)_{i-0.5}^f\right], \tag{5.76}$$

where $i = 2, 3, \ldots, n\text{-}1$.

The thermal conductivity values in our case are given in the form of a harmonic mean:

$$\begin{aligned} &1.\quad \left(\bar{k}\left(\bar{T}\right)\right)_{i+0.5}^{f-1} = \frac{2\bar{k}\left(\bar{T}_i^{f-1}\right)\bar{k}\left(\bar{T}_{i+1}^{f-1}\right)}{\bar{k}\left(\bar{T}_i^{f-1}\right)+\bar{k}\left(\bar{T}_{i+1}^{f-1}\right)}, \\ &2.\quad \left(\bar{k}\left(\bar{T}\right)\right)_{i-0.5}^{f-1} = \frac{2\bar{k}\left(\bar{T}_i^{f-1}\right)\bar{k}\left(\bar{T}_{i-1}^{f-1}\right)}{\bar{k}\left(\bar{T}_i^{f-1}\right)+\bar{k}\left(\bar{T}_{i-1}^{f-1}\right)}. \end{aligned} \tag{5.77}$$

By introducing interval thermal resistances, differential quotients can be expressed by:

$$\begin{aligned} &1.\quad \bar{k}\left(\bar{T}_{i+0.5}^{f-1}\right)\left(\frac{\partial \bar{T}(z,t)}{\partial z}\right)_{i+0.5,j}^f = \frac{\bar{T}_{i+1}^f - \bar{T}_i^f}{R_{i+1}^{f-1}}, \\ &2.\quad \bar{k}\left(\bar{T}_{i-0.5}^{f-1}\right)\left(\frac{\partial \bar{T}(z,t)}{\partial z}\right)_{i-0.5,j}^f = \frac{\bar{T}_i^f - \bar{T}_{i-1}^f}{R_{i-1}^{f-1}}, \end{aligned} \tag{5.78}$$

where:

$$\begin{aligned} \bar{R}_{i+1}^{f-1} &= \frac{h}{2\bar{k}\left(\bar{T}_i^{f-1}\right)} + \frac{h}{2\bar{k}\left(\bar{T}_{i+1}^{f-1}\right)}, \\ \bar{R}_{i-1}^{f-1} &= \frac{h}{2\bar{k}\left(\bar{T}_i^{f-1}\right)} + \frac{h}{2\bar{k}\left(\bar{T}_{i-1}^{f-1}\right)}. \end{aligned} \tag{5.79}$$

Finally, for internal nodes, the Equation (5.65) in the implicit scheme is of the form:

$$\bar{c}_p\left(\bar{T}_i^{f-1}\right)\rho\frac{\bar{T}_i^f - \bar{T}_i^{f-1}}{\Delta t} = \left[\sum_{a=1}^{2}\frac{\Phi}{\bar{R}_e^{f-1}}\left(\bar{T}_e^f - \bar{T}_i^f\right)\right] + \rho_w L_w \frac{\bar{\chi}_i^f - \bar{\chi}_i^{f-1}}{\Delta t}, \tag{5.80}$$

where $i = 2, 3, \ldots, n\text{-}1$, the individual a corresponds to $e = \{i + 1, i\text{-}1\}$ and Φ is the shape function:

$$\Phi = \frac{1}{h}. \tag{5.81}$$

Let us also analyse the temperature calculations at points A, B and C. At point A, the heat flux is known, and its value depends on the temperature. It is assumed that:

$$\bar{q}_{\Gamma_A}\left(\bar{T}\right) = \bar{q}_{\Gamma_A}\left(\bar{T}_1^{f-1}\right) = \frac{\alpha_\Gamma\left(\bar{T}_1^{f-1} - T_f\right)\left(W_f + 2\bar{\eta}H_f\right)}{\left(W_f + 2W_w\right)}. \tag{5.82}$$

When we introduce the relationship from Fourier's law (see Equation (3.3) in Chapter 3) into the above formula, one obtains the dependence:

$$\frac{\bar{T}_2^f - \bar{T}_1^f}{h} = \frac{\bar{q}_{\Gamma_A}\left(\bar{T}_1^{f-1}\right)}{\bar{k}\left(\bar{T}_1^{f-1}\right)} = \frac{1}{\bar{k}\left(\bar{T}_1^{f-1}\right)} \frac{\alpha_\Gamma\left(\bar{T}_1^{f-1} - T_f\right)\left(W_f + 2\bar{\eta}H_f\right)}{\left(W_f + 2W_w\right)}. \tag{5.83}$$

On the other hand point B is characterised by ideal contact between two different bodies. It implies that for nodes near this point, the equation derived for internal nodes (Equation (5.80)) is valid.

At the centre of the sample layer is point C. As the microfluidic system is symmetrical, an adiabatic condition is given at this point, therefore:

$$\frac{\bar{T}_n^f - \bar{T}_{n-1}^f}{h} = -\frac{\bar{q}_{\Gamma_C}\left(\bar{T}_n^{f-1}\right)}{\bar{k}\left(\bar{T}_n^{f-1}\right)} = 0. \tag{5.84}$$

Knowing the relationships shown for the internal nodes (Equation (5.80)), a matrix system of equations can be determined:

$$\bar{A}_i\bar{T}_{i-1}^f + \bar{B}_i\bar{T}_i^f + \bar{C}_i\bar{T}_{i+1}^f = \bar{T}_i^{f-1} + \bar{Q}_i\ , \tag{5.85}$$

where:

$$\begin{aligned}
\bar{A}_i &= -\frac{2\Delta t}{h^2 \bar{c}_p\left(\bar{T}_i^{\,f-1}\right)\rho} \cdot \frac{\bar{k}\left(\bar{T}_{i-1}^{\,f-1}\right)\bar{k}\left(\bar{T}_i^{\,f-1}\right)}{\bar{k}\left(\bar{T}_{i-1}^{\,f-1}\right)+\bar{k}\left(\bar{T}_i^{\,f-1}\right)}, \\
\bar{B}_i &= \frac{2\Delta t}{h^2 \bar{c}_p\left(\bar{T}_i^{\,f-1}\right)\rho} \cdot \left(\frac{\bar{k}\left(\bar{T}_{i-1}^{\,f-1}\right)\bar{k}\left(\bar{T}_i^{\,f-1}\right)}{\bar{k}\left(\bar{T}_{i-1}^{\,f-1}\right)+\bar{k}\left(\bar{T}_i^{\,f-1}\right)} + \frac{\bar{k}\left(\bar{T}_{i+1}^{\,f-1}\right)\bar{k}\left(\bar{T}_i^{\,f-1}\right)}{\bar{k}\left(\bar{T}_{i+1}^{\,f-1}\right)+\bar{k}\left(\bar{T}_i^{\,f-1}\right)} \right), \\
\bar{C}_i &= -\frac{2\Delta t}{h^2 \bar{c}_p\left(\bar{T}_i^{\,f-1}\right)\rho} \cdot \frac{\bar{k}\left(\bar{T}_{i+1}^{\,f-1}\right)\bar{k}\left(\bar{T}_i^{\,f-1}\right)}{\bar{k}\left(\bar{T}_{i+1}^{\,f-1}\right)+\bar{k}\left(\bar{T}_i^{\,f-1}\right)}, \\
\bar{Q}_i &= \frac{\Delta t}{\bar{c}_p\left(\bar{T}_i^{\,f-1}\right)\rho} \rho_w L_w \frac{\bar{\chi}_i^{\,f} - \bar{\chi}_i^{\,f-1}}{\Delta t},
\end{aligned} \tag{5.86}$$

where $i = 2, 3, \ldots, n\text{-}1$. In a similar procedure, first and n row of the matrix were defined considering the boundary conditions (Equations (5.83) and (5.84)). The resulting matrix equation is as follows:

$$\begin{bmatrix}
-\frac{1}{h} & \frac{1}{h} & 0 & \cdots & \cdots & 0 \\
\bar{A}_2 & \bar{B}_2 & \bar{C}_2 & 0 & \cdots & 0 \\
0 & \ddots & \ddots & \ddots & \ddots & \vdots \\
\vdots & \ddots & \ddots & \ddots & \ddots & 0 \\
\vdots & \ddots & 0 & \bar{A}_{n-1} & \bar{B}_{n-1} & \bar{C}_{n-1} \\
0 & \cdots & \cdots & 0 & -\frac{1}{h} & \frac{1}{h}
\end{bmatrix}_{i\,x\,i} \cdot \begin{bmatrix} T_1^f \\ T_2^f \\ \vdots \\ \vdots \\ T_{n-1}^f \\ T_n^f \end{bmatrix} = \begin{bmatrix} \frac{\bar{q}_{\Gamma_A}\left(\bar{T}_1^{\,f-1}\right)}{\bar{k}\left(\bar{T}_1^{\,f-1}\right)} \\ \bar{T}_2^{\,f-1} + \bar{Q}_2 \\ \vdots \\ \vdots \\ \bar{T}_{n-1}^{\,f-1} + \bar{Q}_{n-1} \\ 0 \end{bmatrix} \tag{5.87}$$

The above numerical model can be considered as incomplete, there is no information about the determination of the value of the degree of crystallisation at a given time *f*. The non-isothermal kinetic equation (see Equation (5.64)) is complex, so computing the degree of crystallisation is difficult [196]. In this example, the fourth-order Runge-Kutta algorithm is applied.

In practice, after estimating the thermal distribution at time level *f*, the value of the degree of crystallisation at time step $f+1$ is determined. According to the differential quotient from Equation (5.75), a relation is derived for the interval degree of crystallisation $\bar{\chi}_i^{\,f+1}$:

$$\bar{\chi}_i^{\,f+1} = \bar{\chi}_i^{\,f} + \left(\frac{\partial \bar{\chi}\left(\bar{\chi}, \bar{T}\right)}{\partial t} \right)_i^{f+1} \cdot \Delta t \,. \tag{5.88}$$

Let us simplify the notation of the derivative:

$$\frac{\partial \bar{\chi}\left(\bar{\chi},\bar{T}\right)}{\partial t} = \bar{\chi}'\left(\bar{\chi},\bar{T}\right). \tag{5.89}$$

Using the Runge-Kutta method, the interval degree of crystallisation $\bar{\chi}_i^{f+1}$ is given as:

$$\bar{\chi}_i^{f+1} = \bar{\chi}_i^{f} + \frac{1}{6}\Delta t\left[\left(\bar{\chi}'\right)_1 + \left(\bar{\chi}'\right)_2 + \left(\bar{\chi}'\right)_3 + \left(\bar{\chi}'\right)_4\right], \tag{5.90}$$

where:

$$\begin{cases} \left(\bar{\chi}'\right)_1 = \bar{\chi}'\left(\bar{\chi}_i^{f},\bar{T}_i^{f}\right), \\ \left(\bar{\chi}'\right)_2 = \bar{\chi}'\left(\bar{\chi}\left(\bar{\chi}_i^{f},\bar{T}_i^{f}\right) + \frac{1}{2}\Delta t\left(\bar{\chi}'\right)_1, \bar{T}_i^{f} + \frac{1}{2}\Delta\bar{T}\right), \\ \left(\bar{\chi}'\right)_3 = \bar{\chi}'\left(\bar{\chi}\left(\bar{\chi}_i^{f},\bar{T}_i^{f}\right) + \frac{1}{2}\Delta t\left(\bar{\chi}'\right)_2, \bar{T}_i^{f} + \frac{1}{2}\Delta\bar{T}\right), \\ \left(\bar{\chi}'\right)_4 = \bar{\chi}'\left(\bar{\chi}\left(\bar{\chi}_i^{f},\bar{T}_i^{f}\right) + \Delta t\left(\bar{\chi}'\right)_3, \bar{T}_i^{f} + \Delta\bar{T}\right), \end{cases} \tag{5.91}$$

and:

$$\Delta\bar{T} = \bar{T}^{f} - \bar{T}^{f-1}. \tag{5.92}$$

Once the interval degree of crystallisation has been determined for time level f+1, it is possible to proceed from time moment f to f+1 and re-estimate the temperature in the domain concerned.

The parameters input to the numerical model are: the mesh step $h = 2.0202 \cdot 10^{-6}$ m and the time step Δt = 0.01 s. The domain is divided into 99 elements and the interval temperature or the interval degree of crystallisation are estimated in 100 nodes [130].

The general procedures for the algorithm to simulate heat transfer and crystallisation phenomena are presented in Figure 5.20. The author's program was prepared in MATLAB R2021a environment (The MathWorks, Inc.).

Before showing the simulation results, the effect of temperature on the deterministic values of the thermophysical parameters was analysed. Using Equations (5.66) and (5.67) for the deterministic temperature, the following graphs have been prepared – see Figure 5.21. These diagrams indicate the importance of introducing temperature-dependent parameters as a function of temperature into the model.

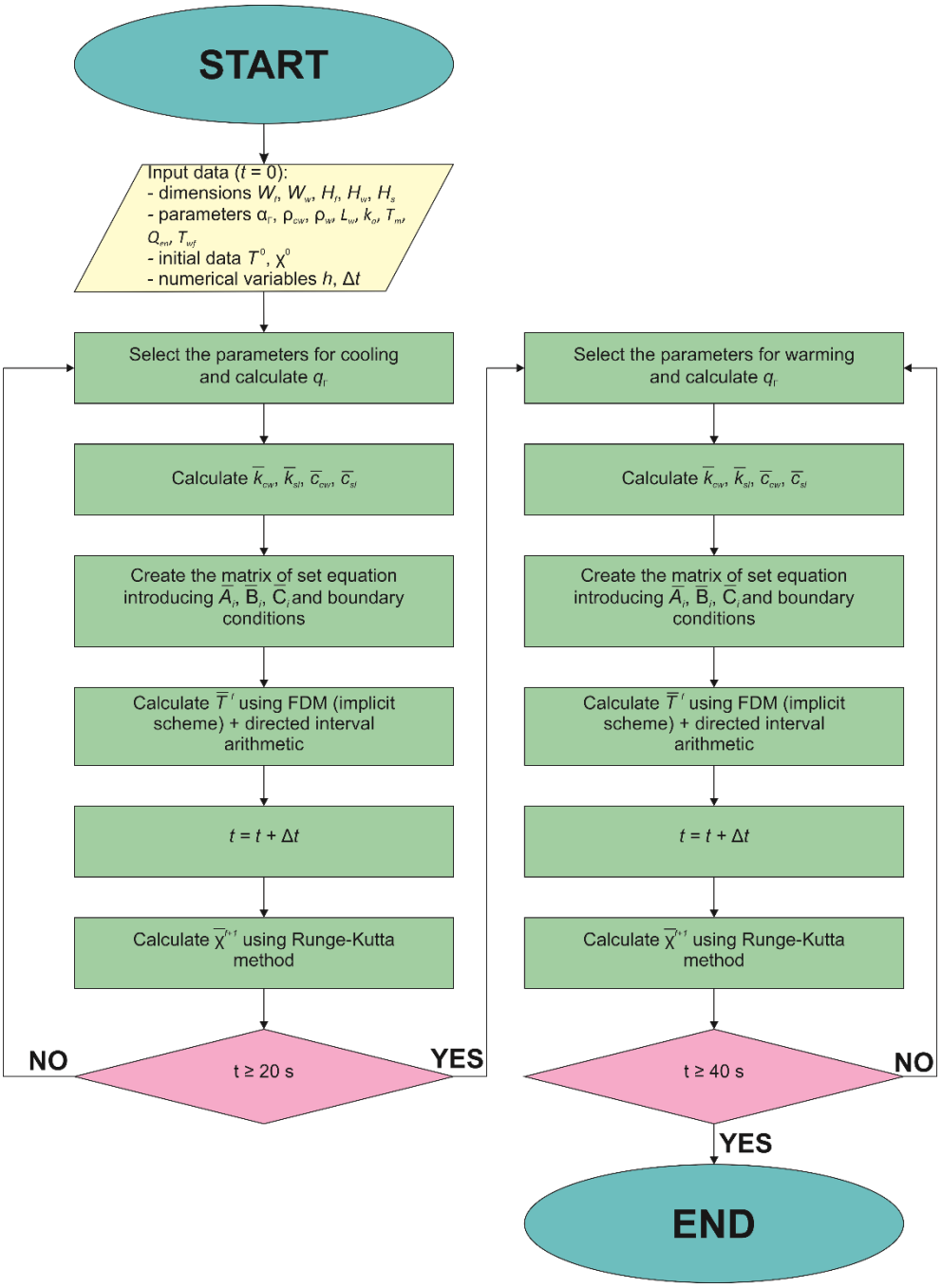

Figure 5.20. Flowchart of algorithm to simulate heat transfer phenomena including crystallisation (interval arithmetic)

The subsequent section introduces the simulation products describing the change in temperature distribution with relation to the degree of crystallisation. Figure 5.22 demonstrates the alterations of the interval temperature during cooling. The results are presented at the point which is situated in the central part of the sample layer, for $z = H_w + H_s$ (point C). As can be seen, the interval widths obtained are quite narrow. For this reason, it was decided to create an approximation for the time interval

0.00 – 0.02 s and 0.30 – 0.32 s. The temperature of the sample layer reaches the desired values given by the working fluid within a few seconds. The domain of the whole sample is cooled to −196 °C after 14.1 s.

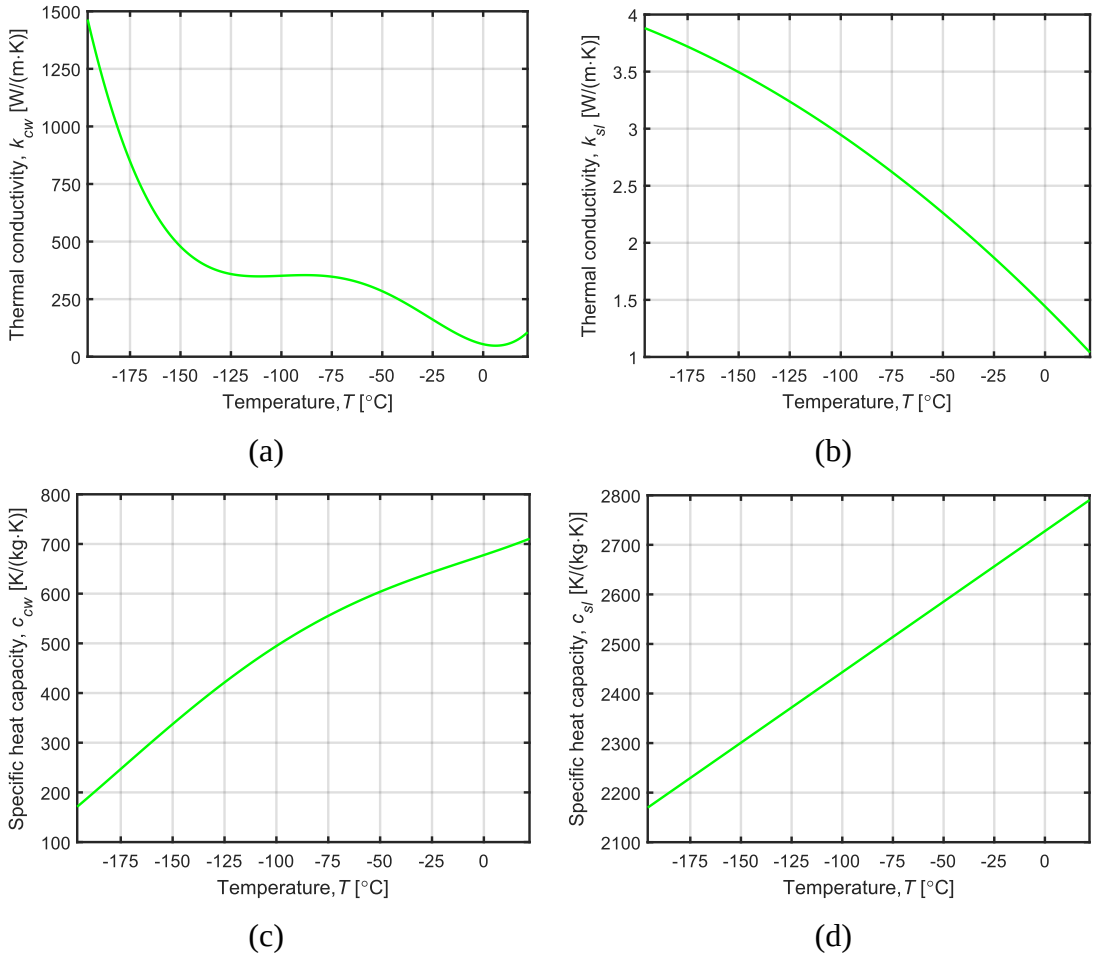

Figure 5.21. Thermal conductivity temperature for chip wall (a) and sample layer (b); and specific heat capacity for chip wall (c) and sample layer (d) as a function of time

Analogically, the results are provided for warming. Figure 5.23 shows the changes of the interval temperature over time in the centre of the sample layer (point C). It takes 7.15 s to warm the analysed domain to 40 °C. In the graph (see Figure 5.23), one notices a sudden and temporary reduction in temperature over a certain time interval, which can suggest the existence of a recrystallisation phenomenon.

Complementing the thermal study are the computational results obtained for the degree of crystallisation. In Figure 5.24, there are diagrams representing the history of the interval degree of crystallisation for cooling. The obtained results also indicate

changes in the central part of the sample (point C). After some time, the degree of crystallisation stabilises.

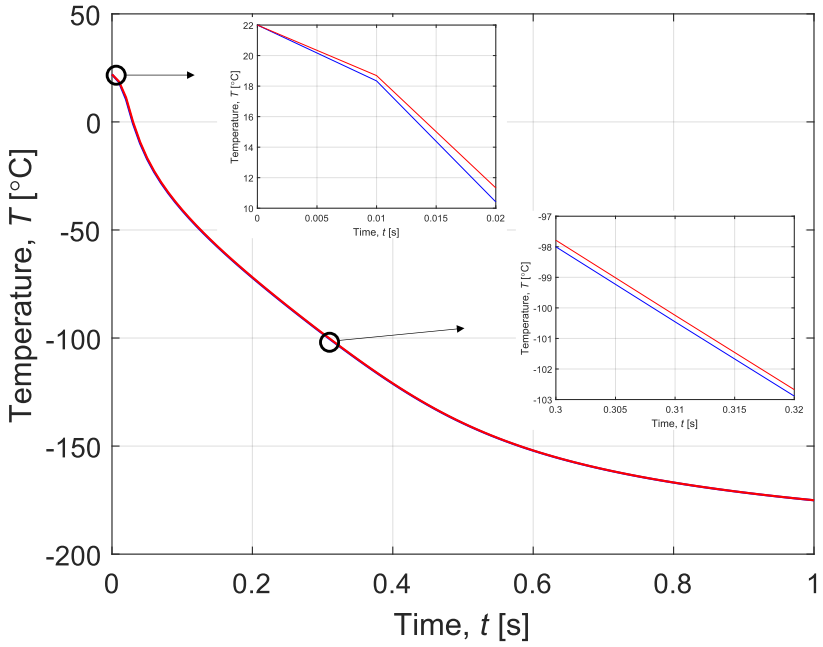

Figure 5.22. Interval temperature as a function of time during cooling with zoomed fragments

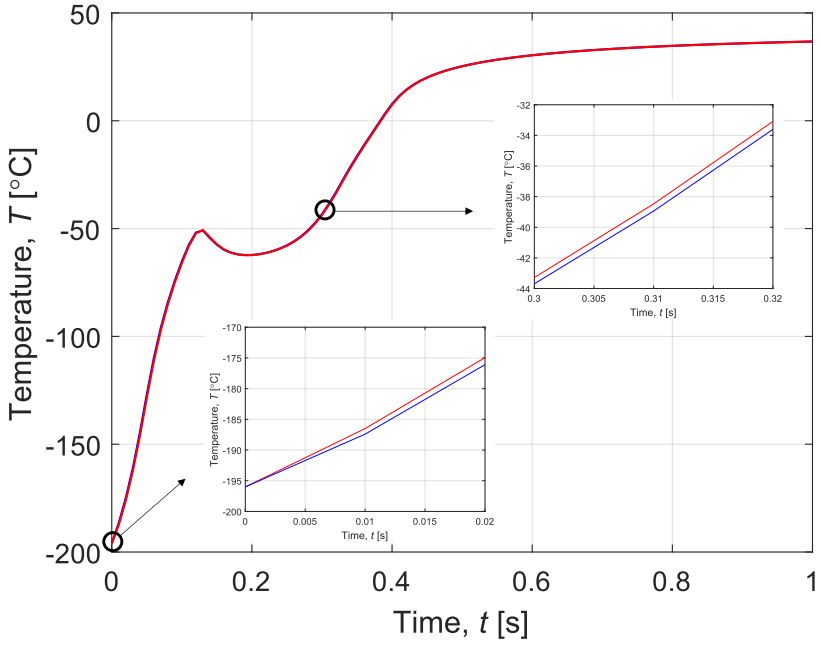

Figure 5.23. Interval temperature as a function of time during warming with zoomed fragments

Figure 5.25 illustrates similar graphs prepared for warming. At a certain time during the simulation, the interval degree of crystallisation increases sharply, after which it decreases to 0. This indicates the existence of a recrystallisation phenomenon that disappears when the sample domain is warmed.

In the characteristics shown in Figures 5.24 and 5.25, a peak can be observed, which occurs when the temperature in the sample domain is between −90 °C and −20 °C. In the literature, this range is defined as the dangerous temperature region (DTR) which particularly impacts the value of the total degree of crystallisation [140, 196]. Consequently, the DTR is a critical moment for ice crystal formation, and its duration should be as short as possible. In our case, the DTR durations are equal to 0.2 s and 0.26 s for cooling and warming, respectively.

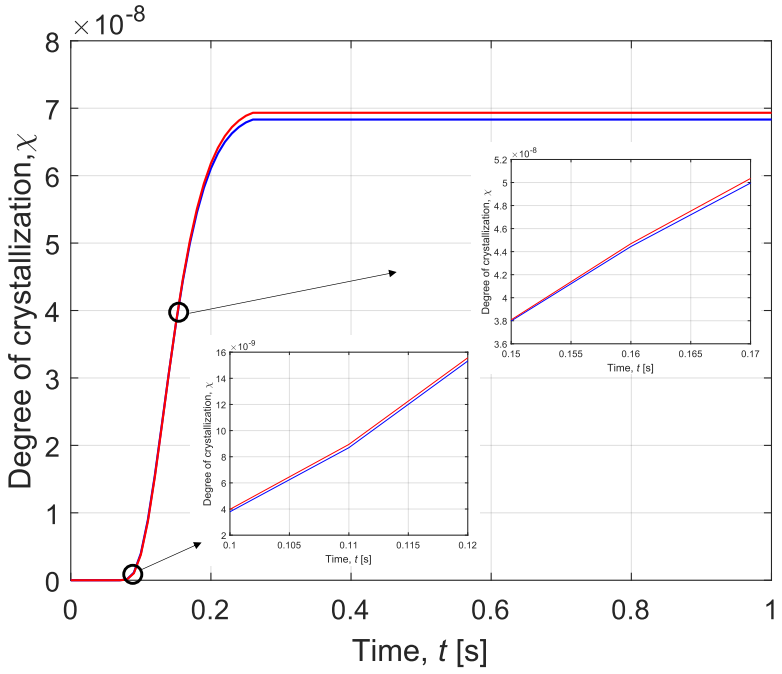

Figure 5.24. Interval degree of crystallisation as a function of time during cooling with zoomed fragments

It is also worth considering the highest mean value of the interval degree of crystallisation. On this basis, it is possible to estimate whether cell damage will occur due to ice crystallisation. According to the results of simulation, the maximum values of this parameter are: for cooling $\chi_{max} = 1.075 \cdot 10^{-7}$ and for warming $\chi_{max} = 0.999$. This may suggest that during warming there is a higher risk of sample destruction caused by ice crystallisation. This is the effect of recrystallisation, which disappears during warming of

the sample layer. In the case of cooling, after passing through the DTR, the interval degree of crystallisation remains stable and constant.

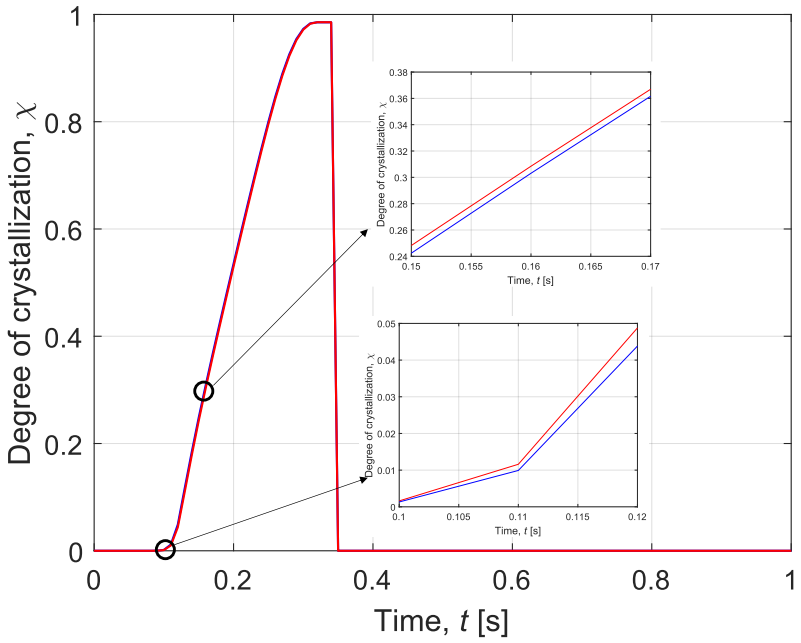

Figure 5.25. Interval degree of crystallisation as a function of time during warming with zoomed fragments

In addition, the examples of the results obtained in the central part of the sample (point C) are included in Table 5.8. This provides a better view of the interval values, whose interval widths are relatively narrow.

The last series of plots for this task concerns the interval temperature development at a selected moment of the simulation in the cross section of the sample layer. Figure 5.26 presents the interval temperature at time $t = 0.1$ s for cooling (a) and warming (b). At point B, which is the contact point between the chip wall and the sample layer, the temperature is the lowest (highest) at a given moment in the simulation. The reason for this is that point B reacts most rapidly to changes caused by the thermal interaction between the silicon housing and the working fluid. Of course, after some time the interval temperature equalizes across the domain.

Table 5.8. Selected results for interval variables

Time, t [s]	**Interval thermal conductivity, $\bar{k}_{sl}$ [W·m^{-1}·K^{-1}]**	**Interval specific heat coefficient, $\bar{c}_{sl}$ ×10^{3} [J·kg^{-1}·K^{-1}]**	**Interval temperature, $\bar{T}$ [°C]**	**Interval degree of crystallisation, $\bar{\chi}$ ×10^{-8}**
During cooling				
0.0	[0.987; 1.091]	[2.651; 2.930]	[22.000; 22.000]	[0.000; 0.000]
0.1	[2.125; 2.120]	[2.611; 2.612]	[−41.007; −40.677]	[0.3976; 0.3789]
0.2	[2.582; 2.578]	[2.522; 2.523]	[−72.112; −71.873]	[6.108; 6.182]
0.4	[3.195; 3.193]	[2.383; 2.383]	[−121.158; −120.973]	[6.832; 6.932]
0.8	[3.651; 3.650]	[2.253; 2.253]	[−166.894; −66.848]	[6.832; 6.932]
1.0	[3.720; 3.720]	[2.229; 2.229]	[−175.088; −175.040	[6.832; 6.932]
During warming				
0.0	[3.6872; 4.0753]	[2.061; 2.278]	[−196.000; −196.000]	[6.832; 6.932]
0.1	[2.485; 2.496]	[2.542; 2.540]	[−65.211; −65.984]	[1.6×10^{5}; 1.3×10^{5}]
0.2	[2.442; 2.443]	[2.551; 2.550]	[−62.254; −62.270]	[5.352×10^{7}; 5.301×10^{7}]
0.4	[1.303; 1.310]	[2.750; 2.749]	[7.811; 7.427]	[7.811×10^{8}; 0.000]
0.8	[0.794; 0.794]	[2.827; 2.827]	[34.752; 34.739]	[0.000; 0.000]
1.0	[0.754; 0.754]	[2.832; 2.832]	[36.765; 36.758]	[0.000; 0.000]

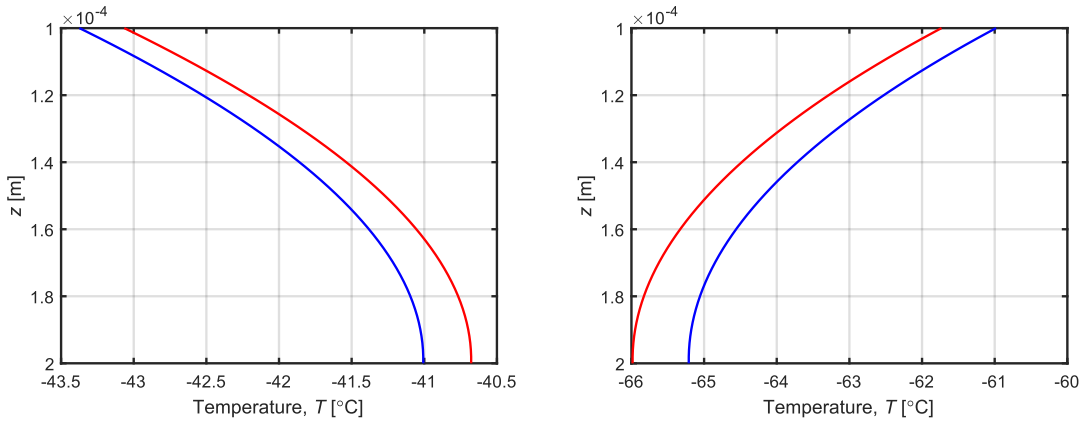

(a) (b)

Figure 5.26. Interval temperature in the cross-section of the sample at simulation time t = 0.1 s: (a) for cooling; (b) for warming

5.4.2. Example 3 – fuzzy numbers

Complementing the above example, an analysis was also carried out for the given model using triangular fuzzy numbers. Introducing fuzzy arithmetic, the heat transfer equation for a one-dimensional system is of the form (compare with Equations (5.64) and (5.65)):

$$\rho\frac{\partial\left(\tilde{c}_p\left(\tilde{T}\right)\tilde{T}\left(z,t\right)\right)}{\partial t}=\frac{\partial}{\partial z}\left(\tilde{k}\left(\tilde{T}\right)\frac{\partial\tilde{T}\left(z,t\right)}{\partial z}\right)+\rho_w L_w\frac{\partial\tilde{\chi}\left(\tilde{\chi},\tilde{T}\right)}{\partial t}, \tag{5.93}$$

where:

$$\frac{\partial\tilde{\chi}\left(\tilde{\chi},\tilde{T}\right)}{\partial t}=k_a\tilde{\chi}^{\frac{2}{3}}\left(1-\tilde{\chi}\right)\left(T_m-\tilde{T}\left(z,t\right)\right)e^{\frac{-Q_{en}}{R\tilde{T}\left(z,t\right)}}. \tag{5.94}$$

The parameters, geometry (see Figures 5.17 and 5.18) and numerical variables that are applied in this case are exactly the same as in example with interval arithmetic (Subsection 5.4.1). However, the difference is in the definition of the thermal conductivity and the specific heat for the respective layers. The polynomials determined in Equations (5.66)-(5.67) are exploited here; the triangular fuzzy numbers are inserted in place of the thermophysical parameters:

$$\begin{aligned}\tilde{c}_w\left(\tilde{T}\right) &= 2.4923\cdot 10^{-7}\tilde{T}^4 + 9.1657\cdot 10^{-5}\tilde{T}^3 + 0.0023\tilde{T}^2 \\ &\quad +1.395\tilde{T} + 677.6804, \\ \tilde{k}_w\left(\tilde{T}\right) &= 1.3496\cdot 10^{-8}\tilde{T}^5 + 1.1636\cdot 10^{-5}\tilde{T}^4 + 0.0024\tilde{T}^3 + 0.1416\tilde{T}^2 \\ &\quad -2.0261\tilde{T} + 54.3813,\end{aligned} \tag{5.95}$$

and:

$$\begin{aligned}\tilde{c}_s\left(\tilde{T}\right) &= 2.8467\tilde{T} + 2727.7, \\ \tilde{k}_s\left(\tilde{T}\right) &= \left(-2.7041\cdot 10^{-2}\tilde{T}^2 - 17.741\tilde{T} + 1442.8\right)/1000.\end{aligned} \tag{5.96}$$

The values of triangular fuzzy numbers for the above thermophysical parameters determined as: $\tilde{k} = (k - 0.05k; k;\ k + 0.05k)$ and $\tilde{c} = (c - 0.05c; c;\ c + 0.05c)$, where k and c are the deterministic value calculate in the initial moment for T^0, while in each subsequent step for the interval temperature.

Analogously, the initial-boundary conditions are defined. The interval numbers were replaced by fuzzy numbers, while the descriptions of the individual relationships (Equations (5.68)-(5.72)) remained unchanged. Therefore, it was decided to omit the rest of the mathematical formulas for fuzzy arithmetic.

In preparing the numerical model for this example, the implicit scheme of the FDM was adopted. As in the previous section, a discretisation of the time scale axis and computational domain was performed according to Equation (5.14) and the three-points star concept (see Figure 5.19).

All derivations of the relationships for calculating the interval temperatures and the interval degree of crystallisation at the individual nodes, which are shown in Equations (5.15) and (5.75)-(5.92), are also appropriate for the example with fuzzy arithmetic, where the interval numbers are replaced by fuzzy numbers. Therefore, in this part of the work only the final versions of the individual relationships will be demonstrated.

The governing equations in the internal nodes for the heat transfer are as follows:

$$\tilde{c}_p\left(\tilde{T}_i^{f-1}\right)\rho\frac{\tilde{T}_i^f - \tilde{T}_i^{f-1}}{\Delta t} = \left[\sum_{a=1}^{2}\frac{\Phi}{\tilde{R}_e^{f-1}}\left(\tilde{T}_e^f - \tilde{T}_i^f\right)\right] + \rho_w L_w\frac{\tilde{\chi}_i^f - \tilde{\chi}_i^{f-1}}{\Delta t}, \tag{5.97}$$

where i = 2, 3, …, n-1. Obviously, once the relationships for the boundary nodes have been defined, a matrix system of equations containing fuzzy numbers can be created (compare with Equation (5.87)).

Meanwhile, the fuzzy degree of crystallisation is estimated based on the Runge-Kutta algorithm, that the value at moment f+1 is:

$$\tilde{\chi}_i^{f+1} = \tilde{\chi}_i^{f} + \frac{1}{6}\Delta t\left[(\tilde{\chi}')_1 + (\tilde{\chi}')_2 + (\tilde{\chi}')_3 + (\tilde{\chi}')_4\right], \tag{5.98}$$

where the individual components of the partial derivatives $(\tilde{\chi}')_{1-4}$ are obtained as in Equation (5.92), where the interval numbers are substituted by fuzzy number.

Next, this example is computed by using the fuzzy algorithms with α-cuts (see Chapter 4). This approach makes it possible to perform calculations by omitting complex operations on sets of fuzzy numbers. It is worth noting that the model was simulated for different values of the parameter α.

The general simulation procedure in Figure 5.27 for this case is very similar to the algorithm prepared in Subsection 2.4.1 (compare with Figure 5.20). The author's programme was developed in the MATLAB R2021a environment (The MathWorks, Inc.).

Figures 5.28 and 5.29 depict the distribution of the fuzzy temperature and the fuzzy degree of crystallisation at the centre of the sample layer (point C) for different values of the parameter α. It can be observed that the width of intervals changes depending on the value of the parameter α, while for α = 0 deterministic results are obtained.

Figures 5.30 and 5.31 present the history of the interval temperature and the interval degree of crystallisation for chosen values of the parameter α. It can be see that the width of the intervals depends on the value of the parameter α – the intervals for α = 0.75 are narrower than for α = 0.25. These differences are mainly visible for interval temperatures.

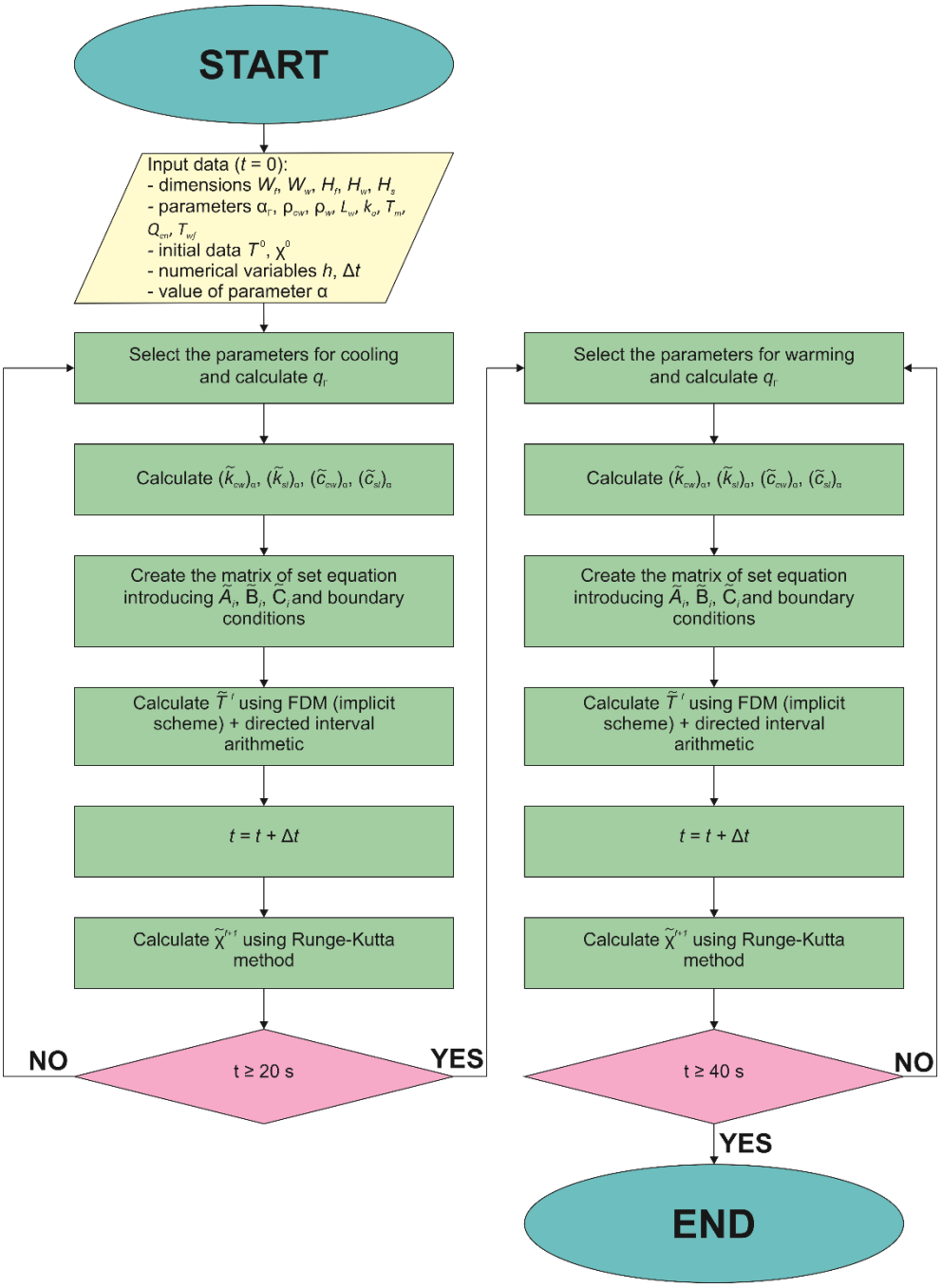

Figure 5.27. Flowchart of algorithm to simulate heat transfer phenomena including crystallisation (fuzzy arithmetic)

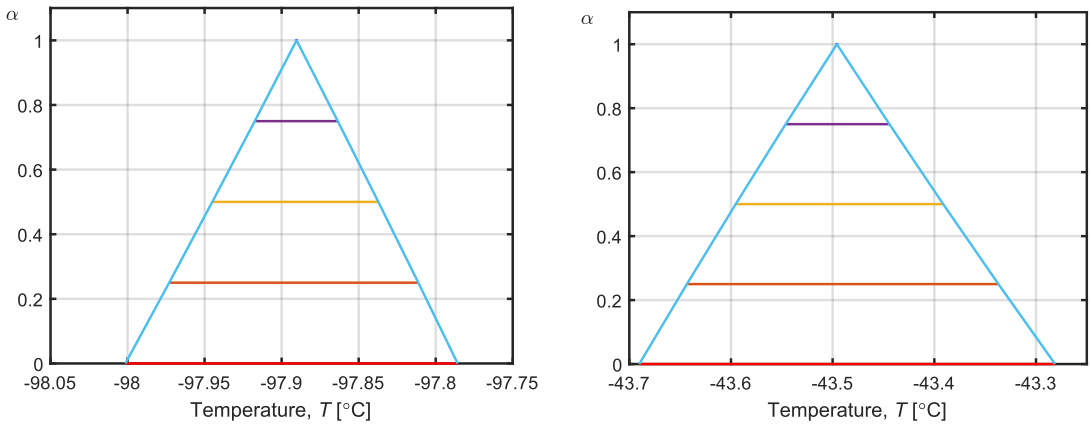

(a) (b)

Figure 5.28. Interval temperature after 0.3 s for different values of parameter α (triangular fuzzy numbers) for: (a) cooling; (b) warming

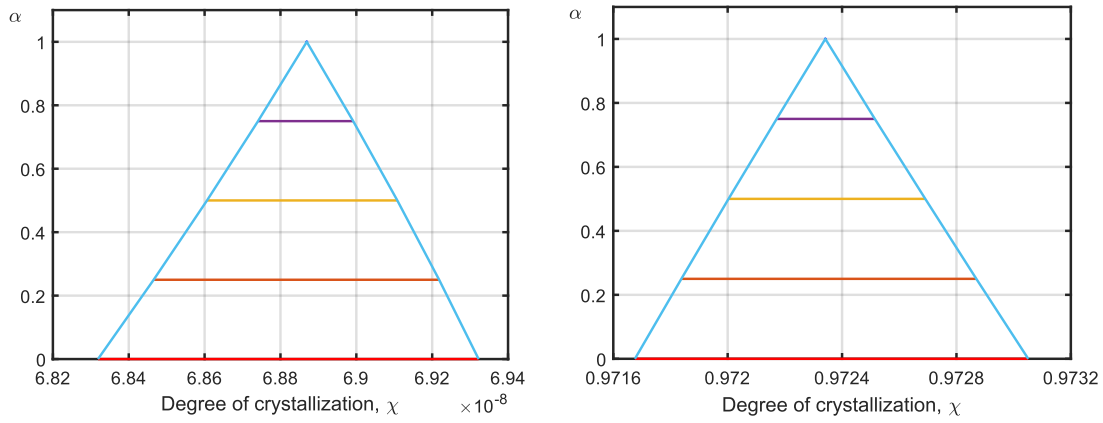

(a) (b)

Figure 5.29. Interval degree of crystallisation after 0.3 s for different values of parameter α (triangular fuzzy numbers) for: (a) cooling; (b) warming

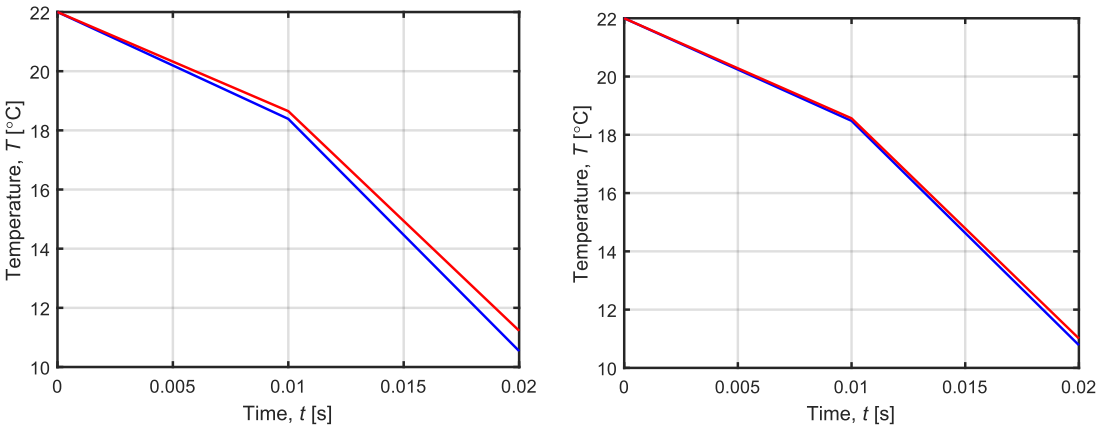

(a) (b)

Figure 5.30. Interval temperature as a function of time during cooling for: (a) α = 0.25; (b) α=0.75

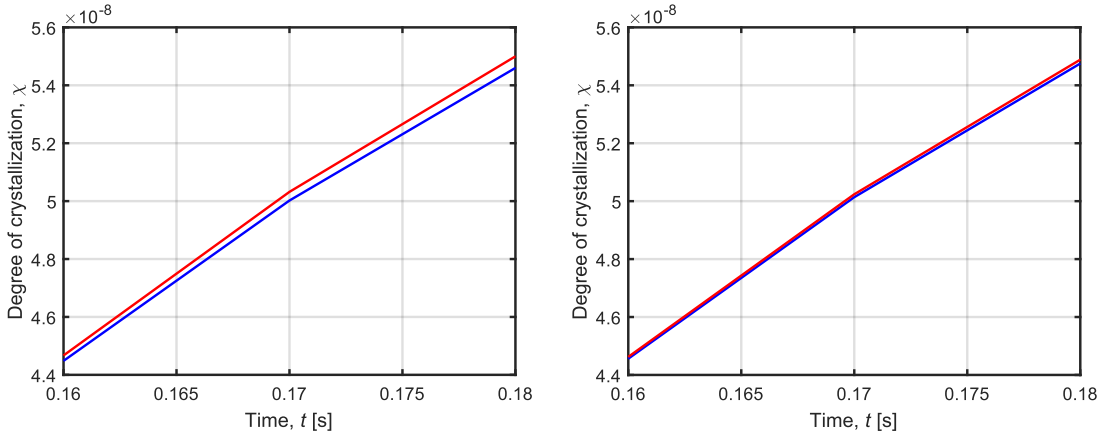

(a) (b)

Figure 5.31. Interval degree of crystallisation as a function of time during cooling for: (a) α = 0.25; (b) α = 0.75

5.4.3. Summary and conclusions

To summarise Example 3, it can be said that thermal processes are investigated including the phenomenon of crystallisation. In the study, the thermophysical parameters are in the form of characteristics described by polynomial functions. The data used to create these relationships are taken from the experiment, which provides an additional argument for the use of interval and fuzzy arithmetic.

Our results are collated with data from a simulation conducted by Zhou et al. [196]. First of all, it can be concluded that the temperature distributions in the centre of the sample layer (point C) are similar in both cases. There is little difference in the warming curve, because in our case the temperature decrease is higher and more noticeable than in Zhou et al. [196]. This may mean that in our calculations the impact of recrystallisation is higher. Furthermore, the temperature reaches equilibrium in the whole domain after a relatively short period of time (14.1 s for cooling and 7.15 s for warming). This confirms that the main vitrification assumption of high cooling rate is fulfilled.

On the other hand, comparing our graphs of the degree of crystallisation as a function of time with the curves presented by Zhou et al. [196], one can also deduce that they coincide to each other. Nevertheless, it can be noted a difference in the magnitude that occurs on the diagrams during the warming process (in paper of Zhou et al. [196] the scale is lower).

The time required for the DTR transition is also noteworthy. In our case, it seems to be very short compared to the entire process of stabilisation (these time is equal to 0.20 s and 0.26 s for cooling and warming, respectively). However, the obtained values are higher than those reported by Zhou et al. [196] (the time in paper of Zhou et al. [196] is equal to 0.042 s and 0.057 s for cooling and warming, respectively). Therefore, in further work, the geometry of the device can be improved and the process parameters can be modified to reduce the time in the DTR.

When analysing the degree of crystallisation, it is also interesting to consider it as an indicator of damage to biological material. The literature provides methods for finding a criterion for the total volume of the crystallised fraction [64]. In our research, the degree of crystallisation is assumed to be lower than 10^{-6} [11, 140, 196]. A similar criterion was set in the work of Zhou et al. where the maximum degree of crystallisation is $2 \cdot 10^{-11}$ and $2.4 \cdot 10^{-3}$ for cooling and warming, respectively.

The indicated criterion is also confronted with the maximum average values of the interval (fuzzy) degree of crystallisation in our case. It can be deduced that during cooling, the risk of damage of biological structure is negligible. The situation is slightly different during warming. The maximum average value of the interval (fuzzy) degree of crystallisation is greater than the given criterion. This is the effect of recrystallisation, which disappears after passing the DTR; it can therefore be assumed that no damage of the sample occurs.

Finally, it is reasonable to compare the results obtained for interval and fuzzy numbers. It can be seen that the received ranges coincide with each other. In addition, fuzzy arithmetic enables the width of the intervals to be adjusted by an appropriate choice of the parameter α. Although both techniques are suitable for carrying out calculations of problems with imprecisely defined variables.

Example 3 provides a kind of introduction to further research into the phenomenon of crystallisation. Determining the degree of crystallisation, it is possible to assess whether the biological material would be damaged by the formation of ice crystals.

The extended model of heat transfer including crystallisation phenomena should include examination of the value of activation energy and also information about ice nucleation by investigating the nucleation rate and ice crystal growth (measured by changing the radius of the ice crystals). As a result, the maximum volume of crystallised ice can be estimated. In addition, the presence of CPA impacts the water content of the cells through osmotic transport, as well as the processes of nucleation and further

growth. Therefore, the mass transfer model taking osmotic transport into account should be included in the mathematical description of cryopreservation. The changes in cell volume thus detected provide an additional marker of damage to the biological sample. Examples of such an expanded model can be found in the literature in [50, 64]. Obviously, the listed examples from literature are presented for a deterministic model, hence in the future they would additionally require the introduction of interval or fuzzy numbers.

6. Numerical examples: mass transfer

6.1. Introduction

The heat transfer mentioned in Chapter 5 is not the only transport phenomenon to be considered in simulating cryopreservation. During the process, there is also mass transfer induced by molecular diffusion, as well as osmotic transport describing cellular behaviour.

In the beginning, it is worth adding that mass transfer is related to the infiltration of moles of CPA into the sample structure. The CPA is presented in the bath solution and can be distributed in different ways. When the sample is placed in the test tube and immersed in the solution, diffusion is predominant and advection is negligible. In this situation, the mass transfer equation is based on the Fick's second law.

On the other hand, cryopreservation is increasingly being performed using more complex apparatus, such as microfluidic systems, in which CPA is continuously delivered via microchannels to a sample placed in a microchamber. The moving fluid induces an advection process that affects the transport of CPA particles into the sample structures. For this reason, both advection and diffusion phenomena must be taken into account when modelling mass transfer. One component of the advection-diffusion equation is the velocity vector of the moving fluid, which is determined using the Navier-Stokes equations.

The quantity determined from the mass transfer equation is the molar concentration in the extracellular matrix. Changes in the extracellular solution contribute to the phenomenon of osmotic transport, because the presence of CPA disrupts the osmotic balance between the intracellular solution and the extracellular matrix. To restore the osmotic balance, an exchange of water, CPA, and other solution components proceeds across the cell membrane. This phenomenon is described by the 2-P formalism or the Kedem-Katchalsky model.

In the following section, three examples are explored. Example 1 analyses the mass transfer defined by the Fick's second law for the instance, which is a continuation of

Example 1 from Chapter 5. Example 2, on the other hand, is a supplement to Example 1 with an osmotic transport model. Meanwhile, Example 3 provides a comprehensive model introducing the phenomena of heat and mass transfer, fluid (bath solution) flow, and osmotic transport for a cryopreservation problem using a microfluidic system. All computations have been performed using directed interval and fuzzy arithmetic.

6.2. Example 1: Mass transfer – diffusion phenomena

It should be mentioned at the beginning that this example is a continuation of Example 1 in Chapter 5. This example presents a mass transfer model for the sample that is an articular cartilage disk. For experimental research, such samples are prepared from the knee joint of animals, for example, lambs [116, 178].

Example 1 of the previous chapter assumes that the simulation presented models the LT protocol. The LT protocol is divided into several steps in the cooling phase and in the warming phase. When considering mass transfer, it is worth examining in more detail the device system used to control temperature and concentration. In our case, the device invented by Wang et al. [178] was applied. Figure 6.1 illustrates the diagram of the apparatus for performing cryopreservation by the LT method. The idea is to place the sample in a tube filled with a solution that is regularly replaced depending on the desired concentration of CPA. The whole is installed in a temperature-controlled chamber. It should be noted that the sample is immersed in the bath solution, therefore convection is neglected and $\mathbf{u} = 0$ is assumed.

Let us introduce some information about the composition of the bath solution. The basis of the solution is CPTes2, which was proposed by Taylor and Hunt [171] and modified by Pegg et al. [116]. The CPTes2 solution contains DMSO as the CPA with different concentrations depending on given steps of the process. The other components of CPTes2 are water and KCl, which makes the bath solution a potassium-rich mixture [178].

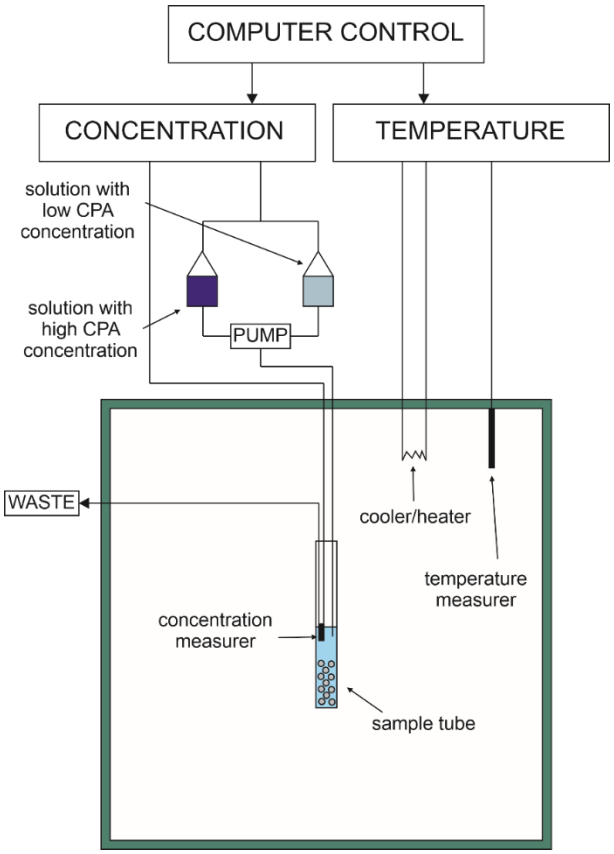

Figure 6.1. System for performing cryopreservation by LT protocol

Analysing the mass transfer without considering convection (**u** = 0), the governing equation is defined as follows [21]:

$$\dot{c} = \nabla\left(D\nabla c\right). \tag{6.1}$$

Obviously, this is a mass transfer equation describing molecular diffusion based on Fick's second law. In addition [79, 100, 177]:

$$D = \frac{k_B T}{6\pi r_s \mu}, \tag{6.2}$$

where the temperature T is in K.

As in the case of thermal phenomena, unambiguity conditions must also be formulated. When preparing a mathematical model of the unsteady state, the geometry of the domain considered, the biomaterial parameters, and initial-boundary conditions need to be defined. The initial condition determines the molar concentration at the starting moment [21]:

$$c(X,0) = c^0, \tag{6.3}$$

where c^0 is the initial molar concentrations for $t = 0$.

Next, the following boundary conditions are defined. The mass diffusion equation is comparable to the heat transfer equation, therefore the boundary conditions are also determined in a similar way. To calculate the concentration distribution, mainly two boundary conditions are used, which determine the concentration in a given domain (1st type) and the mass flux (2nd type) [21].

The boundary condition of the 1st type (Dirichlet) specifies the molar concentration at a given edge [21]:

$$c\left(X,t\right)=c_{\Gamma}, \tag{6.4}$$

where c_Γ is the molar concentration at the boundary.

The boundary condition of the 2nd type (Neumann) concerns the mass flux [21]:

$$q_{\Gamma}\left(X,t\right)=-\mathbf{n}D\cdot\nabla c \tag{6.5}$$

where q_Γ is the given mass flux.

As this instance is a continuation of Example 1 from Chapter 5, therefore, all mathematical operations are performed on the basis of the rules of directed interval and fuzzy arithmetic. It is worth noting that this is a novel approach to mass transfer analysis. Previous publications including the study of molecular diffusion, have mainly used a deterministic model [8, 104, 132, 147, 148, 150, 153, 187, 189].

6.2.1. Example 1 – interval numbers

In this example, calculations for directed interval arithmetic will be presented first. In the mass transfer equation (Equation (6.1)), takes into account the interval diffusion coefficient, which is weakly coupled to the temperature obtained in the form of intervals. Consequently:

$$\frac{\partial\overline{c}_d^e\left(X,t\right)}{\partial t}=\nabla\left[\bar{D}\left(\bar{T}\right)\nabla\overline{c}_d^e\left(X,t\right)\right], \tag{6.6}$$

and:

$$\bar{D}\left(\bar{T}\right)=\frac{k_B\bar{T}\left(X,t\right)}{6\pi r_s\mu}, \tag{6.7}$$

where the superscript *e* denotes the extracellular matrix and the subscript *d* represents DMSO as CPA. The division into extra- and intracellular regions in this section is crucial in the context of multiscale analysis. As mentioned in Chapter 5 (Section 5.2), articular

cartilage tissue consists mainly of collagen and extracellular matrix (proteoglycans) with chondrocytes (intracellular region). From Equation (6.6), the concentration in the extracellular matrix can be determined, where mass diffusion is caused by changes in concentration in the surrounding medium.

As the sample under analysis is cylindrical in shape (see Figure 5.1), the following coordinate system is adopted:

$$\frac{\partial \bar{c}_d^e\left(r,z,t\right)}{\partial t}=\frac{1}{r}\frac{\partial}{\partial r}\left(\bar{D}\left(\bar{T}\right)r\frac{\partial \bar{c}_d^e(r,z,t)}{\partial r}\right)+\frac{\partial}{\partial z}\left(\bar{D}\left(\bar{T}\right)\frac{\partial \bar{c}_d^e(r,z,t)}{\partial z}\right). \tag{6.8}$$

When considering unambiguity conditions, it is first necessary to introduce the boundary conditions determined by the LT protocol invented by Pegg et al. [116]. Information about controlling the temperature in the chamber is shown in Table 5.1, while the mass fraction (concentration) of the bath solution is specified in Table 6.1. It is important to note that the concentration of DMSO in the CPTes2 solution is expressed as a mass fraction, which describes the mass percentage ratio of the substrate to the mixture. Knowing the mass fraction, the molar concentration is determined using the following relationship:

$$c_i=\frac{w_i\rho}{M_{at.,i}}, \tag{6.9}$$

where the subscript *i* denotes the given component and w_i is the mass fraction, $M_{at.,i}$ is the molar mass related to the molecular mass M_u ($M_{at.,i} \approx M_u \cdot 1$ g·mol^{-1}), ρ is the density of the solution determined according to the rule of mixtures.

The geometry of the system and the dimensions of the considered domain remain unchanged from Example 1 in Chapter 5 (see Figure 5.1). As the marked area (Ω) is axisymmetric, an adiabatic condition is given on the boundaries Γ_2 and Γ_3:

$$\bar{q}_\Gamma\left(r,z,t\right)=-\mathbf{n}\cdot\bar{D}\left(\bar{T}\right)\nabla\bar{c}_d^e=\bar{0}. \tag{6.10}$$

On the other hand, at the boundaries Γ_1 and Γ_4, unlike in the case of thermal analysis, a boundary condition of 1st type is fixed:

$$\bar{c}_d^e\left(r,z,t\right)=0.9\bar{c}_\Gamma, \tag{6.11}$$

where the interval molar concentration $\bar{c}_\Gamma$ calculated from mass fraction w_{bath} provided by LT protocol and the coefficient of 0.9 reflect the real exchange phenomenon between the external solution and the sample.

Table 6.1. LT protocol according to Pegg et al. [116, 187]

Phase	Step	Time, t [min]	Mass fraction (concentration) of bath solution, w_{bath} [% (w/w)]
Cooling	1	10	10
	2	10	20
	3	30	29
	4	30	38
	5	30	47
	6	30	56
	7	30	63
	8	30	72
Warming	1	30	63
	2	30	56
	3	30	47
	4	30	38
	5	30	29
	6	30	20
	7	45	0

When preparing the mathematical model, the initial condition should also be given: $\bar{c}^{e,0} = 0$ mol·m^{-3} [153]. Other parameters required for further calculations are the constants needed to determine the diffusion coefficient, namely the radius of the spherical particle $r_s = 2.541 \cdot 10^{-10}$ m [145] and the dynamic viscosity $\mu = 1.996 \cdot 10^{-3}$ Pa·s [208]. It is also useful to know the quantities such as: the density of DMSO $\rho_d = 1.1$ kg·m^{-3}, the density of water $\rho_w = 997$ kg·m^{-3} and the molar mass of DMSO $M_{at.,d} = 78.13\ 10^{-3}$ kg·m^{-3} [208].

The next step is to develop a numerical model using an explicit scheme of FDM. The mass transfer is an unsteady problem, therefore the time grid has to be discretised similarly to the heat transfer problem (compare with Equation (5.14)):

$$t^0 < t^1 < \ldots < t^{f-2} < t^{f-1} < t^f < \ldots < t^F < \infty, \tag{6.12}$$

where $\Delta t = t^{f+1} - t^f$ is a constant time step.

As in the previous chapter, the domain considered has been divided using a regular grid. The nodes that store the temperature values coincide with the nodes for the molar concentration. The mesh is constructed based on the five-points star already used in Example 1 in Chapter 5 (see Figure 5.2).

Then, relationships for calculating the interval molar concentration at the individual nodes have been established. In the mass flow equation on the left-hand side, the time derivative takes the form of:

$$\left(\frac{\partial \overline{c}_d^e\left(r,z,t\right)}{\partial t}\right)_{i,j}^{f} = \frac{\left(\overline{c}_d^e\right)_{i,j}^{f} - \left(\overline{c}_d^e\right)_{i,j}^{f-1}}{\Delta t}, \tag{6.13}$$

where $i = 1, 2, \ldots, n$ and $j = 1, 2, \ldots, m$; n and m are the number of nodes.

Mean quotients are applied to determine the interval molar concentration at the internal nodes (i, j):

$$\begin{aligned}\left[\bar{D}\left(\overline{T}\right)\nabla^2\overline{c}_d^e\left(r,z,t\right)\right]_{i,j}^{f-1} = \frac{1}{r_{i,j}}\frac{1}{h_1}\Bigg[\bar{D}\left(\overline{T}_{i,j+0.5}^{\,f}\right)r_{i,j+0.5}\left(\frac{\partial \overline{c}_d^e}{\partial r}\right)_{i,j+0.5}^{f-1} \\ -\bar{D}\left(\overline{T}_{i,j-0.5}^{\,f}\right)r_{i,j-0.5}\left(\frac{\partial \overline{c}_d^e}{\partial r}\right)_{i,j-0.5}^{f-1}\Bigg] + \frac{1}{h_2}\Bigg[\bar{D}\left(\overline{T}_{i+0.5,j}^{\,f}\right)\left(\frac{\partial \overline{c}_d^e}{\partial z}\right)_{i+0.5,j}^{f-1} \\ -\bar{D}\left(\overline{T}_{i-0.5,j}^{\,f}\right)\left(\frac{\partial \overline{c}_d^e}{\partial z}\right)_{i-0.5,j}^{f-1}\Bigg],\end{aligned} \tag{6.14}$$

where $i = 2, 3, \ldots, n-1$ and $j = 2, 3, \ldots, m-1$.

Detailing exactly the individual elements of the above equation:

$$\begin{aligned}
&1.\quad \bar{D}\left(\overline{T}_{i,j+0.5}^{\,f}\right)r_{i,j+0.5}\left(\frac{\partial \overline{c}_d^e}{\partial r}\right)_{i,j+0.5}^{f-1} = \left(r_{i,j}+\frac{1}{2}h_1\right)\frac{\left(\overline{c}_d^e\right)_{i,j+1}^{f-1} - \left(\overline{c}_d^e\right)_{i,j}^{f-1}}{\overline{W}_{i,j+1}^{\,f-1}},\\
&2.\quad \bar{D}\left(\overline{T}_{i,j-0.5}^{\,f}\right)r_{i,j-0.5}\left(\frac{\partial \overline{c}_d^e}{\partial r}\right)_{i,j-0.5}^{f-1} = \left(r_{i,j}-\frac{1}{2}h_1\right)\frac{\left(\overline{c}_d^e\right)_{i,j}^{f-1} - \left(\overline{c}_d^e\right)_{i,j-1}^{f-1}}{\overline{W}_{i,j-1}^{\,f-1}},\\
&3.\quad \bar{D}\left(\overline{T}_{i+0.5,j}^{\,f}\right)\left(\frac{\partial \overline{c}_d^e}{\partial z}\right)_{i+0.5,j}^{f-1} = \frac{\left(\overline{c}_d^e\right)_{i+1,j}^{f-1} - \left(\overline{c}_d^e\right)_{i,j}^{f-1}}{\overline{W}_{i+1,j}^{\,f-1}},\\
&4.\quad \bar{D}\left(\overline{T}_{i-0.5,j}^{\,f}\right)\left(\frac{\partial \overline{c}_d^e}{\partial z}\right)_{i-0.5,j}^{f-1} = \frac{\left(\overline{c}_d^e\right)_{i,j}^{f-1} - \left(\overline{c}_d^e\right)_{i-1,j}^{f-1}}{\overline{W}_{i-1,j}^{\,f-1}},
\end{aligned} \tag{6.15}$$

while $\bar{W}_e$ are the interval mass diffusion resistances formulated as:

$$\begin{cases} \bar{W}_e^{f-1} = \dfrac{h_1}{2\bar{D}\left(\bar{T}_{i,j}^{f}\right)} + \dfrac{h_1}{2\bar{D}\left(\bar{T}_e^{f}\right)}, & \text{if } e = \left\{(i, j+1) \text{ or } (i, j-1)\right\}, \\ \bar{W}_e^{f-1} = \dfrac{h_2}{2\bar{D}\left(\bar{T}_{i,j}^{f}\right)} + \dfrac{h_2}{2\bar{D}\left(\bar{T}_e^{f}\right)}, & \text{if } e = \left\{(i+1, j) \text{ or } (i-1, j)\right\}. \end{cases} \tag{6.16}$$

Based on Equation (6.8) and the above derivation, the interval molar concentration at the internal nodes (i, j) is calculated:

$$\frac{\left(\bar{c}_d^e\right)_{i,j}^{f} - \left(\bar{c}_d^e\right)_{i,j}^{f-1}}{\Delta t} = \sum_{a=1}^{4} \frac{\Phi_e}{\bar{W}_e^{f-1}} \left(\left(\bar{c}_d^e\right)_e^{f-1} - \left(\bar{c}_d^e\right)_{i,j}^{f-1} \right), \tag{6.17}$$

and as a result:

$$\left(\bar{c}_d^e\right)_{i,j}^{f} = \left(\bar{c}_d^e\right)_{i,j}^{f-1} + \Delta t \sum_{a=1}^{4} \frac{\Phi_e}{\bar{W}_e^{f-1}} \left[\left(\bar{c}_d^e\right)_e^{f-1} - \left(\bar{c}_d^e\right)_{i,j}^{f-1} \right], \tag{6.18}$$

where $i = 2, 3, \ldots, n-1$ and $j = 2, 3, \ldots, m-1$, the individual a corresponds to $e = \{(i, j+1); (i, j-1); (i+1, j); (i-1, j)\}$, while Φ_e is the shape function defined in the same way as in thermal analysis:

$$\begin{cases} \Phi_e = \dfrac{1}{h_1}\left(1 - \dfrac{h_1}{2r_{i,j}}\right), & \text{if } e = (i, j-1), \\ \Phi_e = \dfrac{1}{h_1}\left(1 + \dfrac{h_1}{2r_{i,j}}\right), & \text{if } e = (i, j+1), \\ \Phi_e = \dfrac{1}{h_2}, & \text{if } e = \left\{(i+1, j) \text{ or } (i-1, j)\right\}. \end{cases} \tag{6.19}$$

The following stability condition needs to be defined for an explicit scheme of FDM:

$$1 - \Delta t \sum_{a=1}^{4} \frac{\Phi_e}{\bar{W}_e^{f-1}} \geq 0, \tag{6.20}$$

and after the conversion the time step is:

$$\Delta t \leq \sum_{a=1}^{4} \frac{\bar{W}_e^{f-1}}{\Phi_e}, \tag{6.21}$$

Let us also introduce information about boundary nodes. Considering the boundaries with condition of the 1st type (Γ_1 and Γ_4 – see on Figure 5.1), the relationships are as follows:

$$\begin{cases} \left(\overline{c}_d^e\right)_{i,m}^f = 0.9c_\Gamma, & \text{for } \Gamma_1, \\ \left(\overline{c}_d^e\right)_{1,j}^f = 0.9c_\Gamma, & \text{for } \Gamma_4, \end{cases} \tag{6.22}$$

where $i = 2, 3, \ldots, n-1$ and $j = 2, 3, \ldots, m-1$.

The interval molar concentration for boundary nodes with an adiabatic condition consists of replacing one of the "element" in Equation (6.14) with the relationship received from Equation (6.10). For the boundary Γ_2 (see Figure 5.1), it is expressed as:

$$\left(\overline{c}_d^e\right)_{i,1}^f = \left(\overline{c}_d^e\right)_{i,1}^{f-1} + \Delta t\left[\left(\sum_{a=1}^{3}\frac{\Phi_e}{\overline{W}_e^{f-1}}\left(\left(\overline{c}_d^e\right)_e^{f-1} - \left(\overline{c}_d^e\right)_{i,1}^{f-1}\right)\right) + \overline{q}_\Gamma\Phi_{i,j-1}\right] \tag{6.23}$$

where $i = 2, 3, \ldots, n-1$ and individual a corresponds to $e = \{(i, j+1); (i+1, j); (i-1, j)\}$.

For the edge Γ_3, the boundary condition it of the form:

$$\left(\overline{c}_d^e\right)_{n,j}^f = \left(\overline{c}_d^e\right)_{n,j}^{f-1} + \Delta t\left[\left(\sum_{a=1}^{3}\frac{\Phi_e}{\overline{W}_e^{f-1}}\left(\left(\overline{c}_d^e\right)_e^{f-1} - \left(\overline{c}_d^e\right)_{n,j}^{f-1}\right)\right) + \overline{q}_\Gamma\Phi_{i+1,j}\right] \tag{6.24}$$

where $j = 2, 3, \ldots, m-1$ and individual a corresponds to $e = \{(i, j+1); (i, j-1); (i-1, j)\}$.

To conclude the description of the numerical model, it is worth recalling its parameters, which coincide with those specified for the time-space mesh for heat transfer. They are equal to: the time step $\Delta t = 10^{-3}$ s, the mesh steps $h_1 = 10^{-4}$ m and $h_2 = 5\cdot10^{-5}$ m.

The above mathematical and numerical model was implemented in an author's program prepared in Embarcadero Delphi 10.4 Community Edition environment software (Embarcadero Technologies, Inc.). A flowchart compactly representing the algorithm is shown in Figure 6.2.

The following section presents the results obtained during the mass transfer investigation applying directed interval arithmetic – see Figures 6.3-6.5. Please note that all results for the interval molar concentration have been converted to the interval mass fraction. This makes it easier to compare the received values with the mass fraction of the bath solution.

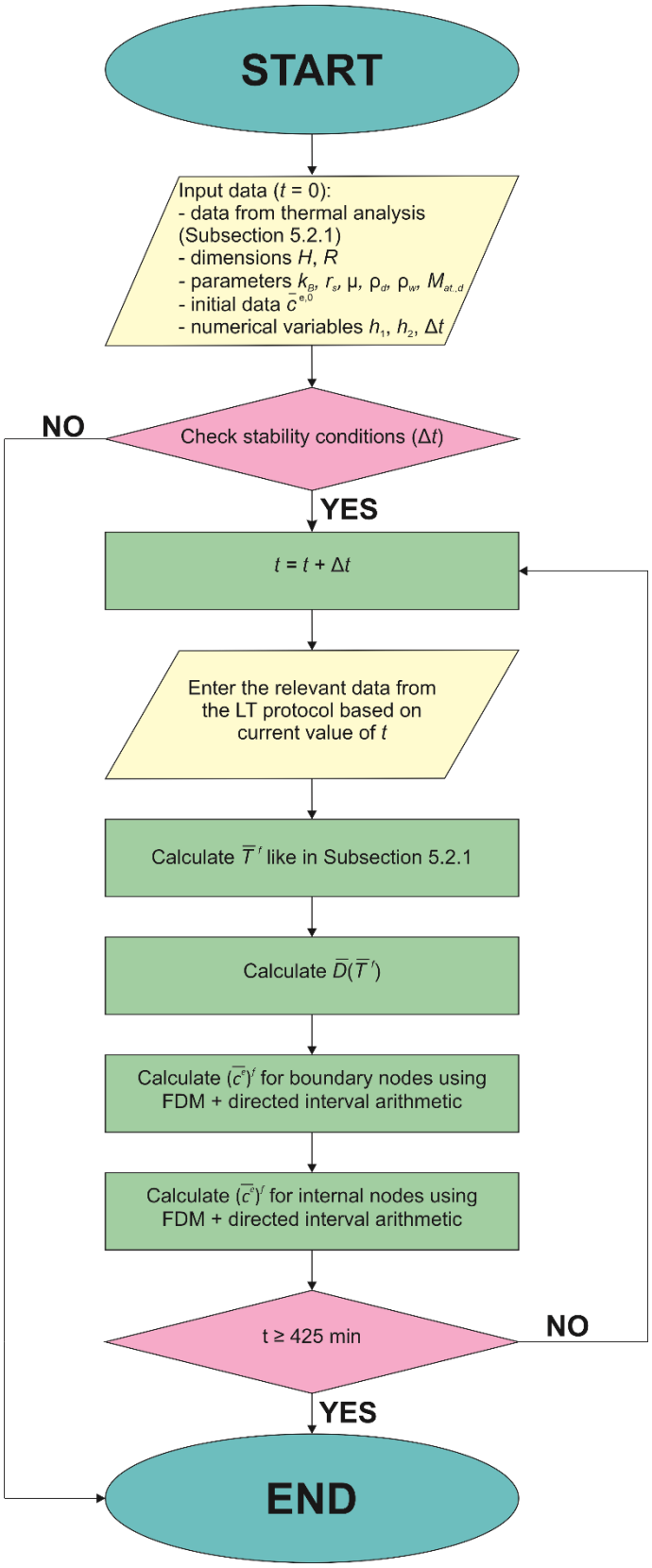

Figure 6.2. Flowchart of algorithm to simulate mass (diffusion) transfer phenomena (interval arithmetic)

Figure 6.3 represents the history of the interval mass fraction over the complete simulation time at the point with coordinates r = 0.050 mm and z = 0.475 mm. It can be seen that in the first few iterations of a given step, the concentration rises rapidly, but then it gradually stabilises. The interval mass fraction in the sample never reaches the value desired by the bath solution. It can be observed that the results obtained are close to the mass fraction multiplied by a factor of 0.9 determined by the boundary conditions.

Table 6.2 contains the exact values obtained at the end of each process step at the given point. These results were also compared with the experimental data reported by Pegg et al. [116] and the simulation results received by Yu et al. [187]. The relative error, which varies for each step, was also calculated. It can be said that the simulation results from Yu et al. [187] are more compatible with experimental data [116].

As the interval widths are narrow, Figure 6.4 only illustrates a certain fragment of the entire simulation in a few seconds of step 8 for the cooling phase (a) and the first few seconds of step 1 for the warming phase (b). The solid and the dashed line represent the history for points with coordinates r = 0.050 mm, z = 0.475 mm and r = 2.950 mm, z = 0.125 mm, respectively.

Figure 6.5 presents the distribution of the interval mass fraction (in % (w/w)) in 10 s of step 8 for the cooling phase. It confirms that the domain is axisymmetric. Unfortunately, the interval widths are so small that it is difficult to see the difference between the upper and lower bounds of intervals on the distribution maps.

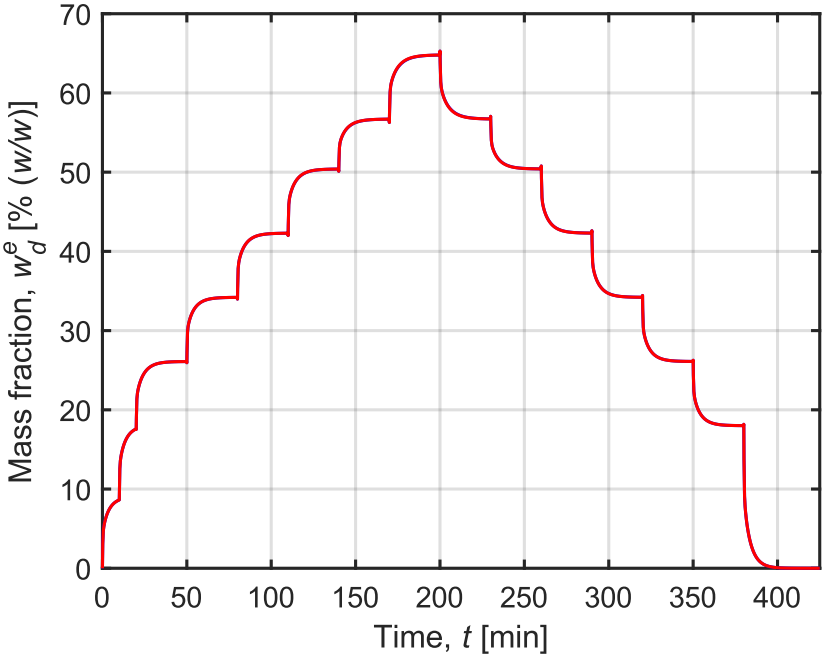

Figure 6.3. Interval mass fraction over whole simulation time

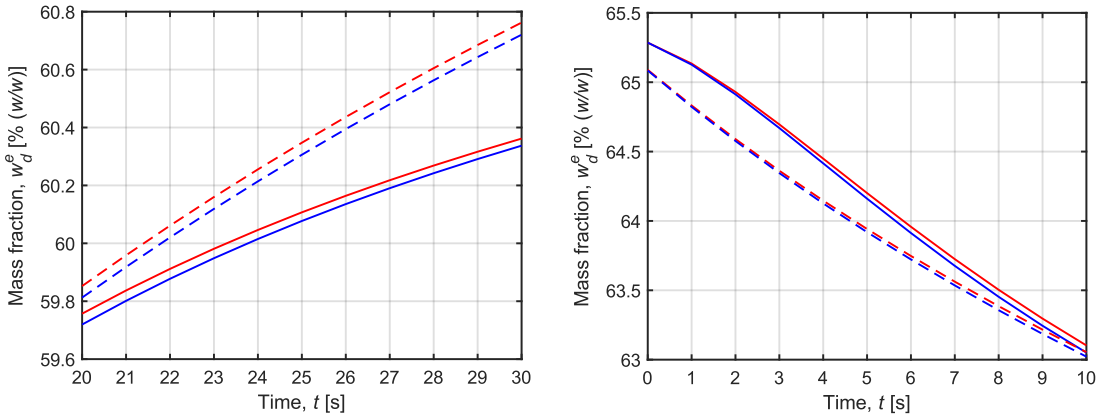

(a) (b)

Figure 6.4. Interval mass fraction as a function of time for: (a) step 8 in cooling phase and (b) step 1 in warming phase

Table 6.2. Comparison of interval mass fraction with experimental data [116] and simulation data [187]

Phase	**Step**	**Interval mass fraction, $\bar{w}_d^e$ [% (w/w)]**	**Experimental data**	**Relative error, δ [%]**	**Simulation data, w [% (w/w)]**
Cooling	1	[8.6281; 8.6281]	–	–	8.04
	2	[17.5895; 17.5895]	16.3 ± 1.3	7.91	16.97
	3	[26.0937; 26.0938]	24.5 ± 1.1	6.50	25.87
	4	[34.1936; 34.1938]	34.2 ± 0.9	0.02	33.86
	5	[42.2921; 42.2927]	41.7 ± 3.3	1.42	41.10
	6	[50.3905; 50.3913]	47.8 ± 2.8	5.42	48.03
	7	[56.6897; 56.6911]	52.2 ± 1.3	8.60	52.52
	8	[64.7810; 64.7844]	55.9 ± 2.9	15.89	55.85
Warming	1	[56.7191; 56.7156]	–	–	54.78
	2	[50.4104; 50.4090]	–	–	51.98
	3	[42.3096; 42.3087]	–	–	44.62
	4	[34.2079; 34.2087]	–	–	35.83
	5	[26.1064; 26.1062]	–	–	26.75
	6	[18.0058; 18.0057]	–	–	18.18
	7	[0.0002; 0.0002]	–	–	0.01

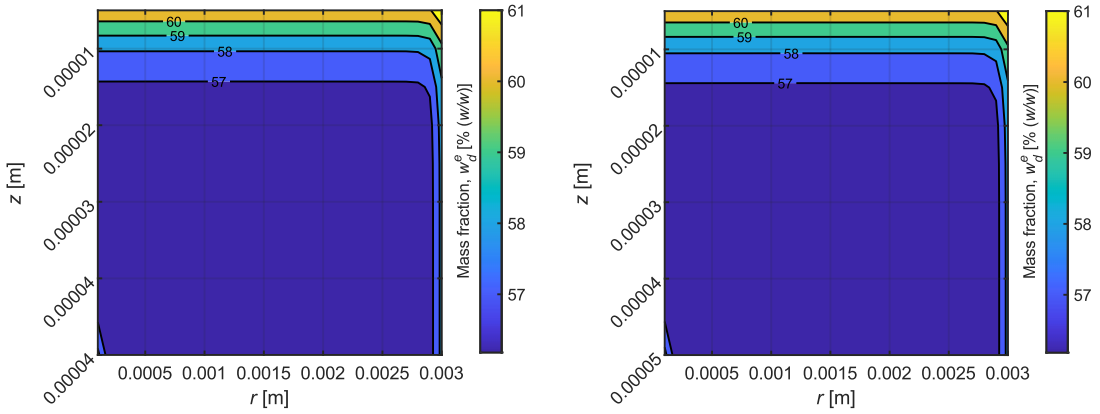

(a) (b)

Figure 6.5. Distribution of the interval mass fraction in 10 s of step 8 for cooling phase: (a) $\overline{w}_d^{e-}$ and (b) $\overline{w}_d^{e+}$

6.2.2. Example 1 – fuzzy numbers

After presenting the mathematical and numerical model and example calculations for interval numbers, the discussions conducted for fuzzy numbers will be demonstrated. Obviously, this is still a continuation of Example 1 from Chapter 5 (Subsection 5.2.2).

The mass transfer equation for fuzzy arithmetic for this example is formulated in the following form:

$$\frac{\partial \tilde{c}_d^e(r,z,t)}{\partial t} = \frac{1}{r}\frac{\partial}{\partial r}\left(\tilde{D}\left(\tilde{T}\right) r \frac{\partial \tilde{c}_d^e(r,z,t)}{\partial r}\right) + \frac{\partial}{\partial z}\left(\tilde{D}\left(\tilde{T}\right)\frac{\partial \tilde{c}_d^e(r,z,t)}{\partial z}\right), \tag{6.25}$$

where:

$$\tilde{D}\left(\tilde{T}\right) = \frac{k_B \tilde{T}(r,z,t)}{6\pi r_s \mu}. \tag{6.26}$$

The previously specified boundary conditions remain unchanged, therefore:

$$\begin{cases} \tilde{c}_d^e(r,z,t) = 0.9\tilde{c}_\Gamma, & \text{for } \Gamma_1 \text{ and } \Gamma_4, \\ \tilde{q}_\Gamma(r,z,t) = -\mathbf{n}\cdot\tilde{D}\left(\tilde{T}\right)\nabla\tilde{c}_d^e = \tilde{0}, & \text{for } \Gamma_2 \text{ and } \Gamma_3. \end{cases} \tag{6.27}$$

It is very important to note that calculations for fuzzy numbers have been performed for the LT protocol improved by Yu et al. [187] This protocol neglects the last step for cooling and the first step for warming of the Pegg et al. protocol [116], while modifying the exposure times of the sample to the bath solution with specific parameters.

Detailed procedures for mass fraction regulation are provided in Table 6.3. It should be noted the initial condition is as follows: $\tilde{c}^{e,0} = 0$ mol·m^{-3}.

All parameters completing the mathematical model are the same as in Example 1 in Chapter 5 (Subsection 5.2.2), including volumetric specific heat and thermal conductivity defined as triangular and trapezoidal fuzzy numbers, respectively (see Table 5.4). Whereas the parameters directly related to the CPA are the same as those listed in the previous example considering interval analysis.

Table 6.3. LT protocol proposed by Yu et al. [187]

Phase	**Step**	**Time, *t* [min]**	**Mass fraction of bath solution, w_{bath} [% (*w*/*w*)]**
Cooling	1	10	10
	2	9.8	20
	3	18.2	29
	4	25	38
	5	19.8	47
	6	26.4	56
	7	23.8	63
Warming	1	23.8	63
	2	26.4	56
	3	19.8	47
	4	25	38
	5	18.2	29
	6	29.8	20

In the next part, the numerical model is derived using explicit scheme of FDM. The mass transfer Equation (6.25) in fuzzy form can be expressed as follows:

$$\left(\tilde{c}_d^e\right)_{i,j}^{f} = \left(\tilde{c}_d^e\right)_{i,j}^{f-1} + \Delta t \sum_{a=1}^{4} \frac{\Phi_e}{\tilde{W}_e^{f-1}} \left[\left(\tilde{c}_d^e\right)_e^{f-1} - \left(\tilde{c}_d^e\right)_{i,j}^{f-1} \right], \tag{6.28}$$

where $i = 2, 3, \ldots, n-1$ and $j = 2, 3, \ldots, m-1$, the individual a corresponds to $e = \{(i, j+1); (i, j-1); (i+1, j); (i-1, j)\}$, while the fuzzy mass diffusion resistances are expressed by the formulas:

$$\begin{cases} \tilde{W}_e^{f-1} = \dfrac{h_1}{2\tilde{D}\left(\tilde{T}_{i,j}^{f-1}\right)} + \dfrac{h_1}{2\tilde{D}\left(\tilde{T}_e^{f-1}\right)}, & \text{if } e = \left\{(i, j+1) \text{ or } (i, j-1)\right\}, \\ \tilde{W}_e^{f-1} = \dfrac{h_2}{2\tilde{D}\left(\tilde{T}_{i,j}^{f-1}\right)} + \dfrac{h_2}{2\tilde{D}\left(\tilde{T}_e^{f-1}\right)}, & \text{if } e = \left\{(i+1, j) \text{ or } (i-1, j)\right\}. \end{cases} \tag{6.29}$$

The stability condition for the explicit scheme of FDM is as follows:

$$1 - \Delta t \sum_{a=1}^{4} \frac{\Phi_e}{\tilde{W}_e^{f-1}} \geq 0, \tag{6.30}$$

and

$$\Delta t \leq \sum_{a=1}^{4} \frac{\tilde{W}_e^{f-1}}{\Phi_e}. \tag{6.31}$$

Based on Equation (6.27), the relationships for the boundary nodes have been determined. As these relations are very similar to those presented in the version with interval arithmetic, it was decided not to show these derivations in the thesis.

The author's program was written to perform the appropriate calculations – its flowchart is included in Figure 6.6. The simulation was carried out in Embarcadero Delphi 10.4 Community Edition (Embarcadero Technologies, Inc.) environment software.

It should be noted that α-cuts were used for the numerical calculations, which allow the simplification of complex mathematical operations in the set of fuzzy numbers. By using the α-cuts, elementary mathematical operations are performed at the ends of the intervals. Numerical simulations were carried out for several values of the parameter α.

Figure 6.7 shows diagrams of the interval mass fraction values for triangular (a) and trapezoidal (b) fuzzy numbers, depending on the value of the parameter α. The results were obtained for nodes with coordinates r = 0.050 mm and z = 0.475 mm for step 3 of the cooling phase (in 20 s). One can observe from both graphs that the largest interval width occurs for α = 0. In contrast, for α = 1 the width is the lowest, and for triangular numbers it is equal to $\tilde{0}$.

This conclusion is also evident in Figure 6.8, which demonstrates a certain fragment of step 7 for the cooling phase for α = 0.25 (a) and α = 0.75 (b) for triangular fuzzy numbers in selected point. Meanwhile, Figure 6.9 depicts the same moment of simulation for two selected values of the parameter α for trapezoidal fuzzy numbers.

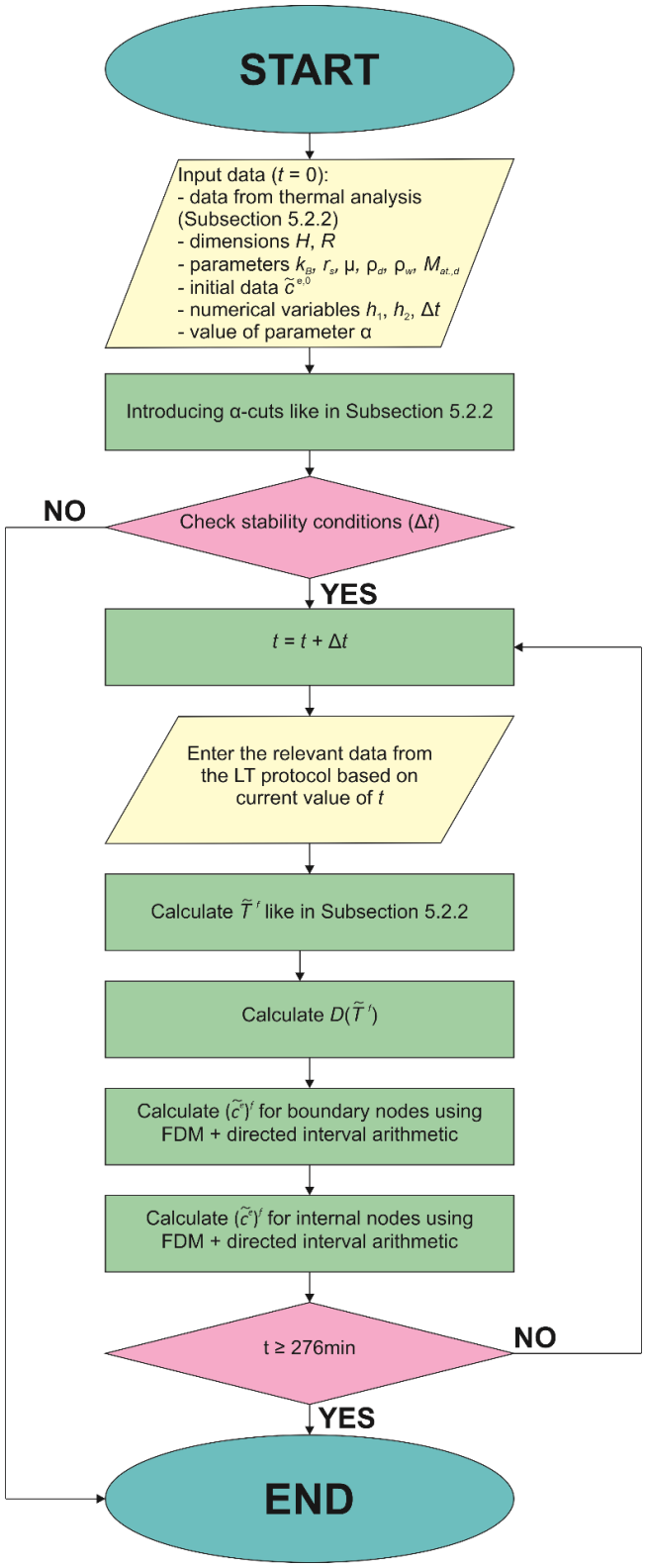

Figure 6.6. Flowchart of algorithm to simulate mass (diffusion) transfer phenomena (fuzzy arithmetic)

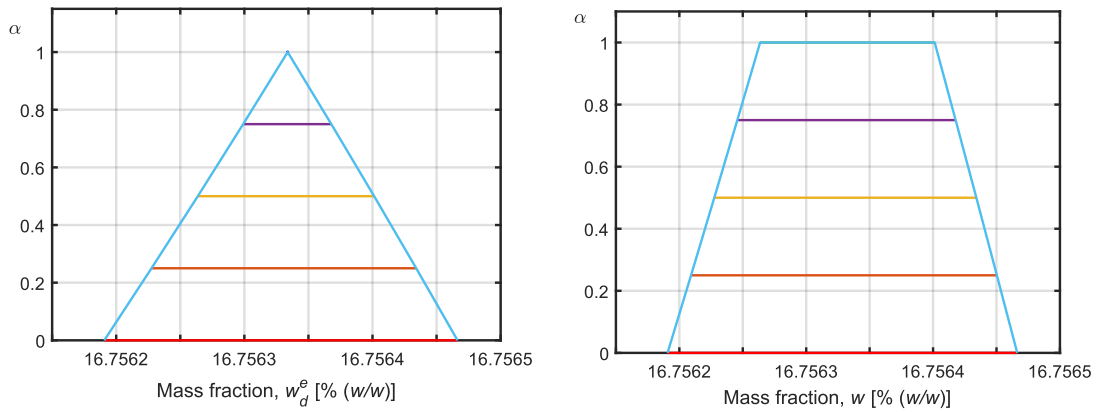

(a) (b)

Figure 6.7. Values of interval mass fraction after 20 s of step 3 in cooling phase for different values of parameter α: (a) triangular and (b) trapezoidal fuzzy number

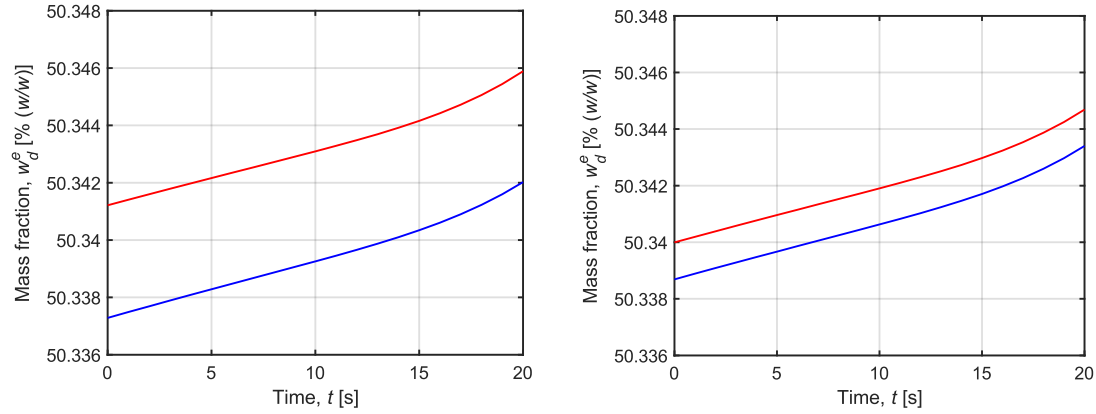

(a) (b)

Figure 6.8. The interval mass fraction as a function of time for triangular fuzzy numbers: (a) α = 0.25; (b) α = 0.75

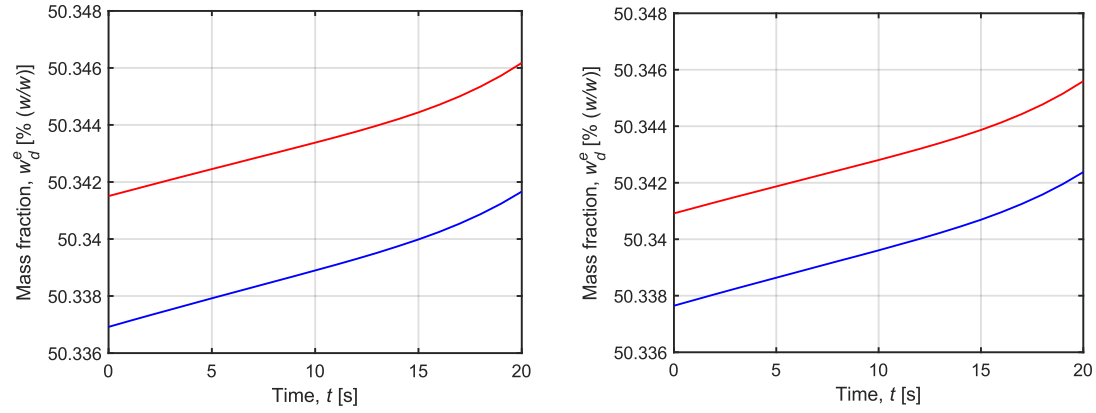

(a) (b)

Figure 6.9. The interval mass fraction as a function of time for trapezoidal fuzzy numbers: (a) α = 0.25; (b) α = 0.75

Furthermore, Table 6.4 presents a comparison of the values obtained for the interval mass fraction for α = 0.5 in given point with the result of the simulation performed by Yu et al. [187]. Unfortunately, the fuzzy mass fraction values do not always include the values obtained by Yu et al. [187]. In our case, a different mathematical model has been used, e.g. to determine the diffusion coefficient, which can induce differences in the results.

Table 6.4. Interval mass fraction obtained in the simulation for α = 0.5 (fuzzy arithmetic)

Phase	**Step**	**Interval mass fraction, $\overline{w}_d^e$ [% (*w*/*w*)]**		**Simulation data (centre of disk), *w* [% (*w*/*w*)]**
		Triangular fuzzy numbers	**Trapezoidal fuzzy numbers**	
Cooling	1	[7.839; 7.839]	[7.839; 7.839]	6.80
	2	[16.663; 16.663]	[16.663; 16.663]	15.73
	3	[25.838; 25.839]	[25.837; 25.840]	23.23
	4	[34.139; 34.140]	[34.139; 34.140]	32.22
	5	[42.099; 42.104]	[42.098; 42.105]	37.62
	6	[50.338; 50.340]	[50.337; 50.341]	44.30
	7	[56.599; 56.605]	[56.597; 56.606]	47.50
Warming	1	[50.500; 50.494]	[50.501; 50.493]	–
	2	[42.362; 42.360]	[42.362; 42.359]	–
	3	[34.401; 34.396]	[34.402; 34.395]	–
	4	[26.161; 26.160]	[26.161; 26.160]	–
	5	[18.235; 18.234]	[18.2356; 18.233]	–
	6	[0.0232; 0.0232]	[0.0232; 0.0232]	–

6.2.3. Summary and conclusions

In summary, Example 1 introduces an analysis of mass transfer caused by molecular diffusion. The model presents the system in which the articular cartilage sample has a form of a disk immersed in a bath solution derived from the CPTes2 mixture. Therefore, the phenomenon of mass convection has been neglected and the governing equation is based on the second Fick's law equation. The mass transfer equation also includes the diffusion coefficient, which is weakly coupled to temperature.

For that reason, this example is closely related to Example 1 in Chapter 5, where a thermal analysis of the same sample was performed.

Both examinations, conducted on interval numbers (LT protocol by Pegg et al. [116]) and fuzzy numbers (LT protocol by Yu et al. [187]), have been compared with simulation data from Yu et al. [187] and, in the case of the analysis with interval numbers, also with experimental data from Pegg et al. [116]. It can be noted that not all ranges coincide with the values indicated in the literature (the relative error oscillates between 0.02% and 15.89%). Differently from Yu et al. [187], the model presented in this study uses the Einstein-Stokes equation to determine the diffusion coefficient, which could be the reason for the differences observed in the results. In the above examples, after each step of the LT protocol the mass fraction is close to the mass fraction of the bath solution multiplied by a factor of 0.9, which results from the boundary conditions.

Then, let us compare the results received for both interval and fuzzy numbers, for which two various LT protocols were used (compare, for example, results in Tables 6.2 and 6.4). It can be noticed that the interval mass fraction values obtained in both cases are quite similar, even though the LT protocol proposed by Yu et al. [187] involves a shorter exposure of the sample to the bath solution with the given concentration. The interesting thing to note is that for each step of the process, Yu et al. in their paper [187] determine the freezing point of the tissue based on the concentration of CPA in the extracellular solution (according to the equation in [119]). Thanks to that it is possible to estimate the risk of formation of ice crystals. This is a marker of tissue damage and it is worth considering in the analysis of the cryopreservation process in the future.

Another factor of dangerous behaviour of biological cells are changes in cell volume induced by osmotic transport of CPA and water into intracellular matrix. Such considerations will be presented in the next example.

6.3. Example 2: Osmotic transport

Example 2 is devoted to a description of the exchange of water and CPA molecules across the cell membrane. Osmotic transport is caused by the chemical potential difference between the extracellular matrix and the intracellular solution. The presence of CPA in the extracellular solution results in the transport of water from the intracellular

space (dehydration). After that, water enriched with CPA molecules is again transferred to the intracellular solution. In our case, changes in cell volume have been estimated from alterations in the volume of water and the number of CPA moles in the cell. To determine these parameters, the 2-P formalism has been used, which is commonly adopted in the literature [8, 36, 67, 76, 129, 132, 184, 193–195].

The bath solution presented here is the same as in Example 1 (Subsection 6.2). It is the CPTes2 mixture proposed by Pegg et al. [116], which consists mainly of water, DMSO as CPA, KCl and other components.

It is worth adding that in this example, the change in volume of articular cartilage cells and chondrocytes was analysed. Chondrocytes are dispersed in the extracellular (proteoglycan) matrix and constitute approximately 1% – 2% of the total articular cartilage composition. Close to the contact surface of the articular cartilage with the external membrane layer, chondrocytes are relatively densely distributed, tangential to the surface. In contrast, near the cartilage-bone interface, chondrocytes are evenly dispersed vertically. In the intermediate zone, chondrocytes are randomly placed and their density of distribution decreases. Chondrocytes are responsible for the production and maintenance of the extracellular matrix (not only proteoglycans, but also collagen). Articular cartilage does not contain blood vessels, so the process of nutrient delivery occurs through the extracellular matrix [1].

Generally, the 2-P formalism is defined by the following pair of governing equations [36]:

$$\dot{V}_w = -L_p ART\left(M^e - M^i\right), \tag{6.32}$$

$$\dot{N}_s = P_s A\left(M^e - M^i\right). \tag{6.33}$$

Please note that the subscript *s* denotes the solute molecules and, in our case, this is represented by CPA, more specifically DMSO. In the following work, the subscript *d* is inserted instead of *s*.

The above equations need only to be supplemented by an initial condition ($t = 0$):

$$V_w\left(X,0\right) = V_w^0, \tag{6.34}$$

$$N_d\left(X,0\right) = N_d^0, \tag{6.35}$$

where V_w^0 and N_s^0 are, respectively, intracellular water volume in cell and intracellular number of permeating solute molecules in the initial moment.

As can be seen, Equations (6.32)-(6.33) are weakly coupled to temperature. In addition, in the model it is necessary to know the osmolarity of the extracellular and intracellular solution. Osmolarity is calculated on the basis of mass fraction, and it indicates that the model is also weakly coupled to the concentration of cellular solutions. Hence, to conduct the osmotic transport examination, the thermal and the mass diffusion analysis performed in Chapter 5 (Example 1) and Chapter 6 (Example 1) have been applied. In this example, only the considerations for the rules of directed interval arithmetic are shown.

6.3.1. Example 2 – interval numbers

For the mass diffusion problem (Example 1), the introduction of interval numbers into the osmotic transport model is a novel approach compared to previous publications [8, 36, 67, 76, 129, 132, 184, 193–195]. As a result, no stochastic model needs to be prepared. In addition, the interval results better illustrate natural cellular processes due to osmotic changes compared to the deterministic approach.

The interval 2-P formalism can be expressed as:

$$\frac{\mathrm{d}\bar{V}_w(t)}{\mathrm{d}t} = -\bar{L}_p\left(\bar{T}\right) AR\bar{T}\left(r,z,t\right)\left(\bar{M}^e - \bar{M}^i\right), \tag{6.36}$$

$$\frac{\mathrm{d}\bar{N}_d(t)}{\mathrm{d}t} = \bar{P}_s\left(\bar{T}\right) A\left(\bar{M}^e - \bar{M}^i\right), \tag{6.37}$$

where the interval hydraulic conductivity and the interval permeability of CPA through cell membrane explain the water and CPA permeability across the cell membrane, respectively. These quantities are calculated from the relationships [187]:

$$\bar{L}_p\left(\bar{T}\right) = A_{Lp}\exp\left(\frac{E_{A,Lp}}{R_g\bar{T}(r,z,t)}\right), \tag{6.38}$$

$$\bar{P}_s\left(\bar{T}\right) = A_{Ps}\exp\left(\frac{E_{A,Ps}}{R_g\bar{T}(r,z,t)}\right), \tag{6.39}$$

where A_{Lp} and A_{Ps} are the pre-exponential factors for $\bar{L}_P$ and $\bar{P}_S$, respectively, while $E_{A,Lp}$ and $E_{A,Ps}$ are the activation energies for $\bar{L}_P$ and $\bar{P}_S$, respectively.

Equations (6.36)-(6.37) also include the interval osmolarity, which can be determined from the interval osmolality [187]:

$$\bar{M}^{s} = \frac{\bar{\pi}^{s}\bar{w}_{w}^{s}\left(r,z,t\right)}{\sum \bar{V}m_{j}^{s}\left(\bar{w}\right)}, \tag{6.40}$$

where the superscript *s* denotes extracellular (*e*) or intracellular (*i*) solution, the subscript *j* denotes the species *j*, $\bar{\pi}^{s}$ is the interval osmolality, $\bar{w}_{w}^{s}$ is the interval mass fraction of water in solution *s* and $\bar{V}m_{j}^{s}$ is the interval volume per unit of mass of species *j* in solution *s*. In our considerations, the following types *j* are included: *w*, *d*, *k*. They represent water (*w*) as the main element of the bath solution, DMSO (*d*) as CPA, and KCl (*k*) as the component of CPTes2, which is a potassium-rich mixture.

The interval volume per unit of mass of types *j* can be defined as [187]:

$$\bar{V}m_{j}^{s}\left(\bar{w}\right) = \frac{\bar{w}_{j}^{s}(r,z,t)}{M_{at.j}}v_{j}, \tag{6.41}$$

where v_j is the partial molar volume of types *j*.

There is also an interval osmolality in Equation (6.40), which is defined as [36, 187]:

$$\begin{aligned}\bar{\pi}^{s} = {} & k_{diss}\bar{m}_{k}^{s}\left(\bar{w}\right)+\bar{m}_{d}^{s}\left(\bar{w}\right)+B_{k}\left[k_{diss}\bar{m}_{k}^{s}\left(\bar{w}\right)\right]^{2} \\ & +B_{d}\left[\bar{m}_{d}^{s}\left(\bar{w}\right)\right]^{2}+\left(B_{k}+B_{d}\right)k_{diss}\bar{m}_{k}^{s}\left(\bar{w}\right)\bar{m}_{d}^{s}\left(\bar{w}\right),\end{aligned} \tag{6.42}$$

where the interval molality of types *j* (*d* or *k*) is computed according to the mass fraction of the solution *s*:

$$\bar{m}_{j}^{s}\left(\bar{w}\right) = \frac{\bar{w}_{j}^{s}\left(r,z,t\right)}{\left[1-\bar{w}_{j}^{s}\left(r,z,t\right)\right]M_{at.j}}. \tag{6.43}$$

At this moment, it is worth considering how to determine the mass fraction for extracellular and intracellular solutions. The problem of calculating the interval molar concentration of DMSO in the extracellular matrix is demonstrated in Example 1 in Chapter 6 (Subsection 6.2.1)., and the results obtained previously have been implemented for this case.

The interval molar concentration of KCl in the extracellular matrix is a constant isotonic concentration. Assuming that it is equal to the molar concentration of KCl in the bath solution:

$$\bar{c}_{k}^{e} = c_{k,bath}, \tag{6.44}$$

where $c_{k,bath}$ is the isotonic molar concentration of KCl in the bath solution including CPTes2 mixture.

In contrast, intracellular solution parameters have been determined from the relationships [144, 183, 184]:

$$\bar{c}_d^i = \frac{\bar{N}_d(t)}{\bar{V}_{cell}(t) - V_b - v_d \bar{N}_d(t)}, \tag{6.45}$$

$$\bar{c}_k^i = c_k^{e,0}\left(\frac{V_{cell}^0 - V_b - v_d N_d^0}{\bar{V}_{cell}(t) - V_b - v_d \bar{N}_d(t)}\right), \tag{6.46}$$

where $\bar{V}_{cell}$ is the interval cell volume, V_b is the osmotically inactive volume of cells equal to $V_b = 0.41V_0$ [96, 118, 183], where V_0 is the is the isotonic volume of cells calculated from the isotonic cell radius r_{cell}. Obviously, the superscript 0 denotes the initial moment of the simulation. The initial cell volume is assumed to be equal to the isotonic cell volume at the initial moment of the simulation.

The interval cell volume is the sum of the volume of water, DMSO and the osmotically inactive volume of cells in the intracellular solution (compare with Equation (3.25)) [36, 67]:

$$\bar{V}_{cell}(t) = \bar{V}_w(t) + \bar{V}_d(t) + V_b, \tag{6.47}$$

and introducing the time derivative, which occurs in the 2-P formalism [79], one obtains:

$$\frac{\mathrm{d}\bar{V}_{cell}(t)}{\mathrm{d}t} = \frac{\mathrm{d}\bar{V}_w(t)}{\mathrm{d}t} + \frac{\mathrm{d}\bar{V}_d(t)}{\mathrm{d}t} = \frac{\mathrm{d}\bar{V}_w(t)}{\mathrm{d}t} + \frac{\mathrm{d}\bar{N}_d(t)}{\mathrm{d}t} v_d . \tag{6.48}$$

Analysing the formulae from which the intracellular molar concentrations are determined, it can be seen that they are strongly coupled. This is a logical conclusion, as the number of moles of DMSO depends on the concentration of DMSO in the intracellular solution and inversely.

Equations (6.36)-(6.46) should also be supplemented with information on the initial state of the intracellular solution:

$$\bar{V}_d(0) = V_d^0, \tag{6.49}$$

$$\bar{N}_d(0) = N_d^0, \tag{6.50}$$

$$\bar{V}_{cell}(0) = V_{cell}^0, \tag{6.51}$$

$$\bar{c}_k^e(r, z, 0) = c_k^{e,0}, \tag{6.52}$$

$$\overline{c}_k^i(r,z,0) = \overline{c}_d^i(r,z,0) = c^{i,0}. \tag{6.53}$$

The next step is to define the parameters of chondrocytes and bath solution necessary in the mathematical model. Table 6.5 contains the input data for the osmotic transport model. Please note that the molar concentration of KCl at the initial moment is equal to the isotonic molar concentration of KCl in the bath solution. The table provides concentration of KCl as a mass fraction, not as its molar concentration.

The rest of parameters that are necessary to analyse the thermal and mass transfer from the bath solution to the extracellular matrix problem are given in the previous examples (thermal analysis – Subsection 5.2.1, extracellular mass transfer problem – Subsection 6.2.1).

Table 6.5. Input data for osmotic transport model [129, 132, 187]

Parameters of cells (chondrocytes)				
Parameters		**Values**		
A	[m^2]	8.04×10^{-10}		
r_{cell}	[m]	8×10^{-6}		
Chemical properties of bath solution				
Parameters		**Values**		
		DMSO	KCl	H_2O
ρ_j	[kg·m^{-3}]	1.1×10^{3}	1.98×10^{3}	997
$M_{at.,j}$	[kg·mol^{-1}]	7.813×10^{-4}	7.455×10^{-4}	1.802×10^{-4}
B_j	[kg·mol^{-1}]	0.108	0	–
v_j	[L·mol^{-1}]	7.097×10^{-4}	3.75×10^{-4}	1.807×10^{-4}
k_{diss}	–	–	1.772	–
Initial data				
Parameters		**Values**		
$w_k^{e,0} = w_{k,bath}$	[% (*w*/*w*)]	0.85		
$c^{i,0}$	[mol·m^{-3}]	0		
$V_{cell}^0 = V_0$	[m^3]	2.144×10^{-15}		
$V_w^0 = V_{cell}^0$	[m^3]	2.144×10^{-15}		
N_d^0	[mol]	0		

Let us now introduce a numerical model for the 2-P formalism approach. For this purpose, FDM has been applied considering the rules of interval arithmetic. The process of time meshing and domain discretization is the same as for heat and mass transfer by diffusion (see Equations (5.15) and (6.12) and Figure 5.2).

Please note that in Equations (6.36) and (6.37) are only time derivatives, therefore the following differential quotients have been introduced:

$$\left(\frac{\mathrm{d}\bar{V}_w(t)}{\mathrm{d}t}\right)_{i,j}^{f} = \frac{\left(\bar{V}_w\right)_{i,j}^{f} - \left(\bar{V}_w\right)_{i,j}^{f-1}}{\Delta t}, \tag{6.54}$$

$$\left(\frac{\mathrm{d}\bar{N}_d(t)}{\mathrm{d}t}\right)_{i,j}^{f} = \frac{\left(\bar{N}_d\right)_{i,j}^{f} - \left(\bar{N}_d\right)_{i,j}^{f-1}}{\Delta t}, \tag{6.55}$$

and as a result:

$$\left(\bar{V}_w\right)_{i,j}^{f} = \left(\bar{V}_w\right)_{i,j}^{f-1} - \Delta t \cdot \bar{L}_p\left(\bar{T}_{i,j}^{f-1}\right) AR\bar{T}_{i,j}^{f-1}\left(\bar{M}^e - \bar{M}^i\right), \tag{6.56}$$

$$\left(\bar{N}_d\right)_{i,j}^{f} = \left(\bar{N}_d\right)_{i,j}^{f-1} + \Delta t \cdot \bar{P}_s\left(\bar{T}_{i,j}^{f-1}\right) A\left(\bar{M}^e - \bar{M}^i\right). \tag{6.57}$$

The mesh parameters are assumed as in previous coupled analyses: the time step $\Delta t = 10^{-3}$ s, the mesh steps $h_1 = 10^{-4}$ m and $h_2 = 5 \cdot 10^{-5}$ m [132].

To perform the numerical calculations, the author's program written in the Embarcadero Delphi 10.4 Community Edition (Embarcadero Technologies, Inc.) environment was used. Figure 6.10 shows the flowchart which shortly explains its working procedures.

Figures 6.11-6.16 present the simulation results for the osmotic transport analysis during cryopreservation performed by LT protocol. Figure 6.11 depicts the change in the interval mass fraction of DMSO during the entire process. These results are presented for the point at the centre of the sample (r = 0.050 mm, z = 0.475 mm). As can be seen, the appearance of the graph coincides with the interval mass fraction characteristic of the extracellular matrix (see Figure 6.3).

Table 6.6 shows the results at the end of each step of the individual simulation phases. These data were compared with the simulation data from Yu et al. [187].

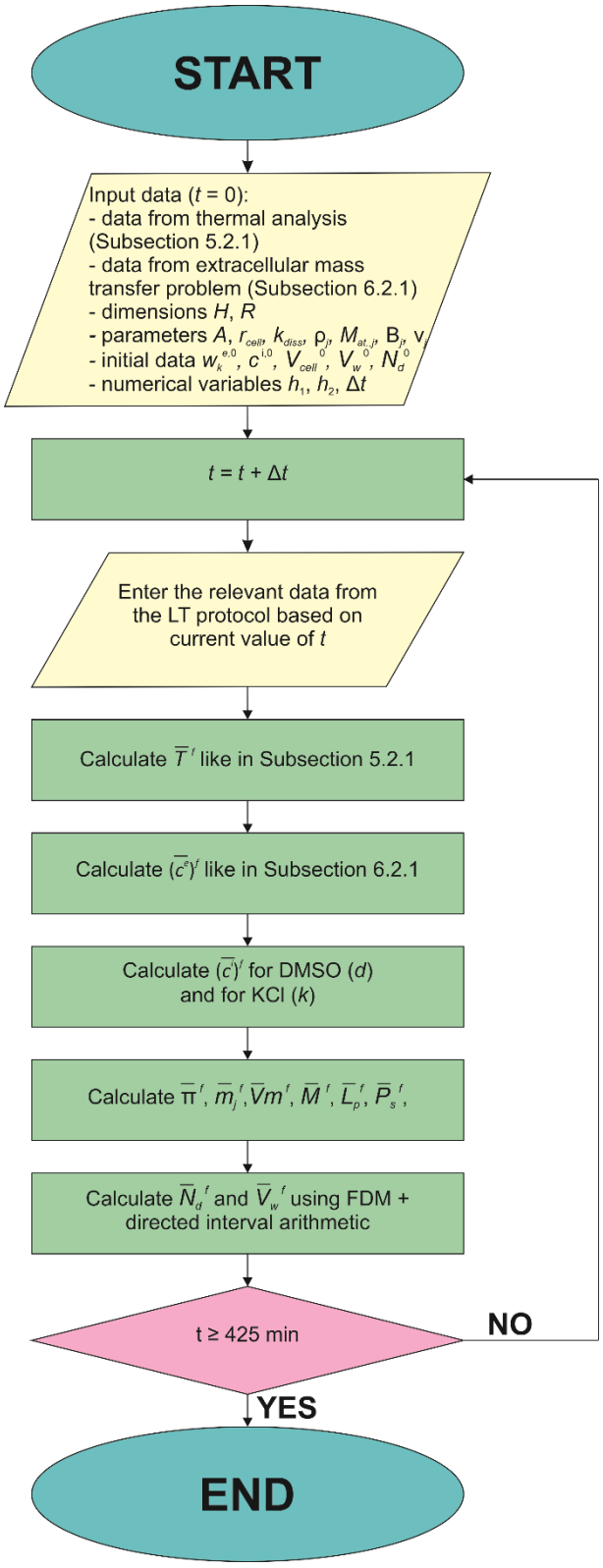

Figure 6.10. Flowchart of algorithm to simulate osmotic transport phenomena (interval arithmetic)

Due to the small width of the intervals, other diagrams have also been prepared. Figure 6.12 demonstrates a certain part of the simulation results in step 8 of the cooling phase (a) and step 1 of the warming phase (b).

Moreover, Figure 6.13 illustrates the distribution of the interval intracellular mass fraction of DMSO in the whole domain. It represents the history of interval mass fraction of DMSO in cell after 20 s of step 8 of the cooling phase. As for the interval extracellular mass fraction (see Figure 6.5), the differences between the lower and upper limits of the interval are very small.

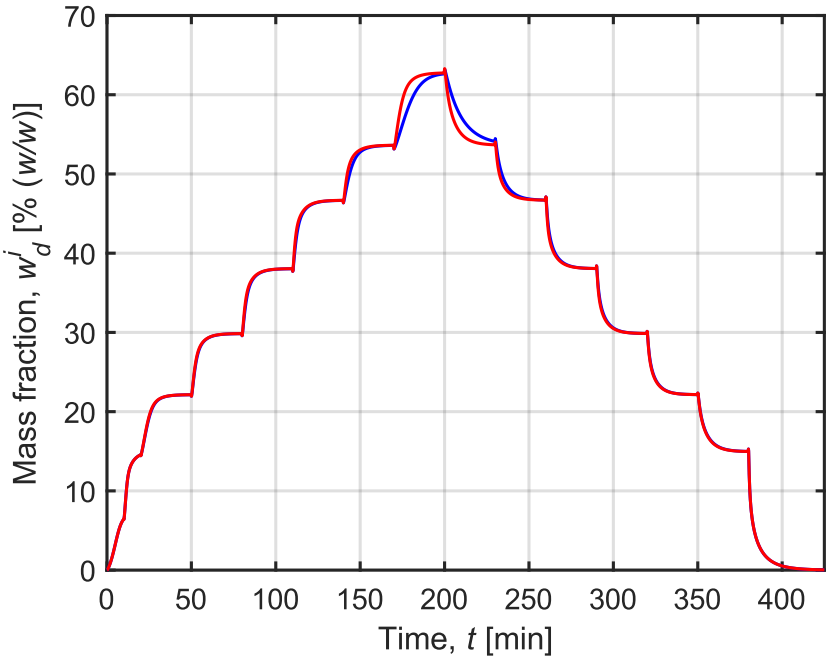

Figure 6.11. Interval mass fraction of DMSO in chondrocytes over whole simulation time

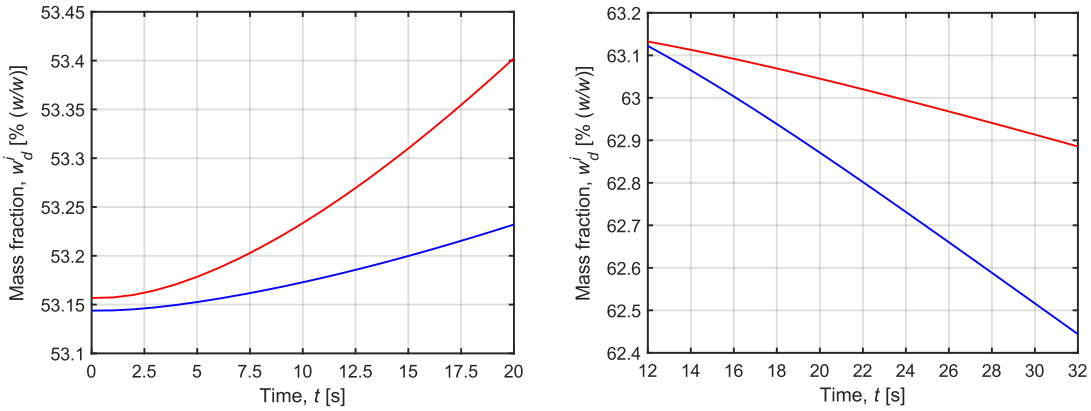

(a) (b)

Figure 6.12. Interval mass fraction as a function of time: (a) step 8 in cooling phase and (b) step 1 in warming phase

Table 6.6. Interval results compared with simulation data from Yu et al. [187]

Phase	Step	Interval mass fraction, $\overline{w}_d^i$ [% (*w*/*w*)]	Simulation data, *w* [% (*w*/*w*)]
Cooling	1	[6.455; 6.455]	6.70
	2	[14.562; 14.562]	15.69
	3	[21.132; 21.137]	24.42
	4	[29.842; 29.850]	31.86
	5	[38.035; 38.046]	38.33
	6	[46.661; 46.672]	44.02
	7	[53.609; 53.622]	47.26
	8	[62.640; 62.748]	48.63
Warming	1	[54. 097; 53.678]	50.32
	2	[46.702; 46.697]	50.75
	3	[38.061; 38.067]	44.99
	4	[29.862; 29.867]	36.27
	5	[21.152; 21.155]	27.05
	6	[14.977; 14.973]	18.86
	7	[0.032; 0.033]	0.03

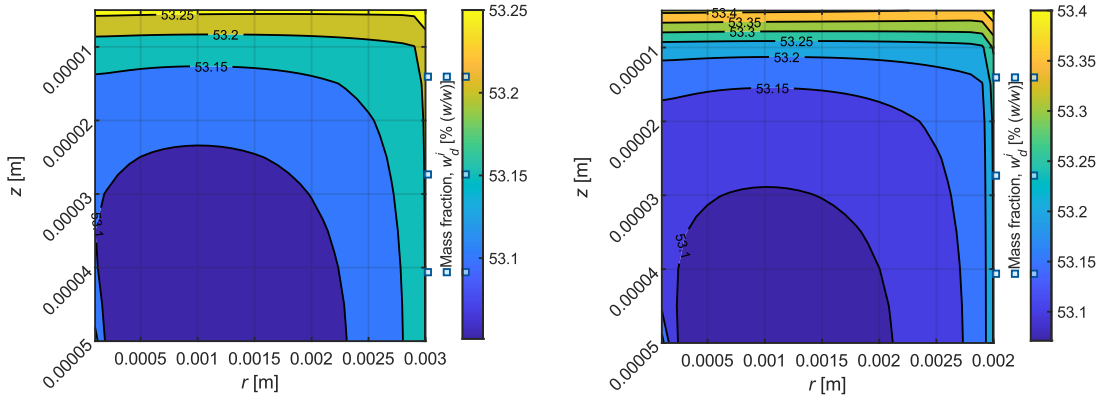

(a) (b)

Figure 6.13. Distribution of the interval mass fraction in 20 s of step 8 for cooling phase: (a) $\overline{w}_d^{i-}$ and (b) $\overline{w}_d^{i+}$

Using the 2-P formalism, it has been also determined the changes in the interval number of DMSO moles and the interval volume of water in chondrocytes. Figure 6.14 shows the history of these parameters during the entire simulation. The plots present

the results obtained in the centre of the sample (r = 0.050 mm, z = 0.475 mm). It can be observed that the interval number of DMSO moles increases rapidly to a certain level, and then stabilises at them. In contrast, the interval volume of water decreases to a specific level, which indicates the occurrence of dehydration. Figure 6.15 depicts an enlarged fragment for step 3 of the cooling phase.

Consequently, the interval normalised cell volume throughout the process has also been estimated. This is the relation of the interval cell volume $\bar{V}_{cell}$ to its initial volume V_{cell}^{0}, which coincides with the isotonic cell volume V_0. From the graph in Figure 6.16, it can be seen that the cells have been shrinking for most of the process. This indicates a greater influence of dehydration than the infusion of DMSO moles.

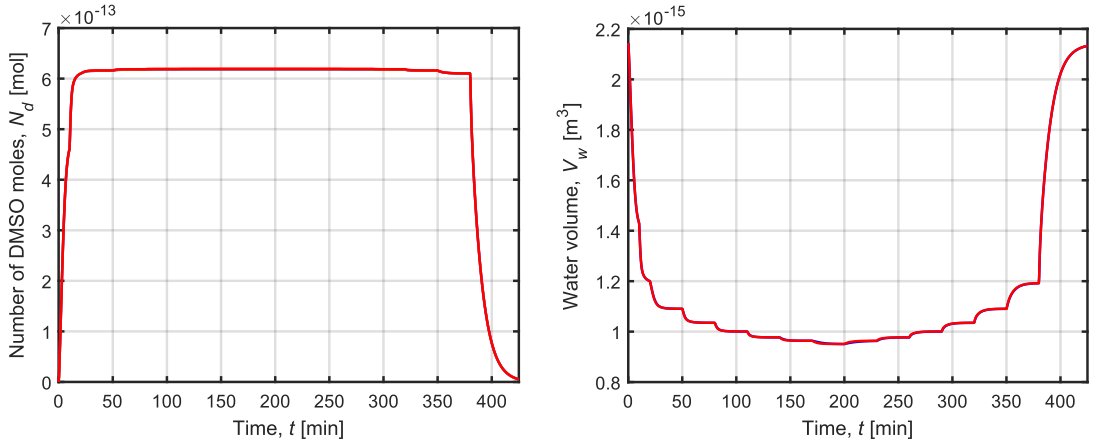

(a) (b)

Figure 6.14. Interval number of DMSO moles (a) and interval volume of water (b) in chondrocytes over whole simulation time

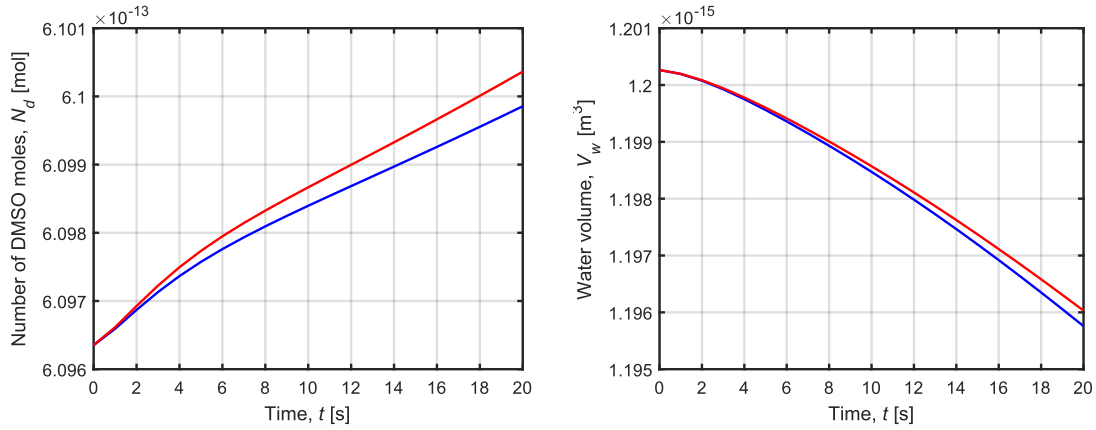

(a) (b)

Figure 6.15. Interval number of DMSO moles (a) and interval volume of water (b) in chondrocytes in the certain fragment of step 3

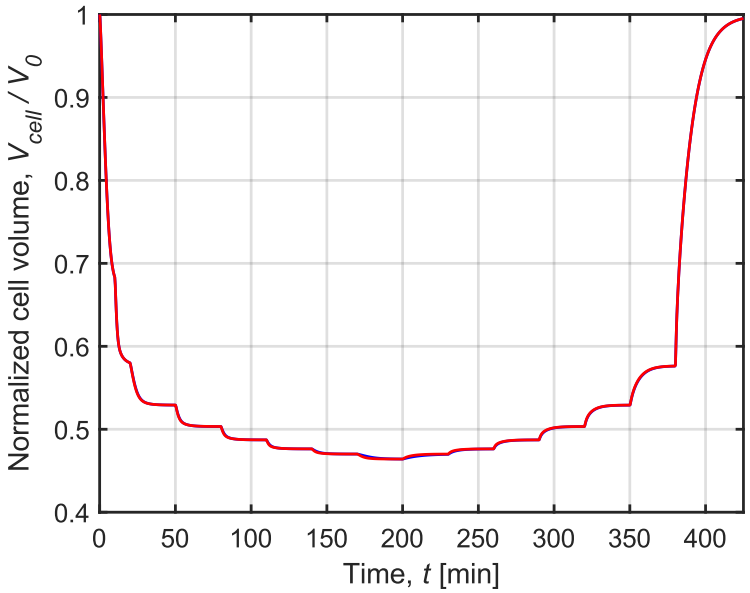

Figure 6.16. Interval normalized volume of chondrocytes over whole simulation time

6.3.2. Summary and conclusions

In summary, the above example provides a numerical analysis of osmotic transport during cryopreservation. This phenomenon is described using the 2-P formalism that is coupled to both the heat and mass distribution problem. Therefore, in this case, the previous instances presented in Example 1 in Chapter 5 (Subsection 5.2.1) and Example 1 in Chapter 6 (Subsection 6.2.1) are used. This example uses the previously proposed sample geometry (see Figure 5.1) and the composition of the bath solution (CPTes2 consisting of water, DMSO and a potassium-rich mixture).

The study primarily considered the interval molar concentration of DMSO as CPA in chondrocytes (see Figure 6.11). As can be seen, these changes are dependent on alterations in the concentration of CPA in the extracellular matrix (compare with Figure 6.3). In addition, the intracellular interval mass fraction of DMSO is compared with the simulation data from Yu et al. [187] (see Table 6.6). It can be concluded that these results are quite compatible with each other, with the most significant discrepancies occurring at high mass fraction values.

After calculating the interval molar concentrations of DMSO in the cell solutions, the interval number of DMSO moles and the interval volume of water in the intracellular space have also been estimated (see Figure 6.14). It can be observed that the interval number of DMSO moles initially increases to a specific level. This value remains constant

until a certain moment, at which lasts the removal of CPA process. Obviously, this is closely related to a decrease and then an increase in the interval water volume. This illustrates the phenomenon of dehydration, in which water leaves the intracellular solution and DMSO moles enter at the same time. When the sample is warmed up, the interval volume of water returns to its original level.

It is worth noting the graph of interval normalised cell volume as a function of time (Figure 6.16). Based on this, it can be concluded that chondrocytes shrink for a longer time during the process and that the influx of DMSO into the intracellular space contributes less to this than dehydration.

Yu et al. [187] suggest that the dehydration rate should be higher than the addition of DMSO. For this purpose, Yu et al. [187] convert the hydraulic conductivity (L_P) into a filtration coefficient and compare it with the cell membrane permeation coefficient (P_S). They report that the difference between dehydration rate and DMSO penetration rate increases with decreasing temperature.

Although the phenomenon of cell shrinkage is very dangerous, it should be mentioned that chondrocytes are assumed to be active if the relevant conditions are fulfilled. The normalised volume must be in the range of 0.46 – 2.49, while the intracellular mass fraction of KCl is to be equal to a value in the range 0.24 – 9.50 % (*w*/*w*) [187]. In this case, only the volumetric condition was considered, and it was satisfied (the minimum value of the interval normalized cell volume is equal to [0.4641; 0.4640]).

6.4. Example 3: Mass transfer – convection and diffusion phenomena

Example 3 presents a model of heat and mass transfer as well as osmotic transport, considering the method of CPA delivery to the sample. Improper loading and unloading of CPA can cause osmotic damage to cells induced by osmolality imbalance. For this reason, it is often a time-consuming process. Satisfactory CPA delivery can be achieved using, for example, a microfluidic system. Such devices are often complex techniques, as shown in [143, 144, 176, 191, 193–195].

The preparation of a model of the entire microfluidic device can be complicated, so a simplified geometry has been created. In the case considered, a system similar to the concept proposed by Liu et al. was prepared [79]. The geometric model of the system

is schematically illustrated in Figure 6.17. The main element of the microfluidic system is a cylindrical microchannel, which is enclosed in a glass slide. Input and output holes are drilled in the housing and a bath of solution is injected and extracted continuously. Therefore, the mass transfer model takes into account not only the diffusion phenomenon, but also convection caused by the movement of the bath solution ($\mathbf{u} \neq 0$).

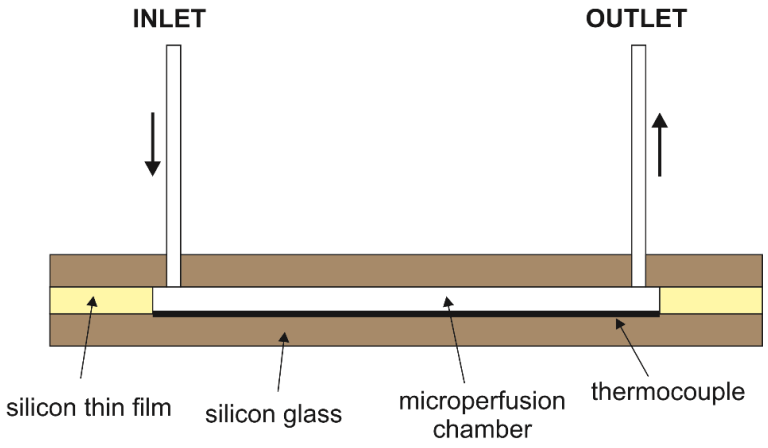

Figure 6.17. Simplified microfluidic system

Several further elements of the model were adopted from previous examples, mainly from Example 1 in Chapter 5 and Examples 1 and 2 in Chapter 6. The bath solution is again based on the potassium-rich CPTes2 mixture with DMSO as CPA [116]. Moreover, the temperature and the concentration of the bath solution is controlled according to the LT protocol suggested by Yu et al. [187]. Consequently, the phenomena of ice crystal formation and phase transitions were ignored. The simulation was performed on a sample of articular cartilage, which has a cylindrical disc shape. The articular cartilage does not contain lymphatic or blood vessels [1], therefore perfusion and metabolic heat source were neglected ($Q_{int} = 0$).

The following governing equations have been applied to describe this multiscale problem. First, thermal phenomena are defined by the Fourier equation [40]:

$$c_p \rho \dot{T} = \nabla \left(k \nabla T \right). \tag{6.58}$$

It can be said that the heat transfer equation occurs in the same form as in Example 1 of Chapter 5. Similarly, the phenomenon of osmotic transport is specified using the 2-P formalism presented in Example 2 in Chapter 6 [36]:

$$\dot{V}_w = -L_p ART \left(M^e - M^i \right), \tag{6.59}$$

$$\dot{N}_d = P_s A\left(M^e - M^i\right). \tag{6.60}$$

In contrast, the mass transfer equation differs from the relationship considered in Chapter 6 (Subsection 6.2.1 and 6.2.2). This equation describes the mass migration from the bath solution into the extracellular matrix of the biological sample, which is caused by diffusion of CPA (DMSO) molecules. However, in the case of microfluidic systems, where there is a continuous flow of the bath solution, advection must also be taken into account. The mass transfer phenomenon is determined by the convection-diffusion equation (compare with Equation (3.22)) [79, 194]:

$$\dot{c}_d^e = \nabla\left(D\nabla c_d^e\right) - \nabla\cdot\left(\mathbf{u}c_d^e\right) + R_s. \tag{6.61}$$

The advection (convection) phenomenon is related to the velocity vector, which describes the flow of the solution through a microfluidic system. The bath solution is a viscous and Newtonian fluid, hence the fluid flow is explained by the Navier-Stokes equations [52, 142]:

$$\frac{\partial(\rho\mathbf{u})}{\partial t} + (\mathbf{u}\cdot\nabla)(\rho\mathbf{u}) = \rho\mathbf{g} - \nabla p + \mu\nabla^2\mathbf{u} + \frac{\mu}{3}\nabla(\nabla\cdot\mathbf{u}), \tag{6.62}$$

and the continuity equation:

$$\dot{\rho} + \nabla\cdot(\rho\mathbf{u}) = 0. \tag{6.63}$$

In the problem under consideration, the fluid is assumed to be incompressible (p = const. and $\partial p/\partial t = 0$), while the fluid acceleration vector is ignored ($\mathbf{g} = 0$), thus:

$$\frac{\partial(\rho\mathbf{u})}{\partial t} + (\mathbf{u}\cdot\nabla)(\rho\mathbf{u}) = -\nabla p + \mu\nabla^2\mathbf{u}, \tag{6.64}$$

and:

$$\nabla\cdot\mathbf{u} = 0. \tag{6.65}$$

The fluid flow equations should be supplemented with initial and boundary conditions. When defining them, it is important to remember that it is a vector field. By setting boundary conditions for considered edge, an exact value can be given to the values of the components of the velocity vector, for example [20]:

$$\begin{bmatrix} u(X,t) \\ v(X,t) \\ w(X,t) \end{bmatrix} = \begin{bmatrix} u_\Gamma \\ v_\Gamma \\ w_\Gamma \end{bmatrix}, \tag{6.66}$$

where u_Γ, v_Γ, w_Γ are constant values of the velocity on the boundary.

A special type of boundary condition occurring in fluid mechanics is the no-slip condition. This condition appears at the boundary between a fluid and a solid. It is associated with the phenomenon of "sticking" of fluid particles to the wall surface as a result of viscosity [20].

The initial condition, on the other hand, determines the values of the velocity vector at the initial moment:

$$\begin{bmatrix} u(X,0) \\ v(X,0) \\ w(X,0) \end{bmatrix} = \begin{bmatrix} u^0 \\ v^0 \\ w^0 \end{bmatrix}, \tag{6.67}$$

where the superscript 0 represents the initial moment.

When considering this extended multiscale model describing the behaviour of the sample during cryopreservation, it can be seen that, also in this case, some of the parameters can be treated as inaccurate. In earlier publications [79, 143, 144, 176, 193–195], experimentally determined parameters are introduced into the model as deterministic values, ignoring the stochastic nature of biological phenomena. The concept presented in this paper involves a novel approach implementing interval and fuzzy arithmetic. In this example, thermophysical parameters such as volumetric specific heat as well as thermal conductivity coefficient are provided as imprecise.

6.4.1. Example 3 – interval numbers

As a first step, some quantities were introduced into the mathematical model in the form of interval numbers. A two-dimensional domain oriented in a cylindrical coordinate system was analysed. A simplified computational domain in Figure 6.18 was prepared based on the microfluidic system presented in Figure 6.17.

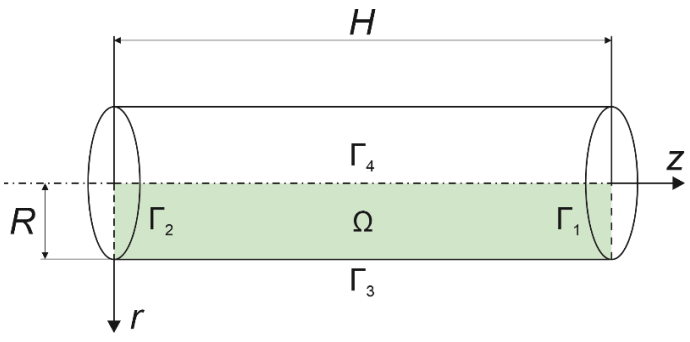

Figure 6.18. Model of microchannel

The interval heat transfer equation is of the form (see Equations (5.10) and (5.11)):

$$\overline{c}_V \frac{\partial \overline{T}\left(r,z,t\right)}{\partial t} = \overline{k}\left[\frac{1}{r}\frac{\partial}{\partial r}\left(r\frac{\partial \overline{T}(r,z,t)}{\partial r}\right)+\frac{\partial^2 \overline{T}(r,z,t)}{\partial z^2}\right], \tag{6.68}$$

or:

$$\overline{c}_V \frac{\partial \overline{T}\left(r,z,t\right)}{\partial t} = \overline{k}\left[\frac{1}{r}\frac{\partial \overline{T}(r,z,t)}{\partial r}+\frac{\partial^2 \overline{T}(r,z,t)}{\partial r^2}+\frac{\partial^2 \overline{T}(r,z,t)}{\partial z^2}\right]. \tag{6.69}$$

Please note that this example assumes that the thermal conductivity coefficient and the volumetric specific heat are independent of temperature.

Another transfer phenomenon is the migration of CPAs associated with advection initiated by the flow of the bath solution in the microfluidic system. The interval convection-diffusion equation for a two-dimensional domain can be expressed as:

$$\begin{aligned}\frac{\partial \overline{c}_d^e\left(r,z,t\right)}{\partial t} = {} & \frac{1}{r}\frac{\partial}{\partial r}\left(\overline{D}\left(\overline{T}\right)r\frac{\partial \overline{c}_d^e(r,z,t)}{\partial r}\right)+\frac{\partial}{\partial z}\left(\overline{D}\left(\overline{T}\right)\frac{\partial \overline{c}_d^e(r,z,t)}{\partial z}\right) \\ & -\nabla\cdot\left(\mathbf{u}\overline{c}_d^e\right)+R_s.\end{aligned} \tag{6.70}$$

This equation describes a multiphysical field weak coupling problem, which combines mass transfer caused by fluid flow and diffusive mass migration, as well as thermal analysis due to the presence of a temperature-dependent interval diffusion coefficient (see Equation (6.7)). Please also note that no chemical reactions take place during the supply of the bath solution, therefore $R_s = 0$.

Let us analyse the component related to convection that remains undetermined in Equation (6.70). As the velocity determines the movement of the incompressible fluid and its divergence is equal to 0, the following form is obtained:

$$\nabla\cdot\left(\mathbf{u}\overline{c}_d^e\right) = \mathbf{u}\cdot\nabla\overline{c}_d^e. \tag{6.71}$$

When considering a two-dimensional domain Ω (see Figure 6.18), the velocity vector is defined by two components: $\mathbf{u} = [v\,(r, z, t), u\,(r, z, t)]$. In the model under consideration, there are no obstacles disrupting the flow. Therefore, the considered model of the convection phenomenon is simplified to a one-dimensional and $\mathbf{u} = u\,(z, t)$. As a result, the interval convection-diffusion equation is of the following form:

$$\frac{\partial \bar{c}_d^e(r,z,t)}{\partial t} = \frac{1}{r}\frac{\partial}{\partial r}\left(\bar{D}(\bar{T})\, r \frac{\partial \bar{c}_d^e(r,z,t)}{\partial r}\right) + \frac{\partial}{\partial z}\left(\bar{D}(\bar{T})\frac{\partial \bar{c}_d^e(r,z,t)}{\partial z}\right) - u(z,t)\frac{\partial \bar{c}_d^e(r,z,t)}{\partial z}. \tag{6.72}$$

The exact value of the velocity vector is calculated from the Navier-Stokes equations (Equation (6.64)). These equations for the one-dimensional model, considering the previous assumptions, can be formulated as follows:

$$\frac{\partial u(z,t)}{\partial t} + u(z,t)\frac{\partial u(z,t)}{\partial z} = -\frac{1}{\rho}\frac{\partial p(z,t)}{\partial z} + \nu \frac{\partial^2 u(z,t)}{\partial z^2}, \tag{6.73}$$

while the continuity equation is of the form:

$$\frac{\partial u(z,t)}{\partial z} = 0, \tag{6.74}$$

where $\nu = \mu \cdot \rho^{-1}$ is the kinetic viscosity coefficient.

Remembering that the fluid is incompressible and introducing the Equation (6.74) (continuity equation) into the Equation (6.73):

$$\frac{\partial u(z,t)}{\partial t} = 0. \tag{6.75}$$

It causes the velocity to be constant in the entire domain Ω.

The aforementioned model represents the macroscopic movement of molecules and their diffusion into the extracellular matrix. During cryopreservation, the phenomenon of osmotic transport also occurs. The interval 2-P formalism for the two dimensional model can be expressed as follows:

$$\frac{\mathrm{d}\bar{V}_w(t)}{\mathrm{d}t} = -\bar{L}_p(\bar{T})\, AR\bar{T}(r,z,t)\left(\bar{M}^e - \bar{M}^i\right), \tag{6.76}$$

$$\frac{\mathrm{d}\bar{N}_d(t)}{\mathrm{d}t} = \bar{P}_s(\bar{T})\, A\left(\bar{M}^e - \bar{M}^i\right). \tag{6.77}$$

The derivations and explanations of the individual components occurring in this equations can be found in previous example – Subsection 6.3.1 (see Equations (6.38)-(6.43)).

The mathematical model needs to be supplemented with boundary and initial conditions. For the domain Ω shown in Figure 6.18, the following boundary conditions are formulated for the heat transfer problem:

$$\begin{cases} \Gamma_1 \text{ and } \Gamma_4: & \bar{q}_\Gamma\left(r,z,t\right) = -\mathbf{n}\bar{k}\cdot\nabla\bar{T} = \bar{0}, \\ \Gamma_2 \text{ and } \Gamma_3: & \bar{q}_\Gamma\left(r,z,t\right) = -\mathbf{n}\bar{k}\cdot\nabla\bar{T} = \alpha_\Gamma\left[\bar{T}\left(r,z,t\right) - T_{bath}\right], \end{cases} \tag{6.78}$$

and initial condition:

$$\bar{T}\left(r,z,0\right) = T^0. \tag{6.79}$$

Similarly, the boundary and initial conditions for the mass transfer problem from the bath solution into the extracellular matrix of the sample are determined:

$$\begin{cases} \Gamma_1 \text{ and } \Gamma_4: & \bar{q}_\Gamma\left(r,z,t\right) = -\mathbf{n}\bar{D}\cdot\nabla\bar{c}_d^e = \bar{0}, \\ \Gamma_2 \text{ and } \Gamma_3: & \bar{c}_d^e = 0.9\bar{c}_\Gamma, \end{cases} \tag{6.80}$$

and:

$$\begin{cases} \bar{c}_d^e\left(r,z,0\right) = c_d^{e,0}, \\ \bar{c}_k^e\left(r,z,0\right) = c_k^{e,0}. \end{cases} \tag{6.81}$$

For fluid flow problem, the boundary-initial conditions are as follows:

$$\begin{cases} \Gamma_1: & \dfrac{\partial u(z,t)}{\partial n} = 0, \\ \Gamma_2: & u\left(z,t\right) = u_{in}, \end{cases} \tag{6.82}$$

and:

$$u\left(z,0\right) = u^0, \tag{6.83}$$

where u_{in} is the inlet velocity.

Please note that the velocity vector is provided only at the inlet. At the outlet, the normal derivative of the velocity is equal to 0, which is equivalent to the adiabatic condition. In addition, knowing that the time derivative of the velocity is equal to 0 (compare with Equation (6.75)):

$$u\left(z,t\right) = u_{in}. \tag{6.84}$$

The final problem to be considered in the example under consideration is osmotic transport involving the exchange of particular components between extracellular and intracellular solution. The boundary-initial conditions for this problem reduce to the initial condition of the form:

$$\begin{cases} \bar{V}_{cell}\left(0\right) = V_{cell}^0, \\ \bar{c}_k^i(r,z,0) = \bar{c}_d^i(r,z,0) = c^{i,0}. \end{cases} \tag{6.85}$$

All the parameters needed to complete the mathematical model are shown in Table 6.7. Most of the variables are repeated from the previous examples (Example 1 in Chapter 5 and Examples 1 and 2 in Chapter 6). Noteworthy is the information regarding the description of the fluid flow part. Interesting is the fact that the given inlet velocity represents the volumetric flow rate $Q_{vol} = 2.5 \cdot 10^{-10}$ $m^3 \cdot s^{-1}$ [79]. The value of the inlet velocity on the basis of the volumetric flow rate can be easily calculated from the relation:

$$u_{in} = \frac{Q_{vol}}{A}, \tag{6.86}$$

where A is the surface area of the cylinder.

In this example, the lower and upper limits of the interval numbers correspond to a 5% deviation from the deterministic value of $k = 0.518$ $W \cdot m^{-1} \cdot K^{-1}$ and $c_v = 3.924 \cdot 10^6$ $J \cdot m^{-3} \cdot K^{-1}$ [129].

Table 6.7 should be complemented by the values of the variables at the initial moment defined by the initial condition, as detailed in Table 6.8. It is necessary to determine at the initial time: (1) the interval initial temperature (for the heat transfer problem); (2) the interval molar concentration in the extracellular solution for DMSO and KCl and the value of the initial component of the velocity vector (for the mass transfer problem); (3) the interval cell volume and water volume in the intracellular solution, the interval molar concentration in intracellular solution, the interval mole number of DMSO in the intracellular solution (for osmotic transport).

No values for the bath solution parameters have yet been introduced. Apart from the fact that the microfluidic channel system differs from the device proposed by Wang et al. [178], for example (see Figure 6.1), it was decided to use the LT protocol. The idea of this approach has already been explained in some previous examples. In this case, an improved procedure invented by Yu et al. [187] was applied. Table 6.9 represents the LT protocol as conceived by Yu et al. [187].

Table 6.7. Parameters of modelled sample

Parameters		**Values**		
Dimensions of microfluidic channel [79]				
R	[m]	2×10^{-3}		
H	[m]	5.5×10^{-2}		
Thermal analysis parameters [129, 187]				
$\bar{k}$	[W·m^{-1}·K^{-1}]	[0.492; 0.544]		
$\bar{c}_V$	[J·m^{-3}·K^{-1}]	[3.728×10^{6}; 4.120×10^{6}]		
α	[W·m^{-2}·K^{-1}]	525		
Mass diffusion analysis into extracellular matrix [145, 208]				
r_s	[m]	2.541×10^{-10}		
μ	[Pa·s]	1.996×10^{-3}		
$w_{k,bath}$	[% (*w*/*w*)]	0.85		
Fluid flow analysis [79]				
u_{in}	[m·s^{-1}]	1.99×10^{-5}		
Osmotic transport analysis [187]				
A_{Lp}	[m^2·s·kg^{-1}]	9.1×10^{-6}		
A_{Ps}	[m·s^{-1}]	1.2×10^{12}		
$E_{A,Lp}$	[J·mol^{-1}]	45.73×10^{3}		
$E_{A,Ps}$	[J·mol^{-1}]	107.40×10^{3}		
Parameters of cells [145, 187]				
A	[m^2]	8.04×10^{-10}		
r_{cell}	[m]	8×10^{-6}		
Chemical properties of bath solution [187, 208]				
		DMSO	**KCl**	**H_2O**
ρ_j	[kg·m^{-3}]	1.1×10^{3}	1.98×10^{3}	997
ν_j	[m^2·s^{-1}]	1.945×10^{-6}	–	10^{-6}
$M_{at.,j}$	[kg·mol^{-1}]	7.813×10^{-4}	7.455×10^{-4}	1.802×10^{-4}
B_j	[kg·mol^{-1}]	0.108	0	–
v_j	[L·mol^{-1}]	7.097×10^{-4}	3.75×10^{-4}	1.807×10^{-4}
k_{diss}	–	–	1.772	–

Table 6.8. Initial data [129]

Parameters		Values
T^0	[°C]	22
$c_d^{e,0}$	[mol·m^{-3}]	0
$w_k^{e,0}$	[% (*w*/*w*)]	0.85
u^0	[m·s^{-2}]	0
$c^{i,0}$	[mol·m^{-3}]	0
$V_w^0 = V_{cell}^0$	[m^3]	2.144×10^{-15}
N_d^0	[mol]	0
$V_{cell}^0 = V_0$	[m^3]	2.144×10^{-15}

Table 6.9. LT protocol according to Yu et al. [187]

Phase	**Step**	**Duration, *t* [min]**	**Temperature, T_{bath} [°C]**	**Molar concentration, w_{bath} [% (w/w)]**
cooling	1	10	22	10
	2	9.8	22	20
	3	18.2	−5	29
	4	25	−8.5	38
	5	19.8	−16	47
	6	26.4	−23	56
	7	23.8	−35	63
warming	1	23.8	−35	56
	2	26.4	−23	47
	3	19.8	−16	38
	4	25	−8.5	29
	5	18.2	−5	20
	6	29.8	22	0
Total:	13	276	–	–

Let us introduce a numerical model for this problem. The numerical model is based on an explicit scheme of FDM combined with interval arithmetic. Analogously to the earlier examples, the time axis is discretised with a constant time step Δt (compare Equations (5.15) and (6.12)). On the other hand, the geometric mesh differs from the previous approach. Its base is a five-points star, whereas the nodes where the velocity vector is stored do not coincide with the nodes representing temperature and molar concentration. The mesh step between individual nodes are h_1 and h_2 in the r- and z-axis directions, respectively. In contrast, the value of mesh step between nodes for the velocity vector component and for the other components (interval temperature, interval molar concentration, etc.) is equal to $h_2/2$. This concept is demonstrated in Figure 6.19.

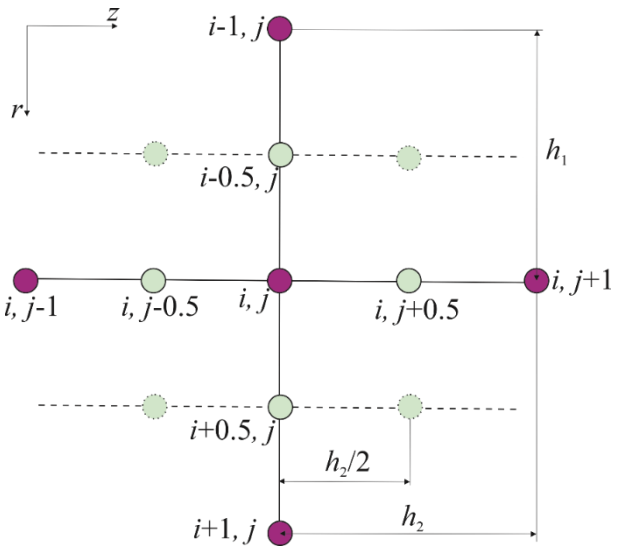

Figure 6.19. Five-points star

The derivations for the thermal analysis correspond to the procedure presented in Example 1 in Chapter 5. For this reason, it was decided to show only the final relationship for determining the interval temperature at the internal nodes:

$$\overline{T}_{i,j}^{\,f} = \overline{T}_{i,j}^{\,f-1} + \frac{\Delta t \overline{k}}{\overline{c}} \left[\frac{1}{r_{i,j}} \frac{\overline{T}_{i+1,j}^{\,f-1} - \overline{T}_{i-1,j}^{\,f-1}}{2h_1} + \frac{\overline{T}_{i+1,j}^{\,f-1} - 2\overline{T}_{i,j}^{\,f-1} + \overline{T}_{i-1,j}^{\,f-1}}{h_1^2} + \frac{\overline{T}_{i,j+1}^{\,f-1} - 2\overline{T}_{i,j}^{\,f-1} + \overline{T}_{i,j-1}^{\,f-1}}{h_2^2} \right], \tag{6.87}$$

where $i = 2, 3, \ldots, n-1$ and $j = 2, 3, \ldots, m-1$; n and m are the number of nodes.

It should be remembered that in the case of an explicit scheme, the stability condition has to be respected (see Equation (5.22)).

In the next step, a relation was prepared to calculate the interval molar concentration at internal nodes. Three main components can be distinguished in the convection-diffusion equation (Equation (6.72)). The first of them is the time derivative of the interval molar concentration, which is replaced by the differential quotient – see Equation (6.13). The second component is related to the diffusion phenomenon. Its derivation is presented in Example 1 in Chapter 6 (Subsection 6.2.1) – compare with Equations (6.14)-(6.18). The last element contains the velocity vector **u** for which the differential quotient has the following form [129]:

$$\left[\mathbf{u}\cdot\nabla\overline{c}_d^{\,e}\right]_{i,j}^{f-1}=\frac{\left(u\overline{c}_d^{\,e}\right)_{i,j+1}^{f-1}-\left(u\overline{c}_d^{\,e}\right)_{i,j-1}^{f-1}}{2h_2}, \tag{6.88}$$

where $i = 2, 3, \ldots, n-1$ and $j = 2, 3, \ldots, m-1$.

The convection-diffusion equation using the explicit scheme of the interval version of FDM can be expressed as follows:

$$\frac{\left(\overline{c}_d^{\,e}\right)_{i,j}^{f}-\left(\overline{c}_d^{\,e}\right)_{i,j}^{f-1}}{\Delta t}=\sum_{a=1}^{4}\frac{\Phi_e}{\overline{W}_e^{\,f-1}}\left[\left(\overline{c}_d^{\,e}\right)_{e}^{f-1}-\left(\overline{c}_d^{\,e}\right)_{i,j}^{f-1}\right]-\frac{\left(u\overline{c}_d^{\,e}\right)_{i,j+1}^{f-1}-\left(u\overline{c}_d^{\,e}\right)_{i,j-1}^{f-1}}{2h_2}, \tag{6.89}$$

and after transformation:

$$\left(\overline{c}_d^{\,e}\right)_{i,j}^{f}=\left(\overline{c}_d^{\,e}\right)_{i,j}^{f-1}+\Delta t\left[\sum_{a=1}^{4}\frac{\Phi_e}{\overline{W}_e^{\,f-1}}\left[\left(\overline{c}_d^{\,e}\right)_{e}^{f-1}-\left(\overline{c}_d^{\,e}\right)_{i,j}^{f-1}\right]-\frac{\left(u\overline{c}_d^{\,e}\right)_{i,j+1}^{f-1}-\left(u\overline{c}_d^{\,e}\right)_{i,j-1}^{f-1}}{2h_2}\right], \tag{6.90}$$

where $i = 2, 3, \ldots, n-1$ and $j = 2, 3, \ldots, m-1$, the individual a corresponds to $e = \{(i, j+1); (i, j-1); (i+1, j); (i-1, j)\}$, and:

$$\begin{aligned}
\overline{W}_e^{\,f-1}&=\frac{h_1}{2\overline{D}\left(\overline{T}_{i,j}^{\,f-1}\right)}+\frac{h_1}{2\overline{D}\left(\overline{T}_{e}^{\,f-1}\right)}, \quad \text{if} \quad e=\left\{(i+1,j)\ \text{or}\ (i-1,j)\right\},\\
\overline{W}_e^{\,f-1}&=\frac{h_2}{2\overline{D}\left(\overline{T}_{i,j}^{\,f-1}\right)}+\frac{h_2}{2\overline{D}\left(\overline{T}_{e}^{\,f-1}\right)}, \quad \text{if} \quad e=\left\{(i,j+1)\ \text{or}\ (i,j-1)\right\},
\end{aligned} \tag{6.91}$$

$$\begin{cases}
\Phi_e=\dfrac{1}{h_1}\left(1-\dfrac{h_1}{2r_{i,j}}\right), & \text{if} \quad e=(i-1,j),\\
\Phi_e=\dfrac{1}{h_1}\left(1+\dfrac{h_1}{2r_{i,j}}\right), & \text{if} \quad e=(i+1,j),\\
\Phi_e=\dfrac{1}{h_2}, & \text{if} \quad e=\left\{(i,j+1)\ \text{or}\ (i,j-1)\right\}.
\end{cases} \tag{6.92}$$

It is worth considering the multiplication product of the velocity vector component u and the interval molar concentration $\bar{c}_d^e$. It is calculated from the relationship [142, 163]:

$$\begin{aligned}\left(u\bar{c}_d^e\right)_{i,j+1}^{f-1} &= \begin{cases} u_{j+0.5}^{f-1}\left(\bar{c}_d^e\right)_{i,j}^{f-1}, & u_{j+0.5}^{f-1} \geq 0, \\ u_{j+0.5}^{f-1}\left(\bar{c}_d^e\right)_{i,j+1}^{f-1}, & u_{j+0.5}^{f-1} < 0, \end{cases} \\ \left(u\bar{c}_d^e\right)_{i,j-1}^{f-1} &= \begin{cases} u_{j-0.5}^{f-1}\left(\bar{c}_d^e\right)_{i,j-1}^{f-1}, & u_{j-0.5}^{f-1} \geq 0, \\ u_{j-0.5}^{f-1}\left(\bar{c}_d^e\right)_{i,j}^{f-1}, & u_{j-0.5}^{f-1} < 0. \end{cases} \end{aligned} \tag{6.93}$$

Importantly, for Equation (6.90), it must satisfy the stability condition indicated in Equations (6.20)-(6.21).

Another coupled phenomenon modelled numerically is the osmotic transport of CPA particles and water into intracellular solution across the cell membrane. In this case, only the differential quotient is introduced instead of the time derivative (compare with Equations (6.54)-(6.55)):

$$\left(\bar{V}_w\right)_{i,j}^{f} = \left(\bar{V}_w\right)_{i,j}^{f-1} - \Delta t \cdot \bar{L}_p\left(\bar{T}_{i,j}^{f-1}\right) AR\bar{T}_{i,j}^{f-1}\left(\bar{M}^e - \bar{M}^i\right) \tag{6.94}$$

$$\left(\bar{N}_d\right)_{i,j}^{f} = \left(\bar{N}_d\right)_{i,j}^{f-1} + \Delta t \cdot \bar{P}_s\left(\bar{T}\right) A\left(\bar{M}^e - \bar{M}^i\right) \tag{6.95}$$

As in previous examples, relationships for the boundary and initials conditions were derived:

For Γ_1 ($j = m$; $i = 2, 3, \ldots, n\text{-}1$):

$$\begin{cases} \bar{q}_\Gamma\left(r,z,t\right) = -\mathbf{n}\bar{k}\cdot\nabla\bar{T} = 0, & \text{therefore} \quad \bar{T}_{i,m}^{f} = \bar{T}_{i,m-1}^{f}, \\ \bar{q}_\Gamma\left(r,z,t\right) = -\mathbf{n}\bar{D}\cdot\nabla\bar{c}_d^e = 0, & \text{therefore} \quad \left(\bar{c}_d^e\right)_{i,m}^{f} = \left(\bar{c}_d^e\right)_{i,m-1}^{f}. \end{cases} \tag{6.96}$$

For Γ_2 ($j = 1$; $i = 2, 3, \ldots, n\text{-}1$):

$$\begin{cases} \bar{T}_{i,1}^{f} = \bar{T}_{i,1}^{f} + \Delta t \dfrac{\bar{k}}{\bar{c}_V}\left[\dfrac{1}{r_{i,j}}\dfrac{\bar{T}_{i+1,1}^{f-1} - \bar{T}_{i-1,1}^{f-1}}{2h_1} + \dfrac{\bar{T}_{i+1,1}^{f-1} - 2\bar{T}_{i,1}^{f-1} + \bar{T}_{i-1,1}^{f-1}}{h_1^2}\right. \\ \qquad \left. + \dfrac{1}{h_2}\left(\dfrac{\bar{T}_{i,2}^{f-1} - \bar{T}_{i,1}^{f-1}}{h_2} - \dfrac{T_{bath}^{f-1} - \bar{T}_{i,1}^{f-1}}{\dfrac{1}{2}h_2 + \dfrac{\bar{k}}{\alpha_\Gamma}}\right)\right], \\ \left(\bar{c}_d^e\right)_{i,1}^{f} = 0.9c_\Gamma. \end{cases} \tag{6.97}$$

For Γ_3 ($i = n$; $j = 2, 3, \ldots, m\text{-}1$):

$$\begin{cases} \overline{T}_{n,j}^{f} = \overline{T}_{n,1}^{f} + \Delta t \dfrac{\overline{k}}{\overline{c}_V} \left[\left(\dfrac{1}{h_1} + \dfrac{1}{2r_{i,j}} \right) \dfrac{T_{bath}^{f-1} - \overline{T}_{i,j}^{f-1}}{\dfrac{1}{2}h_1 + \dfrac{\overline{k}}{\alpha_\Gamma}} - \dfrac{\overline{T}_{i,j}^{f-1} - \overline{T}_{i,j-1}^{f-1}}{h_1^2} \right. \\ \qquad \left. - \dfrac{1}{r_{i,j}} \dfrac{\overline{T}_{i,j}^{f-1} - \overline{T}_{i,j-1}^{f-1}}{2h_1} + \dfrac{\overline{T}_{n,j+1}^{f-1} - 2\overline{T}_{n,j}^{f-1} + \overline{T}_{n,j-1}^{f-1}}{h_2^2} \right], \\ \left(\overline{c}_d^{\,e} \right)_{i,1}^{f} = 0.9 c_\Gamma . \end{cases} \tag{6.98}$$

For Γ_4 ($i = 1$; $j = 2, 3, \ldots, m\text{-}1$):

$$\begin{cases} \overline{q}_\Gamma (r,z,t) = -\mathbf{n}\overline{k} \cdot \nabla \overline{T} = 0, \quad \text{therefore} \quad \overline{T}_{1,j}^{f} = \overline{T}_{2,j}^{f}, \\ \overline{q}_\Gamma (r,z,t) = -\mathbf{n}\overline{D} \cdot \nabla \overline{c}_d^{\,e} = 0, \quad \text{therefore} \quad \left(\overline{c}_d^{\,e} \right)_{1,j}^{f} = \left(\overline{c}_d^{\,e} \right)_{2,j}^{f}. \end{cases} \tag{6.99}$$

In addition, the following constant values are given in the entire domain ($i = 1, 2, \ldots, n$ and $j = 1, 2, \ldots, m$):

$$\begin{cases} u_j^{f} = u_{in}, & \text{where } j = 0.5, 1.5, \ldots, m + 0.5, \\ \left(c_k^{e} \right)_{i,j}^{f} = c_{k,bath}, & \text{where } i = 1, 2, \ldots, n;\ j = 1, 2, \ldots, m. \end{cases} \tag{6.100}$$

The following input variables were introduced into the numerical model: the time step $\Delta t = 0.001$ s, the mesh steps $h_1 = 4 \cdot 10^{-4}$ m, $h_2 = 5 \cdot 10^{-4}$ m and $h_2/2 = 2.25 \cdot 10^{-4}$ m (the step between the nodes with the values of the velocity vector component u and the other variables).

To solve the problem, an algorithm has been developed in the Embarcadero Delphi 10.4 Community Edition environment (Embarcadero Technologies, Inc.). Figure 6.20 provides a flowchart briefly describing the calculation procedures.

Let us present the results obtained in the simulation. Figure 6.21 shows the change in interval temperature as a function of time for a selected portion of the step 3 in the cooling phase (a) and the step 4 in the warming phase (b). Obviously, the red line indicates the upper limit and the blue line the lower limit of the interval temperature. In all graphs relating to this example, the results were prepared for points with coordinates $r = 0.0002$ m and $z = 0.0548$ m (point A) and $r = 0.0006$ m and $z = 0.00075$ m (point B). Figure 6.22, on the other hand, presents the temperature distribution in the domain after 20 s of step 7 of the cooling phase.

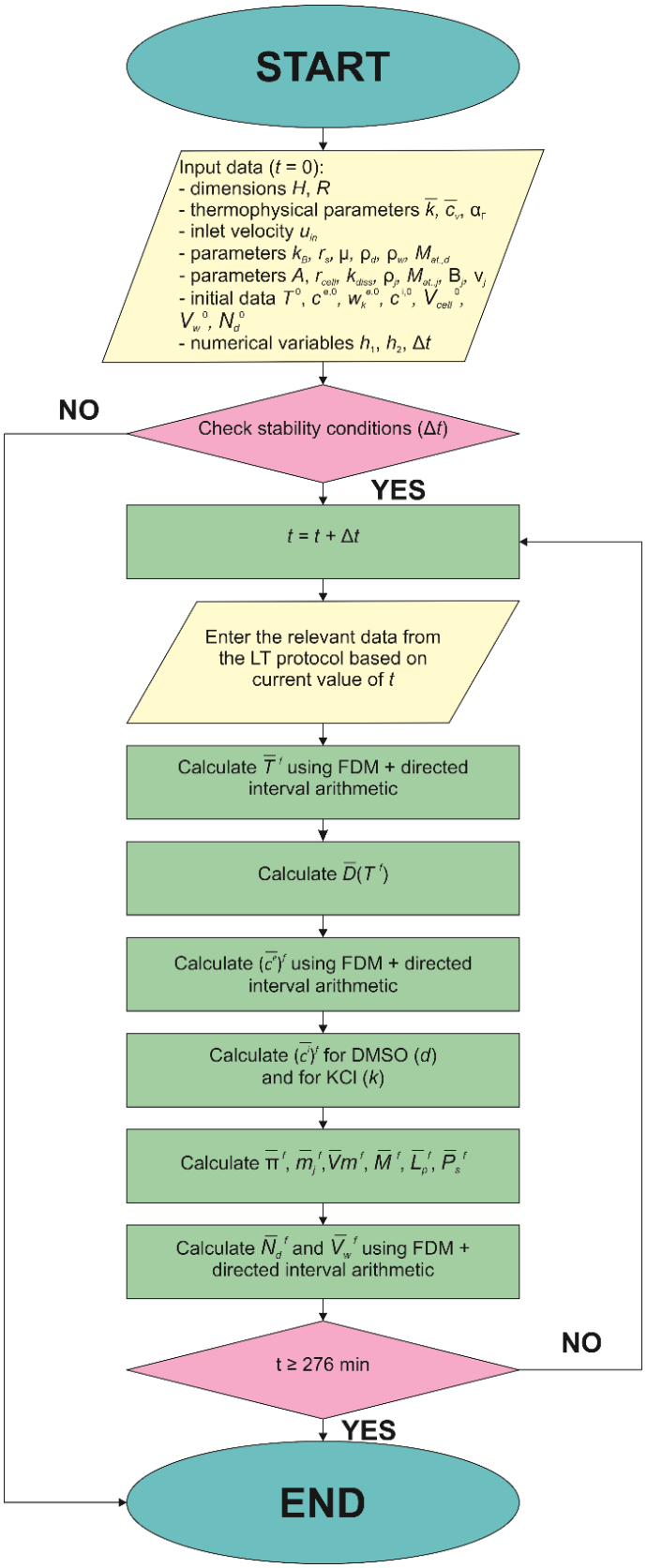

Figure 6.20. Flowchart of algorithm to simulate multiphysical coupled field (interval arithmetic)

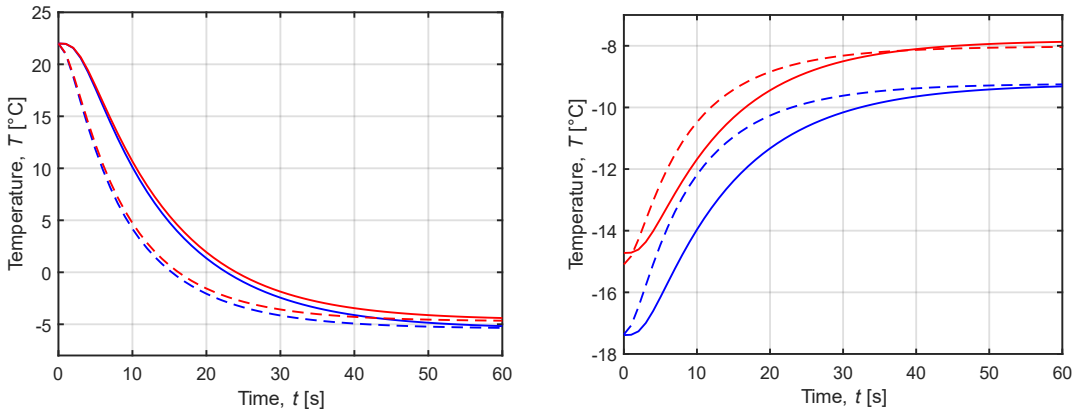

(a) (b)

Figure 6.21. Interval temperature as a function of time for a change (a) from 22 to −5 °C and (b) from −16 °C to −8.5 °C; point A – solid line, point B – dashed line

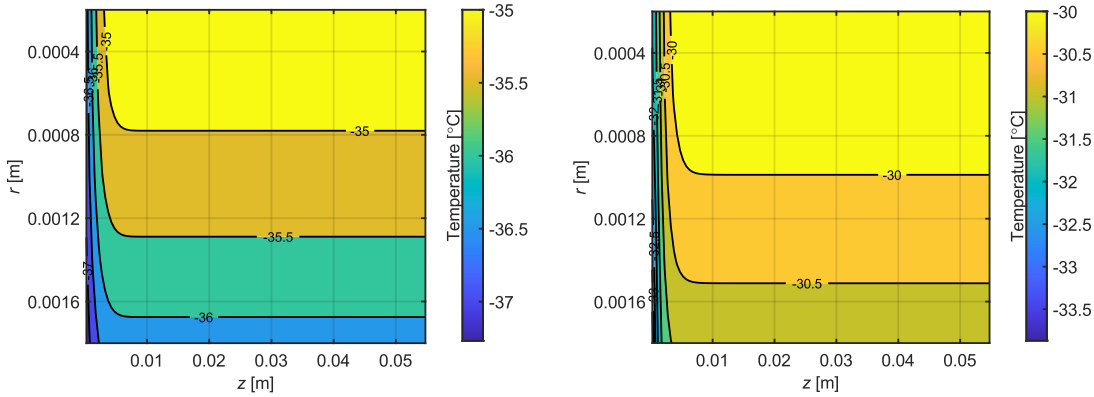

(a) (b)

Figure 6.22. Distribution of the interval temperature in 20 s of step 7 for cooling phase: (a) $\bar{T}^{-}$ and (b) $\bar{T}^{+}$

Figure 6.23, in turn, depicts the curve of interval mass fraction of DMSO change as a function of time in the extracellular (a) and intracellular (b) space. The results were prepared for mean values of interval mass fraction for the entire simulation. In the graph, the solid and the dashed lines indicate the results for point A and for point B, respectively. It can be seen that there is a difference in the concentration of DMSO for points A and B. The point B, which is located closer to the inlet, faster reaches the concentration given by the bath solution. In addition, the curves with asterisks represent the mean results obtained for **u** = 0. It can be concluded that, for microfluidic systems, it is important to specify the appropriate input velocity for the bath solution. The lack of the velocity vector (**u** = 0) can cause the sample to be inadequately enriched in CPA and consequently, for example, induce the formation of ice crystals.

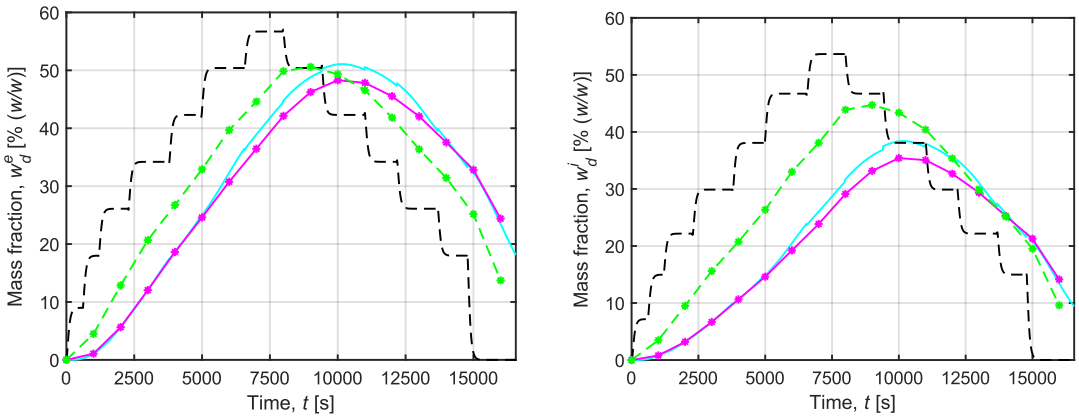

(a) (b)

Figure 6.23. Mean value of interval mass fraction as a function of time over whole simulation time in: (a) extracellular solution; (b) intracellular solution; point A – solid line, point B – dashed line; asterisks – results for **u** = 0

Figure 6.24 illustrates the history of interval mass fraction for a certain moment of step 3 in the cooling phase in point A. Figure 6.25 shows maps of the mean values of interval mass fraction distribution for the extracellular (a) and intracellular (b) region, respectively, after 20 s of step 7 of the cooling phase. It can be seen that the two graphs are similar to each other, which confirms the fact that the magnitude of CPA concentration in the extracellular matrix directly influences the presence of CPA molecules inside the cells.

The example also examines the response of cells to phenomena induced by osmotic transport. Figure 6.26 shows the progression of mean values of the interval number of DMSO moles (a) and the interval water volume (b) in the cells as a function of time. It can be seen that results in point A coincide with results obtained for case when **u** = 0. However, for point B, the discrepancy between these curves is more significant. This shows that the speed of CPA delivery has a greater impact for nodes located closer to the inlet. Figure 6.27 demonstrates interval number of DMSO moles (a) and the interval water volume (b) in the cells at a certain part of step 3 during the cooling phase.

The normalised interval cell volume was determined on the basis of these two quantities (Figure 6.28). It can be seen that the cells of the biological sample are compressed and the dehydration phenomenon dominates for the longer duration of the process.

Table 6.10 contains the comparison of the selected results at point A For two variants of the simulation when **u** ≠ 0 and **u** = 0.

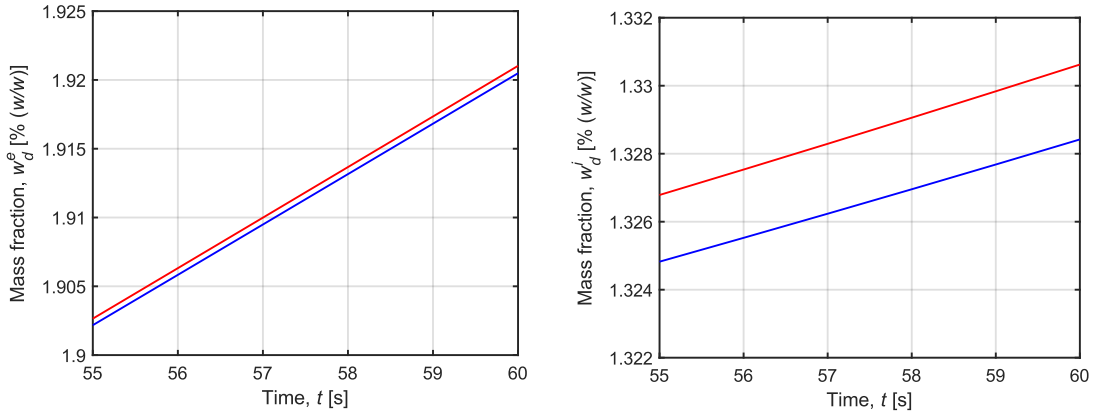

(a) (b)

Figure 6.24. Interval mass fraction as a function of time in extracellular (a) and intracellular (b) solution in certain moment of step 3 during cooling phase

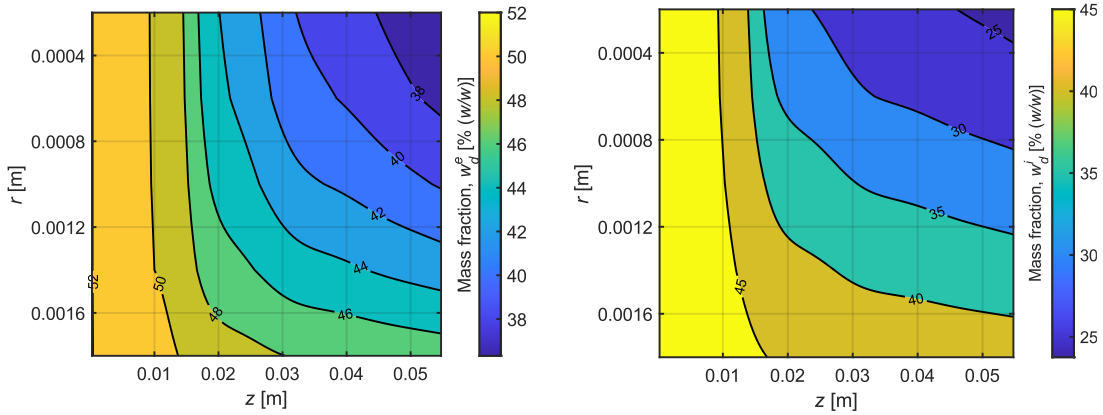

(a) (b)

Figure 6.25. Distribution of mean values of the interval mass fraction for step 7 after 20 s in the cooling phase for: (a) extracellular solution; (b) intracellular solution

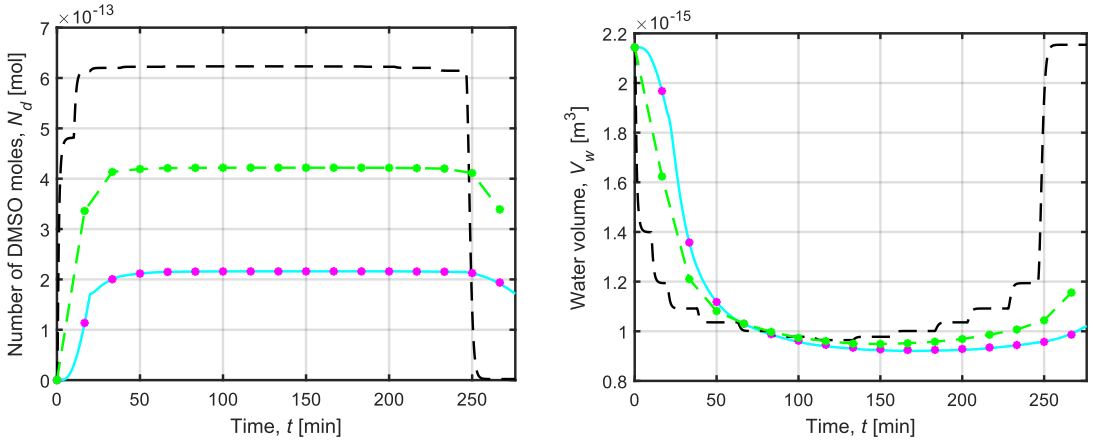

(a) (b)

Figure 6.26. Mean values of interval number of DMSO moles (a) and interval water volume (b) in cell as a function of time over whole simulation time; point A – solid line; point B – dashed line; asterisks – results for **u** = 0

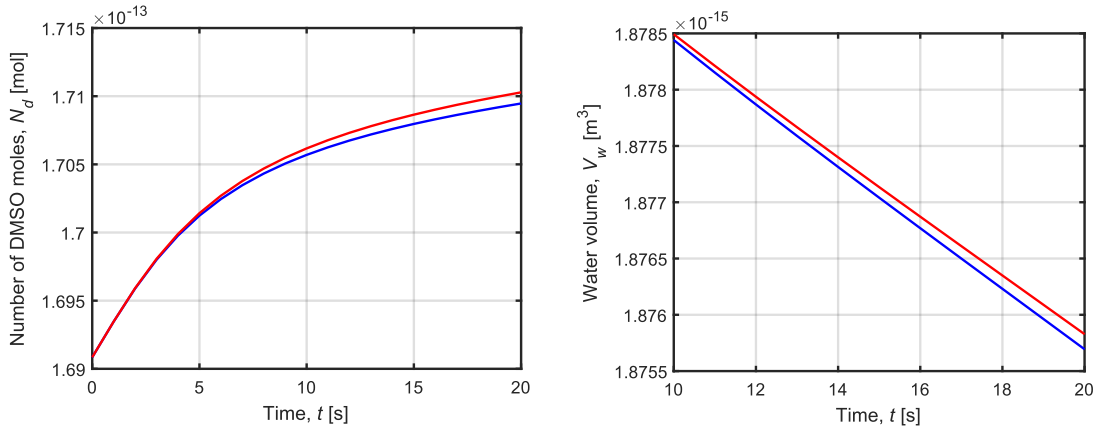

(a) (b)

Figure 6.27. Interval number of DMSO moles (a) and interval water volume (b) in cell as a function of time in certain moment of step 3 during cooling phase

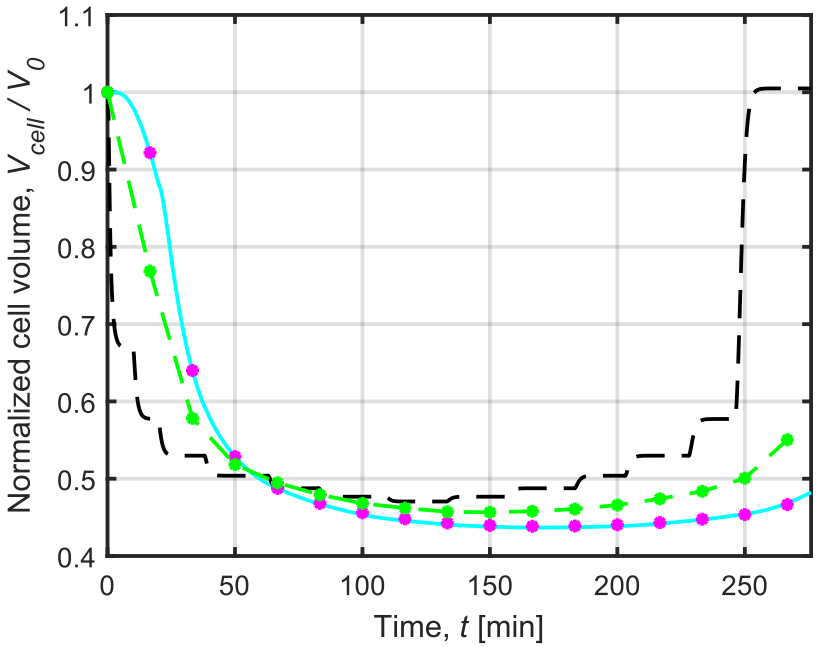

Figure 6.28. Mean value of normalized interval cell volume over whole simulation time; point A – solid line; point B – dashed line; asterisks – results for **u** = 0

Table 6.10. Selected results for simulations when **u** = 0 and **u** ≠ 0 at point A

Phase	Step	$\bar{\omega}_d^e$ [%], when **u = 0**	$\bar{\omega}_d^e$ [%], when **u** ≠ 0	$\bar{\omega}_d^i$ [%], when **u = 0**	$\bar{\omega}_d^i$ [%] when **u** ≠ 0	$\bar{N}_d$ ×10^{-13} [mol], when **u = 0**	$\bar{N}_d$ ×10^{-13} [mol], when **u** ≠ 0	$\bar{V}_w$ ×10^{-15}, when **u =0** [m^3]	$\bar{V}_w$ ×10^{-15} [m^3], when **u** ≠ 0
Cooling	1	[0.25; 0.25]	[0.25; 0.25]	[0.18; 0.18]	[0.18; 0.18]	[0.29; 0.29]	[0.29; 0.29]	[2.14; 2.14]	[2.14; 2.14]
	2	[1.71; 1.71]	[1.71; 1.71]	[1.29; 1.29]	[1.29; 1.29]	[1.69; 1.69]	[1.69; 1.69]	[2.10; 2.10]	[2.10; 2.10]
	3	[7.34; 7.38]	[7.34; 7.38]	[4.08; 4.13]	[4.08; 4.13]	[2.05; 2.07]	[2.05; 2.07]	[1.88; 1.88]	[1.88; 1.88]
	4	[17.20; 17.34]	[17.20; 17.34]	[9.75; 9.93]	[9.75; 9.93]	[2.13; 2.17]	[2.13; 2.16]	[1.26; 1.26]	[1.26; 1.26]
	5	[24.27; 24.53]	[24.56; 24.81]	[14.60; 14.93]	[14.60; 14.93]	[2.13; 2.18]	[2.13; 2.18]	[1.04; 1.04]	[1.04; 1.04]
	6	[33.76; 34.24]	[36.00; 36.38]	[21.60; 22.21]	[23.50; 24.05]	[2.14; 2.18]	[2.14; 2.18]	[0.99; 0.99]	[0.99; 0.99]
	7	[41.66; 42.38]	[44.44; 44.93]	[28.38; 29.32]	[31.04; 31.81]	[2.14; 2.18]	[2.14; 2.18]	[0.95; 0.95]	[0.95; 0.95]
Warming	1	[47.21; 47.91]	[50.02; 50.42]	[33.88; 34.90]	[36.83; 37.56]	[2.14; 2.18]	[2.14; 2.18]	[0.93; 0.93]	[0.93; 0.93]
	2	[47.62; 48.08]	[50.45; 50.69]	[34.43; 35.20]	[37.42; 37.98]	[2.14; 2.18]	[2.14; 2.18]	[0.92; 0.92]	[0.92; 0.92]
	3	[45.15; 45.53]	[47.62; 47.92]	[32.03; 32.70]	[34.55; 35.15]	[2.14; 2.18]	[2.14; 2.18]	[0.92; 0.92]	[0.92; 0.92]
	4	[38.92; 39.24]	[39.81; 40.06]	26.21; 26.74]	27.02; 27.50]	[2.13; 2.18]	[2.13; 2.18]	[0.94; 0.94]	[0.94; 0.94]
	5	[34.09; 34.35]	[33.87; 34.04]	[22.00; 22.43]	[21.81; 22.17]	[2.12; 2.17]	[2.12; 2.17]	[0.95; 0.95]	[0.96; 0.96]
	6	[19.22; 19.34]	[18.08; 18.13]	[10.13; 10.34]	[9.32; 9.48]	[1.74; 1.78]	[1.69; 1.73]	[1.01; 1.01]	[1.02; 1.02]

6.4.2. Example 3 – fuzzy numbers

In the next example, coupled phenomena are modelled for a microfluidic system during the cryopreservation process applying fuzzy arithmetic. Using the previously prepared relationships, the governing equations are determined.

Knowing that the problem involves a two-dimensional domain in a cylindrical system, the heat transfer equation including fuzzy numbers is of the form (compare with Equations (5.27) and (5.28)):

$$\tilde{c}_V \frac{\partial \tilde{T}(r,z,t)}{\partial t} = \tilde{k}\left[\frac{1}{r}\frac{\partial}{\partial r}\left(r\frac{\partial \tilde{T}(r,z,t)}{\partial r}\right)+\frac{\partial^2 \tilde{T}(r,z,t)}{\partial z^2}\right], \tag{6.101}$$

or:

$$\tilde{c}_V \frac{\partial \tilde{T}(r,z,t)}{\partial t} = \tilde{k}\left[\frac{1}{r}\frac{\partial \tilde{T}(r,z,t)}{\partial r}+\frac{\partial^2 \tilde{T}(r,z,t)}{\partial r^2}+\frac{\partial^2 \tilde{T}(r,z,t)}{\partial z^2}\right]. \tag{6.102}$$

Meanwhile, the mass transfer in macroscopic terms is defined by the convection-diffusion equation. Considering that the mass transfer is coupled to a fuzzy temperature via a fuzzy diffusion coefficient, this equation is expressed (see also Equations (6.26) and (6.70)):

$$\begin{aligned}\frac{\partial \tilde{c}_d^e(r,z,t)}{\partial t} = {} & \frac{1}{r}\frac{\partial}{\partial r}\left(\tilde{D}\left(\tilde{T}\right)r\frac{\partial \tilde{c}_d^e(r,z,t)}{\partial r}\right)+\frac{\partial}{\partial z}\left(\tilde{D}\left(\tilde{T}\right)\frac{\partial \tilde{c}_d^e(r,z,t)}{\partial z}\right) \\ & -u(z,t)\frac{\partial \tilde{c}_d^e(r,z,t)}{\partial z},\end{aligned} \tag{6.103}$$

where:

$$\tilde{D}\left(\tilde{T}\right) = \frac{k_B \tilde{T}}{6\pi r_s \mu}. \tag{6.104}$$

It should be noted that this time the velocity vector contains only one non-zero component relative to the *z*-direction (**u** = [0; *u*(*z*, *t*); 0]). The derivation of its value from the Navier-Stokes equations are shown in Equations (6.73)-(6.75). Finally, the following relationship has been obtained:

$$\frac{\partial u(z,t)}{\partial t} = 0. \tag{6.105}$$

The phenomenon of osmotic transport is described using the 2-P formalism (compare with Equations (6.36)-(6.37)):

$$\frac{\mathrm{d}\tilde{V}_w(t)}{\mathrm{d}t} = -\tilde{L}_p\left(\tilde{T}\right) ARTilde\left(r,z,t\right)\left(\tilde{M}^e - \tilde{M}^i\right), \tag{6.106}$$

$$\frac{\mathrm{d}\tilde{N}_d(t)}{\mathrm{d}t} = \tilde{P}_s\left(\tilde{T}\right) A\left(\tilde{M}^e - \tilde{M}^i\right). \tag{6.107}$$

The mathematical model has to be supplemented with boundary and initial conditions defined similarly to the case of interval numbers presented in Subsection 6.4.1 (compare with Equations (6.78)-(6.85)).

For the boundary Γ_1, the boundary conditions are of the form:

$$\begin{cases} \tilde{q}_\Gamma\left(r,z,t\right) = -\mathbf{n}\tilde{k}\cdot\nabla\tilde{T} = \tilde{0}, \\ \tilde{q}_\Gamma\left(r,z,t\right) = -\mathbf{n}\tilde{D}\cdot\nabla\tilde{c}_d^e = \tilde{0}, \\ \dfrac{\partial u(z,t)}{\partial n} = 0. \end{cases} \tag{6.108}$$

For the boundary Γ_2:

$$\begin{cases} \tilde{q}_\Gamma\left(r,z,t\right) = -\mathbf{n}\tilde{k}\cdot\nabla\tilde{T} = \alpha_\Gamma\left[\tilde{T}\left(r,z,t\right) - T_{bath}\right], \\ \tilde{c}_d^e = 0.9c_\Gamma, \\ u\left(z,t\right) = u_{in}. \end{cases} \tag{6.109}$$

For the boundary Γ_3:

$$\begin{cases} \tilde{q}_\Gamma\left(r,z,t\right) = -\mathbf{n}\tilde{k}\cdot\nabla\tilde{T} = \alpha_\Gamma\left[\tilde{T}\left(r,z,t\right) - T_{bath}\right], \\ \tilde{c}_d^e = 0.9c_\Gamma. \end{cases} \tag{6.110}$$

For the boundary Γ_4:

$$\begin{cases} \tilde{q}_\Gamma\left(r,z,t\right) = -\mathbf{n}\tilde{k}\cdot\nabla\tilde{T} = \tilde{0}, \\ \tilde{q}_\Gamma\left(r,z,t\right) = -\mathbf{n}\tilde{D}\cdot\nabla\tilde{c}_d^e = \tilde{0}. \end{cases} \tag{6.111}$$

However, the initial conditions are as follows:

$$\begin{cases} \tilde{T}\left(r,z,0\right)=T^{0}, \\ \tilde{c}_{d}^{e}\left(r,z,0\right)=c_{d}^{e,0}, \\ \tilde{c}_{k}^{e}\left(r,z,0\right)=c_{k}^{e,0}, \\ u\left(z,0\right)=u^{0}, \\ \tilde{V}_{cell}\left(0\right)=V_{cell}^{0}, \\ \tilde{V}_{w}\left(0\right)=V_{w}^{0}, \\ \tilde{N}_{d}\left(0\right)=N_{d}^{0}, \\ \tilde{c}_{k}^{i}(r,z,0)=\tilde{c}_{d}^{i}(r,z,0)=c^{i,0}. \end{cases} \tag{6.112}$$

The inputs to the mathematical model are given in Tables 6.6 and 6.8. In turn, the following thermophysical parameters were introduced as triangular fuzzy numbers: $\tilde{k}$ = (0.492, 0.518, 0.544) W·m^{-1}·K^{-1} and $\tilde{c}_V$ = (3.798·10^6, 3.924·10^6, 4.12·10^6) J·m^{-3}·K^{-1}. The bath solution properties were assumed to change according to the LT protocol by Yu et al. [187], as shown in Table 6.9.

The numerical model for Example 3 using triangular fuzzy numbers was prepared on the basis of the explicit scheme of FDM. First, the time and geometric mesh was established in a similar way as for interval numbers. The time mesh consists of fixed and constant time steps determined according to the relation given in Equation (6.12), where the time step was taken as Δt = 0.001 s. A divergent grid was again used to discretise the domain (see Figure 6.19). This means that the nodes for the velocity vector component are separated by $h_2/2$ from the other nodes. The mesh steps are equal to: $h_1 = 4\cdot10^{-4}$ m, $h_2 = 5\cdot10^{-4}$ m and $h_2/2 = 2.55\cdot10^{-4}$ m.

Using the explicit scheme of FDM, it is possible to determine the relationships for individual variables. As the derivations of these formulas are similar to previous considerations (see Subsection 6.4.1), it was decided to indicate only the final relationships. The fuzzy temperature at the internal nodes is calculated from the fuzzy heat transfer equation (compare with Equation (6.87)):

$$\begin{aligned} \tilde{T}_{i,j}^{f} = \tilde{T}_{i,j}^{f-1} + \frac{\Delta t\tilde{k}}{\tilde{c}_V}\Bigg[& \frac{1}{r_{i,j}}\frac{\tilde{T}_{i+1,j}^{f-1}-\tilde{T}_{i-1,j}^{f-1}}{2h_1} + \frac{\tilde{T}_{i+1,j}^{f-1}-2\tilde{T}_{i,j}^{f-1}+\tilde{T}_{i-1,j}^{f-1}}{h_1^2} \\ & + \frac{\tilde{T}_{i,j+1}^{f-1}-2\tilde{T}_{i,j}^{f-1}+\tilde{T}_{i,j-1}^{f-1}}{h_2^2}\Bigg], \end{aligned} \tag{6.113}$$

where i = 2, 3, …, n – 1 and j = 2, 3, …, m – 1; n and m are the number of nodes. In addition, a stability condition is given for the explicit scheme – see Equation (5.21).

Using the fuzzy convection-diffusion equation, the fuzzy molar concentration at the internal nodes is determined:

$$\left(\tilde{c}_d^e\right)_{i,j}^f = \left(\tilde{c}_d^e\right)_{i,j}^{f-1} + \Delta t\left[\sum_{a=1}^{4}\frac{\Phi_e}{\tilde{W}_e^{f-1}}\left[\left(\tilde{c}_d^e\right)_e^{f-1} - \left(\tilde{c}_d^e\right)_{i,j}^{f-1}\right] - \frac{\left(u\tilde{c}_d^e\right)_{i,j+1}^{f-1} - \left(u\tilde{c}_d^e\right)_{i,j-1}^{f-1}}{2h_2}\right], \tag{6.114}$$

where i = 2, 3, …, n – 1 and j = 2, 3, …, m – 1, the individual a corresponds to $e = \{(i, j+1); (i, j-1); (i+1, j); (i-1, j)\}$, while the fuzzy shape functions are defined as in Equation (6.19). The fuzzy mass diffusion resistances are as follows:

$$\begin{aligned}\tilde{W}_e^{f-1} &= \frac{h_1}{2\tilde{D}\left(\tilde{T}_{i,j}^{f-1}\right)} + \frac{h_1}{2\tilde{D}\left(\tilde{T}_e^{f-1}\right)}, \quad \text{if} \quad e = \left\{\left(i+1, j\right) \text{ or } \left(i-1, j\right)\right\},\\ \tilde{W}_e^{f-1} &= \frac{h_2}{2\tilde{D}\left(\tilde{T}_{i,j}^{f-1}\right)} + \frac{h_2}{2\tilde{D}\left(\tilde{T}_e^{f-1}\right)}, \quad \text{if} \quad e = \left\{\left(i, j+1\right) \text{ or } \left(i, j-1\right)\right\}.\end{aligned} \tag{6.115}$$

The multiplication rules for the velocity vector component and the fuzzy molar concentration are analogous to those presented in Equation (6.93).

Obviously, for the fuzzy mass transfer equation, the stability condition have to be satisfied – see Equation (6.30).

The last important element of the multiscale mathematical model of the cryopreservation process is the description of the osmotic transport phenomenon. The cell response associated with the change the fuzzy number of DMSO moles and the fuzzy volume of water in the intracellular region is expressed by the relations:

$$\left(\tilde{V}_w\right)_{i,j}^f = \left(\tilde{V}_w\right)_{i,j}^{f-1} - \Delta t \cdot \tilde{L}_p\left(\tilde{T}_{i,j}^{f-1}\right) AR\tilde{T}_{i,j}^{f-1}\left(\tilde{M}^e - \tilde{M}^i\right), \tag{6.116}$$

$$\left(\tilde{N}_d\right)_{i,j}^f = \left(\tilde{N}_d\right)_{i,j}^{f-1} + \Delta t \cdot \tilde{P}_s\left(\tilde{T}_{i,j}^{f-1}\right) A\left(\tilde{M}^e - \tilde{M}^i\right), \tag{6.117}$$

where i = 1, 2, …, n and j = 1, 2, …, m.

The procedure for determining the dependencies for boundary nodes is the same as for the previous example considering interval numbers (compare with Equations (6.96)-(6.100)), therefore this part of the numerical model has been omitted for fuzzy numbers.

Based on the mathematical and numerical model presented, an algorithm has been created in Embarcadero Delphi 10.4 Community Edition environment software

(Embarcadero Technologies, Inc.). The flow chart for this example is given in Figure 6.29.

It should be mentioned that also in this example, α-cuts were used for fuzzy numbers, which allowed the simplification of the basic mathematical operations. Figure 6.30 illustrates the variation depending on the value of the parameter α for the interval temperature (a), the interval mass fraction in the extracellular solution (b) as well as the interval number of DMSO moles (c) and the interval volume of water (d) in the intracellular solution. These are the charts for the 20 s simulation time of step 4 in the cooling phase. The results were prepared for the following node: r = 0.0002 m and z = 0.0548 m. It can be concluded that the previously indicated relationship is maintained, according to which the width of the interval decreases with increasing value of the parameter α.

Figures 6.31-6.34 have been prepared to give a better view of certain parts of the simulation. Figure 6.31 depicts the interval temperature as a function of time for step 3 of the cooling phase for α = 0.25 (a) and α = 0.75 (b) for a point with coordinates r = 0.0002 m and z = 0.0548 m. Similar curves are included in Figures 6.32-6.34, which represent the dependence as a function of time of the interval mass fraction (extracellular region), the interval number of DMSO moles, and the interval volume of water in the cell, respectively. It can be clearly seen that for α = 0.25 the width of the interval of the mentioned quantities is greater than for α = 0.75. Table 6.11 presents the selected results for α = 0.5 at given point.

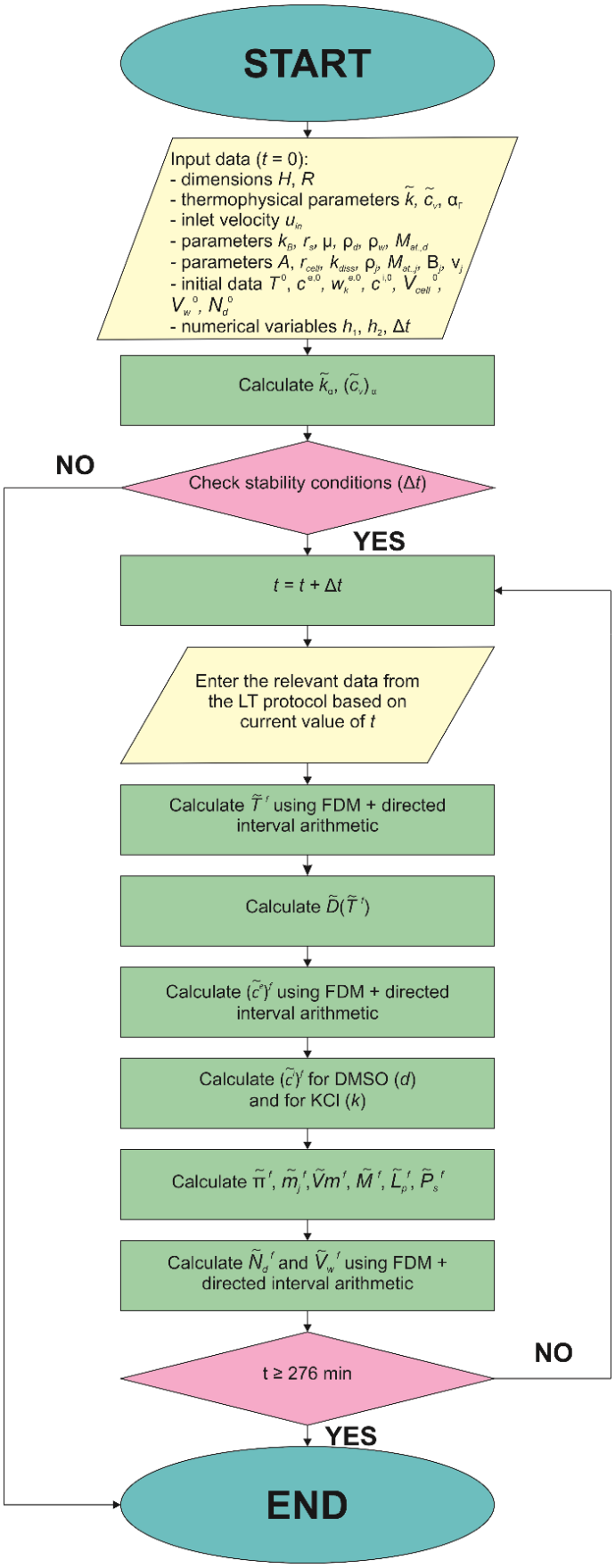

Figure 6.29. Flowchart of algorithm to simulate multiphysical coupled field (fuzzy arithmetic)

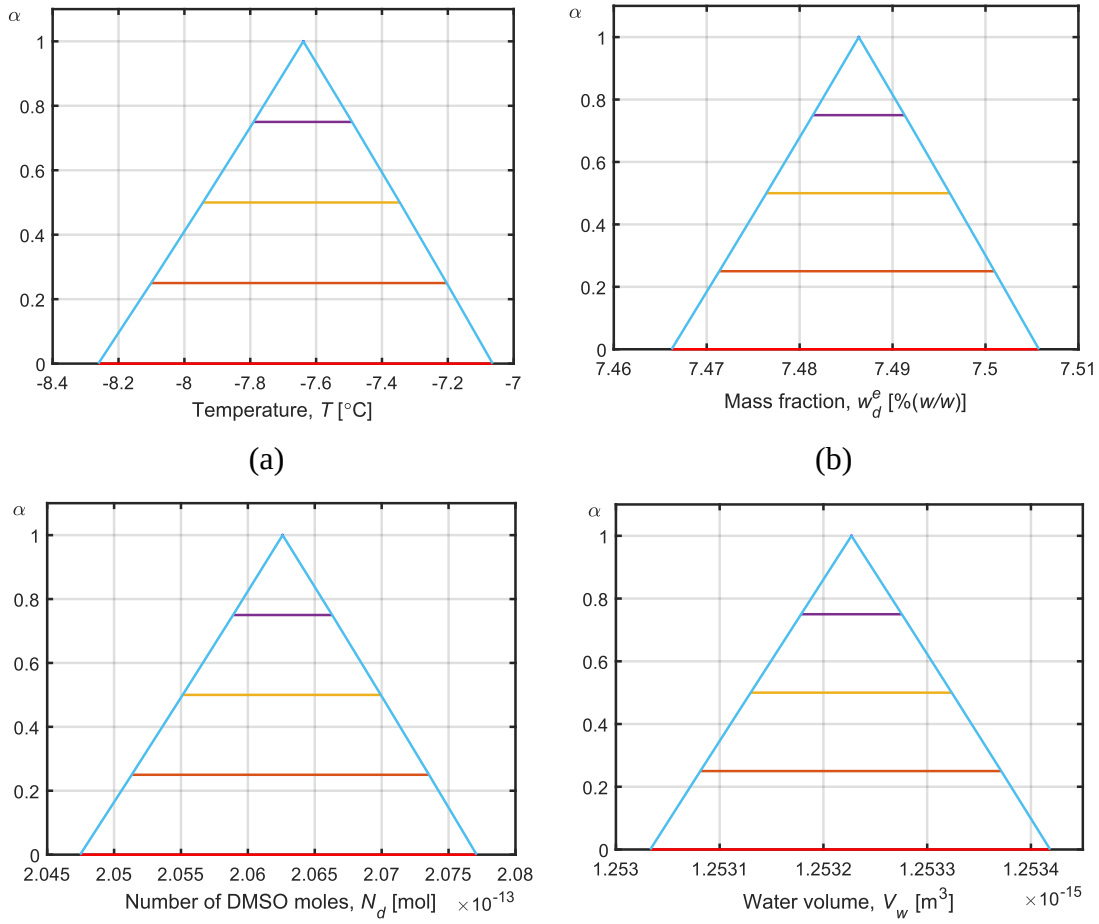

(a) (b)

(c) (d)

Figure 6.30. Values of interval temperature (a), interval extracellular mass fraction (b), interval number of DMSO moles (c) and interval water volume (d) in cell after 20 s of step 4 in cooling phase for different values of parameter α (triangular fuzzy numbers)

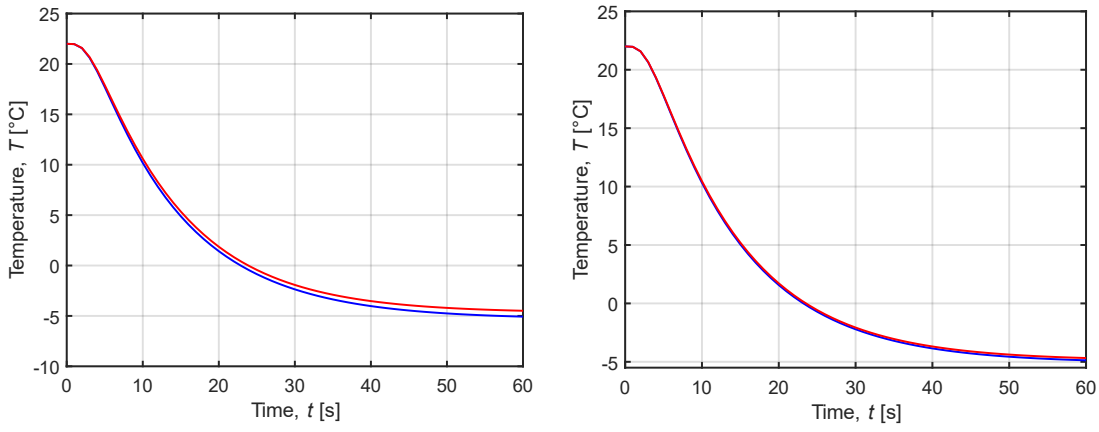

(a) (b)

Figure 6.31. Interval temperature as a function of time for triangular fuzzy numbers: (a) α = 0.25; (b) α = 0.75

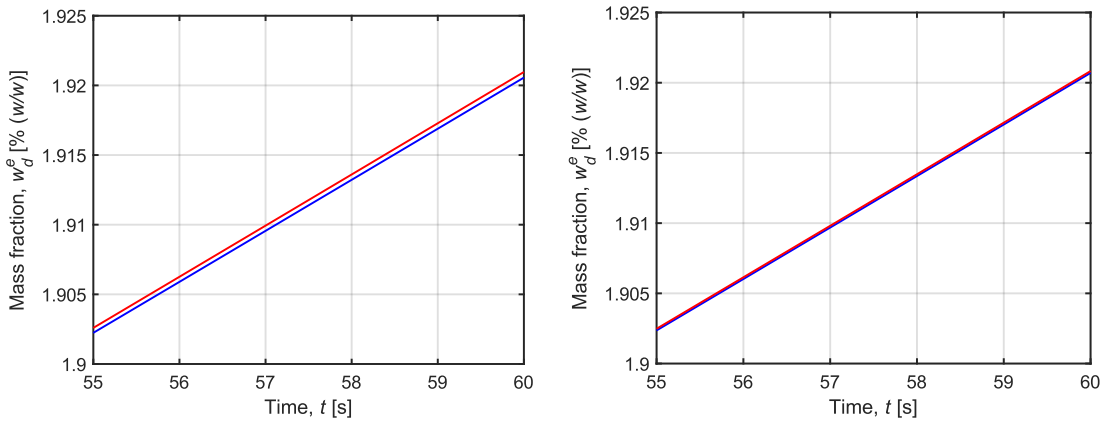

(a) (b)

Figure 6.32. Interval extracellular mass transfer as a function of time for triangular fuzzy numbers: (a) α = 0.25; (b) α = 0.75

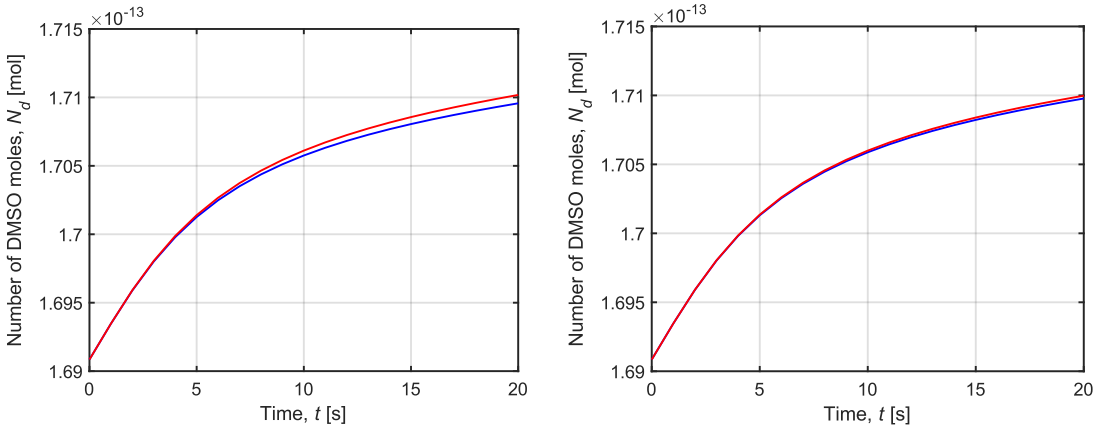

(a) (b)

Figure 6.33. Interval number of DMSO moles in cell as a function of time for triangular fuzzy numbers: (a) α = 0.25; (b) α = 0.75

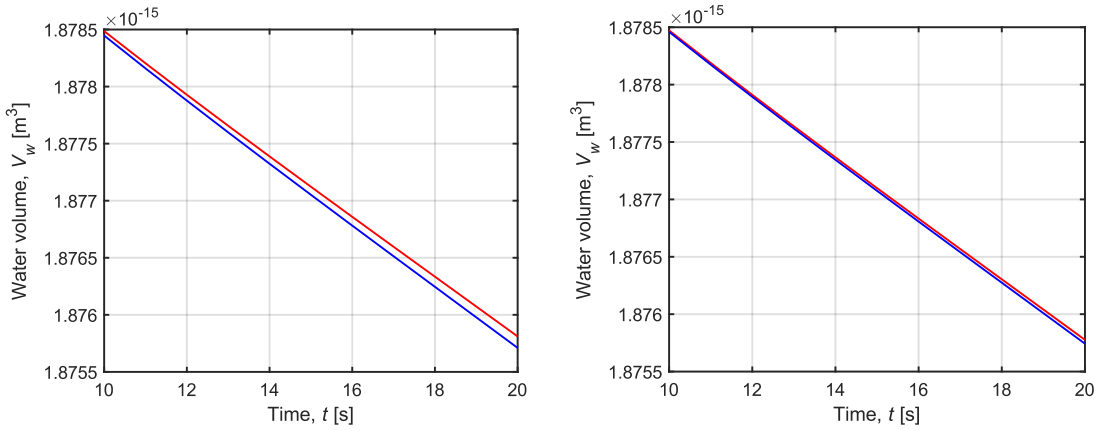

(a) (b)

Figure 6.34. Interval water volume in cell as a function of time for triangular fuzzy numbers: (a) α = 0.25; (b) α = 0.75

Table 6.11. Selected results at given point for α = 0.5

Phase	Step	$\bar{\omega}_d^e$ [%]	$\bar{\omega}_d^i$ [%]	$\bar{N}_d$ $\times 10^{-13}$ [mol]	$\bar{V}_w$ $\times 10^{-15}$ [m^3]
Cooling	1	[0.25; 0.25]	[0.18; 0.18]	[0.29; 0.29]	[2.14; 2.14]
	2	[1.71; 1.71]	[1.29; 1.29]	[1.69; 1.69]	[2.10; 2.10]
	3	[7.34; 7.37]	[4.09; 4.12]	[2.05; 2.07]	[1.88; 1.88]
	4	[17.24; 17.31]	[9.80; 9.89]	[2.14; 2.16]	[1.26; 1.26]
	5	[24.62; 24.75]	[14.68; 14.85]	[2.15; 2.17]	[1.04; 1.04]
	6	[36.10; 36.29]	[23.64; 23.91]	[2.15; 2.17]	[0.99; 0.99]
	7	[44.57; 44.81]	[31.24; 31.62]	[2.15; 2.17]	[0.95; 0.95]
Warming	1	[50.13; 50.32]	[37.02; 37. 39]	[2.15; 2.17]	[0.93; 0.93]
	2	[50.51; 50.63]	[37.56; 37.84]	[2.15; 2.17]	[0.92; 0.92]
	3	[47.69; 47.84]	[34.70; 35.00]	[2.15; 2.17]	[0.93; 0.93]
	4	[39.87; 40.00]	[27.14; 27.38]	[2.15; 2.17]	[0.94; 0.94]
	5	[33.91; 34.00]	[21.90; 22.08]	[2.13; 2.16]	[0.96; 0.96]
	6	[18.09; 18.12]	[9.36; 9.44]	[1.70; 1.72]	[1.02; 1.02]

6.4.3. Summary and conclusions

In summary, Example 3 presents a multiscale model of the cryopreservation process. The problem examines the behaviour of an articular cartilage sample placed in a cylindrical microfluidic system, which is invented according to the idea of Liu et al. [79].

First, the model describes the macroscale phenomena that result directly from the delivery of the bath solution via a microfluidic device. The parameters of the bath solution were again controlled according to the LT procedure according to Yu et al. [187] even though the system is not specifically dedicated to this cryopreservation technique. The fact of bath solution delivery was introduced into the mathematical model through the velocity vector component determined from the Navier-Stokes equations. Analysing mass transfer with fluid flow, in this case both diffusion and advection phenomena occur, defined by the convection-diffusion equation. As for the equation based on the Fick's second law, the convection-diffusion equation is weakly coupled to

the temperature distribution in the biological sample calculated from the Fourier equation. Information extracted from the macroscopic model is implemented into the microscopic model, which focuses on the exchange of components between the cells and the extracellular matrix (osmotic transport phenomenon).

In this example, it is assumed that the thermophysical parameters are imprecisely defined because their deterministic values are determined experimentally. Therefore, two options were considered: thermophysical parameters introduced as interval numbers or triangular fuzzy numbers.

Analysing the results, it is first worth comparing the values of the variables obtained for two cases: when $\mathbf{u} \neq 0$ and when $\mathbf{u} = 0$. This kind of comparison can be seen in the charts prepared for the problem with interval numbers (see Figure 6.23). It can be observed that the discrepancy between these results is significant, mainly in nodes close to the inlet. This means that when modelling, for example, microfluidic systems in which the bath solution is supplied continuously, advection should be included in the mass transfer model. This is an important observation, as researchers are investigating the process of delivering the solution with CPA in relation to its significance on cell damage.

In Example 3, it can be noted that the required temperature is achieved relatively quickly with respect to the individual steps of the LT protocol. In contrast, the mass fraction values in the extracellular matrix are close to the present value of the concentration of the bath solution reduced by a given factor of 0.9. Obviously, the values for $\mathbf{u} = 0$ are underestimated and do not coincide so well with the concentration of the bath solution.

The products of the macroscopic model indicate directly into the results of the microscopic model. It can be stated that the cell volume changes due to osmotic transport. The crucial condition is the range of the normalised volume, which is equal to 0.46 – 2.49 [187], as already mentioned in Example 2 (Subsection 6.3). One can say that in this case the condition is met.

Finally, let us compare the results of the problems for interval and fuzzy numbers, which coincide with each other. It can be observed that the fuzzy results for the $\alpha = 0$ are the same as for interval numbers. However, it should not be forgotten that the nature of the results obtained is different due to different definitions, for example the membership function of them.

In further work on the demonstrated model, it is worth exploring a different protocol to control the temperature and concentration of the bath solution. This involves consideration of the phenomenon of phase transitions and water crystallisation in the sample, including analysis of their nucleation and growth. In addition, the model can be supported by estimates of the changes in freezing temperature that occur with variations in the concentration of CPA.

7. Conclusions and further research recommendations

Theoretical considerations and results of calculations presented in this dissertation lead to the following conclusions:

1. Interval and fuzzy arithmetic are effective instruments for simulating transport phenomena occurring in the cryopreservation process. These methods make it possible to introduce into a mathematical model a set of imprecisely and inaccurately defined parameters, for example experimentally determined quantities describing the thermophysical properties of a given biological tissue, which often depend on many factors, such as age, sex, etc.
2. In the literature, phenomena that occur during cryopreservation are mainly described based on deterministic approach. Behaviour of biological structures is rather random and stochastic, therefore it can be stated that deterministic models are a simplification of natural occurrences. While, stochastic models can be implemented to investigate those problems, which are unfortunately time-consuming. The dissertation presents a novel approach by introducing interval or fuzzy numbers into the model. Consequently, the results are obtained in the form of certain sets (intervals) containing the correct values of computations.
3. Cryopreservation is a complex process that involves many coupled multiphysical phenomena. The complete model should primarily consider heat and mass transfer as well as osmotic transport. It can be noted that Chapter 5 of the work is mainly related to simulation of thermal phenomena, including modelling of phase transitions and crystallisation, while Chapter 6 is devoted to mass transfer at the macroscale and osmotic transport (molecular transfer at the microscale). Undoubtedly, one can observe that the model of the cryopreservation process is a multiscale problem.
4. Example 1 in Chapter 5 (Subsection 5.2) and Examples 1 and 2 in Chapter 6 (Subsections 6.2 and 6.3) demonstrate a multiscale cryopreservation model of an articular cartilage sample using the LT protocol. The particular conclusions are as follows:

4.1. Analysis of the temperature distribution (Subsection 5.2) shows that in the biological tissue, the temperature reaches the desired value relatively quickly compared to the duration of each step.

4.2. In contrast, when considering mass transfer (Subsection 6.2), it can be noted that there are discrepancies in the obtained results compared to data from the literature [116, 187]. This may be caused, for example, by the proposed method of determining the mass diffusion coefficient.

4.3. The transport of moles of DMSO and water across the cell membrane (osmotic transport, Subsection 6.3) was also discussed. Changes in the volume of the cells (chondrocytes) are an indicator of their damage during the process. In this case, the condition, which assumes that the change in normalized volume must be in the range of 0.46 – 2.49 of the initial cell volume, was fulfilled.

5. Example 2 in Chapter 5 (Subsection 5.3) simulates thermal processes including phase transformations by modifying thermophysical parameters. The study was conducted for slow freezing and vitrification. Depending on the method chosen, the width and timing of the intermediate region varies. The results may suggest, for example, that for slow freezing there is a high risk of cell-damaging ice crystal formation.
6. Example 3 in Chapter 5 (Subsection 5.4) presents heat transfer analysis coupled with crystallisation problem. In addition, the thermophysical parameters are defined by temperature-dependent polynomial function. The received results coincided with simulation data from literature [195]. In this example, the marker of cell damage was the maximum degree of crystallisation ($<10^{-6}$), which depended on the time of passage through the DTR. During cooling, this condition was satisfied, while during heating it was temporarily exceeded due to the presence of recrystallisation phenomena.
7. Example 3 in Chapter 6 depicts the multiscale model of cryopreservation performed in the microfluidic system. This issue belongs to the group of coupled multiphysics problems. It considers not only heat and mass transfer with osmotic transport, but also fluid flow. Because of the delivery method of the bath solution to the sample placed in the microchamber, the mass transport equation needs to include the component with advection phenomenon. In this case, no obstacle is presented in the microchannel, therefore the velocity is constant over the entire

domain. The results were compared with an example without a velocity vector. The obtained discrepancies show that for microfluidic systems, the introduction of a velocity vector into the mass transport model is crucial to the correctness of the calculations.

Based on the work completed, the following further research directions can be proposed:

- Introduce of temperature-dependent thermophysical parameters as polynomial functions into presented mathematical models. Currently, this approach is only used in Example 3 in Chapter 5 (Subsection 6.4).
- Preparation of mass transfer and osmotic transport analyses for cryopreservation by slow freezing and vitrification. In Chapter 6, the researches were performed only for the LT protocol.
- Application of other governing equations of heat and mass transfer and osmotic transport for modelling cryopreservation. It would be worthwhile to analyse whether fuzzy and interval arithmetic work effectively, for example, for the Cattaneo-Vernotte equation (heat transfer) or the Kedem-Katchalsky equation (osmotic transport).
- Analysis of other examples of cryopreserved biological samples. In the dissertation, among others, the results of the numerical analysis are presented for a sample of articular cartilage. However, experimental research is also performed on many other biological materials for which numerical models could be supplemented.
- Complete the simulation of the crystallisation process with a study on nucleation. This is related to the analysis of the activation energy that induces nucleation and growth. It also includes an assessment of the nucleation rates and changes in the ice crystals radius (ice crystals growth).
- Determination of the freezing point of the samples, which changes during cryopreservation by exposure to CPA. It would verify whether a cell-dangerous crystallisation process occurs for the specified parameters.
- Extension of a two-dimensional model to a three-dimensional model.

References

[1] A. Abazari, N. M. Jomha, J. A. W. Elliott, and L. E. McGann, Cryopreservation of articular cartilage, *Cryobiology*, vol. 66, no. 3, pp. 201–209, 2013, doi: 10.1016/j.cryobiol.2013.03.001.

[2] H. Ahmadikia and A. Moradi, Non-Fourier phase change heat transfer in biological tissues during solidification, *Heat Mass Transfer*, vol. 48, no. 9, pp. 1559–1568, 2012, doi: 10.1007/s00231-012-1002-1.

[3] R. Al-Attar and K. B. Storey, Lessons from nature: Leveraging the freeze-tolerant wood frog as a model to improve organ cryopreservation and biobanking, *Comparative Biochemistry and Physiology Part B: Biochemistry and Molecular Biology*, vol. 261, p. 110747, 2022, doi: 10.1016/j.cbpb.2022.110747.

[4] D. Anderson and C. Martin, Something Wild: Frozen Wood Frogs Thaw Out | New Hampshire Public Radio, Mar. 25, 2016. https://www.nhpr.org/something-wild/2016-03-25/something-wild-frozen-wood-frogs-thaw-out (accessed Jun. 29, 2022).

[5] G. Astarita and J. M. Kenny, The Stefan and Deborah Numbers in Polymer Crystallization, *Chemical Engineering Communications*, vol. 53, no. 1–6, pp. 69–84, 1987, doi: 10.1080/00986448708911884.

[6] H. E. Atyia and N. A. Hegab, Activation energy during the crystallization transition for Se-based chalcogenide glasses, *Optik*, vol. 243, p. 167527, 2021, doi: 10.1016/j.ijleo.2021.167527.

[7] A. Bénard and S. G. Advani, Energy equation and the crystallization kinetics of semi-crystalline polymers: regimes of coupling, *International Journal of Heat and Mass Transfer*, vol. 38, no. 5, pp. 819–832, 1995, doi: 10.1016/0017-9310(94)00205-A.

[8] J. D. Benson, A. Z. Higgins, K. Desai, and A. Eroglu, A toxicity cost function approach to optimal CPA equilibration in tissues, *Cryobiology*, vol. 80, pp. 144–155, 2018, doi: 10.1016/j.cryobiol.2017.09.005.

[9] J. Berger and W. Schneider, A zone model of rate controlled solidification, *Plastics and rubber processing and applications*, vol. 6, no. 2, pp. 127–133, 1986.

[10] P. Bętkowski, Porównywanie liczb rozmytych i rozmyty opis niepewności w analizie wytrzymałościowej, *Zeszyty Naukowe Politechniki Śląskiej, Seria: Budownictwo*, vol. 89, pp. 19–29, 2000.

[11] P. Boutron and P. Mehl, Theoretical prediction of devitrification tendency: Determination of critical warming rates without using finite expansions, *Cryobiology*, vol. 27, no. 4, pp. 359–377, 1990, doi: 10.1016/0011-2240(90)90015-V.

[12] K. G. M. Brockbank, Z. Z. Chen, and Y. C. Song, Vitrification of porcine articular cartilage, *Cryobiology*, vol. 60, no. 2, pp. 217–221, 2010, doi: 10.1016/j.cryobiol.2009.12.003.

[13] J. J. Buckley and Y. Qu, On using α-cuts to evaluate fuzzy equations, *Fuzzy Sets and Systems*, vol. 38, no. 3, pp. 309–312, 1990, doi: 10.1016/0165-0114(90)90204-J.

[14] J. J. Buckley and Y. Qu, Solving fuzzy equations: A new solution concept, *Fuzzy Sets and Systems*, vol. 39, no. 3, pp. 291–301, 1991, doi: 10.1016/0165-0114(91)90099-C.

[15] R. G. Bunge and J. K. Sherman, Fertilizing Capacity of Frozen Human Spermatozoa, *Nature*, vol. 172, no. 4382, pp. 767–768, 1953, doi: 10.1038/172767b0.

[16] T. Burczyński and J. Skrzypczyk, Theoretical and computational aspects of the stochastic boundary element method, *Computer Methods in Applied Mechanics and Engineering*, vol. 168, no. 1, pp. 321–344, 1999, doi: 10.1016/S0045-7825(98)00148-0.

[17] T. Burczyński, Shape Sensitivity Analysis of Uncertain Static and Vibrating Systems Using Stochastic Boundary Elements, in *Boundary Element Methods*, Berlin, Heidelberg, 1992, pp. 49–58. doi: 10.1007/978-3-662-06153-4_6.

[18] C. Cattaneo, A form of heat conduction equation which eliminates the paradox of instantaneous propagation, *Compte Rendus*, vol. 247, no. 4, pp. 431–433, 1958.

[19] C. Cattaneo, Sulla Conduzione Del Calore, *Atti de Seminario Matematico e Fisico Della Universita di Modena*, vol. 3, no. 3, pp. 3–21, 1948.

[20] Y. A. Çengel and J. M. Cimbala, *Fluid mechanics: fundamentals and applications*. Boston: McGraw-Hill Higher Education, 2006.

[21] Y. A. Çengel and A. J. Ghajar, *Heat and mass transfer: fundamentals and applications*. McGraw-Hill Higher Education, 2015.

[22] C. Chen, Pregnancy after human oocyte cryopreservation, *Lancet*, vol. 1, no. 8486, pp. 884–886, 1986, doi: 10.1016/s0140-6736(86)90989-x.

[23] Z. Chen, K. Memon, Y. Cao, and G. Zhao, A microfluidic approach for synchronous and nondestructive study of the permeability of multiple oocytes, *Microsyst Nanoeng*, vol. 6, no. 1, pp. 1–12, 2020, doi: 10.1038/s41378-020-0160-4.

[24] B. Cichocki, Albert Einstein – praca o ruchach Browna z 1905 roku, *DeltaMi*, 2005. http://www.deltami.edu.pl/temat/fizyka/struktura_materii/2011/01/01/Albert_Einstein-praca_o_ruchach/ (accessed Aug. 02, 2022).

[25] J. P. Costanzo, R. E. Lee, and M. F. Wright, Glucose loading prevents freezing injury in rapidly cooled wood frogs, *American Journal of Physiology-Regulatory, Integrative and Comparative Physiology*, vol. 261, no. 6, pp. R1549–R1553, 1991, doi: 10.1152/ajpregu.1991.261.6.R1549.

[26] E. Czogała and W. Pedrycz, *Elementy i metody teorii zbiorów rozmytych*. Państwowe Wydawnictwo Naukowe, 1985.

[27] Z.-S. Deng and J. Liu, Numerical simulation of selective freezing of target biological tissues following injection of solutions with specific thermal properties, *Cryobiology*, vol. 50, no. 2, pp. 183–192, 2005, doi: 10.1016/j.cryobiol.2004.12.007.

[28] P. D. Desai, Thermodynamic Properties of Iron and Silicon, *Journal of Physical and Chemical Reference Data*, vol. 15, no. 3, pp. 967–983, 1986, doi: 10.1063/1.555761.

[29] D. Devismita and A. Kumar, Effect of cryoprotectant on optimal cooling rate during cryopreservation, *Cryobiology*, vol. 70, no. 1, pp. 53–59, 2015, doi: 10.1016/j.cryobiol.2014.12.002.

[30] D. J. Dubois, *Fuzzy Sets and Systems: Theory and Applications*. Academic Press, 1980.

[31] D. Dubois and H. Prade, Operations on fuzzy numbers, *International Journal of systems science*, vol. 9, no. 6, pp. 613–626, 1978.

[32] M. Dziewoński, *Analiza numeryczna procesu zamrażania tkanki biologicznej*, Doctoral thesis, Politechnika Śląska, Gliwice, 2001.

[33] G. Eder, H. Janeschitz-Kriegl, and S. Liedauer, Crystallization processes in quiescent and moving polymer melts under heat transfer conditions, *Progress in Polymer Science*, vol. 15, no. 4, pp. 629–714, 1990, doi: 10.1016/0079-6700(90)90008-O.

[34] A. Einstein, Über die von der molekularkinetischen Theorie der Wärme geforderte Bewegung von in ruhenden Flüssigkeiten suspendierten Teilchen, *Annalen der Physik*, vol. 322, no. 8, pp. 549–560, 1905, doi: 10.1002/andp.19053220806.

[35] B. C. Elford and C. A. Walter, Effects of electrolyte composition and pH on the structure and function of smooth muscle cooled to −79 °C in unfrozen media, *Cryobiology*, vol. 9, no. 2, pp. 82–100, 1972, doi: 10.1016/0011-2240(72)90015-6.

[36] H. Y. Elmoazzen, J. A. W. Elliott, and L. E. McGann, Osmotic Transport across Cell Membranes in Nondilute Solutions: A New Nondilute Solute Transport Equation, *Biophysical Journal*, vol. 96, no. 7, pp. 2559–2571, 2009, doi: 10.1016/j.bpj.2008.12.3929.

[37] J. Farrant, Mechanism of Cell Damage During Freezing and Thawing and its Prevention, *Nature*, vol. 205, no. 4978, pp. 1284–1287, 1965, doi: 10.1038/2051284a0.

[38] A. Fick, Ueber Diffusion, *Annalen der Physik*, vol. 94, no. 1, pp. 59–86, 1855, doi: 10.1002/andp.18551700105.

[39] A. Fick, V. On liquid diffusion, *Philosophical Magazine*, vol. 10, no. 63, pp. 30–39, 1855, doi: 10.1080/14786445508641925.

[40] J. B. J. Fourier, *Théorie analytique de la chaleur*. Firmin Didot, 1882.

[41] M. Friedman, M. Ming, and A. Kandel, Fuzzy linear systems, *Fuzzy Sets and Systems*, vol. 96, no. 2, pp. 201–209, 1998, doi: 10.1016/S0165-0114(96)00270-9.

[42] B. Gajda and I. Rajska, Aktualny stan i możliwości kriokonserwacji zarodków i oocytów zwierząt gospodarskich, *Roczniki Naukowe Polskiego Towarzystwa Zootechnicznego*, vol. 10, no. 4, pp. 89–111, 2014.

[43] M. Y. Ge, C. Shu, W. M. Yang, and K. J. Chua, Incorporating an immersed boundary method to study thermal effects of vascular systems during tissue cryo-freezing, *Journal of Thermal Biology*, vol. 64, pp. 92–99, 2017, doi: 10.1016/j.jtherbio.2017.01.006.

[44] C. J. Glassbrenner and G. A. Slack, Thermal Conductivity of Silicon and Germanium from 3K to the Melting Point, *Physical Review*, vol. 134, no. 4A, pp. A1058--AI069, 1964.

[45] D. A. Gook, History of oocyte cryopreservation, *Reproductive BioMedicine Online*, vol. 23, no. 3, pp. 281–289, 2011, doi: 10.1016/j.rbmo.2010.10.018.

[46] R. Gryboś, *Mechanika płynów*, 7th ed. Gliwice: Wydawnictwo Politechniki Slaskiej, 1991.

[47] M. L. Guerra and L. Stefanini, Approximate fuzzy arithmetic operations using monotonic interpolations, *Fuzzy Sets and Systems*, vol. 150, no. 1, pp. 5–33, 2005, doi: 10.1016/j.fss.2004.06.007.

[48] M. Hanss, *Applied Fuzzy Arithmetic*. Springer Berlin Heidelberg New York, 2005.

[49] M. Hatłas, *Modelling and optimisation of inhomogeneous materials using granular computations*, Doctoral thesis, Politechnika Śląska, Gliwice, 2021.

[50] Y. Hayashi, I. Horiguchi, M. Kino-oka, and H. Sugiyama, Slow freezing process design for human induced pluripotent stem cells by modeling intracontainer variation, *Computers & Chemical Engineering*, vol. 132, p. 106597, 2020, doi: 10.1016/j.compchemeng.2019.106597.

[51] O. He and W. Yi, On fuzzy differential equations, *Fuzzy Sets and Systems*, vol. 32, no. 3, pp. 321–325, 1989, doi: 10.1016/0165-0114(89)90264-9.

[52] C. W. Hirt, B. D. Nichols, and N. C. Romero, *SOLA: A numerical solution algorithm for transient fluid flows*, Los Alamos Scientific Lab., N. Mex.(USA), LA-5852, 1975.

[53] J. Horacek, *Interval linear and nonlinear systems*, Doctoral thesis, Charles University, Prague, 2019.

[54] S. R. Idelsohn, M. A. Storti, and L. A. Crivelli, Numerical methods in phase-change problems, *ARCO*, vol. 1, no. 1, pp. 49–74, 1994, doi: 10.1007/BF02736180.

[55] M. H. Jacobs, The simultaneous measurement of cell permeability to water and to dissolved substances, *Journal of Cellular and Comparative Physiology*, vol. 2, no. 4, pp. 427–444, 1933, doi: 10.1002/jcp.1030020405.

[56] M. H. Jacobs and D. R. Stewart, A simple method for the quantitative measurement of cell permeability, *Journal of Cellular and Comparative Physiology*, vol. 1, no. 1, pp. 71–82, 1932, doi: 10.1002/jcp.1030010107.

[57] T. H. Jang *et al.*, Cryopreservation and its clinical applications, *Integrative Medicine Research*, vol. 6, no. 1, pp. 12–18, 2017, doi: 10.1016/j.imr.2016.12.001.

[58] M. Jasiński, *Modelowanie matematyczne procesu uszkodzenia tkanki wywołanego oddziaływaniem zewnętrznych źródeł ciepła*, 1 vols. Gliwice: Wydawnictwo Politechniki Slaskiej, 2016.

[59] R. K. June and D. P. Fyhrie, Temperature effects in articular cartilage biomechanics, *Journal of Experimental Biology*, vol. 213, no. 22, pp. 3934–3940, 2010, doi: 10.1242/jeb.042960.

[60] K. A. Jungare, R. Radha, and D. Sreekanth, Cryopreservation of biological samples – A short review, *Materials Today: Proceedings*, vol. 51, pp. 1637–1641, 2022, doi: 10.1016/j.matpr.2021.11.203.

[61] J. Jura, Organizm żywy, *Encyklopedia biologiczna*. Agencja Publicystyczno-Wydawnicza Opres, Kraków, 1999.

[62] J. Kacprzyk, *Zbiory rozmyte w analizie systemowej*. Państwowe Wydaw. Naukowe, 1986.

[63] S. Kandlikar, S. Garimella, D. Li, S. Colin, and M. R. King, *Heat Transfer and Fluid Flow in Minichannels and Microchannels*. Elsevier, 2005.

[64] J. O. M. Karlsson, E. G. Cravalho, and M. Toner, A model of diffusion-limited ice growth inside biological cells during freezing, *Journal of Applied Physics*, vol. 75, no. 9, pp. 4442–4455, 1994, doi: 10.1063/1.355959.

[65] A. G. Kay, J. A. Hoyland, P. Rooney, J. N. Kearney, and D. E. Pegg, A liquidus tracking approach to the cryopreservation of human cartilage allografts, *Cryobiology*, vol. 71, no. 1, pp. 77–84, 2015, doi: 10.1016/j.cryobiol.2015.05.005.

[66] O. Kedem and A. Katchalsky, Thermodynamic analysis of the permeability of biological membranes to non-electrolytes, *Biochimica et Biophysica Acta*, vol. 27, pp. 229–246, 1958, doi: 10.1016/0006-3002(58)90330-5.

[67] F. W. Kleinhans, Membrane Permeability Modeling: Kedem–Katchalsky vs a Two-Parameter Formalism, *Cryobiology*, vol. 37, no. 4, pp. 271–289, 1998, doi: 10.1006/cryo.1998.2135.

[68] A. Korczak, *Interwałowa metoda siatek Boltzmanna w modelowaniu przepływu ciepła w skali nano*, Doctoral thesis, Politechnika Śląska, Gliwice, 2016.

[69] B. Kosko, *Fuzzy engineering*. New Yersey, USA: Prentice-Hall, Inc., 1996.

[70] R. Krawczyk, Newton-Algorithmen zur Bestimmung von Nullstellen mit Fehlerschranken, *Computing*, vol. 4, no. 3, pp. 187–201, 1969, doi: 10.1007/BF02234767.

[71] L. Kuleshova, L. Gianaroli, C. Magli, A. Ferraretti, and A. Trounson, Birth following vitrification of a small number of human oocytes: Case Report, *Human Reproduction*, vol. 14, no. 12, pp. 3077–3079, 1999, doi: 10.1093/humrep/14.12.3077.

[72] L. L. Kuleshova, X. W. Wang, Y. N. Wu, Y. Zhou, and H. Yu, Vitrification of encapsulated hepatocytes with reduced cooling/warming rates, *Cryo-Letters*, vol. 25, no. 4, pp. 241–254, 2004.

[73] S. Kumar and S. Singh, Numerical Study on Biological Tissue Freezing Using Dual Phase Lag Bio-Heat Equation, in *Trends in Biomathematics: Modeling, Optimization and Computational Problems: Selected works from the BIOMAT Consortium Lectures, Moscow 2017*, R. P. Mondaini, Ed. Cham: Springer International Publishing, 2018, pp. 283–300. doi: 10.1007/978-3-319-91092-5_19.

[74] J. Lang, B. Erdmann, and M. Seebass, Impact of nonlinear heat transfer on temperature control in regional hyperthermia, *IEEE Transactions on Biomedical Engineering*, vol. 46, no. 9, pp. 1129–1138, 1999, doi: 10.1109/10.784145.

[75] L. Laouar, K. Fishbein, L. E. McGann, W. E. Horton, R. G. Spencer, and N. M. Jomha, Cryopreservation of porcine articular cartilage: MRI and biochemical results after different freezing protocols, *Cryobiology*, vol. 54, no. 1, pp. 36–43, 2007, doi: 10.1016/j.cryobiol.2006.10.193.

[76] A. Lawson, I. N. Mukherjee, and A. Sambanis, Mathematical modeling of cryoprotectant addition and removal for the cryopreservation of engineered or natural tissues, *Cryobiology*, vol. 64, no. 1, pp. 1–11, 2012, doi: 10.1016/j.cryobiol.2011.11.006.

[77] J. R. Layne Jr. and R. E. Lee Jr., Freeze tolerance and the dynamics of ice formation in wood frogs (*Rana sylvatica*) from southern Ohio, *Can. J. Zool.*, vol. 65, no. 8, pp. 2062–2065, 1987, doi: 10.1139/z87-315.

[78] R. L. Levin, E. G. Cravalho, and C. E. Huggins, A membrane model describing the effect of temperature on the water conductivity of erythrocyte membranes at subzero temperatures, *Cryobiology*, vol. 13, no. 4, pp. 415–429, 1976, doi: 10.1016/0011-2240(76)90097-3.

[79] W. Liu, G. Zhao, Z. Shu, T. Wang, K. Zhu, and D. Gao, High-precision approach based on microfluidic perfusion chamber for quantitative analysis of biophysical properties of cell membrane, *International Journal of Heat and Mass Transfer*, vol. 86, pp. 869–879, 2015, doi: 10.1016/j.ijheatmasstransfer.2015.03.038.

[80] J. E. Lovelock and M. W. H. Bishop, Prevention of Freezing Damage to Living Cells by Dimethyl Sulphoxide, *Nature*, vol. 183, no. 4672, pp. 1394–1395, 1959, doi: 10.1038/1831394a0.

[81] A. V. Luikov, Heat and Mass Transfer in Capillary-Porous Bodies, *Advances in Heat Transfer*, vol. 1, pp. 123–184, 1964, doi: 10.1016/S0065-2717(08)70098-4.

[82] B. Luyet, The vitrification of organic colloids and of protoplasm, *Biodynamica*, vol. 1, pp. 1–14, 1937.

[83] M. Magrzyk, Oszukać śmierć – historia, teraźniejszość i perspektywy krioniki, *Biotechnologia.pl*, May 06, 2021. https://biotechnologia.pl/biotechnologia/oszukac-smierc-historia-terazniejszosc-i-perspektywy-krioniki,20771#fbr (accessed Jun. 29, 2022).

[84] E. Majchrzak and M. Jasinski, Numerical estimation of burn degree of skin tissue using the sensitivity analysis methods, *Acta of Bioengineering and Biomechanics*, vol. 4, pp. 464–465, 2003.

[85] E. Majchrzak, B. Mochnacki, M. Dziewoński, and M. Jasiński, Numerical Modelling of Hyperthermia and Hypothermia Processes, *Advanced Materials Research*, vol. 268–270, pp. 257–262, 2011, doi: 10.4028/www.scientific.net/AMR.268-270.257.

[86] E. Majchrzak and M. Paruch, Identification of electromagnetic field parameters assuring the cancer destruction during hyperthermia treatment, *Inverse Problems in Science and Engineering*, vol. 19, no. 1, pp. 45–58, 2011, doi: 10.1080/17415977.2010.531473.

[87] E. Majchrzak, Ł. Turchan, and J. Dziatkiewicz, Modeling of skin tissue heating using the generalized dual phase-lag equation, *Archives of Mechanics*, vol. 67, no. 6, pp. 417–437, 2015.

[88] E. Majchrzak and B. Mochnacki, *Metody numeryczne: podstawy teoretyczne, aspekty praktyczne i algorytmy*, Wyd. 4 rozsz. i uzup.. Gliwice: Wydaw. Politechniki Śląskiej, 2005.

[89] E. Majchrzak and M. Stryczyński, Dual-phase lag model of heat transfer between blood vessel and biological tissue, *MBE*, vol. 18, no. 2, Art. no. mbe-18-02-081, 2021, doi: 10.3934/mbe.2021081.

[90] P. Mantegazza, Sullo sperma umano, *Rendic reale Instit Lomb*, vol. 13, pp. 183–196, 1866.

[91] S. M. Markov, Extended interval arithmetic involving infinite intervals, *Math. Balkanika, New Ser*, vol. 6, pp. 269–304, 1992.

[92] S. Markov, On directed interval arithmetic and its applications, in *J.UCS The Journal of Universal Computer Science*, H. Maurer, C. Calude, and A. Salomaa, Eds. Berlin, Heidelberg, German: Springer, 1996, pp. 514–526. doi: 10.1007/978-3-642-80350-5_43.

[93] P. Maślankiewicz and H. Wojciechowski, Ogrzewanie zamarzającą wodą, *Źródła ciepła i energii elektrycznej*, pp. 19–24, 2007.

[94] P. Mazur, Kinetics of Water Loss from Cells at Subzero Temperatures and the Likelihood of Intracellular Freezing, *Journal of General Physiology*, vol. 47, no. 2, pp. 347–369, 1963, doi: 10.1085/jgp.47.2.347.

[95] P. Mazur, Studies on Rapidly Frozen Suspensions of Yeast Cells by Differential Thermal Analysis and Conductometry, *Biophysical Journal*, vol. 3, no. 4, pp. 323–353, 1963, doi: 10.1016/S0006-3495(63)86824-1.

[96] L. E. McGann, M. Stevenson, K. Muldrew, and N. Schachar, Kinetics of osmotic water movement in chondrocytes isolated from articular cartilage and applications to cryopreservation, *Journal of Orthopaedic Research*, vol. 6, no. 1, pp. 109–115, 1988, doi: 10.1002/jor.1100060114.

[97] MeGlobalTM, Ethylene Glycol Product Guide, *The MEGlobal Group of Companies*, pp. 20–21, 2008.

[98] B. Mochnacki and E. Majchrzak, Numerical model of thermal interactions between cylindrical cryoprobe and biological tissue using the dual-phase lag equation, *International Journal of Heat and Mass Transfer*, vol. 108, pp. 1–10, 2017, doi: 10.1016/j.ijheatmasstransfer.2016.11.103.

[99] B. Mochnacki and A. Piasecka-Belkhayat, Numerical Modeling of Skin Tissue Heating Using the Interval Finite Difference Method, *Molecular & Cellular Biomechanics*, vol. 10, no. 3, pp. 233–244, 2013, doi: 10.3970/mcb.2013.010.233.

[100] B. Mochnacki and J. Suchy, *Modelowanie i symulacja krzepnięcia odlewów*. Warszawa: Wydawnictwo Naukowe PWN, 1993.

[101] O. M. Moen, The case for cryonics, *Journal of Medical Ethics*, vol. 41, no. 8, pp. 677–681, 2015, doi: 10.1136/medethics-2015-102715.

[102] R. E. Moore, *Interval Analysis*. New Jersey, USA: Printice-Hall, 1966.

[103] A. Moradi and H. Ahmadikia, Numerical study of the solidification process in biological tissue with blood flow and metabolism effects by the dual phase lag model, *Proc Inst Mech Eng H*, vol. 226, no. 5, pp. 406–416, 2012, doi: 10.1177/0954411912441305.

[104] I. N. Mukherjee, Y. Li, Y. C. Song, R. C. Long, and A. Sambanis, Cryoprotectant transport through articular cartilage for long-term storage: experimental and modeling studies, *Osteoarthritis and Cartilage*, vol. 16, no. 11, pp. 1379–1386, 2008, doi: 10.1016/j.joca.2008.03.027.

[105] J. W. Mullin, *Crystallization*, 4th ed. Elsevier, 2001.

[106] A. Nakayama and F. Kuwahara, A general bioheat transfer model based on the theory of porous media, *International Journal of Heat and Mass Transfer*, vol. 51, no. 11, pp. 3190–3199, 2008, doi: 10.1016/j.ijheatmasstransfer.2007.05.030.

[107] R. Nelson and S. Stanley, We Froze the First Man, New York, 1968, pp. 17–20.

[108] A. Neumaier, *Interval Methods for Systems of Equations*. Cambridge: Cambridge University Press, 1990.

[109] F. E. Neumann, C. P. Frank, and R. von Mises, *Die Differential und Integral leichungen der Mechanik und Physik*, 2nd ed. Brauschweig: Vieweg, 1927.

[110] A. Niwińska, Przegląd metod kriokonserwacji pod kątem techniki witryfikacyjnej, *Życie weterynaryjne*, vol. 91, no. 7, pp. 505–508, 2016.

[111] R. Ocone and G. Astarita, Continuous and discontinuous models for transport phenomena in polymers, *AIChE Journal*, vol. 33, no. 3, pp. 423–435, 1987, doi: 10.1002/aic.690330308.

[112] I. Onari, M. Hayashi, N. Ozaki, and H. Tsuchiya, Vitreous preservation of articular cartilage from cryoinjury in rabbits, *Cryobiology*, vol. 65, no. 2, pp. 98–103, 2012, doi: 10.1016/j.cryobiol.2012.05.006.

[113] L. Onsager, Reciprocal Relations in Irreversible Processes. I., *Phys. Rev.*, vol. 37, no. 4, pp. 405–426, 1931, doi: 10.1103/PhysRev.37.405.

[114] L. Onsager, Reciprocal Relations in Irreversible Processes. II., *Phys. Rev.*, vol. 38, no. 12, pp. 2265–2279, 1931, doi: 10.1103/PhysRev.38.2265.

[115] M. Paruch and B. Mochnacki, Cattaneo-Vernotte bio-heat transfer equation. Identificaton of external heat flux and relaxation time in domain of heated skin tissue., *Computer Assisted Methods in Engineering and Science*, vol. 25, no. 2–3, Art. no. 2–3, 2018, doi: 10.24423/cames.243.

[116] D. E. Pegg, L. Wang, and D. Vaughan, Cryopreservation of articular cartilage. Part 3: The liquidus-tracking method, *Cryobiology*, vol. 52, no. 3, pp. 360–368, 2006, doi: 10.1016/j.cryobiol.2006.01.004.

[117] D. E. Pegg, L. Wang, D. Vaughan, and C. J. Hunt, Cryopreservation of articular cartilage. Part 2: Mechanisms of cryoinjury, *Cryobiology*, vol. 52, no. 3, pp. 347–359, 2006, doi: 10.1016/j.cryobiol.2006.01.007.

[118] D. E. Pegg, M. C. Wusteman, and L. Wang, Cryopreservation of articular cartilage. Part 1: Conventional cryopreservation methods, *Cryobiology*, vol. 52, no. 3, pp. 335–346, 2006, doi: 10.1016/j.cryobiol.2006.01.005.

[119] D. E. Pegg, Equations for obtaining melting points and eutectic temperatures for the ternary system dimethyl sulphoxide/sodium chloride/water, *Cryo-Letters*, vol. 7, pp. 387–394, 1986.

[120] H. H. Pennes, Analysis of Tissue and Arterial Blood Temperatures in the Resting Human Forearm, *Journal of Applied Physiology*, vol. 1, no. 2, pp. 93–122, 1948.

[121] R. M. Perry, Suspension Failures: Lessons from the Early Years, *Cryonics*, 1992. Accessed: Jun. 29, 2022. [Online]. Available: https://www.alcor.org/library/suspension-failures-lessons-from-the-early-years/

[122] A. E. Peters, E. J. Comerford, S. Macaulay, K. T. Bates, and R. Akhtar, Micromechanical properties of canine femoral articular cartilage following multiple freeze-thaw cycles, *Journal of the Mechanical Behavior of Biomedical Materials*, vol. 71, pp. 114–121, 2017, doi: 10.1016/j.jmbbm.2017.03.006.

[123] A. Piasecka Belkhayat, Interval boundary element method for 2D transient diffusion problem using the directed interval arithmetic, *Engineering Analysis with Boundary Elements*, vol. 35, no. 3, pp. 259–263, 2011, doi: 10.1016/j.enganabound.2010.11.005.

[124] A. Piasecka-Belkhayat, Numerical modelling of solidification process using interval finite difference method, *Scientific Research of the Institute of Mathematics and Computer Science*, vol. 9, no. 1, pp. 155–163, 2010.

[125] A. Piasecka-Belkhayat, *Przedziałowa metoda elementów brzegowych w nieprecezyjnych zadaniach nieustalonej dyfuzji ciepła*. Gliwice: Wydawnictwo Politechniki Śląskiej, 2011.

[126] A. Piasecka-Belkhayat and A. Korczak, Analysis of ultrashort laser pulse irradiation with 2d thin metal films using the fuzzy lattice Boltzmann method, *Journal of Theoretical and Applied Mechanics*, vol. 58, no. 1, pp. 209–219, 2020, doi: 10.15632/jtam-pl/115448.

[127] A. Piasecka-Belkhayat and A. Korczak, Numerical modelling of the transient heat transport in a thin gold film using the fuzzy lattice Boltzmann method with α-cuts, *Journal of Applied Mathematics and Computational Mechanics*, vol. 15, no. 1, 2016, doi: 10.17512/jamcm.2016.1.13.

[128] A. Piasecka-Belkhayat and A. Skorupa, Application of interval arithmetic in heat transfer modelling in biological tissue domain, in *Engineering Mechanics 2020: book of full texts : 26th International Conference, November 24-25, 2020, Brno, Czech Republic*, Brno: Brno University of Technology, 2020, pp. 412–415.

[129] A. Piasecka-Belkhayat and A. Skorupa, Application of interval arithmetic in numerical modeling of cryopreservation process during cryoprotectant loading to microchamber, *Numerical Heat Transfer, Part A: Applications*, pp. 1–19, 2022, doi: 10.1080/10407782.2022.2105078.

[130] A. Piasecka-Belkhayat and A. Skorupa, Crystallisation Degree Analysis during Cryopreservation of Biological Tissue Applying Interval Arithmetic, *Materials*, vol. 16, no. 6, Art. no. 6, 2023, doi: 10.3390/ma16062186.

[131] A. Piasecka-Belkhayat and A. Skorupa, Numerical modeling of heat and mass transfer during cryopreservation using the fuzzy finite difference method, in *14th WCCM & ECCOMAS Congress 2020 : Virtual Congress 11 - 15 January, 2021. Book of Abstracts*, Barcelona: International Centre for Numerical Methods in Engineering (CIMNE), 2021, p. 1285.

[132] A. Piasecka-Belkhayat and A. Skorupa, Numerical Study of Heat and Mass Transfer during Cryopreservation Process with Application of Directed Interval Arithmetic, *Materials*, vol. 14, no. 11, p. 2966, 2021, doi: 10.3390/ma14112966.

[133] C. Polge, A. U. Smith, and A. S. Parkes, Revival of Spermatozoa after Vitrification and Dehydration at Low Temperatures, *Nature*, vol. 164, no. 4172, p. 666, 1949, doi: 10.1038/164666a0.

[134] C. Polge and L. E. A. Rowson, Fertilizing Capacity of Bull Spermatozoa after Freezing at −79° C., *Nature*, vol. 169, no. 4302, pp. 626–627, 1952, doi: 10.1038/169626b0.

[135] E. J. C. Polge, Low-temperature storage of mammalian spermatozoa, *Proceedings of the Royal Society of London. Series B - Biological Sciences*, vol. 147, no. 929, pp. 498–508, 1957, doi: 10.1098/rspb.1957.0068.

[136] O. Popczyk and G. Dziatkiewicz, Kansa method for solving initial-value problem of hyperbolic heat conduction in nonhomogeneous medium, *International Journal of Heat and Mass Transfer*, vol. 183, p. 122088, 2022, doi: 10.1016/j.ijheatmasstransfer.2021.122088.

[137] E. D. Popova, Multiplication Distributivity of Proper and Improper Intervals, *Reliable Computing*, vol. 7, no. 2, pp. 129–140, 2001, doi: 10.1023/A:1011470131086.

[138] R. W. Powell, C. Y. Ho, and P. E. Liley, *Thermal conductivity of selected materials*, vol. 8. Washington DC: US Department of Commerce, National Bureau of Standards, 1966.

[139] W. F. Rall and G. M. Fahy, Ice-free cryopreservation of mouse embryos at −196 °C by vitrification, *Nature*, vol. 313, no. 6003–2, pp. 573–575, 1985, doi: 10.1038/313573a0.

[140] H. S. Ren, Y. Wei, T. C. Hua, and J. Zhang, Theoretical Prediction of Vitrification and Devitrification Tendencies for Cryoprotective Solutions, *Cryobiology*, vol. 31, no. 1, pp. 47–56, 1994, doi: 10.1006/cryo.1994.1006.

[141] J. Rohn, Systems of linear interval equations, *Linear Algebra and its Applications*, vol. 126, pp. 39–78, 1989, doi: 10.1016/0024-3795(89)90004-9.

[142] E. Scannapieco and F. H. Harlow, *Introduction to finite-difference methods for numerical fluid dynamics*, Los Alamos National Lab.(LANL), Los Alamos, NM (United States), 1995.

[143] T. Scherr, S. Pursley, W. Todd Monroe, and K. Nandakumar, A numerical study on the loading of cryoprotectant cocktails-on-a-chip, Part I: Interacting miscible viscous fluids, *International Journal of Heat and Mass Transfer*, vol. 78, pp. 1284–1291, 2014, doi: 10.1016/j.ijheatmasstransfer.2014.07.026.

[144] T. Scherr, S. Pursley, W. Todd Monroe, and K. Nandakumar, A numerical study on the loading of cryoprotectant cocktails-on-a-chip. Part II: The cellular experience, *International Journal of Heat and Mass Transfer*, vol. 78, pp. 1292–1299, 2014, doi: 10.1016/j.ijheatmasstransfer.2014.07.025.

[145] B. M. Schulze, D. L. Watkins, J. Zhang, I. Ghiviriga, and R. K. Castellano, Estimating the shape and size of supramolecular assemblies by variable temperature diffusion ordered spectroscopy, *Org. Biomol. Chem.*, vol. 12, no. 40, pp. 7932–7936, 2014, doi: 10.1039/C4OB01373E.

[146] Bl. Sendov, Some topics of segment analysis, in *Interval Mathematics 1980*, K. L. E. Nickel, Ed. Academic Press, 1980, pp. 203–222. doi: 10.1016/B978-0-12-518850-0.50016-0.

[147] N. Shardt, K. K. Al-Abbasi, H. Yu, N. M. Jomha, L. E. McGann, and J. A. W. Elliott, Cryoprotectant kinetic analysis of a human articular cartilage vitrification protocol, *Cryobiology*, vol. 73, no. 1, pp. 80–92, 2016, doi: 10.1016/j.cryobiol.2016.05.007.

[148] M. Shi, S. Feng, X. Zhang, C. Ji, F. Xu, and T. J. Lu, Droplet based vitrification for cell aggregates: Numerical analysis, *Journal of the Mechanical Behavior of Biomedical Materials*, vol. 82, pp. 383–393, 2018, doi: 10.1016/j.jmbbm.2018.03.026.

[149] S. Singh and S. Kumar, Freezing of Biological Tissues During Cryosurgery Using Hyperbolic Heat Conduction Model, *Mathematical Modelling and Analysis*, vol. 20, no. 4, pp. 443–456, 2015, doi: 10.3846/13926292.2015.1064486.

[150] A. Skorupa and A. Piasecka-Belkhayat, Application of fuzzy finite difference method in heat and mass transfer during cryopreservation process, in *Recent advances in computational oncology and personalized medicine. Vol. 1, Vol. 1*, Gliwice: Wydawnictwo Politechniki Slaskiej, 2021, pp. 56–66. doi: 10.34918/83565.

[151] A. Skorupa and A. Piasecka-Belkhayat, Comparison of heat transfer phenomena for two different cryopreservation methods: slow freezing and vitrification, *Journal of Applied Mathematics and Computational Mechanics*, vol. 22, no. 1, pp. 53–65, 2023, doi: 10.17512/jamcm.2023.1.05.

[152] A. Skorupa and A. Piasecka-Belkhayat, Modelowanie procesu kriokonserwacji tkanki chrzęstnej z wykorzystaniem arytmetyki interwałowej, in *Studencka Konferencja Naukowa 'Metody Komputerowe - 2020'*, G. Dziatkiewicz and J. Ptaszny, Eds. Gliwice: Wydawnictwo Politechniki Slaskiej, 2020, pp. 137–140.

[153] A. Skorupa and A. Piasecka-Belkhayat, Numerical Modeling of Heat and Mass Transfer during Cryopreservation Using Interval Analysis, *Applied Sciences*, vol. 11, no. 1, p. 302, 2020, doi: 10.3390/app11010302.

[154] M. von Smoluchowski, Zur kinetischen Theorie der Brownschen Molekularbewegung und der Suspensionen, *Annalen der Physik*, vol. 326, no. 14, pp. 756–780, 1906, doi: 10.1002/andp.19063261405.

[155] Y. C. Song *et al.*, Vitreous Preservation of Articular Cartilage Grafts, *Journal of Investigative Surgery*, vol. 17, no. 2, pp. 65–70, 2004, doi: 10.1080/08941930490422438.

[156] Y. C. Song, P.-O. Hagen, F. G. Lightfoot, M. J. Taylor, A. C. Smith Dvm, and K. G. M. Brockbank, In Vivo Evaluation of the Effects of a New Ice-Free Cryopreservation Process on Autologous Vascular Grafts, *Journal of Investigative Surgery*, vol. 13, no. 5, pp. 279–288, 2000, doi: 10.1080/08941930050206300.

[157] Y. C. Song, F. G. Lightfoot, Z. Chen, M. J. Taylor, and K. G. M. Brockbank, Vitreous Preservation of Rabbit Articular Cartilage, *Cell Preservation Technology*, vol. 2, no. 1, pp. 67–74, 2004, doi: 10.1089/153834404322708772.

[158] Y. S. Song *et al.*, Vitrification and levitation of a liquid droplet on liquid nitrogen, *Proceedings of the National Academy of Sciences*, vol. 107, no. 10, pp. 4596–4600, 2010, doi: 10.1073/pnas.0914059107.

[159] Y. S. Song, S. Moon, L. Hulli, S. K. Hasan, E. Kayaalp, and U. Demirci, Microfluidics for cryopreservation, *Lab Chip*, vol. 9, no. 13, pp. 1874–1881, 2009, doi: 10.1039/B823062E.

[160] A. J. Staverman, Apparent osmotic pressure of solutions of heterodisperse polymers, *Recueil des Travaux Chimiques des Pays-Bas*, vol. 71, no. 6, pp. 623–633, 1952, doi: 10.1002/recl.19520710610.

[161] A. J. Staverman, The theory of measurement of osmotic pressure, *Recueil des Travaux Chimiques des Pays-Bas*, vol. 70, no. 4, pp. 344–352, 1951, doi: 10.1002/recl.19510700409.

[162] J. Stefan, Ueber die Theorie der Eisbildung, insbesondere über die Eisbildung im Polarmeere, *Annalen Physik Chemie*, vol. 42, pp. 269–286, 1891, doi: 10.1002/ANDP.18912780206.

[163] M. Stryczyński and E. Majchrzak, Modeling of heat transfer and fluid flow in a rectangular channel with an obstacle, *Journal of Applied Mathematics and Computational Mechanics*, vol. 19, no. 2, pp. 121–132, 2020, doi: 10.17512/jamcm.2020.2.10.

[164] T. Sunaga, Theory of an interval algebra and its application to numerical analysis, *RAAG memoirs*, vol. 2, pp. 29–46, 1958.

[165] W. Sutherland, LXXV. A dynamical theory of diffusion for non-electrolytes and the molecular mass of albumin, *Philosophical Magazine. Series 6*, vol. 9, no. 54, pp. 781–785, 1905, doi: 10.1080/14786440509463331.

[166] L. O. Svaasand, T. Boerslid, and M. Oeveraasen, Thermal and optical properties of living tissue: Application to laser-induced hyperthermia, *Lasers in Surgery and Medicine*, vol. 5, no. 6, pp. 589–602, 1985, doi: 10.1002/lsm.1900050607.

[167] K. W. Swanson, The Birth of the Sperm Bank, *The Annals of Iowa*, vol. 71, no. 3, 2012, doi: 10.17077/0003-4827.1645.

[168] J. M. Sztein, T. Takeo, and N. Nakagata, History of cryobiology, with special emphasis in evolution of mouse sperm cryopreservation, *Cryobiology*, vol. 82, pp. 57–63, 2018, doi: 10.1016/j.cryobiol.2018.04.008.

[169] H. Takamatsu, Y. Komori, S. Zawlodzka, and M. Fujii, Quantitative Examination of a Perfusion Microscope for the Study of Osmotic Response of Cells, *Journal of Biomechanical Engineering*, vol. 126, no. 4, pp. 402–409, 2004, doi: 10.1115/1.1784474.

[170] M. Tan, J. Mei, and J. Xie, The Formation and Control of Ice Crystal and Its Impact on the Quality of Frozen Aquatic Products: A Review, *Crystals*, vol. 11, no. 1, p. 68, 2021, doi: 10.3390/cryst11010068.

[171] M. J. Taylor and C. J. Hunt, A new preservation solution for storage of corneas at low temperatures, *Current Eye Research*, vol. 4, no. 9, pp. 963–973, 1985, doi: 10.3109/02713689509000003.

[172] S. Thirumala, J. M. Gimble, and R. V. Devireddy, Transport phenomena during freezing of adipose tissue derived adult stem cells, *Biotechnology and Bioengineering*, vol. 92, no. 3, pp. 372–383, 2005, doi: 10.1002/bit.20615.

[173] M. Trzcińska and M. Bryła, *Kierunki i możliwości modyfikacji metod kriokonserwacji oraz oceny jakości nasienia knura*. Kraków: Instytut Zootechniki PIB, 2020.

[174] D. B. Tuckerman and R. F. W. Pease, High-performance heat sinking for VLSI, *IEEE Electron Device Letters*, vol. 2, no. 5, pp. 126–129, 1981, doi: 10.1109/EDL.1981.25367.

[175] P. Vernotte, Les paradoxes de la theorie continue de l'equation de la chaleur, *Comptes rendus*, vol. 246, pp. 3154–3155, 1958.

[176] J. Wang, K. Zhu, G. Zhao, J. Ren, C. Yue, and D. Gao, Dual Dependence of Cryobiogical Properties of Sf21 Cell Membrane on the Temperature and the Concentration of the Cryoprotectant, *PLOS ONE*, vol. 8, no. 9, p. e72836, 2013, doi: 10.1371/journal.pone.0072836.

[177] J. Wang and T. Hou, Application of molecular dynamics simulations in molecular property prediction II: Diffusion coefficient, *Journal of Computational Chemistry*, vol. 32, no. 16, pp. 3505–3519, 2011, doi: 10.1002/jcc.21939.

[178] L. Wang, D. E. Pegg, J. Lorrison, D. Vaughan, and P. Rooney, Further work on the cryopreservation of articular cartilage with particular reference to the liquidus tracking (LT) method, *Cryobiology*, vol. 55, no. 2, pp. 138–147, 2007, doi: 10.1016/j.cryobiol.2007.06.005.

[179] Z. Wang, G. Zhao, T. Wang, Q. Yu, M. Su, and X. He, Three-dimensional numerical simulation of the effects of fractal vascular trees on tissue temperature and intracelluar ice formation during combined cancer therapy of cryosurgery and hyperthermia, *Applied Thermal Engineering*, vol. 90, pp. 296–304, 2015, doi: 10.1016/j.applthermaleng.2015.06.103.

[180] H. Witek, *Metoda rozmytych elementów brzegowych w analizie konstrukcji budowlanych o parametrach niepewnych*, Doctoral thesis, Politechnika Śląska, Gliwice, 2005.

[181] W. T. Wu, S.-R. Lyu, and W. H. Hsieh, Cryopreservation and biophysical properties of articular cartilage chondrocytes, *Cryobiology*, vol. 51, no. 3, pp. 330–338, 2005, doi: 10.1016/j.cryobiol.2005.08.006.

[182] F. Xu, S. Moon, X. Zhang, L. Shao, Y. S. Song, and U. Demirci, Multi-scale heat and mass transfer modelling of cell and tissue cryopreservation, *Philosophical Transactions of the Royal Society A: Mathematical, Physical and Engineering Sciences*, vol. 368, no. 1912, pp. 561–583, 2010, doi: 10.1098/rsta.2009.0248.

[183] X. Xu, Z. F. Cui, R. J. Wilkins, and J. P. G. Urban, Intracellular pH changes in isolated bovine articular chondrocytes during the loading and removal of cryoprotective agents, *Cryobiology*, vol. 46, no. 2, pp. 161–173, 2003, doi: 10.1016/S0011-2240(03)00022-1.

[184] X. Xu, Z. Cui, and J. P. G. Urban, Measurement of the chondrocyte membrane permeability to Me2SO, glycerol and 1,2-propanediol, *Medical Engineering & Physics*, vol. 25, no. 7, pp. 573–579, 2003, doi: 10.1016/S1350-4533(03)00073-0.

[185] Y. Xu, L. Zhang, J. Xu, Y. Wei, and X. Xu, Membrane permeability of the human pluripotent stem cells to Me2SO, glycerol and 1,2-propanediol, *Archives of Biochemistry and Biophysics*, vol. 550–551, pp. 67–76, 2014, doi: 10.1016/j.abb.2014.04.010.

[186] R. C. Young, The algebra of many-valued quantities, *Math. Ann.*, vol. 104, no. 1, pp. 260–290, 1931, doi: 10.1007/BF01457934.

[187] X. Yu, S. Zhang, and G. Chen, Modeling the addition/removal of dimethyl sulfoxide into/from articular cartilage treated with the liquidus-tracking method, *International Journal of Heat and Mass Transfer*, vol. 141, pp. 719–730, 2019, doi: 10.1016/j.ijheatmasstransfer.2019.07.032.

[188] L. A. Zadeh, Fuzzy sets, *Information and Control*, vol. 8, no. 3, pp. 338–353, 1965.

[189] S. Zhang, X. Yu, and G. Chen, Permeation of dimethyl sulfoxide into articular cartilage at subzero temperatures, *J. Zhejiang Univ. Sci. B*, vol. 13, no. 3, pp. 213–220, 2012, doi: 10.1631/jzus.B11a0041.

[190] Y. Zhang, G. Zhao, S. M. Chapal Hossain, and X. He, Modeling and experimental studies of enhanced cooling by medical gauze for cell cryopreservation by vitrification, *International Journal of Heat and Mass Transfer*, vol. 114, pp. 1–7, 2017, doi: 10.1016/j.ijheatmasstransfer.2017.06.036.

[191] G. Zhao and J. Fu, Microfluidics for cryopreservation, *Biotechnology Advances*, vol. 35, no. 2, pp. 323–336, 2017, doi: 10.1016/j.biotechadv.2017.01.006.

[192] G. Zhao, Z. Huang, and D. Gao, Microdevices for Measurement of Cell Membrane Biophysical Properties, in *Multiscale Technologies For Cryomedicine: Implementation From Nano To Macroscale*, J. C. Bischof and S. X. He, Eds. World Scientific, 2016.

[193] Y. Zheng, G. Zhao, Y. Zhang, and R. Gao, On-chip loading and unloading of cryoprotectants facilitate cell cryopreservation by rapid freezing, *Sensors and Actuators B: Chemical*, vol. 255, pp. 647–656, 2018, doi: 10.1016/j.snb.2017.08.084.

[194] X. Zhou *et al.*, Microfiltration-based sequential perfusion: A new approach for improved loading/unloading of cryoprotectants, *Sensors and Actuators B: Chemical*, vol. 312, p. 127957, 2020, doi: 10.1016/j.snb.2020.127957.

[195] X. Zhou, X. M. Liang, J. Wang, P. Du, and D. Gao, Theoretical and experimental study of a membrane-based microfluidics for loading and unloading of cryoprotective agents, *International Journal of Heat and Mass Transfer*, vol. 127, pp. 637–644, 2018, doi: 10.1016/j.ijheatmasstransfer.2018.06.137.

[196] X. Zhou, Z. Liu, X. M. Liang, Z. Shu, P. Du, and D. Gao, Theoretical investigations of a novel microfluidic cooling/warming system for cell vitrification cryopreservation, *International Journal of Heat and Mass Transfer*, vol. 65, pp. 381–388, 2013, doi: 10.1016/j.ijheatmasstransfer.2013.06.022.

[197] Biological Miracle - Gates Of The Arctic National Park & Preserve (U.S. National Park Service). https://www.nps.gov/gaar/learn/nature/wood-frog-page-2.htm (accessed Jun. 29, 2022).

[198] Cedar Rapids Gazette Archives, Apr 4, 1954, p. 50, *NewspaperArchive.com*, Apr. 04, 1954. https://newspaperarchive.com/cedar-rapids-gazette-apr-04-1954-p-50/ (accessed Jun. 29, 2022).

[199] A. Mersmann, Ed., *Crystallization Technology Handbook*, Second Ed. Revised and Expanded. CRC Press, 2001.

[200] Definition of cryopreservation | Dictionary.com, *www.dictionary.com*. https://www.dictionary.com/browse/cryopreservation (accessed Feb. 15, 2023).

[201] *Investigations of the Thermal Properties of Human and Animal Tissues*, Doctoral thesis, University of Glasgow, Glasgow, 1998. [Online]. Available: https://theses.gla.ac.uk/1019/1/1998hamiltonphd.pdf

[202] Komórka, *Encyklopedia PWN*. Accessed: Jul. 09, 2022. [Online]. Available: https://encyklopedia.pwn.pl/haslo/komorka;3924552.html

[203] Krionika, *Słownik języka polskiego PWN*. Accessed: Jun. 29, 2022. [Online]. Available: https://sjp.pwn.pl/sjp/krionika;2564945.html

[204] Narząd, *Encyklopedia PWN*. Accessed: Jul. 09, 2022. [Online]. Available: https://encyklopedia.pwn.pl/haslo/;3945924

[205] Thermal Conductivity: Silicon. https://www.efunda.com/materials/elements/TC_Table.cfm?Element_ID=Si (accessed Nov. 17, 2022).

[206] Tkanka, *Encyklopedia PWN*. Accessed: Jul. 09, 2022. [Online]. Available: https://encyklopedia.pwn.pl/haslo/tkanka;3987572.html

[207] Układ narządów, *Encyklopedia PWN*. Accessed: Jul. 09, 2022. [Online]. Available: https://encyklopedia.pwn.pl/haslo/;3990951

[208] Właściwości popularnych rozpuszczalników i cieczy. https://www.trimen.pl/witek/ciecze/old_index.html (accessed Dec. 29, 2022).

Streszczenie

Niniejsza praca poświęcona jest modelowaniu wielkoskalowemu sprzężonych ze sobą zjawisk, które zachodzą podczas kriokonserwacji. Jest to proces, który polega na spowolnieniu aktywności materiału biologicznego poprzez obniżenie temperatury poniżej temperatury fizjologicznej, a następnie na przywróceniu funkcji kriokonserwowanych tkanek lub komórek, zachowując równocześnie ich podstawowe czynności życiowe. W celu uniknięcia negatywnych skutków procesu stosuje się związki chemiczne zwane krioprotektantami oraz regulację szybkości chłodzenia. W pracy zaprezentowano przykładowe metody kriokonserwacji, takie jak wolne zamrażanie, witryfikacja oraz protokół „śledzenia krzywej likwidus". Przedstawiono również zjawiska transportowe, takie jak: przepływ ciepła wraz z krystalizacją, przepływ masy w kontekście dyfuzji masy i przepływu cieczy oraz transport osmotyczny. W rozprawie zamieszczono przykładowe symulacje numeryczne poszczególnych zjawisk transportowych. Rozpatrywano przepływ ciepła opisany równaniem Fouriera lub równaniem Pennesa. Rozważano również zagadnienia związane z przemianami fazowymi oraz krystalizacją kryształów lodu, w której stopień krystalizacji oszacowano za pomocą nieizotermicznego równania kinetycznego Boutrona-Mehla. W pracy badano również przepływ masy sprzężony z zagadnieniem termicznym. Wykorzystując równanie konwekcji-dyfuzji lub drugie prawo Ficka w przypadku pominięcia adwekcji, analizowano problem dyfuzji cząsteczek z roztworu kąpieli do roztworu macierzy zewnątrzkomórkowej. W pracy zawarto również opis zjawiska transportu osmotycznego za pomocą modelu dwuparametrycznego, który pozwala oszacować zmianę objętości komórek wywołaną wymianą cząsteczek wody i krioprotektanta pomiędzy roztworami zewnątrz- i wewnątrzkomórkowym. Występujący w pracy model numeryczny oparto na metodzie różnic skończonych uzupełnionej o arytmetykę interwałową oraz rozmytą, w której wykorzystano koncepcję α-przekrojów. W modelu matematycznym wprowadzono w miejsce parametrów deterministycznych liczby rozmyte oraz interwałowe, biorąc pod uwagę ich nieprecyzyjność. Opracowano algorytmy i autorskie programy komputerowe w środowisku Embarcadero Delphi 10.4 Community Edition.

Abstract

This thesis is devoted to large-scale modelling of the coupled phenomena that occur during cryopreservation. This is a process that involves slowing down the activity of biological material by lowering the temperature below physiological temperature and then restoring the function of the cryopreserved tissues or cells, while preserving their basic vital activities. In order to avoid the negative effects of the process, chemical compounds called cryoprotectants and regulation of the cooling rate are used. This paper presents examples of cryopreservation methods such as slow freezing, vitrification and the “liquidus tracking” protocol. Transport phenomena such as heat transfer with crystallisation, mass transfer in the context of mass diffusion and fluid flow, and osmotic transport are also presented. The work includes examples of numerical simulations of individual transport phenomena. Heat transfer described by the Fourier equation or the Pennes equation was considered. Issues related to phase changes and the crystallisation of ice crystals, in which the degree of crystallisation was estimated using the non-isothermal Boutron-Mehl kinetic equation, were also considered. The work also investigated mass transfer coupled to the thermal problem. Using the convection-diffusion equation or Fick's second law in the case of neglecting advection, the problem of diffusion of molecules from the bath solution to the extracellular matrix solution was analysed. The paper also includes a description of the osmotic transport phenomenon using a two-parameter model to estimate the change in cell volume induced by the exchange of water and cryoprotectant molecules between the extracellular and intracellular solutions. The numerical model appearing in this paper is based on the finite difference method supplemented by interval and fuzzy arithmetic, in which the concept of α-cuts was used. In the mathematical model, fuzzy and interval numbers were introduced in place of deterministic parameters, taking into account their imprecision. Algorithms and original computer programmes were developed in the Embarcadero Delphi 10.4 Community Edition environment.